UNIVERSITY OF Southampton

University of Southampton Research Repository
ePrints Soton

Copyright © and Moral Rights for this thesis are retained by the author and/or other copyright owners. A copy can be downloaded for personal non-commercial research or study, without prior permission or charge. This thesis cannot be reproduced or quoted extensively from without first obtaining permission in writing from the copyright holder/s. The content must not be changed in any way or sold commercially in any format or medium without the formal permission of the copyright holders.

When referring to this work, full bibliographic details including the author, title, awarding institution and date of the thesis must be given e.g.

AUTHOR (year of submission) "Full thesis title", University of Southampton, name of the University School or Department, PhD Thesis, pagination

http://eprints.soton.ac.uk

UNIVERSITY OF SOUTHAMPTON

FACULTY OF NATURAL AND ENVIRONMENTAL SCIENCES

Chemistry

Understanding the catalytic benefits of multi-metallic active sites in microporous aluminophosphates

by

Matthew Edward Potter

Thesis for the degree of Doctor of Philosophy

September 2014

UNIVERSITY OF SOUTHAMPTON

ABSTRACT

FACULTY OF NATURAL AND ENVIRONMENTAL SCIENCES

Chemistry

Thesis for the degree of Doctor of Philosophy

UNDERSTANDING THE CATALYTIC BENEFITS OF MULTI-METALLIC ACTIVE SITES IN MICROPOROUS ALUMINOPHOSPHATES

Matthew Edward Potter

Structure-property correlations, which direct the formation of specific active-acid sites, in nanoporous materials have been explored with the aim to further the notion of rational catalyst design. It is demonstrated that the influence of the specific zeotype framework extends beyond modulating Brønsted acidity, with the framework topology playing a fundamental role in reaction kinetics. The structural integrity and nature of the active site has been probed using a combined catalysis and multi-technique characterisation study, aimed at optimising the sustainable production of ε-Caprolactam, the precursor of the recyclable Nylon-6 polymer.

The effect of bimetallic substitution, with an aim to generate novel acid sites, has been explored using Mg^{2+}, Zn^{2+} and Si^{4+} dopants. Through a combined CO and lutidine-probed FT-IR study, the nature of the acid site has been examined and correlated to the nature of the dopants present. The presence of multiple dopant atoms has had a significant effect on catalytic activity, modulating the presence of acid sites to allow new active species to be discovered, and prompting synergistic interactions in multi-step pathways.

A combined X-ray absorption spectroscopy and *ab initio* DFT theoretical study was used to probe the nature of the active sites responsible for

catalytic synergy in Co-Ti bimetallic nanoporous frameworks. Contrasting the bimetallic and analogous monometallic species has led to the discovery of a unique bimetallic Co-O-Ti bond. The properties of this bond have been explored and contrasted with the analogous monometallic species, with specific reference to their catalytic applicability for sustainable oxidation reactions. The catalytic synergy prompted by the bimetallic substitution in the CoTiAlPO-5 material has been investigated and contrasted to the monometallic system. Specific focus was placed on the *in-situ* production of hydroxylamine as part of the sustainable aerobic ammoximation of cyclohexanone. Periodic DFT calculations have revealed subtle mechanistic differences between the mono- and bimetallic systems which account for energetic differences in the rate determining step of the reaction pathway.

Table of Contents

List of tables

List of figures

DECLARATION OF AUTHORSHIP

I, Matthew Edward Potter

declare that this thesis and the work presented in it are my own and has been generated by me as the result of my own original research.

Understanding the catalytic benefits of multi-metallic active sites in microporous aluminophosphates

I confirm that:

1. This work was done wholly or mainly while in candidature for a research degree at this University;
2. Where any part of this thesis has previously been submitted for a degree or any other qualification at this University or any other institution, this has been clearly stated;
3. Where I have consulted the published work of others, this is always clearly attributed;
4. Where I have quoted from the work of others, the source is always given. With the exception of such quotations, this thesis is entirely my own work;
5. I have acknowledged all main sources of help;
6. Where the thesis is based on work done by myself jointly with others, I have made clear exactly what was done by others and what I have contributed myself;
7. Parts of this work have been published as:
    - A. J. Paterson, M. E. Potter, E. Gianotti and R. Raja, *Chem. Commun.*, **2011**, 47, 517-519. Relevant to chapters 1 and 5.
    - M. E. Potter, A. J. Paterson and R. Raja, *ACS Catal.*, **2012**, 2, 2446-2451. Relevant to chapter 1.
    - M. E. Potter, D. Sun, E. Gianotti, M. Manzoli and R. Raja, *Phys. Chem. Chem. Phys.*, **2013**, 15, 13288-13295. Relevant to chapter 4.

- E. Gianotti, M. Manzoli, M. E. Potter, V. N. Shetti, D. Sun, A. J. Paterson, T. M. Mezza, A. Levy and R. Raja, *Chem. Sci.*, **2014**, 5, 1810-1819. Relevant to chapter 4

- R. Raja, M. E. Potter and S. H. Newland, *Chem. Commun.*, **2014**, 50, 5940-5947. Relevant to chapter 1.

Signed: .....

Date: .....

Definitions and Abbreviations

TON	Turnover number
TOF	Turnover frequency
FCC	Fluid catalytic cracking
MFI	Framework code of ZSM-5
TS-1	Titanium-doped silicate-1
AlPO	Aluminophosphate
MTO	Methanol-to-olefin
XAS	X-ray adsorption spectroscopy
XANES	X-ray absorption near edge spectroscopy
XRD	X-ray diffraction
BET	Brunauer Emmett Teller
EPR	Electron paramagnetic resonance
ENDOR	Electron nuclear double resonance
HYSCORE	Hyperfine sublevel correction
FT-IR	Fourier transform infrared spectroscopy
TPD	Temperature programmed desorption
DFT	Density functional theory
QM/MM	Quantum mechanics/molecular mechanics
AFI	AlPO-5 framework code
SEM	Scanning electron microscopy
EDS	Energy dispersive spectroscopy
MAS	Magic angle spinning

NMR	Nuclear magnetic resonance
LUMO	Lowest unoccupied molecular orbital
ICP	Inductively coupled plasma
AES	Atomic emission spectroscopy
AAS	Atomic adsorption spectroscopy
GC	Gas chromatography
FID	Flame ionized detector
EXAFS	Extended X-ray adsorption fine structure
MO	Molecular orbital
HF	Hartree-Fock
LSDA	Local spin density approximation
GGA	Generalized-gradient approximation
USY	Ultrastable zeolite-Y
BEA	Zeolite Beta
MOR	Mordenite zeolite
DMP	Dimethyl-pyridine
WHSV	Weight-hourly space velocity
Imp	Impregnated
Iono	Ionothermal
Hydro	Hydrothermal
TPR	Temperature programmed reduction
SDA	Structure directing agent
DMOD	([3-(trimethoxysilyl)propyl]-octa-decyldimethyl-ammonium chloride
CTAB	Hexadecyltrimethylammonium bromide

HMF	Hydroxymethyl furfural
DRIFTS	Diffuse reflectance infrared fourier transform
QENS	Quasi-elastic neutron scattering
FDCA	2,5-furandicarboxylic acid
CO	Carbon monoxide

Chapter 1: Designing multi-metallic sites in nanoporous materials

1.1 Introduction to catalysis

A catalyst is defined as a material which modifies the rate of a reaction without itself being consumed in the reaction (Figure 1.1).[1] Since its inception catalysis has become a significant factor in our everyday life. To the extent that 90% of all manufactured products have required the use of a catalyst during their creation. A wide variety of catalysts are now utilised in industrial processes. The catalysts themselves are commonly grouped into two categories, homogeneous and heterogeneous.[1]

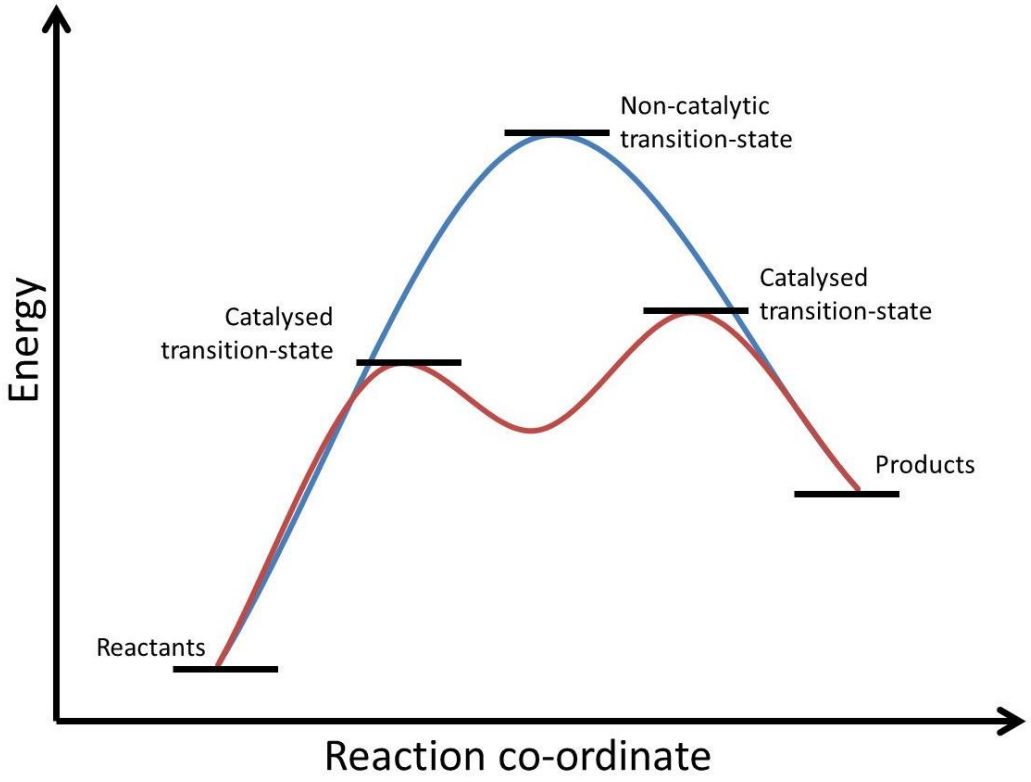

Figure 1.1: Explaining the energetic benefits of catalysed reactions.

A homogeneous catalyst is one which is in the same phase as the reactants, for example when the catalyst itself is in the liquid phase, along with the reactants. Metal-containing homogeneous catalysts are commonly molecules based around a central metal atom with specific organic ligands bound to the metal, constituting a metal complex.[1] This field of catalysis is perhaps best

recognised due to the work of Grubbs, who designed a range of metal complexes designed to perform metathesis polymerisation reactions.[2] This catalytic design strategy has many advantages:

a) By modifying the organic ligands the catalytic environment can be completely controlled.
b) Given the uniformity and crystallinity of different complexes these species are readily characterised.
c) Such species are often highly selective as they can be tailored to perform specific reaction pathways.

However, such materials are also prone to less appealing characteristics:

d) Separating a homogeneous catalyst from the reaction mixture is often challenging and requires multiple purification steps to recover.
e) Given the nature of the metal-organic bonds, such materials are often unstable at elevated temperatures or under more pressing conditions, such as acidity or pressure.
f) A precise coordination environment with high metal content and unusual ligands often translates to an exceptionally high production costs.

In contrast, a heterogeneous catalyst is one which is in a different phase to the reactants. Commonly this is a solid catalyst which resides in a liquid reaction mixture. This may constitute a bulk metal phase,[3] however more recently this tends to be a system where small quantities of dopant atoms are placed amongst the background of an inorganic support or matrix.[4] Given the inorganic nature of these materials precise control over a catalytic active site becomes more difficult. As the active site in such species may constitute less than 5 wt% of the whole system selective characterisation becomes difficult.[5] Inspite of this the disadvantages of homogeneous catalysts (d-f) are primarily placated in such systems, making heterogeneous catalysts attractive for a range of processes.

The effectiveness of a catalyst is judged on a number of factors. Assume the following catalytic reaction:

$$A \rightarrow B + C \qquad (1.1)$$

where A is the reactant, B is the desired product and C is a by-product of the reaction. One of the primary concerns of a reaction is how much of the starting material (in this case A) has been consumed; this is quantified as 'reactant conversion' or 'conversion' and is defined as:

$$Conversion = 100\% \times \frac{Moles\ of\ reactant\ consumed}{Starting\ moles\ of\ reactant} \quad (1.2)$$

It should be noted that in reactions with more than one reactant it is commonly the limiting reagent which is used for conversion, however one can also calculate conversion relative to each reactant involved. Whilst conversion is a good measure of the activity of the reaction it is not a good measure of specificity, it is of course possible that 100 % of the substrate(s) are consumed (A), but none of the desired product is formed (B is not formed, only C), in which case this would not be seen as a particularly successful reaction. Therefore another important metric is 'product selectivity' or just 'selectivity' and is defined as:

$$Selectivity = 100\% \times \frac{Moles\ of\ specific\ product\ formed}{Total\ moles\ of\ product\ formed} \quad (1.3)$$

The selectivity can be measured for each individual product, though is commonly quoted for the desired product. From this it is clear that the ideal catalytic reaction would have both a high conversion and a high selectivity, the two parameters can be combined into one parameter; 'product yield', or 'yield', this is defined as:

$$Yield = 100\% \times \frac{Moles\ of\ specific\ product\ formed}{Starting\ moles\ of\ reactant} \quad (1.4)$$

While these parameters provide a good description of the progress of a reaction they give little information about the catalyst itself as the above descriptions do not take into account the quantity of catalyst used in the process. It can therefore be argued that it is inappropriate to compare results from reactions with different catalyst:substrate ratios, or even to make comparisons between different catalytic systems, as these do not account for the efficiency of the catalyst. As such 'Turnover Number' or 'TON' and Turnover Frequency' (or 'TOF') can be used to make comparisons between different catalytic systems thus:

$$Turnover\ Number = \frac{Moles\ of\ reactant\ consumed}{Moles\ of\ active\ species} \quad (1.5)$$

The Turnover number (TON) metric is a useful measure of catalytic efficiency, however the number is only applicable when comparing TONs from the same time period, as such the time taken to reach a certain TON is also of interest, this can be taken into account using the Turnover Frequency (TOF) metric:

$$Turnover\ Frequency = \frac{Moles\ of\ reactant\ consumed}{Moles\ of\ active\ species} \times \frac{1}{Time\ taken} \qquad (1.6)$$

1.2 Nanoporous materials

The desire to increase the metrics above has provided the motivation for the increasingly articulate design of catalytic materials and active sites. While the active site plays a pivotal role in catalysis the spatial constraints around it can also be just as important. Consider an enzyme, while the active metal centre is precisely controlled.[6] The 'pocket' in which it resides is also stringently controlled, in many cases providing unprecedented reactant specificity.[7] In order to mimic this phenomenon inorganic scientists have developed a range of nanoporous materials, with active species located within the pores of these materials to mimic the spatial constraints of enzymes. The selectivity benefits of nanoporous (particularly microporous materials, possessing pores between 2 – 20 Å) are coveted by the wider catalytic community as they offer vast degrees of control, including reactant, transition state, product, regio- and enantio-selectivity.[8]

Reactant selectivity is the process which discerns whether a molecule may enter the porous framework, and therefore may interact with the active-species confined within the pore. Thus substrates which are too large to enter the pore will be unable to react, whereas the smaller molecules can access the pore and undergo the desired chemical transformation (Figure 1.2).[9]

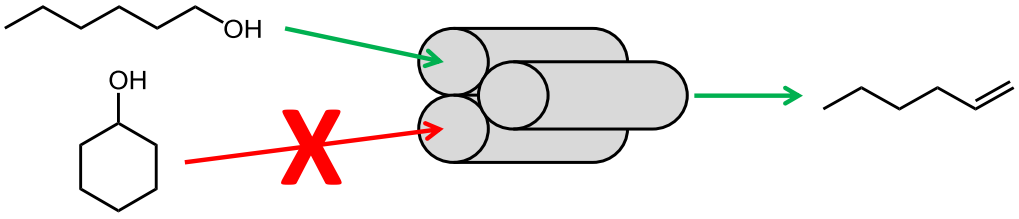

Figure 1.2: Describing reactant selectivity of various hexanols in an acidic porous catalyst.

Transition-state selectivity prevents the formation of specific products by sterically hindering the pivotal transition state, thus increasing its energy, making it infeasible for it to form. This notion is exemplified in the transalkylation of meta-xylene. Studies found that the 1,2,4-trimethyl benzene product was heavily favoured over the symmetric 1,3,5-trimethyl benzene using a protonated mordenite catalyst.[10] Both products and the reactant were found to be able to diffuse through the mordenite framework unabated, and as such no restraints are placed on either reactants or products. The appropriate intermediates were investigated and it was found that the transition state which leads to the 1,2,4-trimethyl benzene product was sterically unhindered (A), whereas the transition state for the symmetric 1,3,5-trimethyl benzene product was sterically hindered. This retarded its formation (Figure 1.3) and subsequent decomposition to the 1,3,5-trimethyl benzene product.[10]

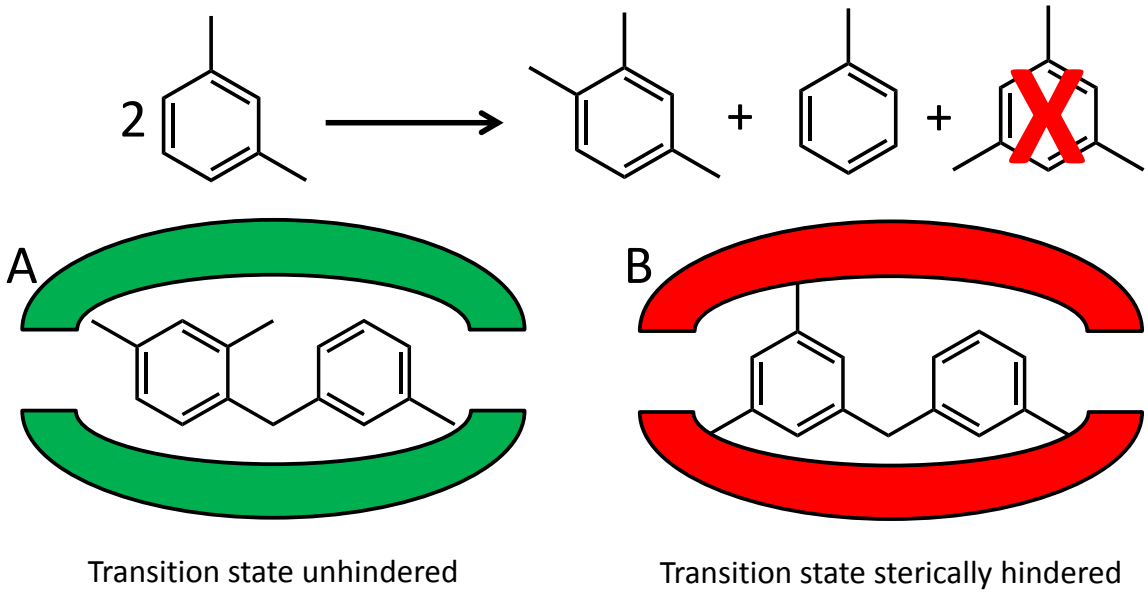

Figure 1.3: Describing the translalkylation of meta-Xylene with reference to transition state selectivity, entry to the pore is initially achieved due to the ability of zeotypes materials to 'breathe', thus widening the pore mouths.

Product selectivity can strongly influence the product distribution of the reaction. Unlike transition state selectivity (which prevents the product from forming in the first place), product selectivity allows the product to form within the pore, but prevents it from leaving, thus capturing it within the framework. The product is then held next to an active site, and forced to react further, into a molecule which is able to exit the pore. An example of this is from the

disproportionation of toluene with a ZSM-5 (MFI) catalyst. Whilst three possible isomers can form (ortho-, meta- and para-xylene) the para-xylene is strongly favoured. When the ortho- and meta-xylene products form they are unable to diffuse out of the porous framework, therefore undergo an acid-catalysed isomerisation reaction to form the para-xylene product (Figure 1.4).[11]

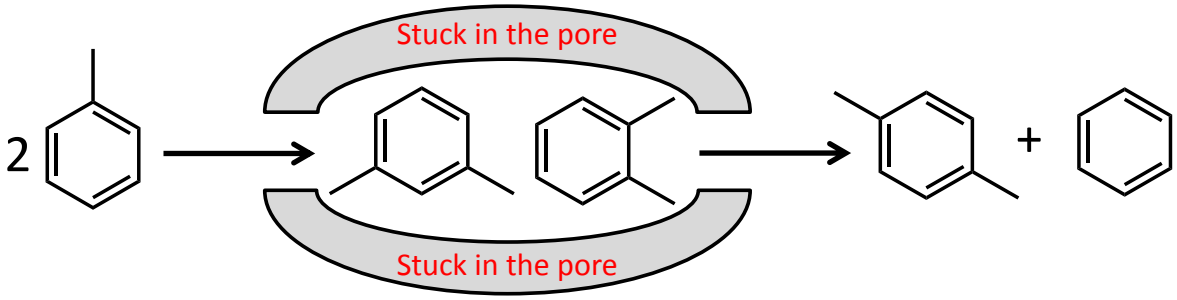

Figure 1.4: Product selectivity for the isomerisation of toluene with MFI catalyst.

Regio-selectivity can occur when multiple isomers may form from the same reaction. The oxidation of n-hexane to hexanol is an excellent example of this. Three different hexanols can be formed: hexan-1-ol, hexan-2-ol and hexan-3-ol. In a non-specific system the distribution of these different products is primarily dictated by the C-H bond strength, with the weaker C-H bond forming the greatest quantity of that particular hexanol. However the selective activation of terminal C-H groups is of great interest, as these products are precursors to monomers in the plastics industry. By selectively employing the correct framework (with the appropriate active site located inside), it is possible to force molecules to access the active sites, only by diffusing in an 'end-on' manner (Figure 1.5A). This only allows the terminus of the molecule to interact with the active site (Figure 1.5B), forming the desired non-thermodynamic product (Figure 1.5C).[12]

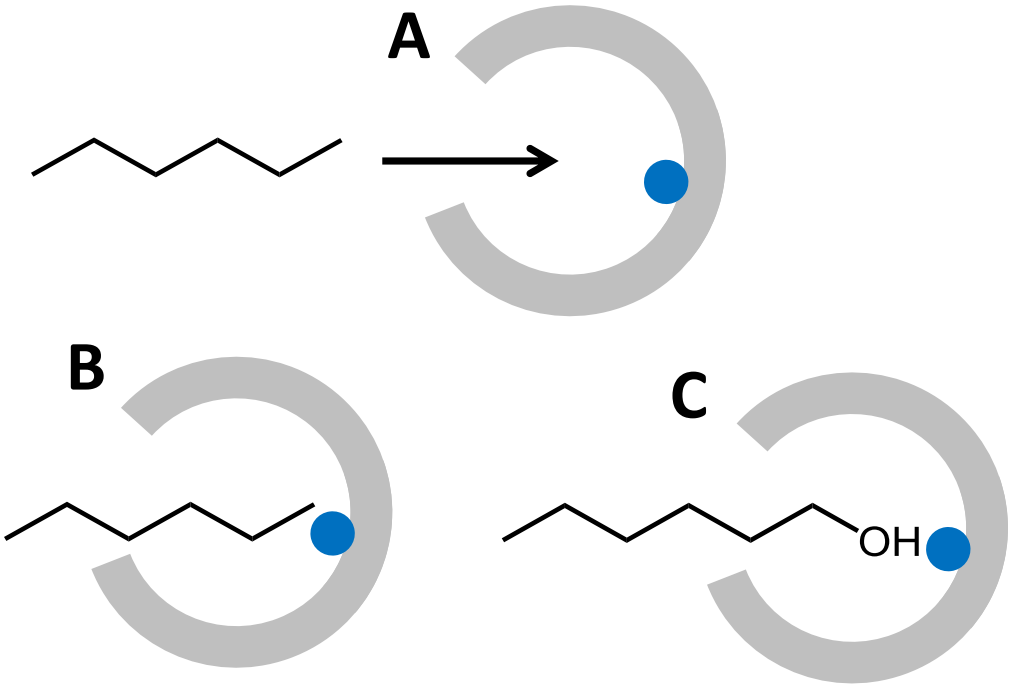

Figure 1.5: Describing the notion of regio-selectivity of the oxidation of n-hexane to hexan-1-ol, within a confined pore containing an isolated oxidation site (blue circles).

Enantioselectivity can occur by advantageously using the curvature of the silica surface, in combination with a single metal centre and chiral linkers to boost the enantioselectivity of specific chiral molecules. The convexity or concavity of the system can ease the formation of specific transition states, thus favouring one enantiomer over another (Figure 1.6).[13]

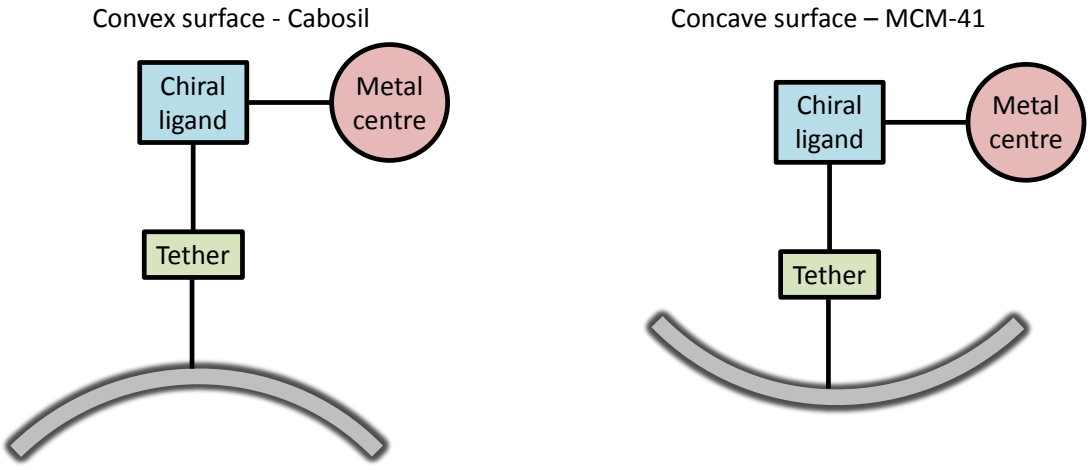

Figure 1.6: Describing enantioselectivity differences with different curvature surfaces.

1.3 Designing the active site

Whilst framework design is vital, significant efforts have gone into the creation of novel catalytically active species. The design of well-defined active centres that are isolated within framework architectures, so as to create discrete single-sites, have long been admired by synthetic and catalytic chemists.[14,15] The ability to engineer multifunctional sites, within these porous architectures, with a view to enhancing their catalytic synergy from a structural, functional and mechanistic perspective has since been rationalised[16,17] affording adequate scope for improving their activity and tuning their selectivity, in industrially significant oxidation and acid-catalysed processes. A "single site" (catalytically active centre) may consist of one or more atoms. These sites are spatially isolated from one another and the activity and functionality of each "site" can be attributable to a particular catalytic function. The choice and proximity of these multifunctional sites coupled with their propensity to modify and tailor the local-structural environment in their immediate vicinity has since instigated the predictive design of novel heterogeneous solids for targeted catalysis. Solid-state chemists have often coveted the intricate design of multifunctional active sites within metalloenzymes and have been intrigued by the efficacy of the three-dimensional protein framework in facilitating highly selective and specific reaction pathways. It is believed that each of these single-sites has a distinct role (structural or functional); yet they do not behave as separate entities. There is a clear interplay and synergy between the two metal sites which is critical for the catalytic performance. With advances in characterisation and *operando* methods, synthetic chemists have utilised the knowledge gained from enzymatic active sites to rationally develop porous inorganic frameworks, such as zeolites, as successful mimics with the added advantage of increased stability making the materials more amenable for industrial processing. Extensive research is now on-going, with the aim of mimicing the nature and catalytic function of these multinuclear sites, through the use of similar zeotype species containing discrete metal sites to create novel multifunctional catalysts, which could capitalise on the notion of multimetallic synergy.

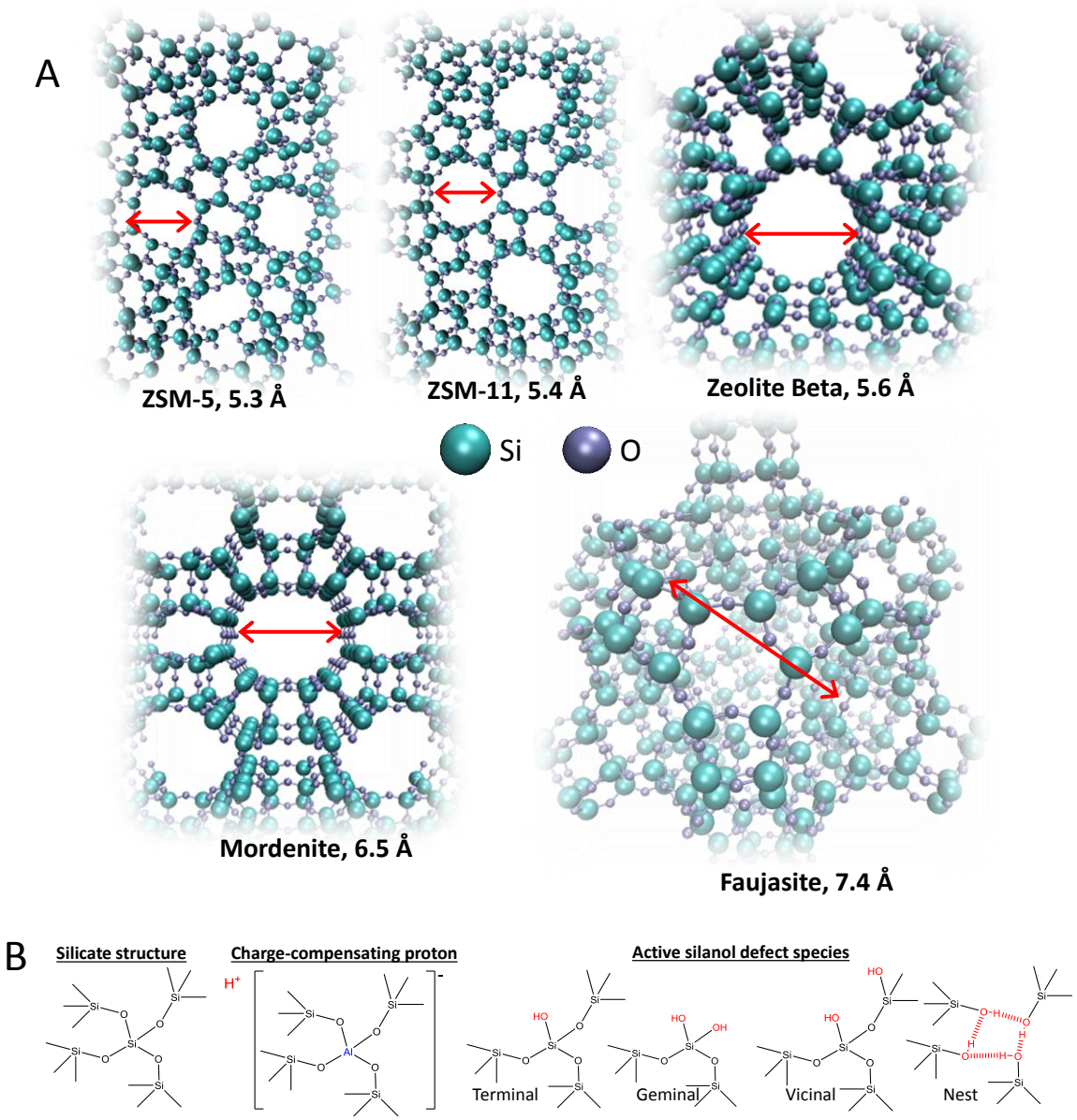

Figure 1.7: Some industrially-significant zeolite frameworks (A) with designed active centres (B).

A wide-range of over 200 different zeolite frameworks have been successfully synthesised, with numerous other hypothetical architectures yet to be actualised. However, amongst these abundant structures, only a handful have been effectively implemented in industrial processes (Figure 1.7A) despite the fact that enormous progress has been made in novel synthetic approaches coupled with advances in *operando* spectroscopy.

These developments have enabled a diverse-range of active sites to be engineered within these porous architectures, whereby any subtle deviation from the bulk silicate structure can potentially lead to the formation of

catalytically active centres. These sites have been effective in the industrial implementation of many important acid-catalysed processes in the chemical industry - it is noteworthy that the employment of zeolites is far from sporadic.

Aluminosilicates are most commonly utilised in the petrochemical industry as FCC catalysts and in isomerisation, dehydration and dewaxing applications. The shape-selectivity bestowed on them by the microporous architectures makes them ideal candidates for selectively targeting specific products, whilst simultaneously hindering the formation of bulkier by-products. It is noteworthy that industrial oxidation processes are currently still dominated by the use of 'bulk' metal oxide materials, comprising in general of a larger fraction of less well-defined active centres over atomically engineered, precise single-sites. From a strategic perspective, there is an enormous potential for the predictive design and development of microporous architectures with well-defined, isolated active sites, which are capable of synergistically enhancing both acid- and oxidation-catalysis, with better atom-economy and energy-efficiency.

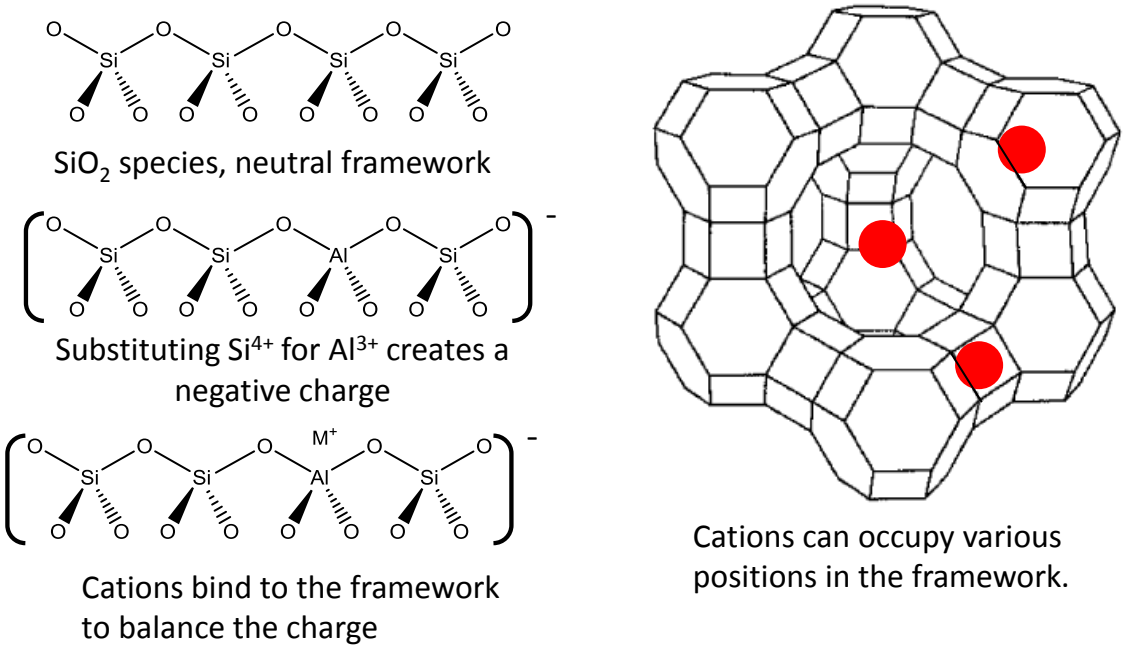

Figure 1.8: Highlighting the origin of charge-balancing cations in zeolites.

The mechanism by which active dopant ions are introduced into a zeolitic framework is well understood (Figure 1.8). While the incorporation of charge balancing cations is the primary way of generating active centres in zeolitic frameworks, it is also possible to induce catalytic activity using defect sites.

While such framework structures are naturally highly crystalline, it is inconceivable that a material could be completely defect free. Figure 1.7B details a range of defect sites that may commonly occur within the pores and on the surfaces of zeolite catalysts. Note that in all cases such sites arise due to an incomplete second coordination sphere; resulting in a deficient number of Si-O-Si bonds. These sites have been shown[18,19] to be acidic and efficiently influence acid-catalysed processes. However, the detection of such species can often prove challenging, as the active centres blend with the background bulk structure. Traditionally, such species are detected by indirect spectroscopic methods and most notably *via* the resultant acidity generated in the material.

It is also possible to generate a much narrower range of active sites through isomorphous substitution, as heteroatoms replace silicon atoms within the porous architecture; although relatively few illustrations of this exist in the literature.[20,21] Arguably the most well-known example from the past decade that successfully demonstrates the advantages that such a strategy could deliver, both from an academic and industrial perspective, relates to the silicalite family, and specifically to titanium silicate; TS-1. In this system, a small percentage of the Si^{4+} ions in the silicalite framework (MFI) have been replaced with Ti^{4+} ions. Therefore, instead of $Si(OSi)_4$, a $Ti(OSi)_4$ species exists, acting as an isolated metal-active centre (see later Figure 1.14). Given the isoionic nature of the substituent, a charge imbalance does not occur from this substitution, and subsequently charge-balancing cations are not required. Instead, the active site is intricately incorporated into the pore walls of the MFI framework and securely anchored within the porous cavity; resulting in a material where the exchange of molecular ions is not readily feasible. This method of creating active sites contrasts with the cationic method (Figure 1.8) in a number of ways:

1) The active site can be designed in such a manner that it is truly isolated, thereby making it possible to close the catalytic cycles (loops) and as such automatically regenerates the active centre.

2) When an active site is securely anchored within the framework, it is less susceptible to leaching; thereby facilitating the facile recovery and recyclability of the catalyst.

3) The substituted species can be contorted into an energetically-unfavourable geometry, with the possibility of becoming coordinatively unsaturated and attuning the catalytic activity.

4) Given that additional metals or species are not required for charge-compensation of the overall framework, it minimises the propensity for side-reactions and confers a single-site nature to the catalytically active centre.

Despite these advantages, comparatively few examples of isomorphous substitution in zeolite species exist owing to the stringent restrictions that are imposed on the ions:

a) The substituted species must be of comparable size to the replaced ion, any significant variance would require the framework to become very locally distorted at a great energetic cost.

b) The substituted species must possess an appropriate charge to compensate for the ion it is substituting: a significantly lower charge will result in insufficient electrostatic interactions to keep the ion in the framework and highly positively-charged ions would prompt a net-positive charge on the zeolite, which cannot be accommodated.

c) The substituted species must be able to adopt a tetrahedral geometry within the framework. Isomorphous substitution of a tetrahedral species within the framework will force the substituted species to adopt a similar coordination; though some exceptions are known.

These strict rules within the zeolitic regime led to an expansion in synthetic research to find alternative materials that would be more amenable to framework modification and active site creation. In 1982 a class of microporous materials, aluminophosphates (AlPOs), were discovered, where isomorphous substitution of heteroatoms was readily plausible and is now commonplace.[22]

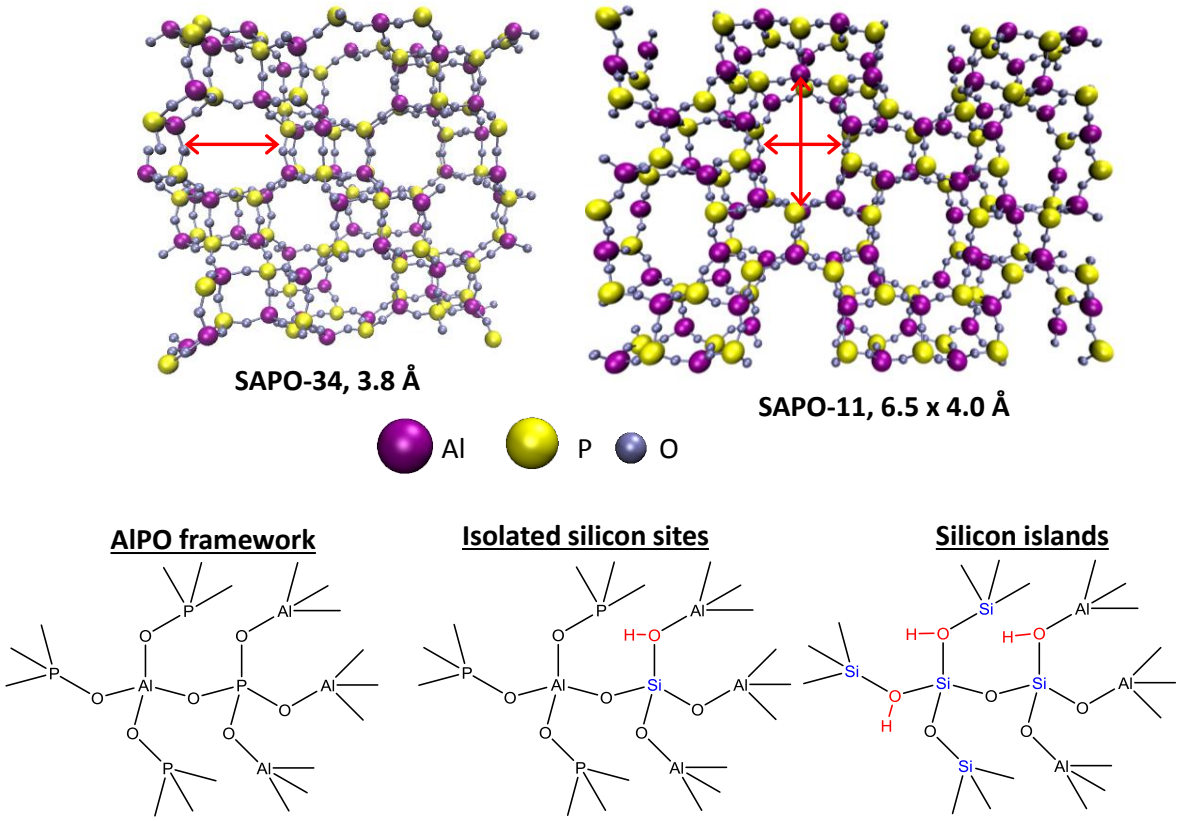

Figure 1.9: AlPO architectures with silicon-based active-sites.

AlPOs often form analogous frameworks to zeolites, though are not exclusively formed from Si and Al T-sites. They are instead derived from alternating AlO_4 and PO_4 tetrahedra; linking together exclusively through Al-O-P bonds (Figure 1.9). As a consequence, unlike zeolite materials, the AlPO framework is strictly neutral and is unable to possess any form of net-charge. In light of this, it is not possible to introduce charge-balancing cations and the only method to introduce individual dopant ions into the framework is through isomorphous substitution. The most common example of this is the incorporation of silicon into the AlPO framework (Figure 1.9). Given the alternating nature of Al and P atom tetrahedra within an AlPO, it is logical that one could substitute either an Al^{3+} or a P^{5+} site, unlike in a zeolite, where only one method of substitution is possible. Subsequently in AlPOs a variety of substitution mechanisms are possible, depending on the oxidation state of the dopant and which framework atom is to be replaced (see Figure 1.10). This choice then broadens the scope of possible framework dopants beyond what was possible for a zeolite; as we are now also able to incorporate dopants with 2+ and 5+ charges. In spite of the relaxed restrictions on substituent charge, the restrictions on dopant size and coordination geometry still apply.

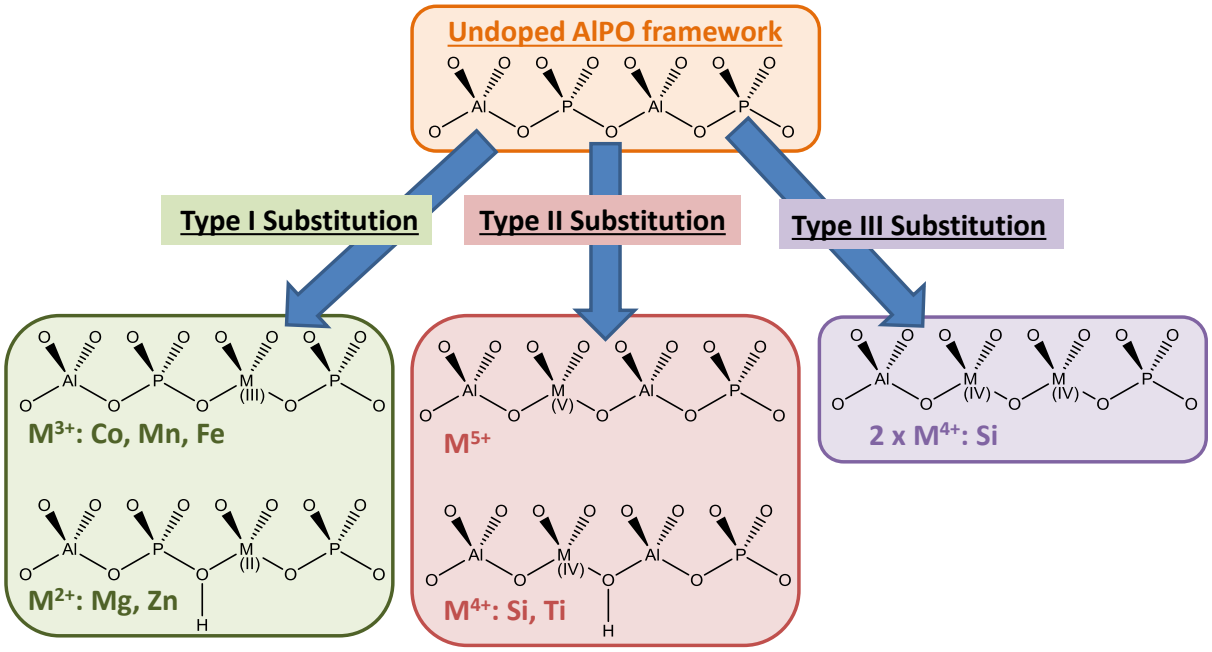

Figure 1.10: Typical isomorphous substitution mechanism for the introduction of active sites in AlPOs.

Through adroit choice of the dopant (as with zeolites) it is possible to engineer a range of active sites within the AlPO catalysts. The creation of Brønsted acid sites can be achieved by exploiting the AlPOs inability to hold a net-charge. By undergoing type I substitution with a M^{2+} dopant or performing type II substitution with a M^{4+} dopant a charge imbalance is created (Figure 1.10). However, this imbalance can be neutralised by a proton binding to the framework on an oxygen atom, adjacent to the substituted dopant, thus creating a Brønsted acid site. This synthetic methodology is fundamental in the synthesis of SiAlPO-34, in which the substituted silicon bestows Brønsted acidity onto the framework. The isolated acid sites, in combination with the confining micropores (3.8 Å), result in an excellent methanol-to-olefin (MTO) catalyst that has been commercialised for many years.[23] In a similar manner, one can also engineer redox active sites by selecting metals with two available adjacent oxidation states; commonly these are first-row transition-metals such as $Mn^{2+/3+}$, $Co^{2+/3+}$ or $Fe^{2+/3+}$. By incorporating these metals into the framework they can then alternate between the two states and operate as an isolated redox centre.

AlPOs first received mainstream attention when it was demonstrated that Co and Mn containing AlPO species were able to aerobically oxidise inert linear alkanes to the appropriate alcohols, obtaining turnover numbers (TONs) in

excess of 100, while overcoming bond energies of ~ 90 kcal mol^{-1}.[10] The effect of pore size was examined and it was shown that activity was inversely linked to the pore size of the material. This was later linked to the redox fraction of the cobalt substituted into the framework, and not directly to the framework dimensions.[24]

This work was then extended with the aim to selectively convert n-hexane to the coveted Nylon-6,6 precursor, adipic acid.[25] It was shown that adipic acid could only be formed in cage-like structures such as AlPO-18 and AlPO-34, and only when there was a sufficiently high level of cobalt substituted into the framework (10 atom%). It was reasoned that the higher loadings were necessary to allow two cobalt ions to substitute at opposite ends of a cage, allowing n-hexane to be attacked simultaneously at both terminal carbons, to form the desired dibasic acid. Alternative routes were explored and higher yields of adipic acid were obtained through analogous experiments in which cyclohexane was used as the starting material with FeAlPO-31 as a catalyst.[26] This catalyst (pore diameter of 5.4 Å) supported a different reaction mechanism, instead of performing simultaneous terminal oxidations, therefore it exploited the notion of product selectivity. The pore size of the catalyst was found to be such that the cyclohexane precursor could diffuse into the pore, but the primary products (cyclohexanol and cyclohexanone) were too sterically hindered to diffuse out. Instead the primary products were trapped near the active site and forced to react further, until the cyclohexyl-ring opened to finally yield the dibasic adipic acid which is able to diffuse out of the pore. A final route to adipic acid was performed using TiAlPO-5 and H_2O_2 with cyclohexene.[27] This was found to reach a 30 % yield of adipic acid after 72 hours, with a TON of 310. Through an in-depth kinetic analysis it was theorized that the reaction began with an epoxidation step to cyclohexene oxide before forming diols, which then proceeds to adipic acid. The three methods are summarized in Figure 1.11.

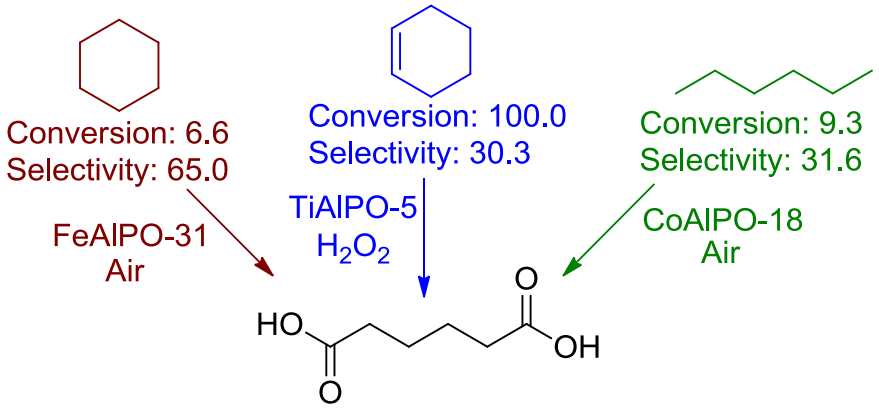

Figure 1.11: Summary of adipic acid production with metal-substituted AlPOs

Other groups have used AlPOs for the oxidation of cyclohexane, Zhou *et al* tested similar materials to those discussed above, but exclusively used a series of Co, Mn and Fe-substituted AlPO-5 materials.[28] In contrast to Raja *et al* the group employed a free-radical initiator to start the catalytic cycle. The yields of adipic acid obtained were typically much lower than those obtained by Raja *et al*, a result of the larger AlPO-5 pore (7.3 Å) not benefitting from product selectivity. It was further hypothesised that higher loadings would enhance the activity of the system further. The same reaction was also investigated using CrAlPO-5 by Sheldon *et al*,[29] concluding that the active site was a distorted Cr^{4+} site adopting an Al position in the AFI framework, however cyclohexanone was the favoured product, with the formation of cyclohexyl-hydroperoxide being the rate determining step.

Phenol hydroxylation is another process that has also been widely investigated using AlPO catalysts. The most common catalysts contain copper,[30] iron[31] or titanium.[32] The latter dopant is of significant interest due to the commercial use of TS-1[33] for this reaction and many other oxidation reactions. In particular TiSiAlPO-5[34] has been used as a mimic to TS-1, despite the titanium and silicon both substituting into the AlPO-5 framework. It was discovered that when H_2O_2 was added slowly as an oxidant, the TiSiAlPO-5 material was more active and selective than the TS-1 material (see Table 1.1) for phenol hydroxylation. This was theorized to be the result of the hydrophilicity of the AlPO surface stabilizing the hydroquinone and catechol products, stopping overactivation of the process.

Table 1.1: Catalytic data for the hydroxylation of phenol, taken from Reference 34.

Catalyst	Conversion /mol%	Catechol selectivity/mol%	Hydroquinone selectivity/mol%	Others selectivity/mol%
TS-1	15.2	45.4	42.1	12.5
TiSiAlPO-5	39.2	53.8	36.5	9.7

A range of Co, Mn and Fe containing AlPO-11 molecular sieves were also tested for the phenol hydroxylation,[35] it was concluded that the FeAlPO-11 and CoAlPO-11 possessed similar activity but MnAlPO-11 was comparatively inactive. Further, the role of the framework was examined by comparing CoAlPO-5, -11, -36 and -50. It was concluded that the AlPO-11 structure was by far the most active. It was suggested that this was not due to the internal sites, but the external surface of the material.

This reaction has also been attempted using a range of copper-containing AlPO materials. CuAlPO-11 has been used,[30] as the elliptical pore is tailored to allow the diffusion of aromatic reactants and products but retards the formation of heavier dimer products that may deactivate the catalyst. The effect of copper loading was examined and it was concluded that lower copper loadings were less active but favoured the formation of the ortho-product over the para. It was noted that AlPO-11 framework was not stable if the CuO/Al_2O_3 ratio was increased past 0.2, as this promoted the formation of a dense phase material. It was however shown that the porous structure was not necessary to facilitate the conversion of phenol, as the dense phase system appeared to be as active as the high loading CuAlPO-11 system, despite a slight decrease (from 65.6 to 61.3 mol%) in the selectivity towards catechol and a similar increase to the hydroquinone selectivity.[30]

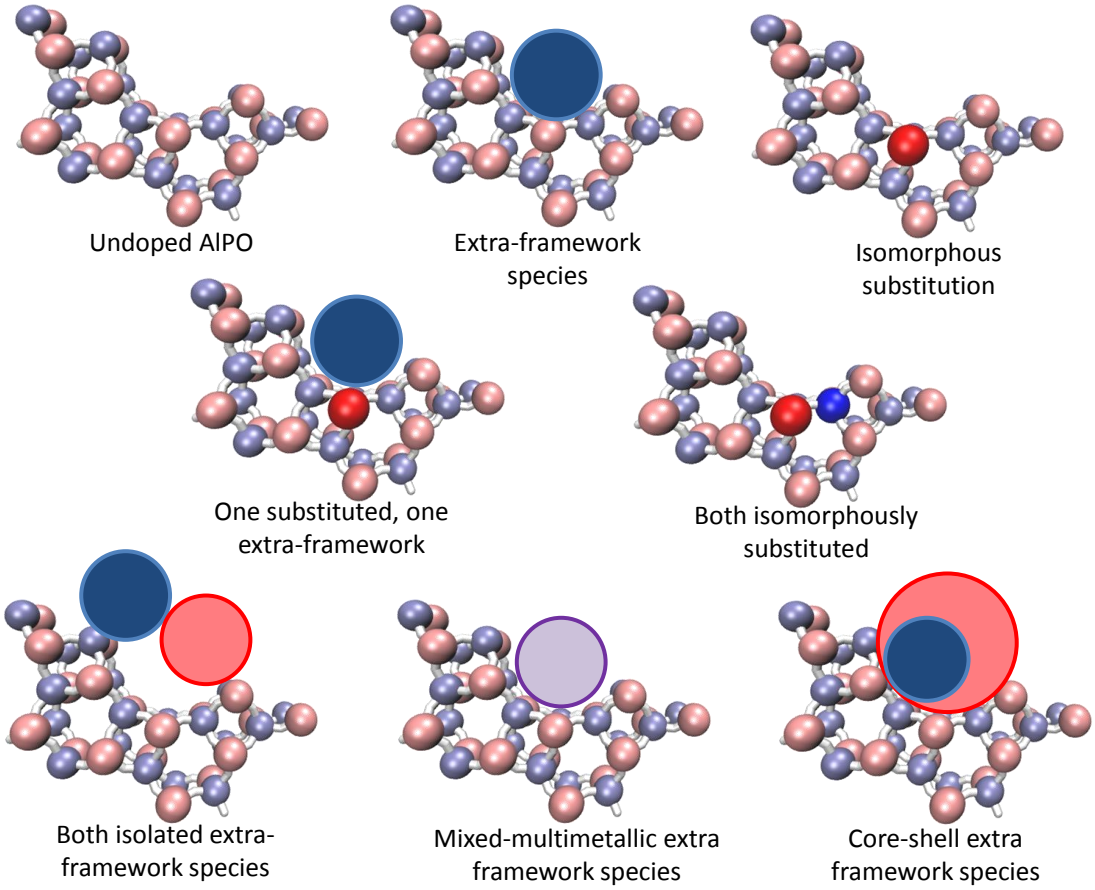

Figure 1.12: Potential for multi-metallic substitutions in AlPO architectures.

The limitations on the range of isomorphously substituted sites that can be formed using these synthetic protocols have been previously discussed.[36] To overcome these restrictions it is possible to extend the range of single-sites present in microporous architectures, by the deliberate application of a range of physical deposition techniques. Therefore, instead of creating isolated active sites, secondary phases are introduced onto and into a host framework, creating species that are more akin to bulk oxides or metallic species.[37] As isomorphous substitution and physical deposition possess complementary advantages, many literature examples exist[38] in which the combination of these doping techniques results in improved catalytic performance (see Figure 1.12). It has been hypothesised[39] that the marked catalytic improvements may stem from the deposition process blocking unfavourable substituted sites. Other examples have observed[40] substituent sites aiding selective impregnation of the bulk oxide and also the stabilisation of specific metal phases.

These microporous molecular sieves have been found to be exceptional catalysts for a range of redox and acid-catalysed processes. Their microporous nature (pore diameters ≤ 20 Å) only allows specific molecules with appropriate dimensions to access the large internal surface area; this enhances their selective adsorptive capacity, and in turn, their specificity. These catalysts are highly stable (≅ 800 ˚C) and by adroit choice of aperture-type (cage vs. channel), their selectivity (shape-, regio-, chemo- and enantio-) in demanding catalytic transformations can be suitably tuned.[12,25,41] However, due to the interconnecting micropores, diffusion can be hindered for larger organic molecules and this can have a detrimental effect of lower reaction rates and, consequently reduced versatility, limiting the range of substrates that can access the active sites. Therefore there is a significant interest[42] into the synthesis of larger-pore zeolites and zeotypes. As a direct consequence, numerous large pore materials have been synthesized, for example, AlPO-8,[43] VPI-5[44] and cloverite,[45] which possess pore diameters in the range of 8-13 Å (see Figure 1.13).

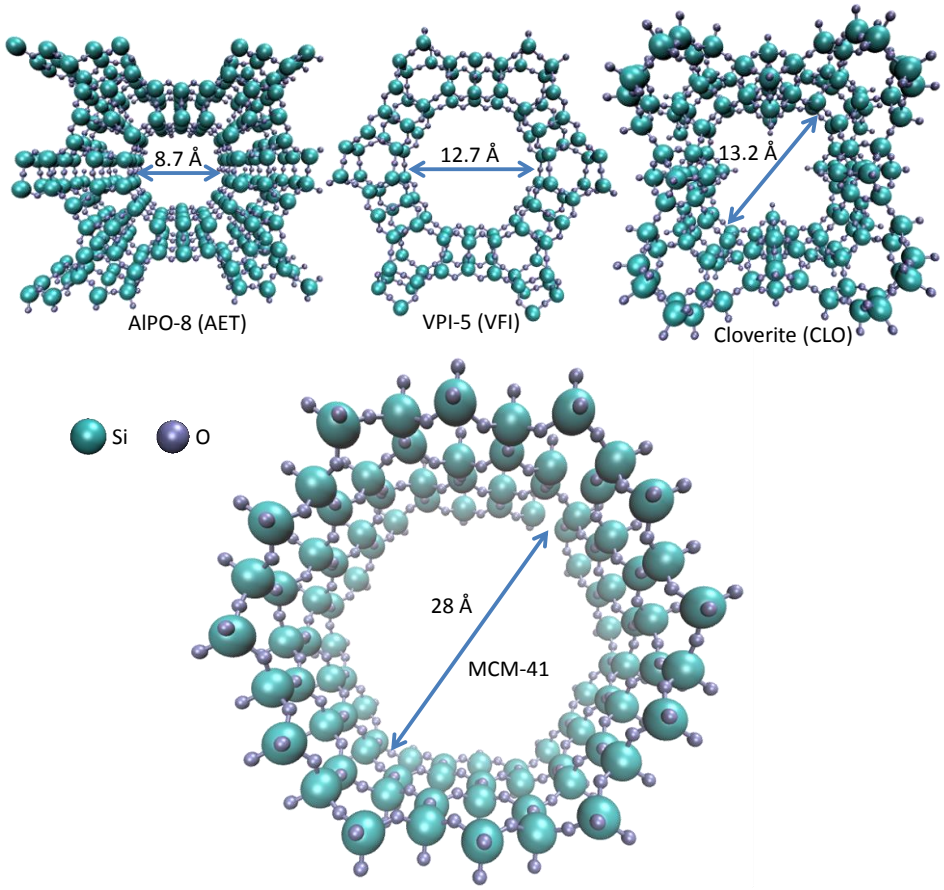

Figure 1.13: Larger-pore synthetic microporous and mesoporous architectures.

Designing multi-metallic sites in nanoporous materials

The precise environment of the active centre (e.g. oxidation state, coordination number, etc.) at the atomic level is of great significance in the design of active catalysts. The most striking example of an active metal dopant within a microporous zeolitic framework, which has proved effective both from an academic and industrial standpoint, is the four-coordinate titanium active centre in TS-1. The oxophilic Ti^{4+} active site in the silicalite framework is the focal point of the well-known TS-1 catalyst that has been commercialised for a range of oxidation applications. In an effort to mimic and further optimise the activity of the versatile TS-1 catalyst, a range of titanium-doped silicon materials have been designed and synthesised. Through in-depth characterisation of these systems it has been possible to contrast the exact nature of these different titanium environments, with an aim to understanding the subtleties that underpin the ensuing catalytic activity. With a view to rationalising this, a range of titanium-doped species were investigated using X-ray absorption spectroscopy (XAS), specifically focussing on the X-ray absorption near edge spectroscopy (XANES) region, owing to the low-energy titanium adsorption edge. Through a rigorous study it was revealed that a significant correlation existed between the XANES pre-edge feature and the coordination number of the titanium site. It was found that[46] the coordination number could be unequivocally determined by consideration of pre-edge energy value, and the peak intensity through the Farges plot (see Figure 1.14). Consequently it was found that the reactivity of the TS-1 catalyst can be emphatically associated with the tetrahedral nature of the titanium site. Similarly Ti-MCM-41 (also possessing tetrahedral titanium active centres) has been found to be highly active in a range of oxidation reactions[4] using peroxides as oxidants. In both cases the tetrahedral titanium, being coordinatively unsaturated, is able to activate the peroxide species, creating desirable transition-states in the vicinity of the active centre for subsequent activation of the substrate molecule (e.g. an olefin). In stark contrast, five- and six-coordinated titanium species, have not proved to be as effective as their four-coordinate Ti^{4+} analogues[47] for the reasons outlined below. Five-coordinate titanium active sites are relatively uncommon (given the propensity for titanium to adopt 4- or 6-coordinated geometries), hence the discovery of JDF-L1[48] was met with great excitement by the heterogeneous catalysis community. Despite this, there are no reports to date of such five-coordinate Ti species being catalytically superior to the tetrahedral Ti analogues (TS-1 and

TiMCM-41), as it is highly likely that the pyramidal structure[48] of the active site in JDF-L1 hinders peroxide activation. Similarly octahedral and other 6-coordinate titanium species (such as ETS-4 and ETS-10) are coordinatively saturated, and as such will retard the interaction of oxidants or reagents, rendering the system comparatively inert.[49] This link between coordination geometry and catalytic activity further emphasises the notion that a profound knowledge of the precise nature of the active site at the molecular level is of fundamental importance in the design of highly active catalysts, and synthetic factors that provoke even a subtle modification to the nature of the active site at the atomic scale deserves a thorough investigation.

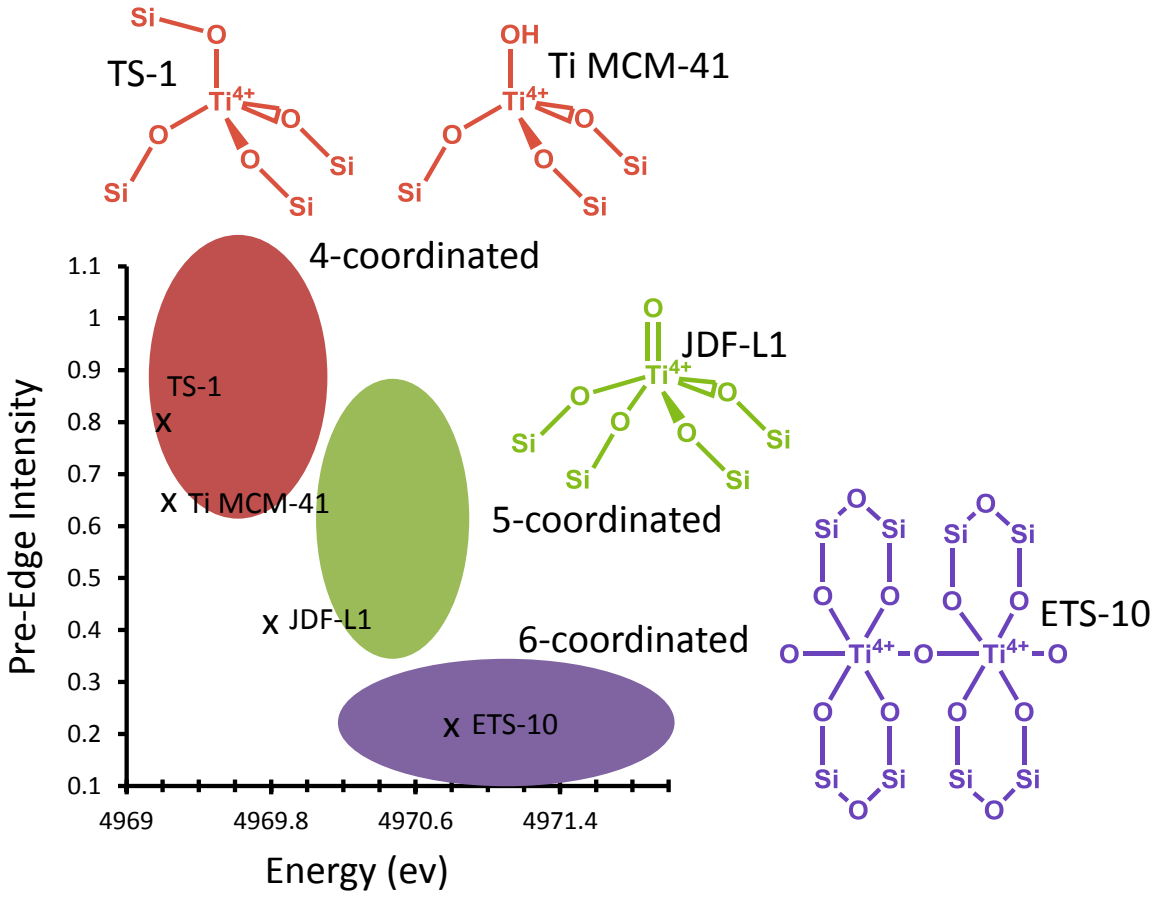

Figure 1.14: Using XANES for probing the local structural geometry and coordination environment in solid catalysts.[46]

Despite the range of post-synthesis techniques that have been well established and developed[50] by the zeolite community to tune framework properties, (such as de-alumination and tethering silanol species to tune the hydrophobicity, to highlight a few) such techniques are not easily translated to their AlPO (or zeotype) counterparts. As such, alternative synthetic strategies must be

developed to allow for subtle modifications (oxidation state, coordination geometry, substitution mechanism) of the active centre in the AlPO framework. In this vein, there has been immense interest over the last decade in combining different metal dopants to modify the catalytic profile; thus generating multifunctionality and synergistic enhancements within AlPO architectures. More specifically active sites (Figure 1.9) can be engineered to bestow targeted catalytic properties in the AlPO framework, through careful choice of dopant precursors, with a view to predictively designing and enhancing the catalytic potential to confer redox and/or acidic capabilities. Through this approach, one is not limited to choosing just one active site, and can in-fact construct a range of different catalytic centres in one system; thereby creating a multifunctional catalytic system. An example of this details the use of a *bimetallic* AlPO catalyst for the formation of the Nylon-6 precursor, ε-caprolactam, in a single-step from cyclohexanone (Figure 1.15A).[51,52] In the initial step, ammonia and air are converted into hydroxylamine (*in situ*) inside the pores of the AlPO catalyst, a step requiring a redox-active site. The hydroxylamine formed consequently converts the cyclohexanone to cyclohexanone oxime.[53,54] In the second-step of this process, the oxime undergoes a Beckmann rearrangement to yield the desired ε-caprolactam, utilising the Brønsted-acid from the same bimetallic catalyst.[55] Therefore, in order to successfully tailor a catalyst for this demanding one-pot process the catalyst requires two different active sites. This is achieved[54] by introducing manganese and magnesium into the same framework to create a bimetallic $Mn^{3+}Mg^{2+}$AlPO-5 catalyst, which was shown to produce ε-caprolactam in a sustainable fashion. The two active centres in the AlPO framework can be thought of as independent single-sites, with each site performing a separate targeted function; Mn^{3+} ions executing the ammoximation step and Mg^{2+} ions enabling the Beckmann rearrangement. Given that both active centres undergo type I substitution (see Figure 1.10), there is very little possibility that the two sites will be in close proximity to one another, and as such, will have little influence on each other; hence they can be considered “truly isolated”.

The benefits of multimetallic substitution, that results in the above bifunctionality, which while elegant for cascade processes in AlPOs, can be extended further to optimise individual reaction steps, with a view to enhancing the synergistic aspects associated with the catalysis. The

introduction of a different metal atom (or atoms) can also regulate the properties of the individual active sites, when the metal centres are able to interact favourably with each other (cooperative effect). An example of this is depicted in the oxidation of cyclohexane (Figure 1.15B), with a multi-metallic FeCoMnAlPO-5 catalyst. In this case, the tri-metallic FeCoMnAlPO-5 catalyst showed an improvement in catalytic potential over all of its corresponding monometallic analogues, FeAlPO-5, CoAlPO-5 and MnAlPO-5, all of which possessed the same total quantity of metal atoms, with equivalent Metal:Aluminium ratios. This was further probed by testing all the appropriate bimetallic samples (FeMnAlPO-5, CoMnAlPO-5 and FeCoAlPO-5), of which only FeCoAlPO-5 was not an improvement over the original monometallic species.

It is important at this stage to reflect on, and contrast the above two examples: In both cases two different metal centres have been incorporated into the same AlPO framework which enhanced the yield of the desired product. In the ε-caprolactam example, the Mn^{3+} and Mg^{2+} sites are, as already stated, operating in a completely isolated fashion, each performing a unique role in *different reaction steps*. In the cyclohexane example, however, the Fe, Co and Mn sites are involved in the *same reaction step* and are influencing each other. The simultaneous incorporation of these metals (during synthesis) here creates subtly different sites than those present in the monometallic analogues. These species are found to be more active in enhancing the oxidation reaction and a synergistic relationship is present between active centres at the molecular level, which extends beyond the scope of bifunctionality.

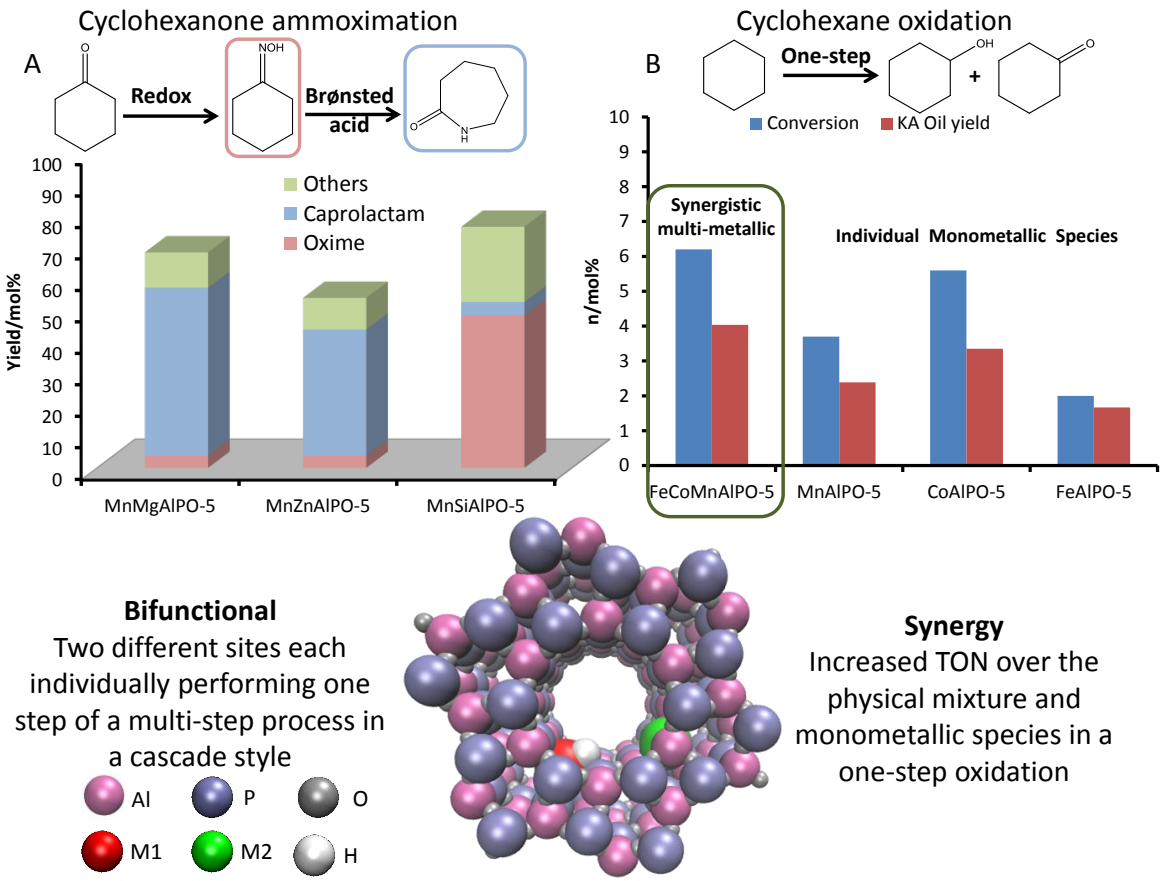

Figure 1.15: Contrasting multifunctionality (A) with catalytic synergy (B).[28,54,56]

1.4 Probing the Nature of the Active Site at the Molecular Level

A range of characterization techniques are required in order to effectively explore the nature of the active site, the framework, and complex inter-play between the two. The most commonly used technique to characterize a zeotype material is powder X-ray diffraction (XRD, Figure 1.16C). As each framework has its own fingerprint set of peaks it is trivial to assess both the phase-purity and the crystallinity of a sample through a single XRD pattern. Some useful information can be gained through careful analysis of powder-XRD data such as the particle size. Using Scherrers equation[57] it is possible to calculate the size of the particles to a greater degree of accuracy than other techniques. Through further analysis of the data more information can be gained. Reitveld analysis compares the experimental peak positions with

calculated “ideal” values to give unit cell parameters. This then generates an insight into the location of the metal dopant. As most dopants have a greater ionic radii than Al^{3+} or P^{5+} then isomorphous substitution should be accompanied by an increase in unit cell size, the extent of the variation depends on several factors such as ionic radii, the degree of substitution and also the initial size of the unit cell. As such an increase in unit cell size is a strong indicator that the dopant has been isomorphously substituted. Despite calculating unit cell parameters powder-XRD is primarily a method for characterizing the framework and not the active site. The framework can be further characterized by BET measurements, whereby gas adsorption produces an isotherm that can be interpreted using BET theory to give a surface area measurement.

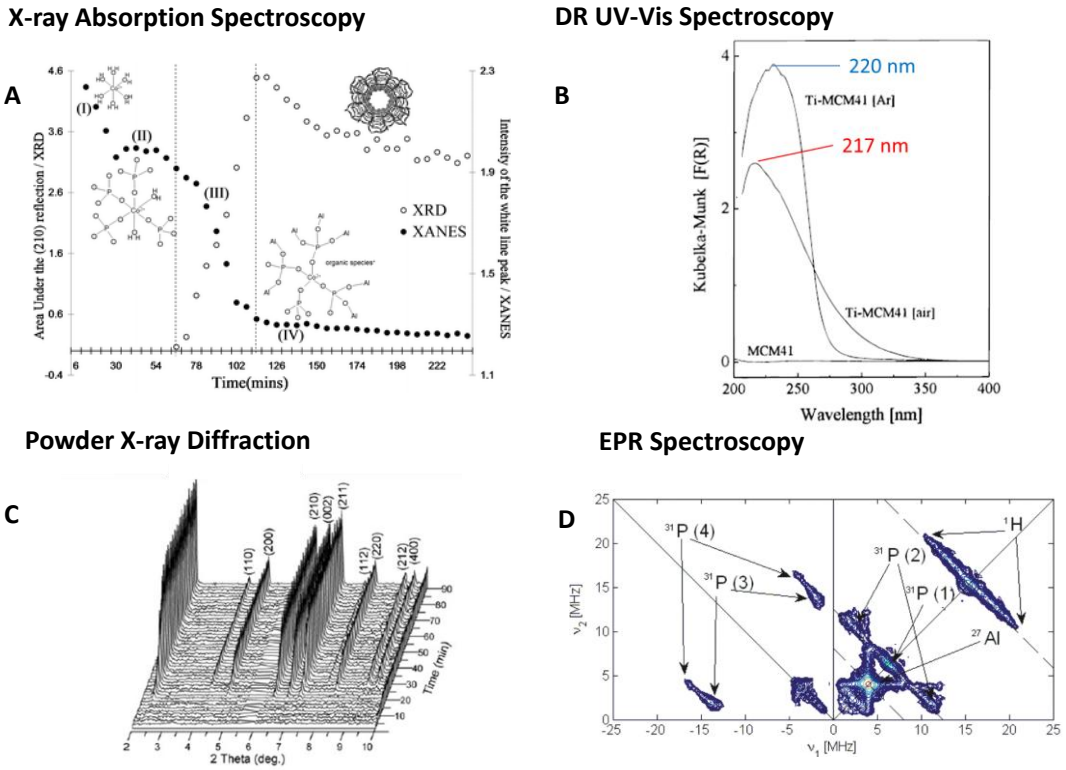

Figure 1.16: Depiction of different characterization techniques for investigating the nature of the framework and active metal species.

In contrast, X-ray adsorption studies (XAS, Figure 1.16A) is considered a definitive technique for characterizing the active site. By focusing on emissions of a specific atom (usually the dopant) it is possible to interpret the scattering pattern of an emitted electron to give bond lengths, bond angles and coordination geometry of nearest neighbours in a framework. This technique is

commonly used to prove framework incorporation. Previous work from Sankar *et al* shows how the incorporation of cobalt into a variety of AlPO frameworks can be proven. By showing that the cobalt is in a tetrahedral environment, with the closest coordination sphere containing 4 oyxgen atoms and the next 4 phosphorus atoms of roughly equal distances away Sankar *et al* confirmed that the cobalt had been isomorphously substituted into the framework.[24] Further to this they were able to show that the average Co-O bond length varies significantly between cobalts divalent and trivalent, with the divalent possessing much longer bonds (~ 1.97 Å) owing to the Co-O(H)- group, whereas the trivalent showed shorter bonds (~ 1.82 Å). Following this discovery it became possible to quantify the fraction of cobalt that can be oxidised to the trivalent state and compare this for different AlPO frameworks. It was found that the larger AlPO-5 framework had a surprisingly low redox fraction (~ 25 %), whereas in contrast nearly all the cobalt was redox active in the smaller-pored AlPO-18 framework, explaining why some CoAlPO systems were more active than others.

Similar studies have been performed by Nilsen *et al* on CuAlPO-5.[58,59] By considering the bond lengths and coordination geometries it was found that the choice of copper precursor (Cu^{2+} acetate or Cu^{2+} oxide) played a key role in the incorporation of the Cu^{2+} ion.[58,59] This was found to affect the activity of the catalyst for the reducing NO species. It was shown that CuAlPO-5 synthesised from Cu^{2+} oxide is more easily incorporated into the framework, and therefore did not undergo autoreduction, as is necessary for this reaction. In contrast when Cu^{2+} acetate was used the copper formed extra framework sites and was not incorporated into the framework, therefore was not as stabilized, so could undergo autoreduction, making it more active for the reduction of NO.

UV/Vis spectroscopy acts as a powerful complement to XAS (Figure 1.16B), as it can yield similar information to that acquired in the XANES (X-ray Adsorption Near Edge Structure) region. Therefore UV/Vis can provide further evidence to the oxidation state and local coordination geometry based on specific electronic transitions of transition metals. This has previously been used to great effect, particularly when considering titanium active sites such as those in Ti-MCM-41 and TS-1.[4,33]

Another more commonly-used technique is electron-paramagnetic resonance (EPR) spectroscopy, a similar technique in principle to NMR, exploiting electron spin, not nuclear spin. This makes it of significant interest for characterizing transition-metal doped AlPOs (Figure 1.16D). TiAlPO-5 is of particular interest and has been studied in depth using EPR, an unlikely choice as the stable quadruvalent ion is d^0, however several sources hypothesise the existence of Ti^{3+} sites within the framework[60]. Prakash *et al* compared the spectra of TiAlPO-5 and of TiO_2/SAPO-5.[61] In the former titanium butoxide was added to the synthesis gel with the aim to incorporate the metal into the framework, in the latter it was simply deposited onto the surface of SAPO-5. Despite both calcined systems being phase-pure AFI, and neither producing an EPR signal (suggesting all the titanium is Ti^{4+}) significant differences occurred under CO and γ-radiation treatment. Both γ-radiation and CO reduction are known to effectively reduce Ti^{4+} to Ti^{3+}, providing the metal with the electron spin to become EPR active. EPR spectra of both samples revealed that TiO_2/SAPO-5 had an axial g tensor with $g_\perp = 1.971$, and $g_\parallel = 1.907$, typical of octahedral Ti^{3+}. Whereas TiAlPO-5 was found to be tetrahedral with a rhombic g tensor of $g_1 = 1.965$, $g_2 = 1.920$ and $g_3 = 1.879$, suggesting framework incorporation. On adsorption of CO the TiO_2/SAPO-5 species showed similar spectra to that after γ-radiation treatment, in contrast the signal was different for TiAlPO-5. This is attributed to the ability of the framework tetrahedral titanium being able to expand its coordination sphere further, unlike the saturated octahedral TiO_2/SAPO-5 species. This finding coupled with accurate metal loadings confirmed that titanium had undergone type II substitution into the AlPO framework.[61] This result has recently been contested by Berlier *et al*, using a combination of EPR, electron nuclear double resonance (ENDOR) and hyperfine sublevel correction (HYSCORE) which through Ti-P coupling suggested that some proportion of the titanium substitutes for the aluminium ion and is able to undergo similar redox processes on reduction with hydrogen.[60] As such the location of titanium in TiAlPO-5 is still under debate.

1.5 Deciphering the nature and strength of solid-acid centres

Given that zeolites and similar zeotype materials are primarily employed as solid-acid catalysts in the chemical industry, there has been a great deal of interest in developing protocols and methods for exploring these specific active sites. Fourier-transform infra-red spectroscopy (FT-IR) is routinely used to qualitatively correlate the bands associated with the O-H stretches to the acid-site strength. However, in order gain detailed quantitative information on the nature and strength of solid acid centres, it becomes imperative to employ a suitable probe molecule (such as CO) for quantifying the nature and type of such sites. It is often beneficial to combine the information garnered from FT-IR with other spectroscopic methods, such as temperature-programmed desorption (TPD, Figure 1.17A), to complement and categorise the respective fractions of ‘strong’, ‘weak’ and ‘intermediate’ acid sites present on a specific species. In many studies it is important to establish selection rules for the classification and quantification of the Brønsted acid centres present in heteroegenous catalysts.

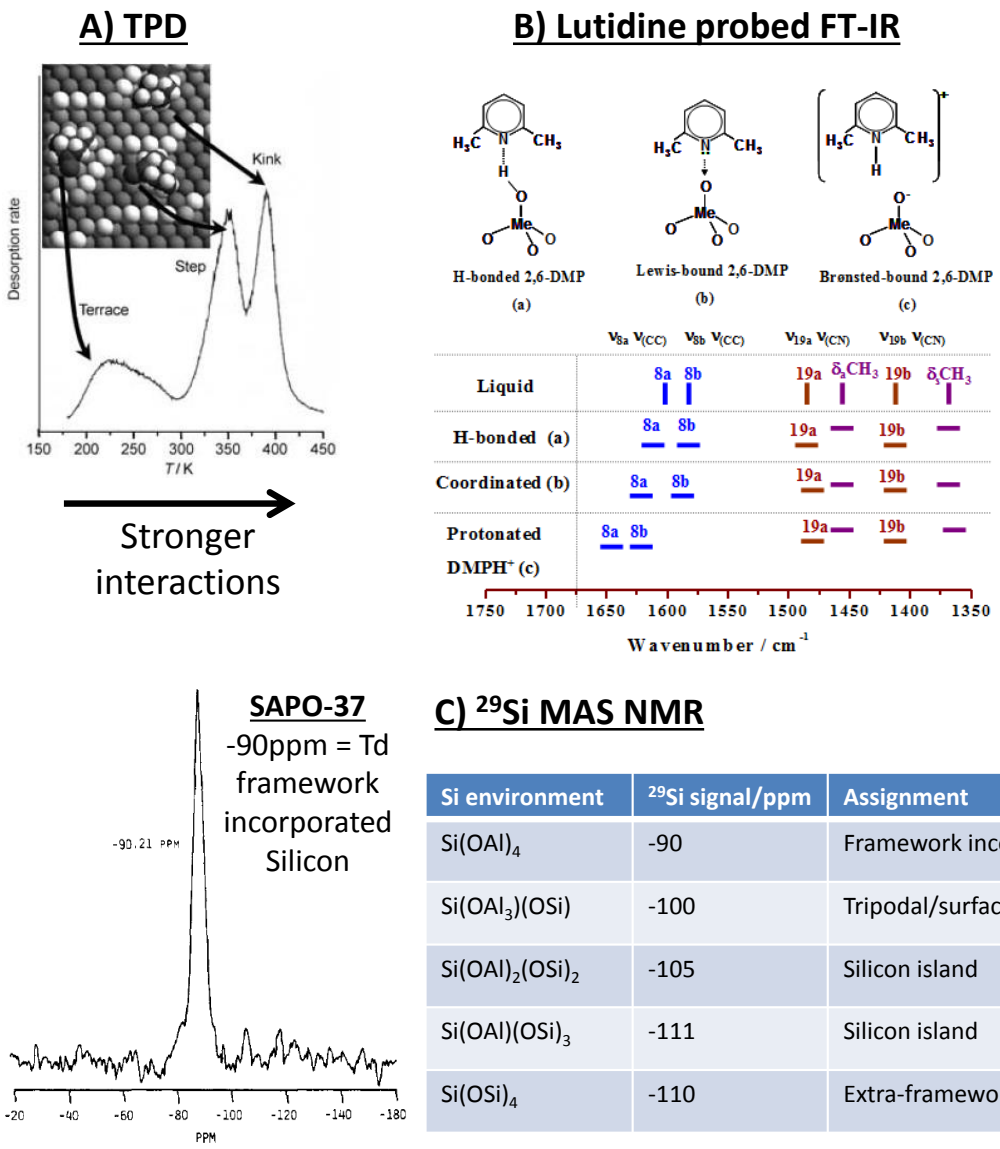

Si environment	^{29}Si signal/ppm	Assignment
$Si(OAl)_4$	-90	Framework incorporated
$Si(OAl_3)(OSi)$	-100	Tripodal/surface site
$Si(OAl)_2(OSi)_2$	-105	Silicon island
$Si(OAl)(OSi)_3$	-111	Silicon island
$Si(OSi)_4$	-110	Extra-framework

Figure 1.17: Detailing the use of molecular probes (CO and 2,6-DMP) for quantifying nature and type of solid-acid centres.[70,71]

While NH_3-TPD and CO FT-IR experiments yield significant amounts of useful information on a range of acid species, it is rarely the case that the reagents used are of comparable size to ammonia or carbon monoxide. Thus in the case of bulkier reagents a different, larger, probe molecule is often appropriate such as a methylated pyridine ring (lutidine or collidine). These larger probes have the advantage of mimicking the behaviour of larger molecules and thus giving significant insights into actual diffusion behaviour in the reaction. It is also possible to analyse the acid site strength with such probe molecules, this may be performed in one of two ways. One such method shares similar principles with TPD. Initially the probe molecule is adsorbed onto the surface

until all the acid sites are saturated. The area of a characteristic signal (applying to the probe molecule) is then monitored. The system is then heated and the spectra measured at specific intervals and the area of the signal recorded, thus constituting a less continuous version of TPD. The second way in which this can also be achieved is by looking at the shift of specific signals, similar to CO probed FT-IR. For lutidine (2,6-DMP) the ν_{8a}(CC) band (Figure 1.17B) is highly sensitive to acid site strength, and type, with the exact position of this band yielding significant information on the nature of the acid site.[62,63] It can be shown that the quantification of the number and strength of acid sites using 2,6-DMP as a probe is invaluable in determining the difference in acidic density, with the TPD providing complementary evidence for these species. By gaining a thorough understanding of the precise nature and strength of the solid-acid active centres, it has been possible to predict the type of substitution mechanism (Figure 1.9) that leads to the creation of isolated single-sites for targeted catalysis.

While the above spectroscopic techniques produce a wealth of information about the nature and strength of the acid-species present, they reveal very little information on the local environment around the active site. This is something that is of fundamental importance and must be well understood for the rational and targeted synthesis of active sites in the future. Preliminary efforts[55] using 1D and 2D MAS ^{29}Si NMR have provided valuable quantitative insights into the Si-substitution mechanism (type II versus type III – see Figure 1.9) within these molecular sieves, which also provide direct evidence for the formation of isolated Si sites and silicon islands that are responsible for regulating the catalytic activity and selectivity (Figure 1.17C).

While modern characterisation tools and *operando* spectroscopy can provide detailed information on the framework and the types of active sites, there are some limitations on the degree of information they can provide on an electronic scale. This is particularly relevant when considering dynamic systems. Recent developments in computational chemistry have provided some of the necessary tools that are required to gain quantitative insights into the nature of a diverse range of catalytically active single sites.[64] There are many complementary theoretical techniques such as cluster-based and periodic DFT,[64] Monte-Carlo simulations, molecular dynamics and QM/MM models that are currently employed in solid-state chemistry (particularly relating to porous

solids),[65] which when allied with sophisticated *operando* characterisation afford a valuable tool for affording structure-activity relationships.

1.6 Computational advances in nanoporous materials

Despite spectroscopic advances there is still a limit to the amount of information that can be gained experimentally, but, due to the advances in computational chemistry over the past few decades it is possible to explore a range of effects and characteristics theoretically. The computational work of AlPO chemistry can be divided into three primary areas: structure, material characteristics and the modelling of reaction pathways.

Initially the aim of the majority of the theoretical work on AlPOs was to simply reproduce the structures and unit cell parameters using a range of computational methods. One of the earliest attempts employed an "electronegativity equalization method", this matched parameters for average electronegativity and "hardness" to those derived from the STO-3G basis set on a range of simple Al, P, Si, H, O, F, N and C containing molecules.[66] The unit cell parameters, space groups, atomic coordinates, framework densities and charges were then calculated for a range of zeolite and AlPO structures and showed good agreement with the experimental values obtained. A variety of interatomic potentials have also been used to describe the AlPO framework, van Beest *et al* used *ab initio* cluster calculations of a variety of $M(OH)_4$ species to obtain a consistent set of pair potentials for the AlPO framework,[67] this system however couldn't accurately describe the structures and resorted to editing one parameter empirically to match experimental findings. Further Vos Burchart *et al* used a molecular mechanics approach to extend their description of silicate species to accurately reproduce the AlPO species.[68] This had the failing of having to recalculate partial charges of species at every point in the optimisation, drastically extending calculation time. A third description came from Gale and Henson using the Born model and deriving parameters from the experimental data of Berlinite.[69] This accurately reproduced a significant amount of Berlinites properties and was then extended to explore the placement of protons in SAPO-37.

One of the greatest challenges of that eluded early computational models was to accurately reproduce the commonly used AlPO-5 (AFI) framework. The original powder-XRD data on the AlPO-5 framework concluded that the material possessed P6cc symmetry, however this was since contested by many groups with P6[68], P31c[69] and Pcc2[70] space groups having since been suggested. One of the main reasons for this contention is that when modelled using a range of potentials the P6cc AlPO-5 structure repeatedly showed some Al-O-P bonds were nearly linear, far outside the normal 140-160° range.[71] This problem was solved by reducing the symmetry of the space group down to P6 or Pcc2 which then meant the Al-O-P all fell into the normal range, it was then shown that the 180° Al-O-P bonds were artifacts caused by averaging the position of 3 different oxygen atoms, hence the "true" lower symmetry of the material as shown in Figure 1.18.

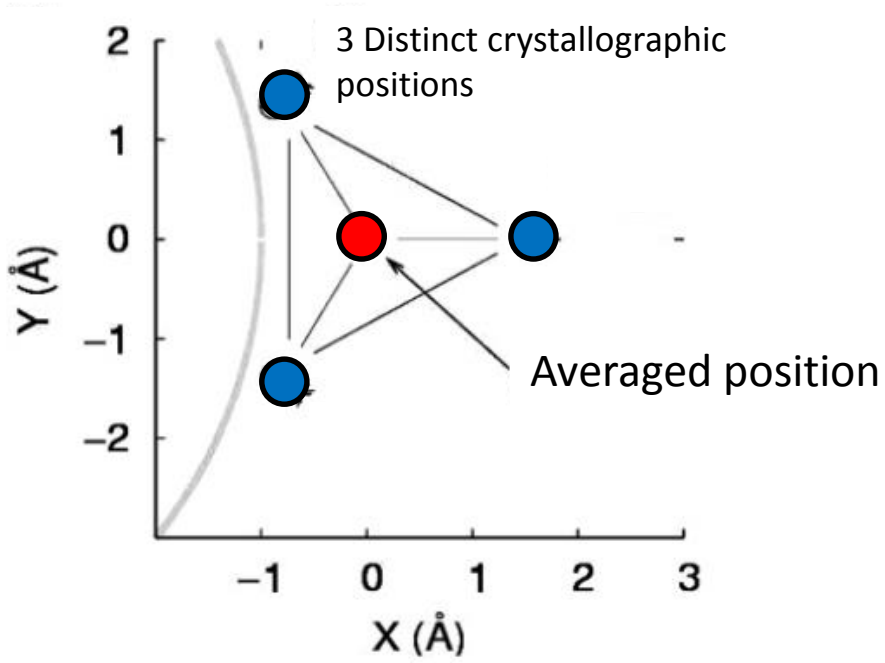

Figure 1.18: The average environment of the oxygen atom which leads to the linear Al-O-P bonds.

Once confidence grew in structure reproduction many groups then began to explore the characteristics of many AlPO materials. Owing to their prolific use as solid acid catalysts, the ability to calculate acid strength, and correlate it to a specific variable was highly attractive. In light of this the calculation of O-H stretching frequencies (ν_{OH}), and also adsorption energies of simple probe molecules such as NH_3 are of great interest. Work from Elenany *et al* contrasted

the acidity of metal-doped AlPO-5[72] and AlPO-34[73] species using periodic DFT methods. With one slight exception it was found that the deprotonation energy and the energy of adsorption of NH_3 correlated exceptionally well for a range of dopants. From these calculations it was concluded that Mn^{2+} was one of the more acidic dopants in an AlPO-34 structure. Comparing the two structures showed that in all cases the AlPO-34 structure was more acidic than the AlPO-5 analogue. Further, the group showed there could potentially be a link between the bond angle of the M-OH-Al bond and the acidity, however this was based on a very small subset of dopants. Previous work on the subject performed by Catlow *et al* investigated the possible link between a wide range of parameters (ionic radius, electronegativity and T-O-T bond angle) and Brønsted acid strength, for a wide range of dopants in the AlPO-34 structure.[74] It was determined that there was no significant correlation between the ν_{OH} any of these parameters, despite previous suggestions from the literature. This was attributed to the large variation in the behaviour and orientation of the different sites around the dopant. Using similar techniques the groups also probed the behaviour of redox metals within the AlPO-34 framework, by calculating the energy of a divalent and trivalent system the redox potential could be compared using Equation 1.7.

$$\Delta E^{2+/3+} = E[HM^{2+}AlPO-34] - E[M^{3+}AlPO-34] - \frac{1}{2}E[H_2] \qquad (1.7)$$

It was shown that while Mn and Co heavily favoured the divalent state, Fe was more energetically stable in the trivalent state, as predicted by Fenton chemistry. This same technique was also able to probe the nature of the fundamental AlPO material, by using difference electron density maps or berlinite and quartz it was shown that while zeolites are primarily covalent systems, AlPOs are actually ionic systems. This then showed that AlPOs were not (as previously believed) made of AlO_4 and PO_4 tetrahedra, but instead are composed of PO_4^{3-} ions and Al^{3+} ions existing as discrete ionic units.

Understanding reaction mechanisms is still one of the most complex problems in catalysis, however this is now becoming possible with the evolution of modern computing techniques, particularly in the field of periodic DFT. Previously simplistic reaction mechanisms for oxidations of titanium-containing zeolites have shown that a qualitative understanding can be gained by modelling just the area of the structure that is of direct interest (the metal

site and its nearest neighbours). Despite the lack of long range order in the models these calculations cannot hope to give quantitative values for reaction pathways. To gain this type of information periodic DFT calculations are required.

As previously stated AlPOs first received mainstream attention from the scientific community for their ability to aerobically oxidise inert alkane molecules such as cyclohexane and hexane with various cobalt-, iron- and manganese-substituted AlPO materials. In the work of Cora *et al* the oxidation of ethane was explored using MnAlPO-5,[64,75] a full detailed mechanism of the process was built which examined the activation[76], peroxide decomposition,[77] propagation[78] and regeneration[79] stages. Each reaction step was monitored by calculating the energy of a system as one variable (the reaction coordinate) is varied thereby generating a potential energy surface, allowing the transition-state to be estimated without the need to calculate computationally demanding frequencies. It may be the case that a step is not dictated by a change in just one reaction coordinate, but several. In this circumstance the methodology is simply extended to varying one reaction coordinate time and finding the transition state in that coordinate, fixing the reaction coordinate at that value and then varying the next coordinate until an accurate transition state can be found. In such situations the calculation of frequencies and transition state optimisation becomes necessary to fully understand the structures. However, as computational methods develop further the scope of reactions that can be modelled is rapidly increasing. The theoretical study of Cora *et al* concluded that the pre-activation step (breaking of the first C-H bond) was the most energetically demanding step in the whole pathway. By repeating the initial stage of this study (pre-activation) with FeAlPO-5 instead of MnAlPO-5, subtle differences in the reaction pathway and energetics were observed.[80] It was shown that as manganese displays a greater preference for the M^{2+} state, it was less energetically demanding for Mn^{3+} to undergo reduction to Mn^{2+}, whilst simultaneously activating the alkane *via* an oxidative transfer. It was also notable that manganese was able to activate the hydrocarbon with greater ease than the iron-analogues. Furthermore, once reactive intermediates were formed, an alternative pre-activation mechanism was accessible (secondary pre-activation). Manganese was also found to accomplish this step at a significantly lower energy cost. It is only when considering the propagation

step that the benefits of iron become apparent (Figure 1.19). In this step, the metal centre is being oxidized from M^{2+} to M^{3+}, whilst producing oxygenated hydrocarbon products; and the iron sites are able to perform this step with much greater ease than manganese. From this work,[80] it was subsequently argued that the complementary behavior of these two different oxidation sites would make them appropriate candidates to unite to form a bimetallic FeMnAlPO-5 catalyst, should one wish to optimize this reaction further. Such theoretical advances significantly influence the molecular design of bimetallic and multifunctional active sites at the atomic level, which facilitate meaningful structure-property relationships to be established in our quest for affecting stimulating catalytic challenges.

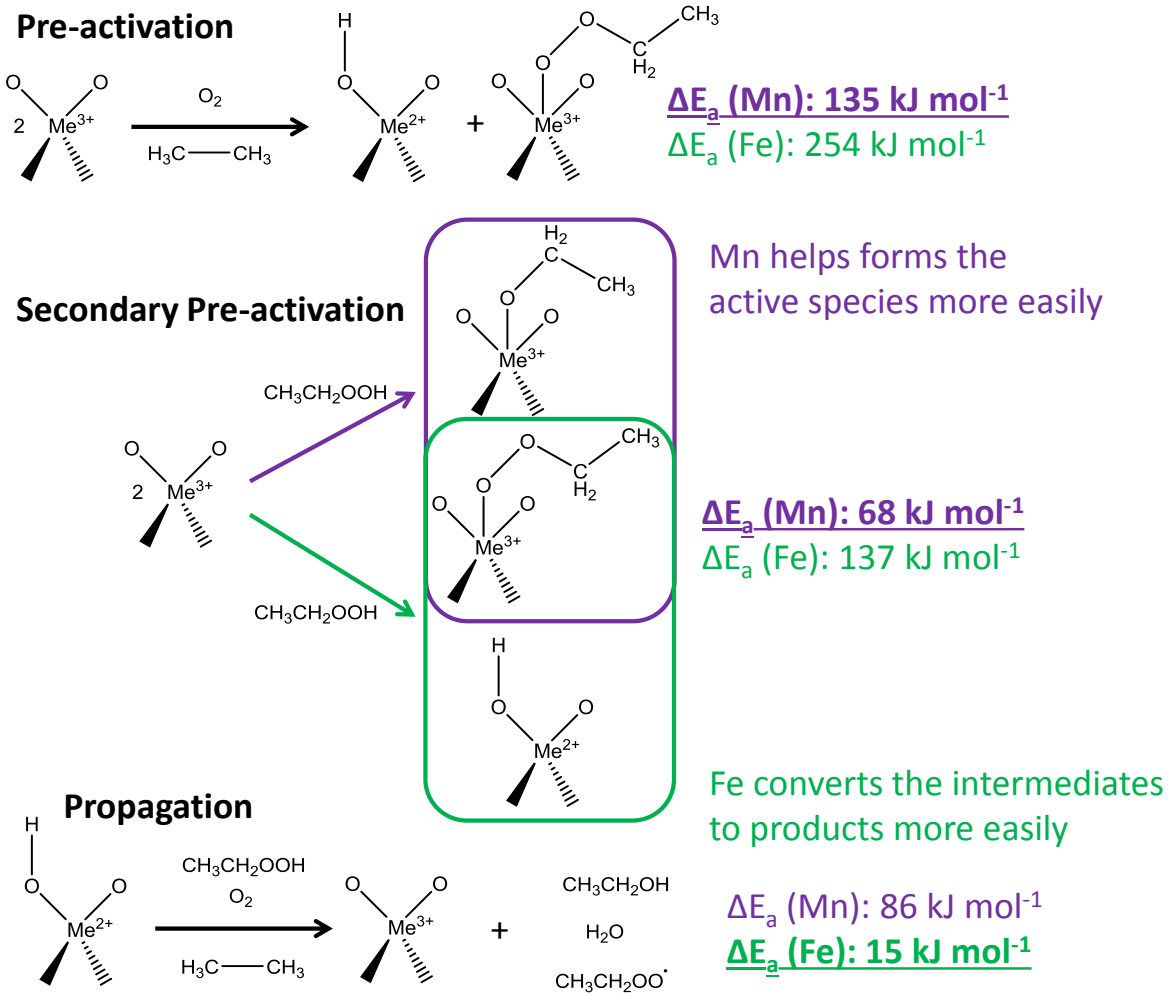

Figure 1.19: Complementary behaviour of Mn and Fe active centres in AlPO-5 catalysts for alkane oxidation.[93]

1.7 Predictive Design and Structure-Property Relationships in Acid Catalysis

Un-doped AlPOs and a vast proportion of mesoporous silicas are charge neutral and hence are not naturally acidic; hindering their direct application in acid-catalysed transformations. Judicious incorporation of transition-metal ions into the inner walls of the nanoporous framework can result in careful tailoring of the acidity by meticulous consideration of the valency and the loading of a chosen metal ion. Acidity, in some cases, can be enhanced by increasing the concentration of the active centres or type of substitution mechanism (see Figure 1.10) and can lead to an increase in catalytic performance.[81] Sufficient caution should be exercised when introducing transition-metals into the framework; if the loading is too high it can promote the transformation of metal ions into extra-framework metal oxide species, resulting in undesired side-reactions.[82]

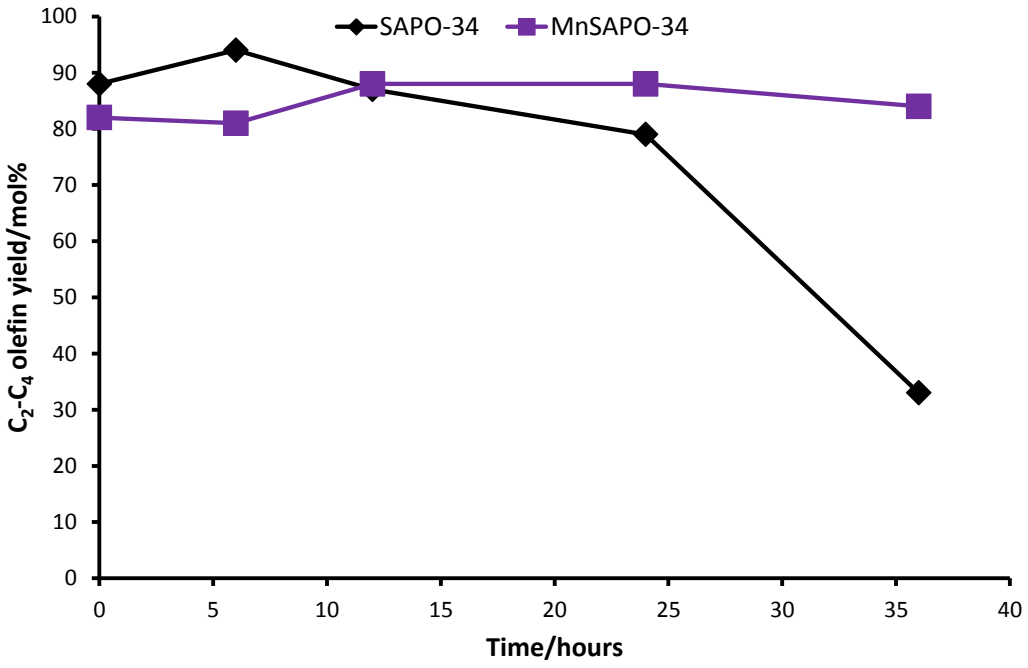

Figure 1.20: Bimetallic substitution enhances catalytic lifetime of the SAPO-34 species in the MTO reaction.

Arguably the most widely investigated reaction involving AlPOs is the methanol-to-olefin (MTO) process. As previously stated, SAPO-34 has been considered the industrial standard catalyst for this reaction, therefore making

it a prime candidate for synthetic improvements to optimise catalytic performance via multi-metallic substitution. In the work of Dubois *et al* a range of bimetallic AlPO-34 architectures were prepared (CoSAPO-34, MnSAPO-34 and NiSAPO-34) and their catalytic behaviour contrasted with the monometallic SAPO-34 species.[83] Within this study it was shown through the metallic dopants (Mn, Co and Ni) had been successfully isomorphously substituted into the framework to create tetrahedral entities via magnetic susceptibility measurements. Despite all the ions successfully substituting into the framework only the MnSAPO-34 showed an improvement on the SAPO-34 species. It was found that the incorporation of Mn into the framework significantly retarded the deactivation process, thus allowing the system to remain active for longer (Figure 1.20). It was found that MnSAPO-34 remained active even after 54 hours on stream, whereas SAPO-34 began to lose activity after 30 hours.[83]

This work also further highlighted the need for delicacy and intricacy when designing bimetallic species. Within this study the synthetic procedure to form NiSAPO-34 was investigated and resulted in the formation of two subtly different species, Ni-SAPO-34, in which the nickel had formed extra-framework nanoparticles, and NiSAPO-34, in which the nickel had isomorphously substituted into the framework (Figure 1.21).[83]

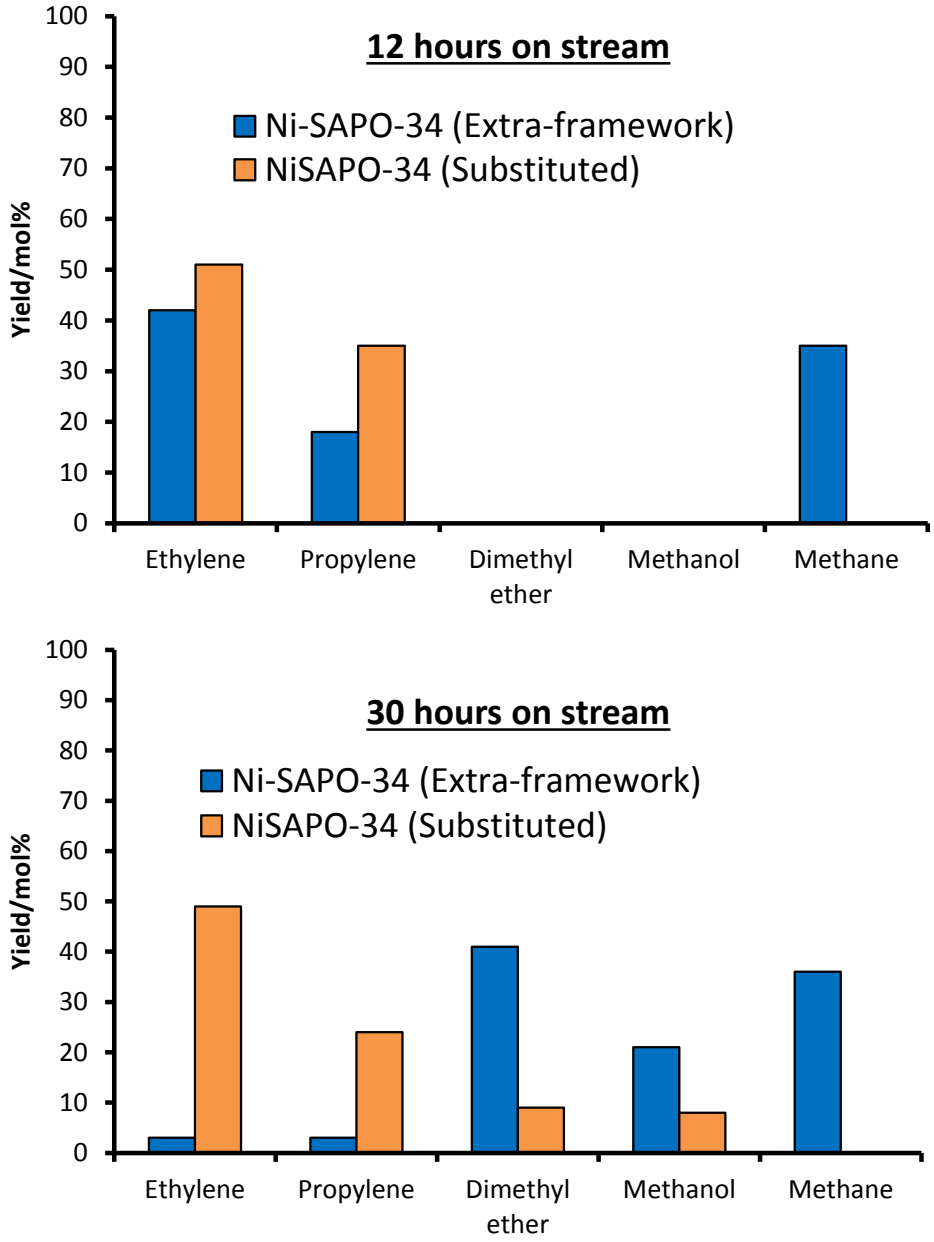

Figure 1.21: Detailing the effect of different bimetallic substitution synthetic procedures.

It is evident from this data that it is imperative to create the correct metal environment in order to improve the reactivity of a species. It can be seen from Figure 1.21 that between 12 and 30 hours only a subtle increase in dimethyl ether and methanol is observed in the product stream, however the extra framework nickel species degenerates more rapidly.[83]

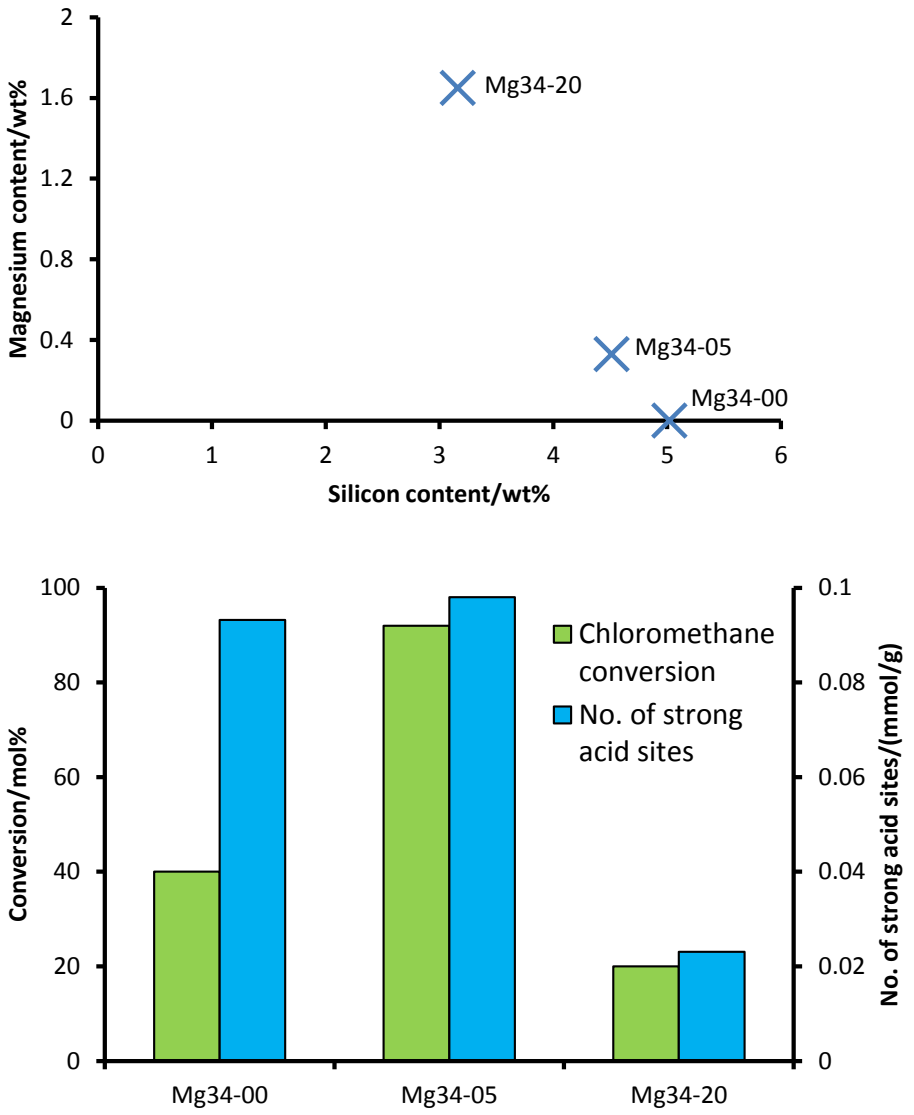

Figure 1.22: Linking bimetallic substitution to improved activity in MgSAPO-34

While improvements can be achieved through bimetallic substitution it should be stressed that this is not a universal rule for all systems, and is in fact, the result of a prodigious design strategy that should take into consideration the nature and type of active sites in question as well as the surrounding pore architecture. One system which epitomises this point is MgSiAlPO-34, which was evaluated for the conversion of chloromethane to light olefins; an alternative to the industrially implemented MTO process (Figure 1.22). In this endeavour[84] a series of SiAlPO-34 catalysts were studied; in which varying amounts of magnesium were introduced into the SiAlPO-34 synthesis procedure, though the silicon quantities were kept constant. It was shown that by incorporating modest amounts of magnesium into the framework, the lifetime and activity of the catalyst could be markedly improved. However, the

introduction of larger quantities of magnesium had the adverse effect of lowering the total acidity of the system, whilst promoting silicon islanding and limiting the catalytic performance. It was also observed that the quantity of silicon present in the catalyst was also inversely proportional to the amount of magnesium incorporated. This observation suggests that the magnesium may have forced the silicon out of the framework, thereby leading to a less active species. This study highlights the delicate balance that exists in bimetallic catalysts, while simultaneously it emphasizes the need for a meticulous and prudent design approach coupled with the prerequisite for a detailed characterisation of the nature of the active site at the atomic level.

1.8 Enhancing Synergy in Oxidation Reactions

The profound link between the precise coordination geometry of a metal centre and its redox potential plays a crucial role in determining its reactivity, and subsequent catalytic potential. As such the aim to manipulate the exact nature of the active site together with its surrounding framework has prompted the design of a range of bimetallic AlPO catalysts for use in selective oxidation reactions. One example of this strategy, employing the tri-metallic FeMnCoAlPO-5 catalyst for the oxidation of cyclohexane, has previously been discussed.[17] This concept has been extended to include other redox-active metals; namely CoTiAlPO-5, MnTiAlPO-5 and VTiAlPO-5. The latter catalyst showed a synergistic enhancement in catalytic potential for the epoxidation of cyclohexene, compared to its individual monometallic counterparts, under analogous conditions (Figure 1.23A). The underlying nature of this catalytic synergy was explored further using a probe-based, *in situ* FT-IR study; in which the active acetyl peroxyborate (APB) oxidant was used as the molecular probe. This *in situ* study revealed that the combination of the Ti^{4+} and vanadyl ions, undergoing simultaneous isomorphous substitution into the same AlPO-5 framework, aided the formation of the active peroxo species in the vicinity of the Ti^{4+} centres, and improved the substrate-oxidant interactions.[16] This resulted in a two-fold improvement in reactivity: as not only a more reactive active centre(s) is generated at the molecular level, but the concomitant advantageous interactions of the oxidant and activated substrate within the

pores minimised wasteful oxidant decomposition, thereby facilitating a greater atom economy, higher product selectivity and better oxidant efficiency.[16]

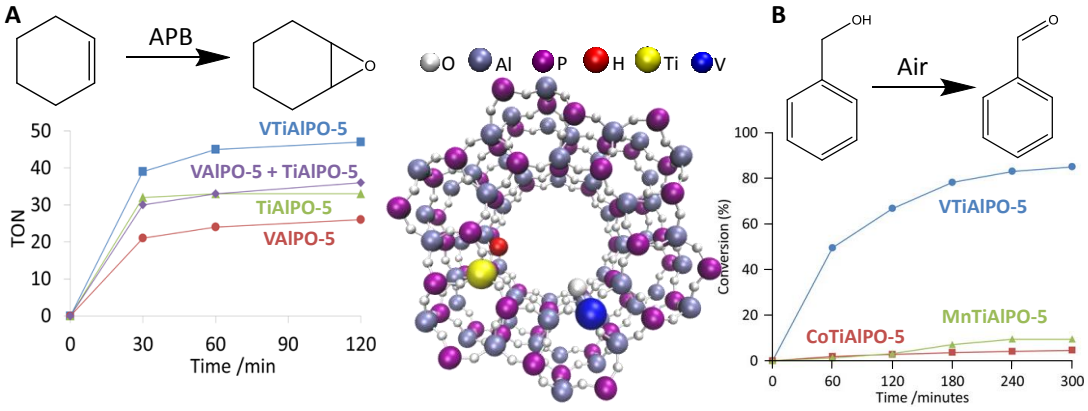

Figure 1.23: Modulating the potential of bimetallic active centres in selective oxidation reactions.[16]

In order to facilitate meaningful structure-property correlations and to understand the catalytic synergy at a more fundamental level, the exact nature of the active sites was probed through a combination of UV/Vis spectroscopy and EPR-HYSCORE (Electron Paramagnetic Resonance – Hyperfine Sub-level Correlation) techniques. It was found that[16,60,85] on reduction of the catalyst some of the titanium species were able to access the Ti^{3+} state and had interestingly undergone framework substitution *via* a type I substitution mechanism (see Figure 1.10). The vanadium species was similarly found to exclusively undergo type I substitution; despite vanadium occupying the V(V) oxidation state. The HYSCORE studies (Figure 1.16D) further revealed that the vanadium ions were found to exist as a vanadyl species (V=O), possessing an overall charge of just 3+, hence its suitability for type I substitution. The EPR investigations were not able to conclusively substantiate the presence of Ti^{4+}-O-V species, given the low levels of doping in the system, and further work is currently in progress to elucidate this. The effect of the various redox metals (V-, Ti- and Co) was catalytically probed by comparing the performance of the bimetallic VTiAlPO-5 catalyst with CoTiAlPO-5 and MnTiAlPO-5 in the aerobic oxidation of benzyl alcohol (Figure 1.23B). It was found that the performance of the VTiAlPO-5 catalyst far exceeded that of the other two systems. By simultaneously employing an *in situ* UV/Vis study, it was found that, unlike the VTiAlPO-5 catalyst, the MnTiAlPO-5 possessed a much higher fraction of titanium sites in an octahedral coordination, which could well be responsible

for its inferior catalytic performance. It is therefore highly likely that the titanium sites in MnTiAlPO-5 would be coordinatively saturated and unable to interact efficiently with the oxidant and effectively generate the active oxidant species. Further, by contrasting the UV/Vis spectra of the oxidised and reduced samples it was found that the CoTiAlPO-5 catalyst had a significantly lower redox fraction than the VTiAlPO-5 system and this could have also played a significant role in hindering the activation of the oxidant, thereby limiting the reactivity with the CoTiAlPO-5 analogue (Figure 1.23B). The individual catalytic profiles (TON) for the monometallic and bimetallic analogues and the corresponding physical mixtures of the V- and Ti-catalysts was also investigated for a different oxidation reaction – the epoxidation of olefins.

Whilst the majority of literature on metal-doped AlPO systems is dedicated to the isomorphous substitution of metals to create isolated sites, it is also possible to engineer synergistic interactions wet-impregnation methods to make extra-framework species. Such a procedure has been employed by Fei *et al* to enhance the lifetime and activity of Pt-containing species for the dehydrogenation of propane to propene.[86] It had previously been shown that the combination of Pt and Sn results in smaller platinum species and is also able to favourably modify the electronic properties of these species. While a range of other hosts had been previously explored (alumina and zeolites) these supports were susceptible to coking and rapid deactivation. As such the choice of support is heavily influential on the catalytic behaviour for this reaction. Through the use of hydrogen temperature-programmed reduction it was found that the Sn lowered the redox potential of the platinum system, thereby enhancing its reactivity for this reaction (Figure 1.24).

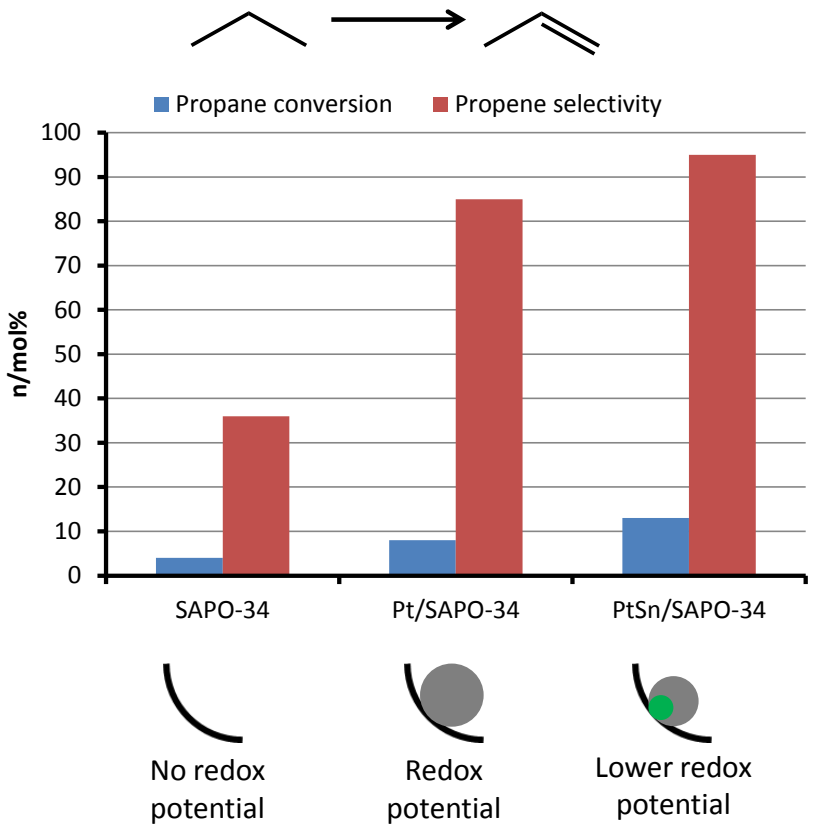

Figure 1.24: Describing the synergistic effects of Pt and Sn species deposited onto SAPO-34.

Therefore, a detailed understanding of the mechanistic pathway in combination with meticulous design at the atomic level is paramount when choosing metal combinations to create specific active sites. This study further emphasises the need to rationally combine metal substituents using all of the facets that have been discussed above (ionic size, coordination geometry, redox potential, type of substitution, etc.), so that the design and combination approach at the molecular level will result in distinctive and subtle modifications to active sites, often translating into startling differences in catalytic activity and selectivity.

These notions are echoed throughout the work presented here. The idea of designing an active site is dependent on many variables including framework structure, method of incorporation and dopant metal to name but a few. During this work a range of active sites are designed, characterised and tailored to optimise industrially interesting processes to generate products for the sustainable production of nylon precursors. Given the increased control offered by microporous materials, and the range of possible active sites, this

work primarily focusses on aluminophosphate (AlPO) materials, with metal dopants aimed to generate specific Brønsted acid active sites.

Intially the role of the framework is investigated. This is done by observing its influence on the formation of specific active sites and also on the specific reaction mechanism of the Beckmann rearrangement of cyclohexanone oxime.

Once framework properties have been understood the effect of bimetallic substitution is explored, observing how the combination of different active sites can modify the reactivity for contrasting acid catalysed reactions.

Finally the effect of bimetallic substitution of cobalt and titanium is explored using a combined theoretical and XAS study within the confines of the AlPO-5 framework.

1.9 References

1. M. Bowker, *The basis of Applications of Heterogeneous Catalysis*, Oxford Science Publications, **1998**.
2. R. H. Grubbs and S. Chang, *Tetrahedron*, **1998**, *54*, 4413-4450.
3. G. C. Chinchen, K. Mansfield and M. S. Spencer, *Chem. Technol.,* **1990**, *20*, 692–699.
4. T. Maschmeyer, F. Rey, G. Sankar and J. M. Thomas, *Nature*, **1995**, *378*, 159–162.
5. K. Simmance, G. Sankar, R. G. Bell, C. Prestipino and W. van Beek, *Phys. Chem. Chem. Phys.,* **2010**, *12*, 559–562.
6. D. J. Xuereb, J. Dzierzak and R. Raja, *Catal. Today*, **2012**, *198*, 19-34.
7. D. J. Xuereb and R. Raja, *Catal. Sci. Tech.*, **2011**, *1*, 517-534.
8. J. M. Thomas and R. Raja, *Topics in Catal.*, **2006**, *40*, 3-17.
9. B. Moden, B. Z. Zhan, J. Dakka, J. G. Santiesteban and E. Iglesia, *J. Phys. Chem. C*, **2007**, *111*, 1402-1411.
10. L. A. Clark, M. Sierka and J. Sauer, *J. Am. Chem. Soc.*, **2004**, *126*, 936-947.
11. J.-H. Kim, S. Namba and T. Yashima, *Appl. Catal. A: Gen.*, **1992**, *83*, 51-58.
12. J. M. Thomas, R. Raja, G. Sankar and R. G. Bell, *Nature*, **1999**, *398*, 227-230.
13. J. M. Thomas and R. Raja, *Acc. Chem. Res.*, **2008**, *41*, 708-720.
14. J. M. Thomas and R. Raja, *Chem. Commun.*, **2001**, *8*, 675-687.
15. J. M. Thomas, R. Raja and D. W. Lewis, *Angew. Chem. Int. Ed.*, **2005**, *44*, 6456-6482.
16. R. M. Leithall, V. N. Shetti, S. Maurelli, M. Chiesa, E. Gianotti and R. Raja, *J. Am. Chem. Soc.*, **2013**, *135*, 2915-2918.
17. J. Paterson, M. E. Potter, E. Gianotti and R. Raja, *Chem. Commun.*, **2011**, *47*, 517-519.
18. W. F. Hoelderich, *Stud. Surf. Sci. Catal.*, **1989**, *46*, 193-209.
19. Y. Izumi, H. Ichihashi, Y. Shimazu, M. Kitamura and H. Sato, *Bull. Chem. Soc. Jpn.*, **2007**, *80*, 1280-1287.
20. B. Guo, L. Zhu, H. Xu, Q. Zhang, D. Tong, G. Li and C. Hu, *Catal. Sci. Tecnol.,* **2011**, *1*, 1060-1067.
21. M. G. Clerici, G. Bellusi and U. Romano, *J. Catal.,* **1991**, *129*, 159-167.

22. S. T. Wilson, B. M. Lok, C. A. Messina, T. R. Cannan and E. M. Flanigen, *J. Am. Chem. Soc.*, **1982**, *104*, 1146-1147.
23. P. T. Barger, *US Pat.*, 5,095,163, **1992**.
24. G. Sankar, R. Raja and J. M. Thomas, *Catal. Lett.*, **1998**, *55*, 15-23.
25. R. Raja, G. Sankar and J. M. Thomas, *Angew. Chem. Int. Ed.*, **2000**, *39*, 2313-2316.
26. M. Dugal, G. Sankar, R. Raja and J. M. Thomas, *Angew. Chem. Int. Ed.*, **2000**, *39*, 2310-2313.
27. S. O. Lee, R. Raja, K.D.M. Harris J.M. Thomas, B. F. G. Johnson and G. Sankar, *Angew. Chem. Int. Ed.*, **2003**, *115*, 1558-1561.
28. L. Zhou, J. Xu, C. Chen, F. Wang and X. Li, *J. Porous. Mater.*, **2008**, *15*, 7-12.
29. J. D. Chen and R. A. Sheldon, *J. Catal.*, **1995**, *153*, 1-8.
30. Q. Xingyi, Z. Lili, X. Wenhua, J. Tianhao and L. Rongguang, *Appl. Catal. A: Gen.*, **2004**, *276*, 89-94.
31. J. S. Choi, S. S. Yoon , S.H. Jang and W. S. Ahn, *Catal. Today*, **2006**, *111*, 280-287.
32. Y. W. Chen and H. Y. Lin, *J. Por. Mater.*, **2002**, *9*, 175-184.
33. A. Thangaraj, R. Kumar and P. Ratnasamy, **1991**, *131*, 2594-297.
34. B. Y. Hsu, S. Cheng and J. M. Chen, *J. Mol. Catal. A: Chem.*, **1999**, *149*, 7-23.
35. P. S. E. Dai, R. H. Petty, C. W. Ingram and R. Szostak, *Appl. Catal. A: Gen*, **1996**, *143*, 101-110.
36. M. Hartmann and L. Kevan, *Chem. Rev.*, **1999**, *99*, 635-663.
37. M. Anilkumar and W. Hoelderich, *Catal. Today*, **2012**, *198*, 289-299.
38. C. X. Wang, L. Zhang and Y. Liu, *Appl. Catal., B,* **2013**, *136-137*, 48-55.
39. Z. Nawaz and W. Fei, *Ind. Eng. Chem. Res.*, **2009**, *48*, 7442-7447.
40. T. Komatsu and H. Ikenaga, *J. Catal.*, **2006**, *241*, 426-434.
41. M. D. Jones, R. Raja, J. M. Thomas, B. F. G. Johnson, D. W. Lewis, J. Rouzand and K. D. M. Harris, *Angew. Chem. Int. Ed.*, **2000**, *39*, 2313-2316.
42. A. Corma, J. Diaz-Cabanas, J. Martinez-Trigero, F. Rey and F. Rius, *Nature*, **2002**, *418*, 514-517.
43. S. T. Wilson, B. M. Lok and E. M. Flanigen, *US Pat.*, 4,310,440, **1982**.
44. M. E. Davis, C. Saldarriaga and C. Montes, *Zeolites*, **1988**, *8*, 362-366.

45. M. Estermann, L. B, McCusker, C. Baerlocher, A. Merrouche and H. Kessler, *Nature*, **1991**, *352*, 320-323.
46. F. Farges and G.E. Brown Jr., *Geochim. Cosmochim. Acta*, **1997**, *61*, 1863-1870.
47. T .Blasco, A. Corma, M. T. Navarro and J. Perez-Pariente, *J. Catal.*, **1995**, *156*, 65-74.
48. M. A. Roberts, G. Sankar, J. M. Thomas, R. H. Jones, H. Du, J. Chen, W. Pang and R. Xu, *Nature*, **1996**, *381*, 401-404.
49. M. W. Anderson, O. Terasaki, T. Oshuna, A. Phillippou, S. P. Mackay, A. Ferreria, J. Rocha an S. Lidin, *Nature*, **1994**, *367*, 347-351.
50. A. Corma, P. Esteve and A. Martinez, *J. Catal.,* **1996**, *161*, 11-19.
51. R. Raja and A. J. Paterson, *US Pat.*, US20130245322, **2013**.
52. R. Raja and J. M. Thomas, *US Pat.*, US20130245323, **2013**.
53. R. Raja, G. Sankar and J. M. Thomas, *J. Am. Chem. Soc.*, **2001**, *123*, 8153-8154.
54. J. M. Thomas and R. Raja, *Proc. Natl. Acad. Sci. U. S. A.*, **2005**, *102*, 13732-13736.
55. A. B. Levy, R. Raja and M. E. Potter, *US Pat.*, US20130109851, **2013**.
56. L. Zhou, J. Xu, H. Miao, X. Li and F. Wang, *Catal. Lett.*, **2005**, *99*, 231-234
57. P. Scherrer, *Gottinger Nachrichten Math. Phys.*, **1918**, *2*, 98-100.
58. D. G. Nicholson and M. H. Nilsen, *J. Mater. Chem.*, **2000**, *10*, 1965-1971.
59. I. D. Burton, J. S. J. Hargreaves, D. G. Nicholson, M. H. Nilsen, and M. Stockenhuber, *J. Mater. Chem.*, **2001**, *11*, 1441-1446.
60. S. Maurelli, M. Vishnuvarthan, M. Chiesa, G. Berlier and S. Van Doorslaer, *J. Am. Chem. Soc.*, **2011**, *133*, 7340-7343.
61. A. M. Prakash, V. Kurshev and L. Kevan, *J. Phys. Chem.* **, 1997**, *101*, 9794-9799.
62. T. Onfroy, G. Clet and M. Houalla, *Micropor. Mesopor. Mater.*, **2005**, *82*, 99-104.
63. T. Armaroli, M. Bevilacqua, M. Trombetta, A. Gutierrez Alejandre, J. Ramirez and G. Busca, *Appl. Catal. A: Gen.*, **2001**, *220*, 181-190.
64. L. Gomez-Hortiguela, F. Cora, G. Sankar, C. M. Zicovich-Wilson and C. R. A. Catlow, *Chem. – Eur. J.*, **2010**, *16*, 13638-13645.
65. S. P. Bates and R. A. Van Santen, *Adv. Catal.*, **1998**, *42*, 1-114.

66. L. Uytterhoeven, W. J. Mortier and P. Geerlings, *J. Phys. Chem. Solids*, **1989**, *50*, 479-486.
67. B. W. H. van Beest, G. J. Kramer and R. A. Van Santen, *Phys. Rev. Lett.*, **1990**, *64*, 1955-1958.
68. E. D. Vos Burchart, H. van Bekkum, B. van de Graaf and E. T. C. Vogt, *J. Chem. Soc. Faraday Trans.*, **1992**, *88*, 2761-2769.
69. J. D. Gale and N. J. Henson, *J. Chem. Soc. Faraday Trans.*, **1994**, *90*, 3175-3179.
70. A. J. Mora, A. N. Fitch, M. Cole, R. Goyal, R. H. Jones, H. Jobic and S. W. Carr, *J. Mater. Chem.*, **1996**, *6*, 1831-1835.
71. A. R. Ruiz-Salvador, G. Sastre, D. W. Lewis and C. R. A. Catlow, *J. Mater. Chem.*, **1996**, *6*, 1837-1842.
72. M. Elanany, D. P. Vercauteren, M. Kubo and A. Miyamoto, *J. Mol. Catal A; Chem.*, **2006**, *248*, 181-184.
73. M. Elanany, M. Koyama, M. Kubo, P. Selvam and A. Miyamoto, *Micro. Meso. Mater.*, **2004**, *71*, 51-56.
74. F. Cora, M. Alfredsson, M. Barker, R. G. Bell, M. D. Foster, I. Saadoune, A. Simperler and C. R. A. Catlow, *J. Solid State Chem.*, **2003**, *176*, 496–529.
75. F. Cora, L. Gomez-Hortiguela and C. R. A. Catlow, *Proc. R. Soc. A.*, **2012**, *468*, 2053-2069.
76. L. Gomez-Hortiguela, F. Cora and C. R. A. Catlow, *ACS Catal.*, **2011**, *1*, 18-28.
77. L. Gomez-Hortiguela, F. Cora and C. R. A. Catlow, *ACS Catal.*, **2011**, *1*, 945-955.
78. L. Gomez-Hortiguela, F. Cora and C. R. A. Catlow, *ACS Catal.*, **2011**, *1*, 1487-1497.
79. L. Gomez-Hortiguela, F. Cora and C. R. A. Catlow, *ACS Catal.*, **2011**, *1*, 1475-1486.
80. L. Gomez-Hortiguela, F. Cora and C. R. A. Catlow, *Phys. Chem. Chem. Phys.*, **2013**, *15*, 6870–6874.
81. A. Vinu, M. Karthik, M. Miyahara, V. Murugesan and K. Ariga, *J. Mol. Catal. A: Chem.*, **2005**, *230*, 151-157.
82. M. Karthik, A. K. Tripathi, N. M. Gupta, A. Vinu, M. Hartmann, M. Palanicharmy and V. Murugesan, *Appl. Catal. A*, **2004**, *268*, 139-149.

83. D. R. Dubois, D. L. Obzrut, J. Liu, J. Thundimadathil, P. M. Adekkanattu, J. A. Guin, A. Punnoose and M. S. Seehra, *Fuel. Proc. Technol.*, **2003**, *83*, 203-218.
84. D. Zhang, Y. Wei, L. Xu, F. Chang, Z. Liu, S. Meng, B. L. Su and Z. Liu, *Microporous Mesoporous Mater.*, **2008**, *116*, 684–692.
85. S. Maurelli, M. Chiesa, E. Gianotti, R. M. Leithall and R. Raja, *Chem. Commun.*, **2012**, *48*, 8700–8702.
86. Z. Nawaz, X. Tang, Q. Zhang, D. Wang and W. Fei, *Catal. Commun.*, **2009**, *10*, 1925-1930.

Chapter 2: Experimental techniques

The following chapter details the theoretical aspects of the characterisation techniques utilised within this work only. Specific experimental details are found in the experimental section of the appropriate results chapters.

2.1 Powder X-Ray diffraction (XRD)

The wavelengths of X-rays commonly lie within the nanometre range, the same range which separates bonding atoms, and also crystallographic planes. This makes them excellent candidates for interacting with zeotype materials to reveal framework morphology. The application of powder X-ray diffraction (XRD) is derived from Braggs law,[1] which relates the wavelength of an X-ray to the distance between crystallographic planes thus:

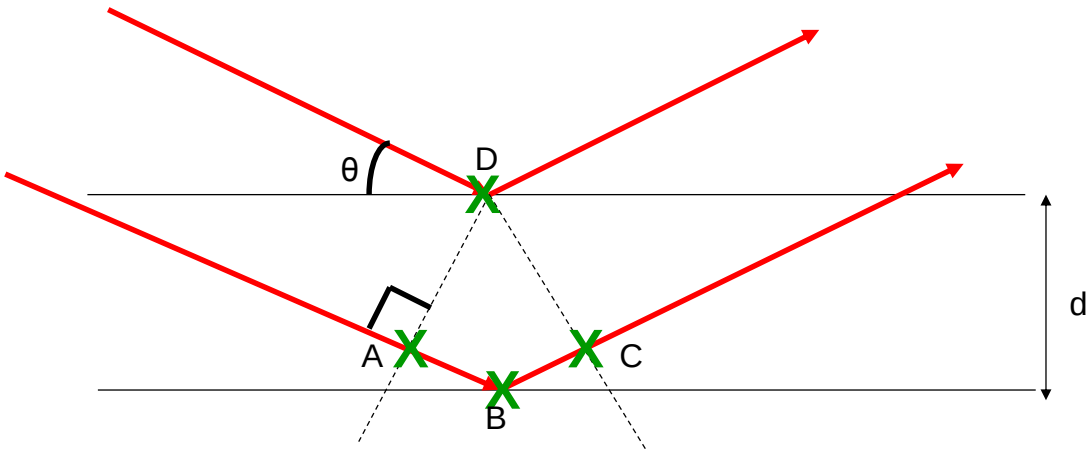

Figure 2.1: Graphical representation of Braggs law.

In figure 2.1 we see two X-rays (red) being diffracted off adjacent crystallographic planes (black), which are separated by a distance d. If the two X-ray waves are not perfectly in-phase with one another then there will be no signal due to destructive interference. However when the waves are in-phase with one another they will undergo constructive interference and the intensities of the two waves will be added together to produce a signal. For them to be in-phase the extra distance travelled by the bottom wave (AB and then BC) must be an integer number of wavelengths. Thus:

$$n\lambda = AB + BC \qquad (2.1)$$

where n is an integer and λ is the wavelength of the X-ray source. Given that the system is symmetric then the distance AB is equal to BC therefore:

$$n\lambda = 2AB \quad (2.2)$$

Using trigonometry the angle ADB is also the angle of incidence labelled as θ, similarly as the distance DB is equal to the distance between crystallographic planes, d, then we can express the distance AB in terms of d and θ:

$$AB = d \times Sin\theta \quad (2.3)$$

Thus we derive Braggs Law:

$$n\lambda = 2d \times Sin\theta \quad (2.4)$$

In order to collect this information a powdered sample is placed on a holder and the X-ray source and the detector move relative to one another to scan through a range of 2θ values (figure 2.2):

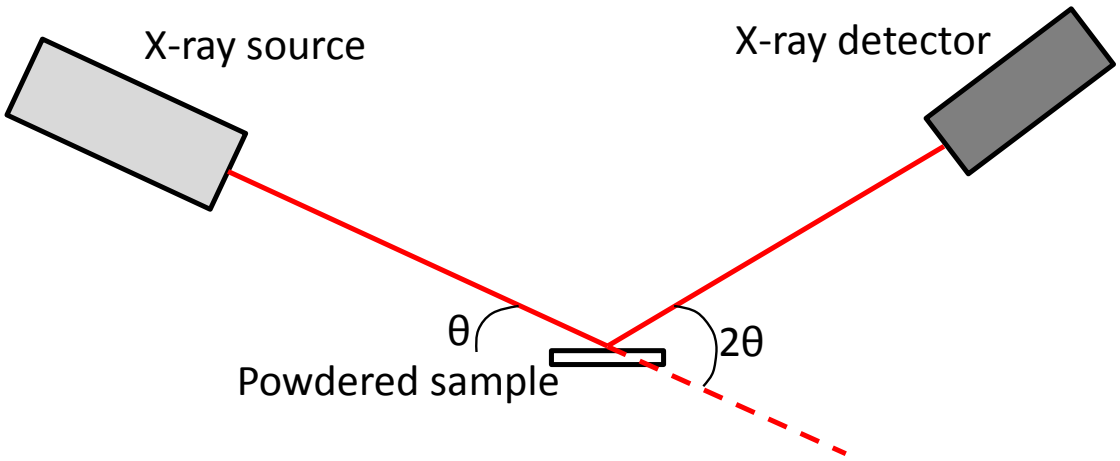

Figure 2.2: Schematic of X-ray detector, source and angle of incidence.

The data in its raw form is then seen as a set of concentric circles (figure 2.3):

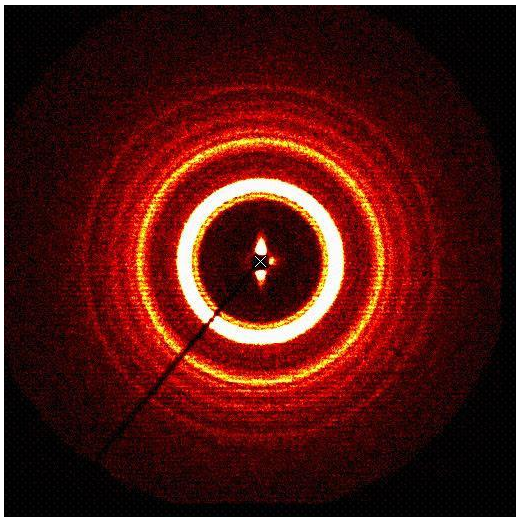

Figure 2.3: Raw data collected from a powder XRD.

The data is then commonly represented by plotting the diffraction angle (2θ) on the x-axis against the intensity (number of counts) on the y-axis to give a powder X-ray diffraction pattern. Every distinct framework has its own fingerprint set of peaks by which it can be identified, often to determine phase-purity of the correct structure, eliminating the possibility of secondary phases. Further XRD data can also be used to investigate particle size through the Scherrer's equation[2] which links the peak-shape and position to particle size thus:

$$Particle\ size = \frac{K\lambda}{FWHM \times Cos\theta} \qquad (2.5)$$

where K is the shape factor of the system, typically 0.9, λ is the wavelength of the X-ray source and FWHM is the width of the XRD peak at half the intensity.

Finally Reitveld analysis can be used to calculate the unit cell-parameters of the crystalline system. This is commonly done by an optimisation algorithm, whereby the unit cell-parameters are modified to achieve the best match with the experimental peak positions.

2.2 Brunauer-Emmett-Teller (BET) Theory

BET theory is primarily used to measure the surface area of solids by adsorbing a probe molecule (commonly nitrogen) onto the surface and monitoring the

change in pressure. Given the porous nature of heterogeneous zeotype catalysts, the surface area is of great interest in determining the amount of available surface (for active-site density calculations) but also determining the correct structure has been formed. The Langmuir isotherm forms the background for this theory,[3] which applies to a system with particles constantly adsorbing and desorbing. Assuming the system is in equilibrium thus:

$$A + S \leftrightarrow AS \tag{2.6}$$

where A is the adsorbing species, S is the available surface sites and AS is the adsorbed species bound to the surface. Changing the nomenclature, such that the number of available sites can be quantified yields:

$$\Theta = 1 - \Theta_E \tag{2.7}$$

where Θ is the fraction of the surface which is covered by adsorbant (linked to AS), and therefore Θ_E is the fraction of empty sites (S). Then the rate of adsorption is then defined as:

$$Rate_{ads} = k_{ads} \times P_A \times (1 - \Theta) \tag{2.8}$$

Thus the rate of adsorption is equal to the rate constant for adsorption, multiplied by the partial pressure of the probe molecule, multiplied by the number of available sites. The higher the partial pressure and the more available sites the faster the molecule will adsorb onto the surface. Similarly the rate of desorption is expressed as:

$$Rate_{des} = k_{des} \times \Theta \tag{2.9}$$

The rate of desorption is equal to the rate constant for desorption multiplied by the fraction of occupied sites. This does not depend on the partial pressure, only on the fraction of occupied sites. As the system is in equilibrium the rate of desorption is equal to the rate of adsorption:

$$k_{des} \times \Theta = k_{ads} \times P_A \times (1 - \Theta) \tag{2.10}$$

By defining $K = k_{ads}/k_{des}$, and rearranging, surface coverage (Θ) can be expressed as:

$$\Theta = \frac{K \times P_A}{(1+(K \times P_A))} \tag{2.11}$$

However there are some failings to this theory. In many cases it oversimplifies, as it assumes that all sites are equivalent, which may not be the case in a real system, and also it assumes that there is only a single monolayer of adsorbant present on the species. However there is likely to be many layers of adsorbant on the system. This can be solved by using a multi-layer adsorption model[4] which can be expressed as:

$$\frac{1}{V\left(\frac{P_0}{P}-1\right)} = \frac{1}{V_m C} + \frac{(C-1)}{V_m C}\left(\frac{P}{P_0}\right) \qquad (2.12)$$

where V is the total volume of adsorbed gas, V_m is the volume of gas adsorbed on the monolayer, C is the BET constant, P_0 is the saturates pressure of the adsorbed gas and finally P is the equilibrium pressure of the adsorbed gas.

The BET isotherm differs from the Langmuir one as it assumes that the probe molecule can form multiple layers. In the first layer the probe molecule adsorbs onto the solid surface. A second layer of probe molecules can then adsorb onto the first layer, a third layer can then adsorb onto the second layer and so on.

It is important to note that the first layer is treated differently from all the other layers, as this forms a solid-gas interface. All other layers are treated identically, as these are assumed to be identical liquid-gas interfaces.

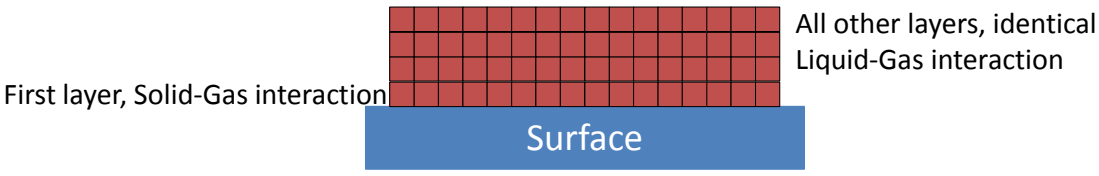

Figure 2.4: Diagram showing the different interactions in multilayer gas adsorption.

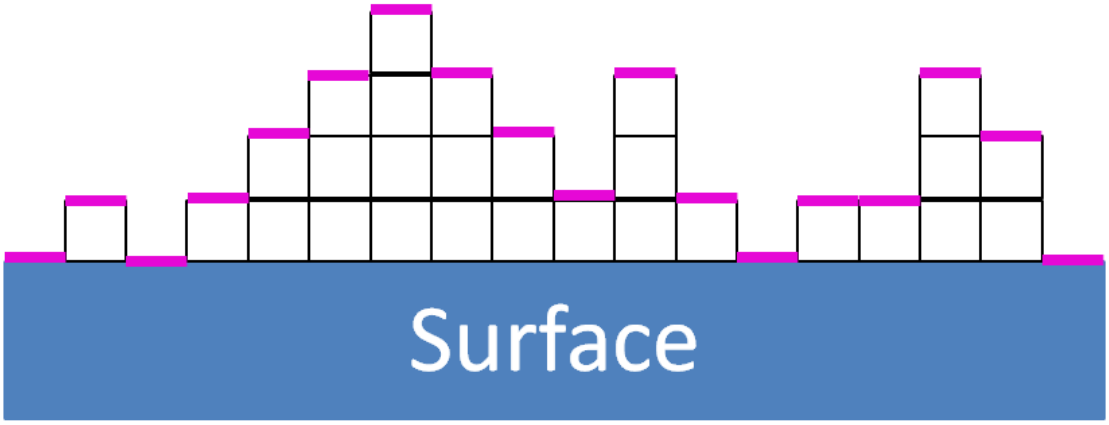

Figure 2.5: Diagram showing the different surface sites in multilayer gas adsorption.

The pink outline will sum to give the total surface area the solid sample. The proportion of surface area on each layer is S_i. For the solid surface, layer 0, we have $S_0 = 4$. The proportion of pink outline on the first layer (i = 1) is 6, so $S_1 = 6$. Similarly $S_2 = 3$, $S_3 = 4$ and $S_4 = 1$.

Each individual layer is in equilibrium. Consider the rate of adsorption for the first layer:

$$Rate_{ads,1} = k_{ads} \times P \times S_0 \qquad (2.13)$$

Similar to the Langmuir isotherm the rate of adsorption is equal to the rate constant of adsorption multiplied by the partial pressure of the probe molecule, multiplied by the number of available sites on the solid surface (the exposed surface area of layer 0). Also the rate of desorption is equal to the rate constant of desorption for the first layer multiplied by the number of molecules that are able to leave, the exposed surface area, a molecule can only desorb if there is not another molecule adsorbed on top of it.

$$Rate_{des,1} = k_{des,1} \times S_1 \qquad (2.14)$$

Given the processes are in equilibrium, the two terms will be equal:

$$k_{ads} \times P \times S_0 = k_{des,1} \times S_1 \qquad (2.15)$$

It is important to differentiate between the first layer and all other layers, as the interactions between surface-gas molecules will be different to those of the layers of liquid-gas molecules. This will then affect the rate of desorption,

though is assumed to not affect the rate of adsorption, thus for every other layer it can be similarly shown that:

$$k_{ads} \times P \times S_i = k_{des,i} \times S_i \quad (2.16)$$

By extending this further and taking into consideration the full volume of gas adsorbed over all layers it is possible to reach the equation for the BET isotherm described above in equation 2.12.

2.3 Scanning-electron microscopy (SEM)

SEM is commonly used in the field of nanoporous catalysts to view the surface morphology and consider the particle size and shape of the material on a micrometre scale. Various studies have been performed showing the differences in catalytic performance based purely on particle shape, as such SEM is a vital tool in catalyst characterisation. The technique involves firing a high-powered electron beam at the sample, which is commonly coated with carbon or gold to improve conductivity. This process can liberate a range of electrons and radiation, though primarily focuses on secondary and backscattered electrons, which are detected by the positively-charged detectors.

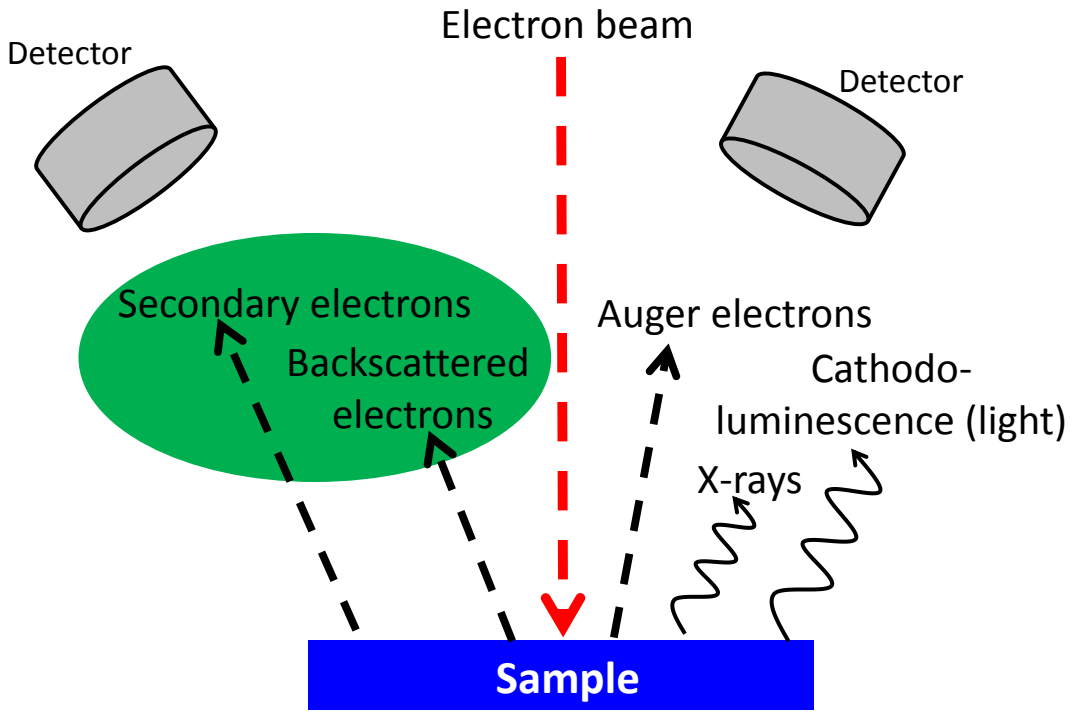

Figure 2.6: Diagram showing the different types of emissions from an electron beam.

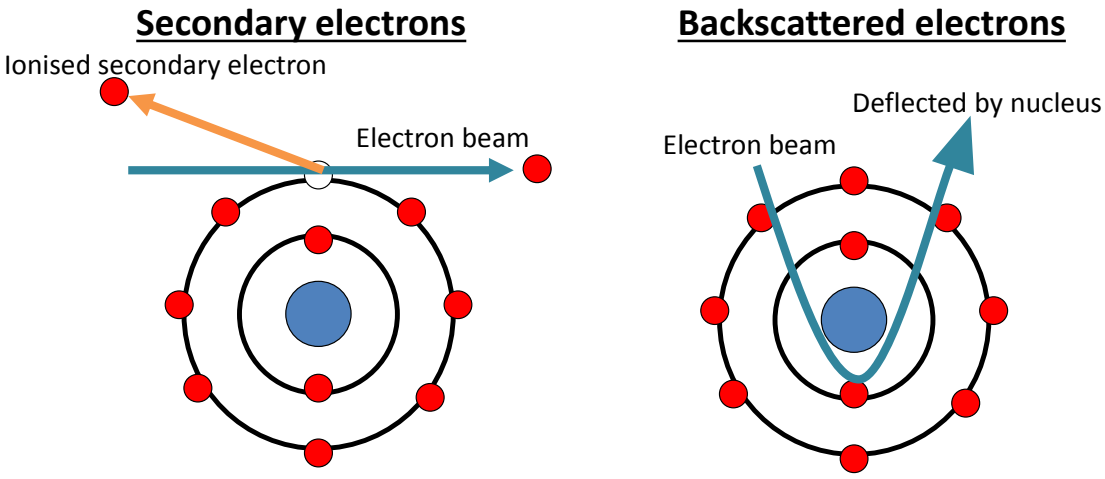

Figure 2.7: Schematic showing the generation of secondary and backscattered electrons.

Secondary electrons are electrons that have been ionised due to the interaction with the electron beam, thus one electron has been removed by another. Backscattered electrons are electrons from the beam itself which have been deflected away from the sample by the nucleus, and then reach the detector. The more secondary electrons that are released, the brighter the image

appears. Therefore steeper surfaces appear lighter than flatter ones as more secondary electrons are closer to the surface and therefore can escape, thus:

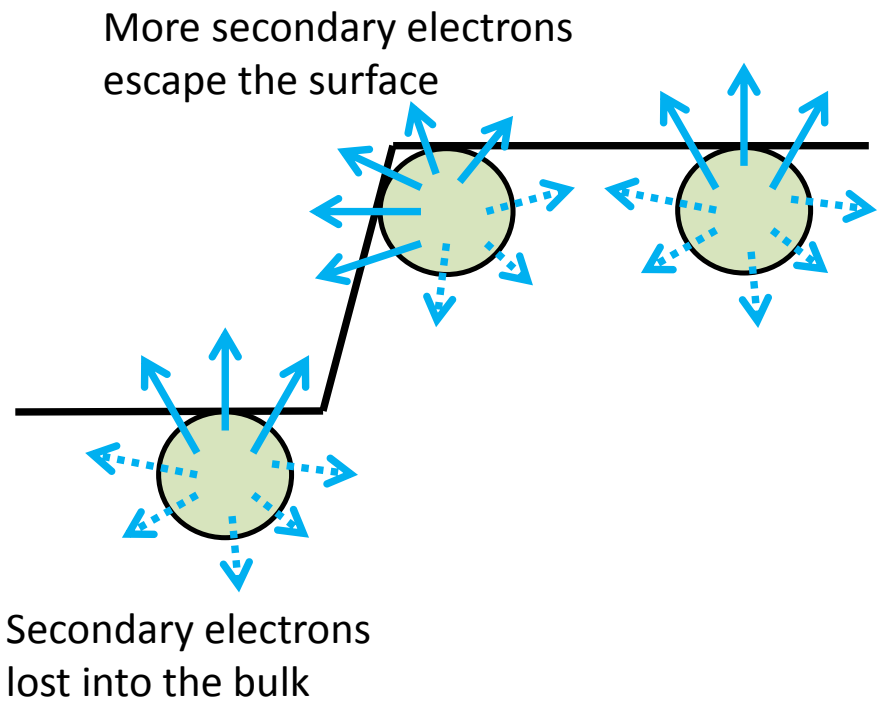

Figure 2.8: Graphical description of emitted secondary electrons in the bulk of a sample.

In contrast backscattered electrons can yield compositional information as heavier nuclei produce more backscattered electrons, due to the stronger interactions. As such the heavier nuclei will appear brighter, compared to the lighter atoms. This is particularly useful when there is a significant contrast between the heavy active site atoms and the lighter framework or support matrix.

2.4 Energy dispersive spectroscopy (EDS)

Energy dispersive spectroscopy utilises similar principles as SEM, though instead of probing the surface morphology it instead provides information on the surface composition. While SEM exploits secondary and backscattered electrons EDS uses Auger electrons. Auger electrons are released when the electron beam removes a deep-lying core-electron. This then prompts a valence

electron to relax and fill the available core electron position. This relaxation produces significant energy to ionise a weakly held electron, which is called an Auger electron.

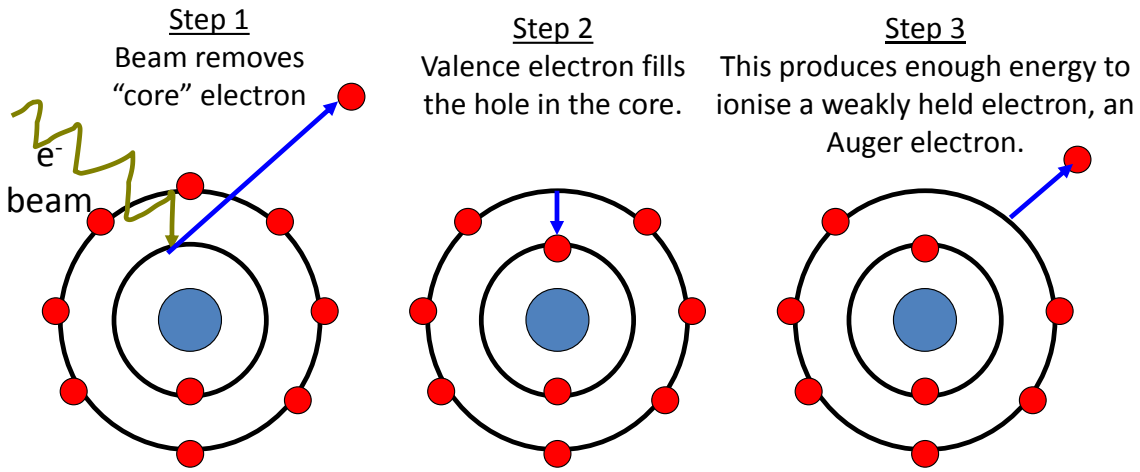

Figure 2.9: Schematic detailing the production of Auger electrons.

The quantised energy levels of the core electron and the valence electron are both element specific, and thus the energy transition between the two is also energy specific:

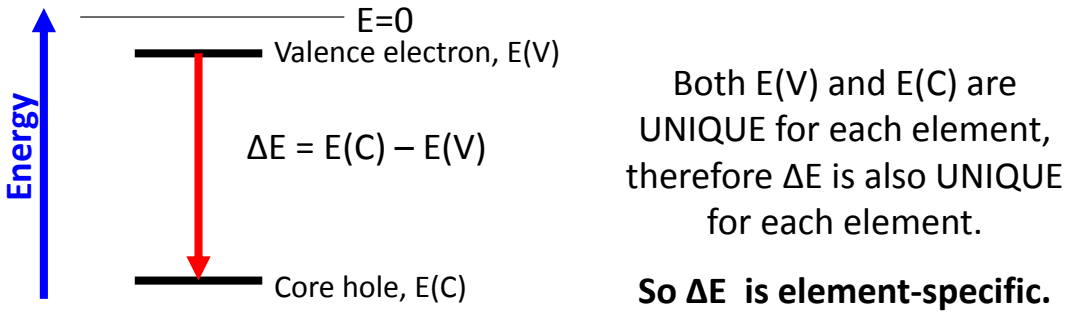

Figure 2.10: Schematic showing the unique energy of the transition.

When the energy difference (ΔE) is sufficient to ionise a valence electron then Koopmans theorem can link the ionisation energy of that valence electron, to the element-specific ΔE and also the kinetic energy of the ionised Auger electron:

$$\Delta E = IE + KE \qquad (2.17)$$

where ΔE is the difference in energy between the emitted core electron and the relaxed valence electron, IE is the ionisation energy of the valence Auger

electron and KE is the kinetic energy of the emitted Auger electron. As ΔE is element specific, and so is the ionisation energy of the Auger electron, then it follows that the kinetic energy of the Auger electrons will also be element specific, by detecting these electrons of different velocities it is then possible to give the composition of the surface of a species.

2.5 Temperature-programmed desorption (TPD)

Thermal desorption techniques are commonly used to measure the strength of interactions between a solid and a probe molecule. In catalysis this technique is more specifically used to probe the strength of active acid sites by monitoring their interactions with a basic probe molecule such as ammonia. Similarly to BET this technique is based on the kinetics and thermodynamics of adsorption and desorption, most importantly the rate of desorption:

$$Rate_{des} = \frac{-d\theta}{dt} \tag{2.18}$$

where t is time and θ is surface coverage. The rate of desorption can be thought of as a first order rate equation with respect to the surface coverage thus:

$$Rate_{des} = k_{des} \times \theta \tag{2.19}$$

Though the rate constant will depend on both the number of vibrations of chemisorbed species and also the energy required to break the interaction, using the Arrhenius equation it can be expressed as:

$$Rate_{des} = \nu \times \exp\left(\frac{-\Delta E_{des}}{RT}\right) \times \theta \tag{2.20}$$

where v is the frequency of the vibrations, ΔE_{des} is the activation energy required to desorb a molecule, R is the perfect gas constant and T is the temperature. Combining these equations provides a first-order differential, which can be solved to find a value for ΔE_{des}:

$$\frac{-d\theta}{dt} = \nu \times \exp\left(\frac{-\Delta E_{des}}{RT}\right) \times \theta \tag{2.21}$$

Experimental techniques

The temperature of the system is usually increased linearly with time. Therefore the two are linked thus:

$$T = T_0 + (A \times t) \quad (2.22)$$

where T is the temperature at a specific time, T_0 is the initial temperature, A is the heating rate and t is the time. From this it can be derived that:

$$\frac{dT}{dt} = A \quad (2.23)$$

Substituting this into the previous equation eliminates time, and instead uses temperature:

$$\frac{d\theta}{dt} = \frac{d\theta}{dT} \times \frac{dT}{dt} \quad (2.24)$$

Given the linear relationship between time and temperature this becomes:

$$\frac{d\theta}{dt} = \frac{d\theta}{dT} \times A \quad (2.25)$$

Substituting this becomes:

$$-\frac{d\theta}{dT} = \left(\frac{\upsilon}{A}\right) \times \exp\left(\frac{-\Delta E_{des}}{RT}\right) \times \theta \quad (2.26)$$

The peak maximum (the point of interest) is a turning point, and therefore the differential = 0. Thus:

$$\frac{d^2\theta}{dT^2} = 0 \quad (2.27)$$

This becomes:

$$-\frac{d^2\theta}{dT^2} = \left[\left(\frac{\upsilon}{A}\right) \times \exp\left(\frac{-\Delta E_{des}}{RT}\right) \times \left(\frac{d\theta}{dT}\right)\right] +$$

$$\left[\left(\frac{\upsilon}{A}\right) \times \left(\frac{\Delta E_{des}}{RT^2}\right) \exp\left(\frac{-\Delta E_{des}}{RT}\right) \times \theta\right] = 0 \quad (2.28)$$

Substituting in the previous value for -dΘ/dT gives the following equation:

$$\Delta E_{des} = RT \times Ln\left[\frac{RT^2\upsilon}{A \times \Delta E_{des}}\right] \quad (2.29)$$

which can be solved iteratively and will converge to the true E_{des}.

Experimentally the system is initially saturated with ammonia over an extended period, and then the system is heated, while simultaneously monitoring the

ammonia concentration. This will produce a graph of ammonia concentration versus temperature, which will yield information on the total amount, the variation and the strength of the acid sites present. The number of peaks directly corresponds to the number of different acid sites. The peak position relates back to the strength of the acid site. The stronger acid sites will form stronger interactions with the basic probe molecule. This will therefore require a greater amount of energy (higher temperature) to initiate the desorption process. Different acid sites will have different strength interactions with the ammonia probe molecule and will require different amounts of energy to overcome this interaction. Finally the area under the graph can be integrated to give the total number of acid sites. Thus:

$$-\int \frac{d\theta}{dT}.dT = \theta \qquad (2.30)$$

2.6 Solid-state magic angle spinning nuclear magnetic resonance (MAS NMR)

NMR techniques are used throughout nanoporous catalysis to determine the environment of specific nuclei within a framework, yielding significant information on the exact nature of an active species. While the basic theory is the same as solution-phase NMR there are a range of added complexities in the solid-phase as the nuclei are not free to orientate themselves as easily. Given that all nuclei are charged and have a spin they also have a magnetic moment:

$$\mu = I \times \gamma \qquad (2.31)$$

where μ is the magnetic moment, I is the magnetic spin and γ is the gyromagnetic ratio (an intrinsic property of the nucleus). If there is no magnetic field then freely mobile nuclei will be randomly distributed, all directions will be energetically equivalent, and as such there will be no net magnetization at all. When an external magnetic field is applied the directions are no longer-energetically equivalent as this introduces a preferred orientation. For a spin-I nuclei (with 2I +1 states), the energy differences between two adjacent states will become:

$$\Delta E = \frac{\gamma h B_0}{2\pi} \qquad (2.32)$$

where ΔE is the difference in energy, h is Plancks constant and B_0 is the strength of the applied field. Thus the stronger the magnetic field applied, the greater the difference in energy between the states. This split in energy levels is known as Zeeman splitting. There are a range of other magnetic interactions that can be analysed using NMR, however the ones which are particularly significant in solid samples are dipolar coupling and quadrupolar interactions.

Dipolar coupling occurs between the magnetic moments of two neighbouring nuclei and is heavily distance dependent. Dipolar coupling is particularly sensitive to the orientation of the nuclei, in an isotropic solution where the nuclei are free to move, this averages to 0. However in a solid-state system the nuclei cannot move as rapidly and significant line-broadening is witnessed.

Significant line-broadening can also be seen in quadrupolar nuclei (I ≥ 1) for solid state samples. Quadrupolar interactions are significant in liquid-phase samples as the system cannot easily align itself with the external magnetic field thus:

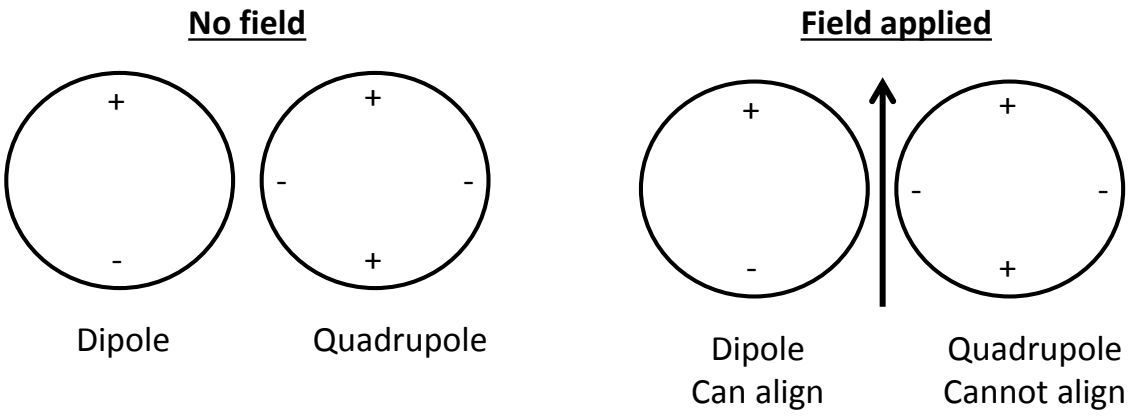

Figure 2.11: Schematic explaining quadrupolar relaxation

Therefore the quadrupole will rotate rapidly in an attempt to orientate itself with the field and lose energy,[5] this can generate a greater energy difference than the Zeeman splitting. This mechanism is important in solid state systems, where the line broadening is related to the spin (I) and quadrupolar moment (Q) thus:

$$Line\ Broadening = \frac{(2I+3)\times Q^2}{I^2\times(2I-1)} \qquad (2.33)$$

While dipolar coupling and quadrupolar interactions do significantly increase the breadth of a signal their effects can be expressed as:

$$Line\ Broadening\ \alpha\ (3Cos^2\theta) - 1 \qquad (2.34)$$

where θ is the angle of the sample relative to the external magnetic field; B_0. Therefore by making the right-hand-side of this equation equal to zero, it becomes possible to cancel out a significant number of interactions, thus when θ = 54.74°, the magic angle.[6] By orientating the sample at this angle, relative to the external magnetic field it then becomes possible to obtain much clearer spectra.

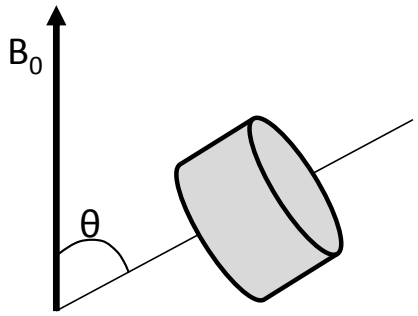

Figure 2.12: Image describing the magic angle for MAS NMR.

2.7 Fourier-transform Infra-red Spectroscopy (FT-IR)

Infra-red radiation is classified as radiation with a wavelength of 1 – 1000 μm. This coincides with the energy range required to perform transitions between rotational and vibrational energy states. For a vibrational mode to be observable using FT-IR, a change in dipole moment must occur. Where the dipole moment is expressed as:

$$\mu = \delta \times d \qquad (2.35)$$

where μ is the dipole moment, δ is the dipolar charge and d is the distance. A range of vibrations exist, including Symmetric, Asymmetric, Scissoring, Rocking, Wagging and Twisting, though not all of these are IR active for each molecule, as shown below with CO_2:

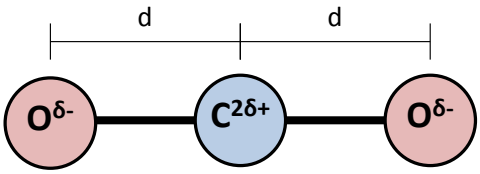

Total dipole moment:
$(2\delta+ \times 0) + (\delta- \times d) + (\delta \times d) = 0$

Symmetric stretch

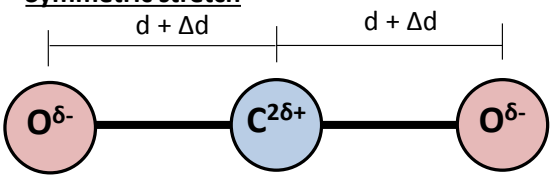

Total dipole moment:
$(2\delta+ \times 0) + (\delta- \times (d + \Delta d)) + (\delta \times (d + \Delta d)) = 0$

No change in dipole moment – IR Inactive

Asymmetric stretch

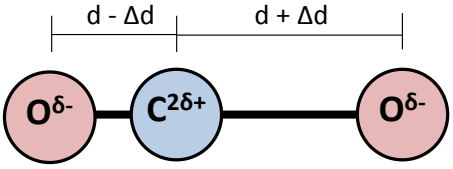

Total dipole moment:
$(2\delta+ \times 0) + (\delta- \times (d - \Delta d)) + (\delta \times (d + \Delta d)) = 2\delta\Delta d$

Change in dipole moment – IR Active

Figure 2.13: Describing the FT-IR selection rules.

The position at which a vibrational transition occurs is characteristic of the strength of the bond and the atoms involved thus:

$$\upsilon = \left(\frac{1}{2\pi}\right)\sqrt{\frac{k}{\mu}} \qquad (2.36)$$

where v is the position of the vibrational mode, k is the force constant of the bond and μ is the reduced mass. The force constant is directly related to the strength of the bond as is often expressed in terms of N/m. The reduced mass relates to the masses of the atoms involved in the bond thus:

$$\mu = \frac{M_a M_b}{M_a + M_b} \qquad (2.37)$$

where M_a and M_b are the masses of the two atoms involved in the bond. As such it is possible to attribute certain stretches and modes to specific functional groups, given the similarities in bond strength and the same atoms being present. FT-IR can also be used to analyse the interactions between catalytic samples and probe molecules.

One of the most widely-used probe molecules is carbon monoxide, CO, which is commonly used to analyse the strength and quantity of different acid sites.[7] Once adsorbed onto a system, the characteristic asymmetric vibrational modes of CO can often be seen around 2100 cm^{-1}. This signal can then be quantified to reveal the total number of acid sites present by using the correct extinction coefficient, in combination with the Beer-Lambert law. The exact position of this band also reveals the nature of the acid site. On adsorption physisorbed (liquid-like) CO is seen commonly at 2140 cm^{-1}, though CO bound to Brønsted acid sites appears at ~2170 cm^{-1}, whilst strong Lewis acid sites occur at 2230 cm^{-1}.[8] The difference in peak position is attributed to the strength of binding with the CO. The LUMO (Lowest Unoccupied Molecular Orbital) of CO is the π* orbital, thus donating any electrons to CO will invariably fill the π* orbital, weakening the C-O bond. However as acids are primarily electron deficient they will remove electrons from the π* orbital, thus strengthening the bond.

On adsorbing CO the OH stretches (commonly between 3700 – 3400 cm^{-1}) are titrated and shifted to the 3400 – 3100 cm^{-1} region. The shift in the peak position is a measure of the strength of the interaction between the acid site and the weakly basic CO molecule, thus the larger this shift, the stronger the acid site.[9]

Other probe molecules can also be used, commonly pyridine or its methylated derivatives such as 2,6-dimethyl pyridine (2,6-DMP, lutidine) are also used to complement the use of CO. Lutidine is known to possess a characteristic band, ν_{8a}(CC) which is highly sensitive to specific acidic interactions.[10]

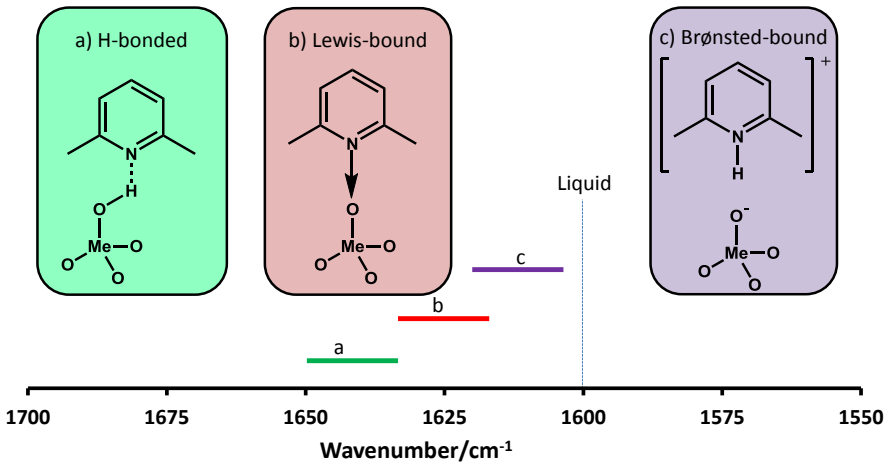

Figure 2.14: Schematic showing the variation of the ν_{8a}(CC) band of lutidine on interacting with different acid sites.

This probe is particularly useful in zeotype materials as it provides an excellent complement to CO in terms of determining accessible active sites. Larger reactants may not be able to access the acid sites which CO can access, thus by employing a bulkier probe molecule and contrasting the peak areas one can gain an insight into diffusion behaviour in porous catalysts.

2.8 Inductively Coupled Plasma (ICP)

In heterogeneous catalysis it is common practice to not only quote the activity as conversion and selectivity, but as turnover number or frequency. Turnover numbers have the advantage that they also give information on not just the overall activity of the catalyst, but also the efficiency of the active sites for ease in comparison between different active sites. In order to do this it is imperative that the amount of metal present in the catalyst is known; as such techniques such as ICP are vital in analysing the content of the bulk system. This information can be used in combination with EDS to compare the morphology of the surface with that of the bulk material.

Solid samples are first digested using a range of acids, commonly HCl, HNO_3 or HF to ensure all chemical bonds are fully broken down. This sample is then introduced into a nebuliser with a flow of argon gas. This allows the samples to form an aerosol with the argon, and is then transported to the plasma, which has been inductively coupled to produce a high energy field. This prompts the atoms to generate characteristic wavelengths of light which can then be related back to the original quantity of metals via the Beer-Lambert law. The method of detection used with ICP is commonly Atomic Emission Spectroscopy (AES). This has the advantage of being able to detect very low concentrations of atoms whilst being able to simultaneously detect a wide range of elements, given their unique emissions. Atom Absorption Spectroscopy (AAS) is another alternative method of detection, which employs powerful reducing and oxidising agents to ensure all the appropriate elements are in the same oxidation state. A light source is then used to excite the samples and detect characteristic transitions. However this can only detect one element at a time.

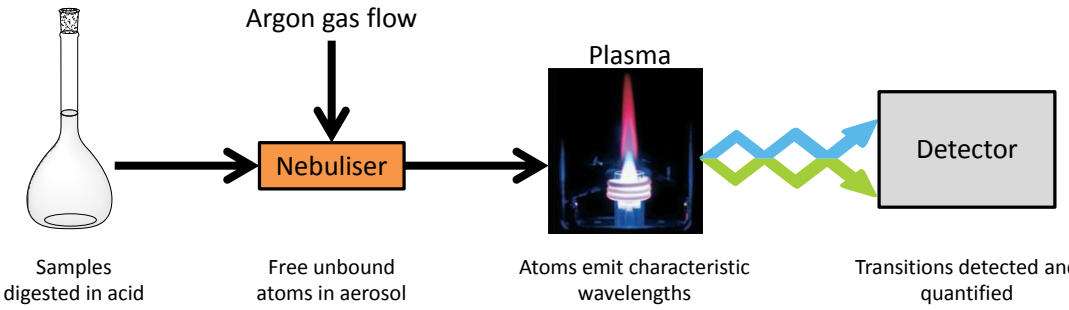

Figure 2.15: Pictorial representation of ICP.

2.9 Gas Chromatography (GC)

Gas chromatography is an analytical technique used to separate different chemical components based on particular properties, most commonly boiling point and polarity. This is primarily used to monitor the progress of organic reactants during catalytic reactions, whereby the components (reactant, solvent, standards and products) could be represented as separate peaks. The area of these peaks would then be quantified and related back to the molar concentrations present in the mixture via a series of calibrations.

The liquid (or gas) sample is injected into the heated injector port. The port is heated to such an extent that the compounds are vaporised. The compounds are then mixed with the mobile phase (Helium carrier gas) and carried through a heated GC column (the stationary phase). The mobile phase also serves the dual purpose of diluting the sample so the system is not saturated. To aid with this the injector port also has a split valve. This allows some of the helium/compounds stream to be ejected from the port before it reaches the GC column, thus lowering the quantity of the compounds that are to be analysed and avoiding saturation.

The different compounds will interact with the stationary phase to different extents, and therefore will become separated. The heating regime and the column will be specifically chosen to separate the intended compounds thus allowing for accurate quantification of peak areas.

Once the samples have travelled through the column they reach the Flame-Ionized-Detector (FID). In the FID the output from the GC column is passed

through a flame which is burnt with a mixture of hydrogen and air to create ions. These ions are then detected by a potential difference across the FID, converted to an analogue signal and recorded as peaks on a computer display unit.

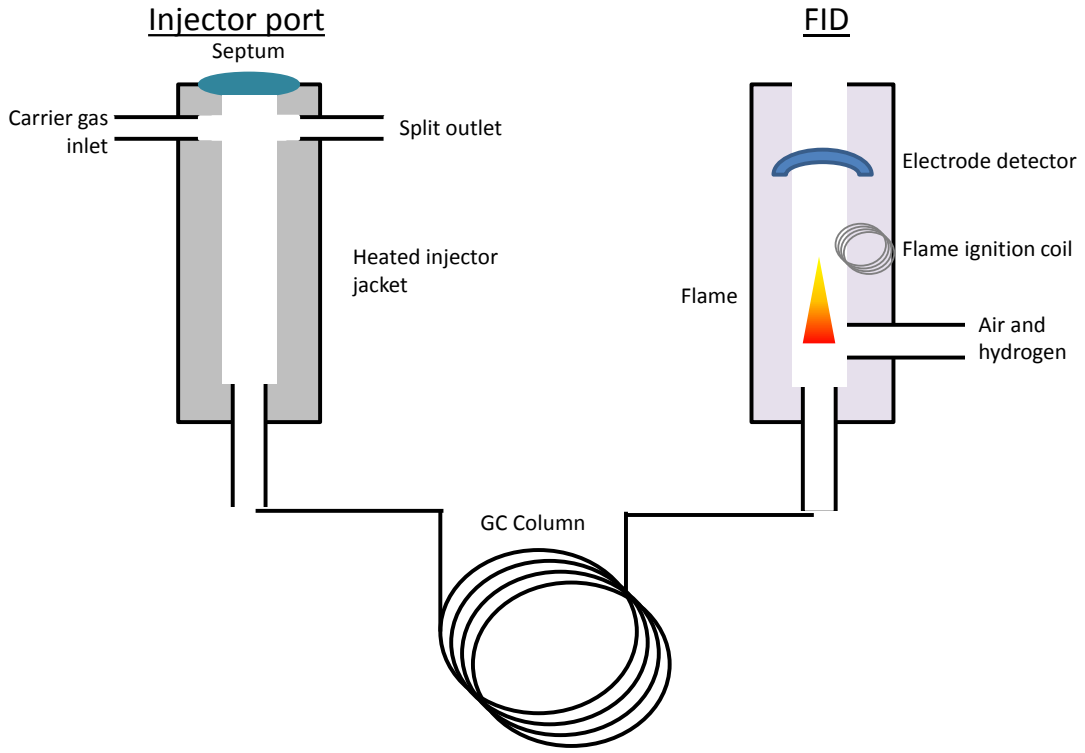

Figure 2.16: Description of the mechanism of a GC.

2.10 Gas Chromatography Calibrations

The area of a GC peak is inherently linked to the moles of the compound that were injected. This relationship however is subtly unique for each compound, as equivalent molar amounts of different compounds rarely result in identical peak areas. Thus the peak area is scaled by the complete response factor (β), which varies for each compound:

$$Moles(X) = \beta_X \times Area(X) \qquad (2.38)$$

where Moles(X) is the number of moles of compound X injected, β_x is the complete response factor for compound X and Area(X) is the area of the GC peak attributed to compound X.

Directly determining the precise response factor of a single compound is highly complex, as day-to-day variations and even slight parameter changes

can influence the area of a peak, therefore interfering with the complete response factor. In light of this it is common practice to measure the response factors of different compounds relative to a known molar quantity of single reference compound (or standard), instead gaining a relative response factor. As any systematic variations in the GC will affect the response factor of these peaks in a similar way, then the relative response factor will be constant. Thus we generate the similar equation for the standard:

$$Moles(Std) = \beta_{Std} \times Area(Std) \tag{2.39}$$

where Moles(Std) is the moles of the standard injected, β_{std} is the complete response factor for the standard and Area(Std) is the area of the GC peak attributed to the standard. By dividing these two equations yields the relationship that:

$$\frac{Moles(X)}{Moles(Std)} = \frac{\beta_X}{\beta_{Std}} \times \frac{Area(X)}{Area(Std)} = \gamma_{\frac{X}{Std}} \times \frac{Area(X)}{Area(Std)} \tag{2.40}$$

where $\gamma_{X/Std}$ is the relative response factor of compound X, relative to the standard.

To obtain the relative response factor a set of calibration solutions (usually 6 or more) are made. Care should be taken such that the solutions are diluted in the same intended solvent for the reaction, and that the calibrations are made such that the concentrations are evenly spread over the range intended to be used for the reaction samples. The closer the composition of the calibration samples to the intended reaction, the more relevant and accurate the calibration will be. Once made, the calibration samples are each injected into the GC three times in a random order (to avoid sample contamination or bias). The data is then plotted as the molar ratio (Moles(X)/Moles(Std)) on the y axis with the area ratio (Area(X)/Area(Std)) on the x axis. This data should yield a straight line, with an intercept of 0. The gradient of this line is the relative response factor, $\gamma_{X/Std}$:

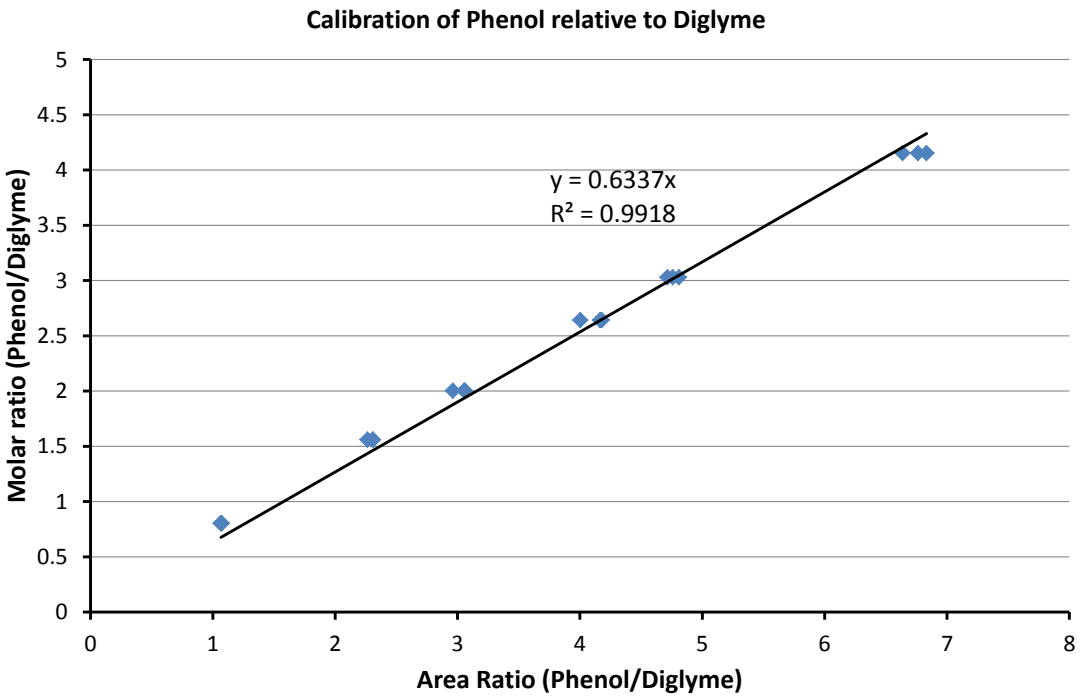

Figure 2.17: GC calibration of phenol relative to a diglyme standard.

To accurately analyse a reaction, a mass balance should be obtained for all reactions. The moles of all significant observable peaks should be summed and compared with the original quantity to quantify the amount of the original reactant that has been 'lost'. In order to do this a standard must be used at some point in the catalytic reaction. This can either be done using an internal or external standard. Internal standards are added to the reaction mixture at the beginning of the experiment and are therefore present throughout the reaction, and the amount will remain constant. In contrast an external standard is added to reaction samples once they have been separated from the reaction mixture but before GC analysis. Both methods have their advantages and disadvantages. The process of using an internal standard is simpler, as it is simply accurately included in the initial reaction mixture. However, choice of internal standard is often challenging as the compound must be completely inert under reaction conditions, and must not modify the reaction in any way, it must act as a spectator only. In contrast the choice of external standard is less difficult as it does not experience reaction conditions; however its use often involves an intricate set of dilutions and sample masses in order to accurately analyse it.

By using a known amount of standard, one can then obtain GC areas for both the standard and a compound to obtain the number of moles once a relative response factor has been obtained thus:

$$Moles(X) = \gamma_{\frac{X}{Std}} \times Moles(Std) \times \frac{Area(X)}{Area(Std)} \quad (2.41)$$

Using this equation the moles of X can then be quantified and used to calculate conversion and selectivity.

2.11 X-ray Adsorption spectroscopy (XAS)

XAS spectroscopy is a divisive tool in exploring the local environment and structure of specific elements within a sample. In light of this it is a powerful technique for probing active sites in heterogeneous catalysts, where the active site will only make up a small proportion of the whole sample.

The technique uses electromagnetic radiation to excite core electrons. The energy required to do this is specific and characteristic to individual elements, as such it is possible to selectively probe a particular element. Further, as the energy levels of core electrons are deeply buried close to the nucleus they are only subtly modified by coordination geometry, neighbouring atoms and oxidation state, as such the energy required to promote the core electron (E_0) shows only slight variations based on the above factors.

Once released, the photoelectron will interact with neighbouring atoms, constructively or destructively, eventually resulting in an oscillating signal. The adsorption of X-rays is measured by comparing the intensities of the X-rays before the sample (incident X-rays) with those after the sample (transmitted X-rays) using the following equation[11]:

$$Ln\left(\frac{I_0}{I}\right) = \mu x \quad (2.42)$$

where I_0 is the intensity of the incident X-rays, I is the intensity of the transmitted X-rays, μ is the adsorption coefficient and x is the width of the sample.

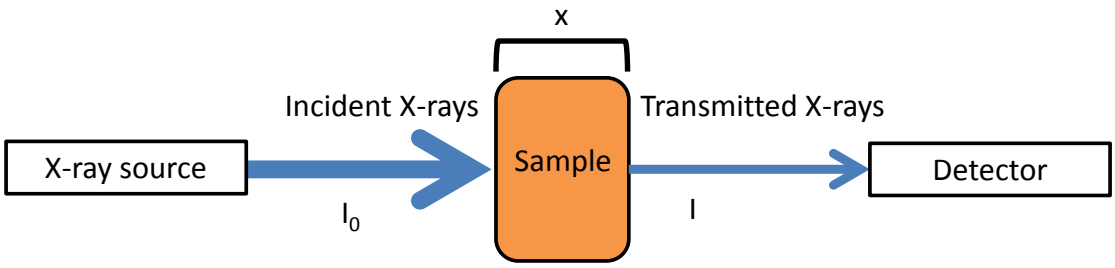

Figure 2.18: Schematic of a XAS experiment in transmission mode.

The spectrum acquired from an XAS spectrum is commonly broken down into two regions, the XANES (X-ray Adsorption Near Edge Spectroscopy) and the EXAFS (Extended X-rays Adsorption Fine Structure) regions. These are defined relative to the E_0 value with XANES occurring for $E \leq E_0 + 50$ eV, whereas the EXAFS region extends much further to $E > E_0 + 50$ eV. The XANES region is known for yielding electronic information, such as oxidation state and geometry. In contrast, the EXAFS region yields bond lengths and information on neighbouring atoms. The XANES region consists of the 'Edge' and 'Pre-edge' features. These are a result of core electrons being promoted into available higher energy orbitals, instead of being fully ionised. The sharp rise to the edge is attributed to the larger number of available high energy orbitals below the continuum of ionisation.

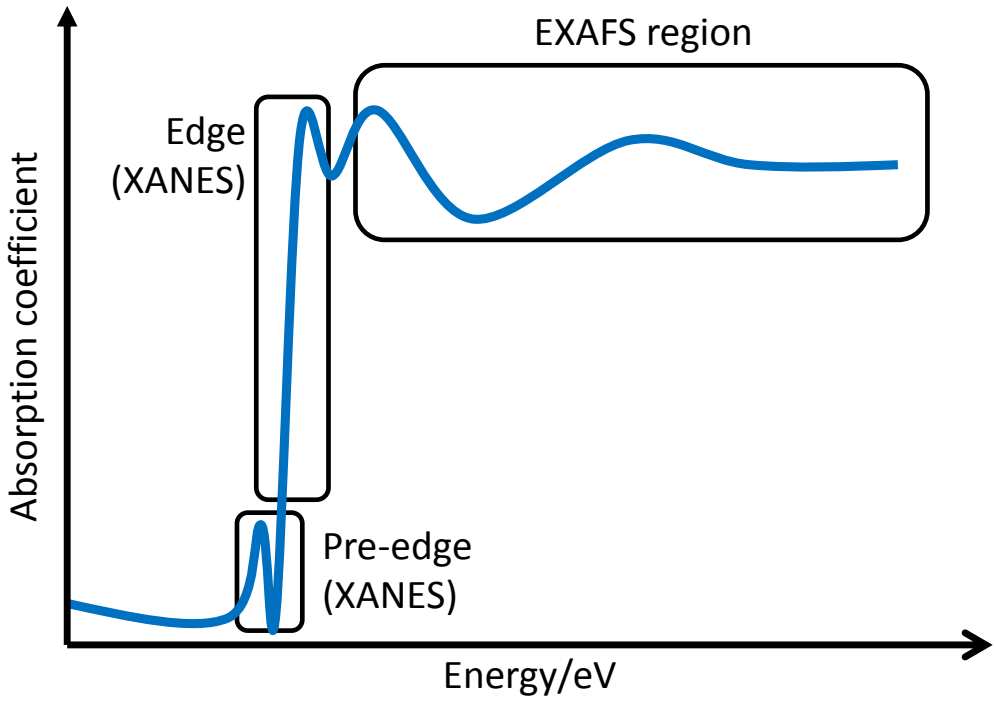

Figure 2.19: Description of different regions of an XAS spectrum.

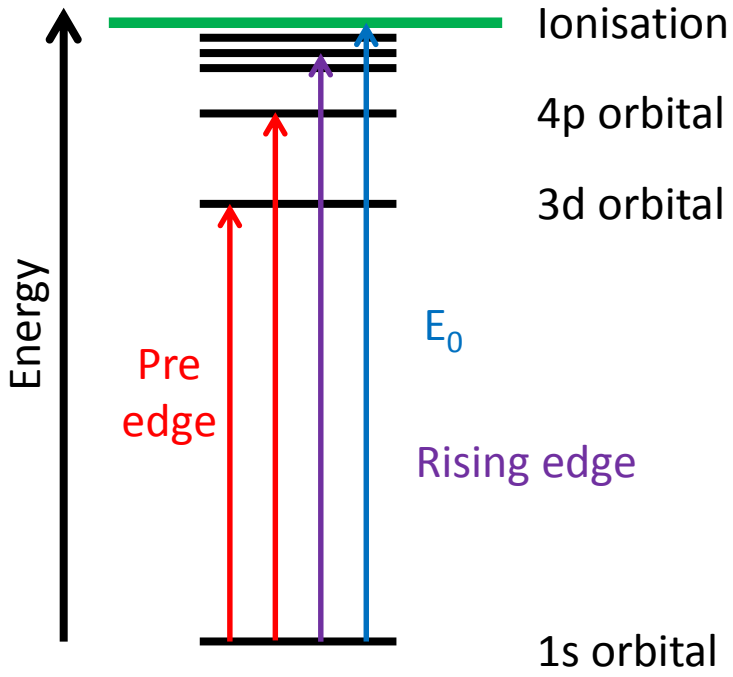

Figure 2.20: Schematic explaining the various transitions that make up the XAS spectra.

Once obtained the experimental EXAFS and XANES data is then fitted to a theoretical model. A range of parameters are then used to find a model that best fits the data, whilst still being chemically feasible. The quality of the data, depends on how much information can be obtained, though commonly the first coordination sphere can be satisfactorily modelled.

2.12 Background of Molecular Orbital (MO) theory

The ability to predict physical and electronic properties of a molecule or system purely from a set of atomic coordinates and a description of those atoms has been the driving force behind the development of computational chemistry techniques. Such methods have been used to great effect in the fields of materials chemistry, bio-chemistry and quantum mechanical calculations. Commonly the scale of the problem will dictate the type of computational tools required. For example diffusion through a lipid bi-layer is a large-scale problem, therefore atoms and even molecules, are grouped together as single entities and defined by a set of parameters. This is

commonplace in a range of molecular mechanics simualtions. In contrast a system of less than 100 atoms can be modelled more accurately, to the point where individual electrons are considered, as in quantum mechanical calculations. To gain an in-depth knowledge of reaction mechanisms or electronic behaviour one must apply quantum mechanical methods to the problem, as only when electrons are considered can quantitative information on bond-breaking, bond-forming and transition states be obtained. In order to do this one must calculate the energy of a system. This must be done by applying an operator to a set of coordinates, the most famous example of this is the Schrodinger equation.[12]

$$H\psi = E\psi \qquad (2.43)$$

This equation has three clear components. The Hamiltonian operator (H), an operator which will allow the calculation of the energy (E) of a system. The Hamiltonian acts upon the wavefunction, Ψ, mathematically this is an eigenfunction, however in molecular orbital theory the wavefunction contains information on all physical, chemical and quantum mechanical properties of a system. The Hamiltonian must incorporate all the interactions of a system. This includes the kinetic energy of the particles and the various interactions. Thus the Hamiltonian can be expressed as:

$$H = -\sum_i \frac{\hbar^2}{2m_e}\nabla_i^2 - \sum_k \frac{\hbar^2}{2m_n}\nabla_k^2 - \sum_i \sum_k \frac{e^2 Z_k}{r_{ik}} + \sum_{i<j} \frac{e^2}{r_{ij}} + \sum_{k<l} \frac{e^2 Z_k Z_l}{r_{kl}} \qquad (2.44)$$

where the first two terms represent the kinetic energy of the electrons and nuclei respectively and the three latter terms represent the electron-nuclear interaction, the electron-electron repulsions and the nuclear-nuclear repulsions respectively. In this form, the equation is dependent upon the positions of the nuclei and the electrons, therefore the wavefunction (Ψ) must be a function of both the nuclear and electronic coordinates. This then makes the problem inherently complex, however it is possible to simplify it via the Born-Oppenhemier approximation.

The Born-Oppenheimer approximation is able to simplify the calculation process by separating the nuclear and electronic interactions.[13] As nuclei move considerably slower than electrons, the contribution of nuclear kinetic energy is minimal, and can therefore be thought of as independent from the electronic motion. It is then convenient to assume that the nuclei are fixed relative to the

electrons, thus the nuclear-nuclear repulsion term is merely a constant, and will not affect the calculation of the electronic wavefunction. This then allows us to solve the 'electronic wavefunction' as a function of electron kinetic motion, electron-electron interactions and electron-nuclear interactions. From here on, it is more convenient to refer to the electronic wavefunction as the wavefunction. The wavefunctions themselves are orthonormal, thus it can be written that:

$$\int \psi_i \psi_j . dr = \delta_{ij} \tag{2.45}$$

where δ_{ij} is the Kronecker delta function, thus $\delta_{ij} = 1$ when $i = j$, if $i \neq j$, $\delta_{ij} = 0$. Using this information the energy of a system can be derived by manipulating the Schrodinger equation thus:

$$\int \psi_i H \psi_j . dr = E\delta_{ij} \tag{2.46}$$

which simplifies to:

$$\int \psi_i H \psi_i . dr = E \tag{2.47}$$

Thus allowing the calculation of the energy from the wavefunctions. Until this point the 'wavefunction' has been discussed but no actual meaning has been attached to it or its form. Commonly the wavefunction is constructed from a linear combination of basis functions that commonly mimic the shapes of atomic orbitals, called a Basis Set. Thus, the use of a basis set allows us to use a molecular wavefunction:

$$\Phi = \sum_i c_i \psi_i \tag{2.48}$$

where c_i represents the set of coefficients for the individual wavefunctions, and Φ is the molecular wavefunction. In light of this, there is now a set of equations to represent Ψ_i, to solve for the molecular wavefunction it becomes necessary to optimise the coefficients, c_i instead. Due to the orthonormal nature of the individual wavefunctions, and the molecular wavefunction it can be shown that:

$$\int \Phi^2 . dr = \sum_i c_i^2 = 1 \tag{2.49}$$

Similarly it can also be shown that:

$$\int \Phi H \Phi . dr = \sum_i c_i^2 E_i \tag{2.50}$$

Combining these two equations it follows that:

$$\frac{\int \Phi H \Phi . dr}{\int \Phi^2 . dr} \geq E_0 \qquad (2.51)$$

This is the Variational Principle in its basic mathematical form,[14] and shows us that the 'True energy' of the system is also the lowest energy of the system. This then allows us to vary the coefficients (c_i) in such a way that we can test whether the system has been improved, and thus solve for the coefficients using an iterative solution.

The basis sets themselves can be expressed in a number of ways. Often these involve an exponential component, representing the decay of electron density away from the nucleus, and an angular component to represent the orbitals shape, thus differentiating between different orbital types. Commonly these are parameterised by α, i, j and k. The former represents the decay of the function, and i, j and k are the directional components. A great deal of work has been performed on optimising best basis sets, however in general a good basis set should be able to accurately describe the behaviour of an atom, whilst using as few equations as possible to speed up the calculation. It is possible to use a variety of different mathematical forms to model these orbitals, though commonly a Slater or Gaussian type orbital is used which have subtly different forms. Both functions have an exponential component to account for the decay of electron density away from the orbital, but the Slater type decays as per e^{-r}, whereas the Gaussian decays as $e^{-r\wedge 2}$. The Slater type orbital provides a better approximation for electron behaviour, though the nature of the exponential means that the calculation time is increased. In contrast the Gaussian type orbitals allow for faster, though less accurate calculations. In light of this 'contracted' basis sets are commonly used which employ a linear combination of Gaussian type-orbitals to mimic a Slater-type orbital, thus:

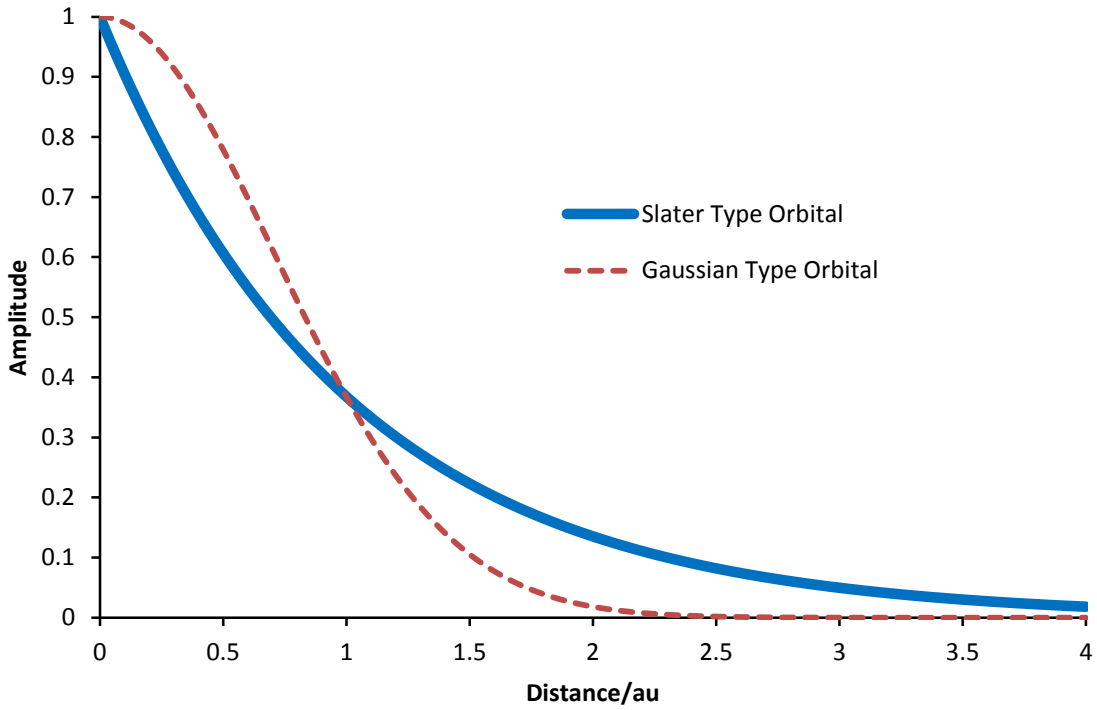

Figure 2.21: Graphical analysis contrasting the effects of Slater and Gaussian Type Oribtals.

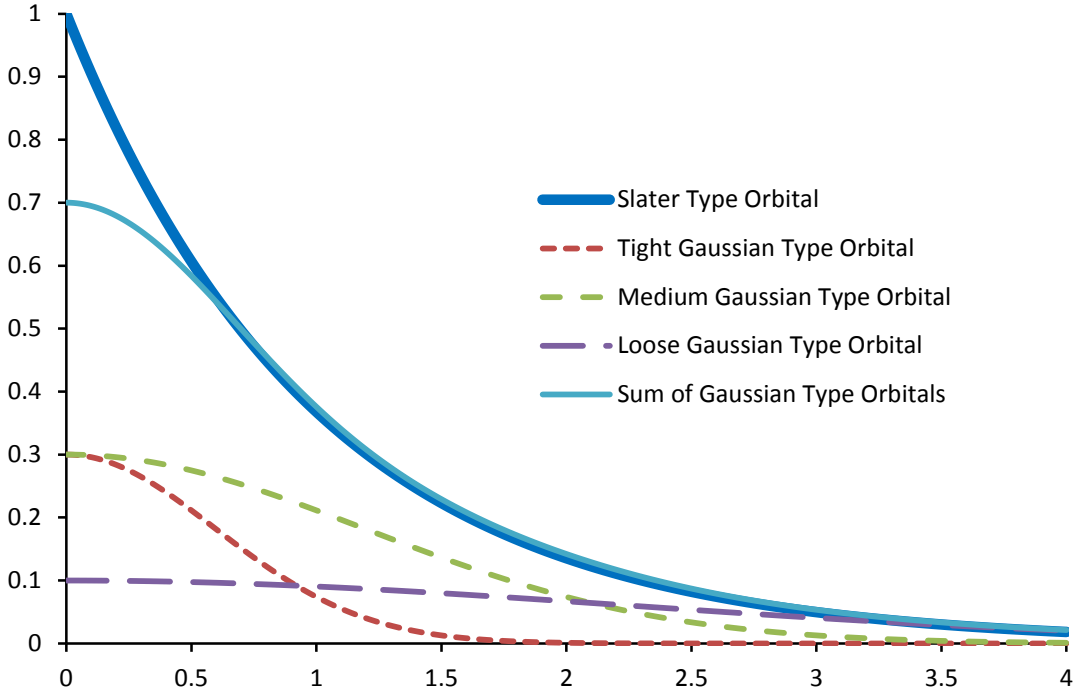

Figure 2.22: Diagram showing how Gaussian Type Orbitals can be summed to mimic Slater Type Orbital behaviour.

It is, of course, possible to obtain a better match by employing a larger number of Gaussian type orbitals to mimic the Slater-type orbital. However this increases the computational time required per calculation, thus a balance must be struck between accuracy and efficiency.

Despite this improved efficiency offered by Gaussian type orbitals the most challenging component of this whole calculation is still the calculation of electron-electron interactions. In the Hamiltonian expressed above (equation 2.43) only classical mechanical electron-electron interactions are considered, the interaction between two charged particles. However, given the nature of the particles there are other interactions to consider, such as the exchange and correlation interactions. The exchange interaction occurs between two electrons of the same spin. The Pauli principle states that two identical particles with half integer spin (electrons in this case) cannot occupy the same quantum state. Thus if two electrons occupy the same molecular or atomic orbital, they cannot also have the same spin. The exchange interaction effectively gives rise to a repulsion between two electrons of the same spin. The calculation of this using molecular orbital theory systems is very time consuming, and requires the use of integrals involving 'four index integrals'. Such integrals are extremely computationally demanding, and mean that the computational time of any calculation is scaled as per N^4, where N is the number of electrons in the system.

The other type of interaction, correlation, refers to the way electrons move relative to one another. In a multi-electron system each electron will interact with each other electron, however molecular orbital approaches (such as Hartree-Fock theory), chose to instead calculate the interaction between an electron and an average field, generated by the other electrons. Thus Hartree-Fock theory (HF) negates the energy from correlation interactions, to the point that the energy of correlation is often defined as:

$$E_{Corr} = E_{True} - E_{HF} \qquad (2.52)$$

where E_{Corr} is the correlation energy, E_{True} is the true energy of the system and E_{HF} is the lowest possible energy achieved using HF methods (known as the Hartree-Fock limit). It should be noted that modifications to the HF theory can be made to include correlation effects, however they do so at great

computational cost, even basic improvements such as those used in the MP2 method[15] will increase the computational time from N^4 to N^5.

In light of the way that exchange and correlation interactions are dealt with (in one case highly time consuming to calculate, in the other neglected) alternative methodologies were investigated to solve the same problems in a different fashion.

2.13 Introduction to Density Functional Theory (DFT)

While MO theory can solve many problems it is often felt that the notion of solving a wavefunction, which requires significant calculation to obtain, is highly counter intuative, given that it, itself, is not readily interpretable. Instead using a physical property such as electron density makes far more sense. While this may seem quite simplistic it can be shown that similar to MO theory, the variational theory still applies. Further if one assumes that the electrons interact with both each other and an external field (generated by the positions of the nuclei), then it can also be shown that the electron density of the ground state also determines the external potential. Thus the electron density is a suitable property to replace the wavefunction. In light of this the energy functional can be expressed as:

$$E[\rho(r)] = T_{ni}[\rho(r)] + V_{ne}[\rho(r)] + V_{ee}[\rho(r)] + \Delta T[\rho(r)] + \Delta V_{ee}[\rho(r)] \qquad (2.53)$$

where T_{ni} is the kinetic energy of a non-interacting electron, V_{ne} is the electron-nuclear interaction, V_{ee} is the classic electron-electron interaction, ΔT is the correction to the kinetic energy based on quantum mechanical interactions (the correlation energy) and ΔV_{ee} represents the correction to all non-classical electron-electron interactions (the exchange energy). Unlike MO theory methods DFT does not try to exactly calculate the exchange (or in some cases correlation) energy of the system, instead it employs different functionals to mimic these interactions as closely as possible. A range of functionals have been used to determine the exchange-correlation interactions.

One such system is called the Local Spin Density Approximation (LSDA) which assumes that the exchange and correlation energy for any point can be

calculated exclusively from the value of the electron density at that point.[16] This is calculated in such a way that four-index integrals are not required, instead the bottleneck at this point is a matrix diagonalisation, which scales as N^3, not N^4 as per MO theory. In light of this the application of DFT is already apparent. Despite this seemingly simple method, difficulties were found as the LSDA approach is rarely spatially uniform, and as such has its limitations. Therefore to improve this a further level of complexity was used which took into account not just the density at each individual point, but also the gradient of the density at that point, thus these methods were known as Generalized-Gradient approximation (GGA) methods.[17]

While such functionals greatly improved calculation speed and accuracy, both DFT and MO theories have their advantages and disadvantages, as such Adibatic (or 'Hybrid') functionals were adopted, whereby different exchange and correlation energies were calculated using different methods. One of the most commonly used functionals, B3LYP, is an example of this.[18] For this the exchange-correlation energy is calculated thus:

$$E_{xc}^{B3LYP} = (1-a)E_x^{LSDA} + aE_x^{HF} + b\Delta E_x^{B} + (1-c)E_c^{LSDA} + cE_c^{LYP} \qquad (2.54)$$

where E_{xc}^{B3LYP} is the exchange-correlation energy for the B3LYP functional, E_x^{LSDA} is the exchange energy as calculated by the LSDA method, E_x^{HF} is the exchange energy as calculated exactly by the Hartree Fock method, ΔE_x^{B} is the correction to the exchange energy, based on Becke's 1988 exchange functional (a generalized-gradient approximation), E_c^{LSDA} is the correlation energy based on the LSDA method, E_c^{LYP} is the correlation energy as calculated by the LYP functional (a different GGA correlation functional). In this equation a, b and c are parameters where a = 0.20, b = 0.72 and c = 0.81. This functional has proven increasingly popular in computational chemistry and as such its use is very widespread in a range of computational studies.

2.14 References

1. G. E. M. Jauncey, *Proc. Natl. Acad. Sci.*, **1924**, *10*, 57-60.
2. P. Scherrer, *Gottinger Nachrichten Math. Phys.*, **1918**, *2*, 98-100.
3. I. Langmuir, *J. Am. Chem. Soc.*, **1916**, *38*, 2221-2295.
4. S. Brunauer, P. H. Emmett and E. Teller, *J. Am. Chem. Soc.*, **1938**, *60*, 309-319.
5. J. A. Pople, *Mol. Phys.*, **1958**, *1*, 168-174.
6. E. R. Andrew, A. Bradbury and R. G. Eades, *Nature*, **1958**, *182*, 1659.
7. G. Ewing, *J. Chem. Phys.*, **1962**, *37*, 2250-2256.
8. E. Gianotti, V. Dellarocca, E. C. Oliveria, S. Coluccia, H. O. Pastore and L. Marchese, *Stud. Surf. Sci. Catal.*, **2001**, *142*, 1419-1426.
9. E. Gianotti, C. Bisio, L. Marchese, M. Guidotti, N. Ravasio, R. Psaro and S. Coluccia, *J. Phys. Chem. C*, **2007**, *111*, 5083-5089.
10. C. Lahousse, A. Aboulayt, F. Mauge', J. Bachelier and J. C. Lavalley, *J. Mol. Catal.*, **1993**, *84*, 283-297.
11. D. E. Sayers, E. A. Stern and F. W. Lytle, *Phys. Rev. Lett.*, **1971**, *27*, 1204-1207.
12. E. Schrödinger, *Phys. Rev.,* **1926**, *28*, 1049-1070.
13. M. Born and R. Oppenheimer, *Annal. Der Phy.*, **1927**, *389*, 457-484.
14. J. Lennard-Jones, *Proc. Roy. Soc. A*, **1949**, *198*, 14-26.
15. M. Head-Gordon, J. A. Pople and M. J. Frisch, *Chem. Phys. Lett.*, **1988**, *6*, 503-506.
16. U. von Barth and L. Hedin, *J. Phys. C: Solid State Phys.*, **1972**, *5*, 1629-1642.
17. A. D. Becke, *Phys. Rev.*, **1988**, *38*, 3098-3100.
18. P. J. Stephens, F. J. Devlin, C. F. Chabalowski and M. J. Frisch, *J. Phys. Chem.*, **1994**, *98*, 11623-11627.

Chapter 3: Exploring the role of framework topologies and the nature of the acid site in the formation of Nylon

The following people have contributed to the work in this chapter:

Tom Mezza of UOP obtained the NH_3-TPD and all the FT-IR data.

Marina Carravetta of the University of Southampton helped obtain the solid state 1D and 2D MAS NMR.

Julija Kezina of the University of Southampton helped in the synthesis of SAPO-41 and obtaining the subsequent liquid and vapour-phase Beckmann rearrangement catalytic data.

3.1 Background summary of Nylon production

Increasing global demands, deriving from expanding and developing populations, place further burdens on the production of ubiquitous materials such as polymers and plastics. These demands facilitate the need to design novel catalytic species, whilst simultaneously probing current catalytic species, with an aim to forming structure-property correlations. These correlations then prompt intelligent and rational design of future optimised catalytic systems.[1-4]

Among these areas that will be expected to burden extraneous demand is the Nylon industry. Currently 4 million tonnes of Nylon-6 is produced per year, which while already constituting a significant contribution to the textiles industry, is predicted to grow to 6.6 million tons by the year 2015.[5] As such the development of new technologies, to expedite the necessary growth in a sustainable manner, is of paramount importance. Presently the industrial method to produce the Nylon-6 precursor, ε-caprolactam, is performed in a non-catalytic fashion and utilisies a cyclohexanone feedstock via the modified Raschig process (Figure 3.1A).[6] However careful use of purposefully designed active sites can improve atom and energy efficiency, potentially offering both environmental and financial benefits. This therefore presents ample opportunities for emerging alternative technologies.

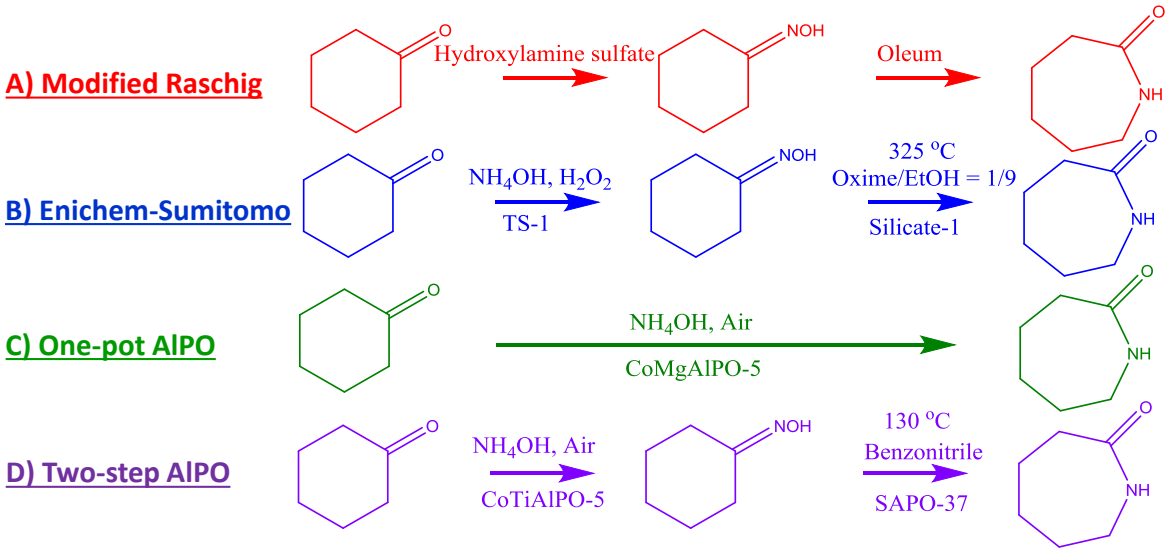

Figure 3.1: Current technologies to synthesise ε-Caprolactam from cyclohexanone. 3.1A is the current industrial process, the modified Raschig process. 3.1B is a newer commercialized technology by the Enichem-Sumitomo venture that utilizes solid catalysts. 3.1C represents a one-pot method which utilizes a bifunctional catalyst. 3.1D is an alternative AlPO –based process which uses sustainable technologies to optimize both steps under low-energy conditions.

One such innovation was jointly developed by Sumitomo and Enichem,[7-9] which employed a two-step process to transform cyclohexanone to ε-caprolactam, achieving compelling yields (> 90 %, Figure 3.1B). The first step utilised the tetrahedrally coordinated titanium sites present in TS-1, capable of activating hydrogen peroxide and an ammonia source, to perform the initial ammoximation step, in favour of hydroxylamine sulphate.[7,8] The subsequent Beckmann rearrangement of cyclohexanone oxime followed, utilising a vapour phase reaction (> 300 °C) with a high-silica ZSM-5 material, circumventing the need for oleum.[7,9] This more sustainable alternative prompted a significant body of research into the two individual reaction steps. As a consequence, the use of HZSM-5 in the vapour-phase Beckmann rearrangement is prodigious in both the academic and patent literature.[9-13] Many of these works aim to uncover the exact nature of active acid species in the ubiquitous HZSM-5 silicate framework, such that synthetic protocols can be modified to enhance the formation of such species.[10-13] A significant body of work has been dedicated to optimising the reaction conditions, procedures and precise morphology of the ZSM-5 (aka MFI or Silicate-1) catalyst, whilst contrasting its

behaviour to other silicate containing zeolite species (Table 3.1). As such studies have been dedicated to the exact nature of the oxime feedstock[14], the deactivation pathways[15] and the nature of the active site.[11]

Table 3.1: Summary of the use of aluminosilicates in the vapour-phase Beckmann rearrangement.

Sample	Cyclohexanone oxime conversion/mol%	ε-Caprolactam Selectivity/mol %	Notes	Ref
Silicate-1 (0.5 μm)	74	N/A	275°C, CO_2 carrier gas, 480 mins on stream	13
Silicate-1 (50 μm)	37	N/A		13
H-USY (Si/Al = 390)	12.8	39.6	350 °C, 10wt% oxime in methanol, N_2 carrier gas, 6 hours on stream	16
H-USY (Si/Al = 6.3)	78.5	80.1		16
H-USY (Si/Al = 390)	17.6	80.3	350 °C, 10wt% oxime in 1-hexanol, N_2 carrier gas, 6 hours on stream	16
H-USY (Si/Al = 6.3)	99.8	86.0		16
Na-FER (Si/Al = 34)	92.9	41.2	400 °C, Nitrogen carrier gas, 10wt% oxime in acetonitrile, 3 hours on stream	17
H-FER (Si/Al = 34)	99.3	74.8		17
H-FER (Si/Al = 73)	84.2	85.3		17
Al-MCM-41 (Si/Al = 18)	> 99	84	350 °C, Nitrogen carrier gas, Toluene, water, methanol feed	14
Al-MCM-41 (Si/Al = 28)	> 99	64		14
Al-MCM-41 (Si/Al = 57)	> 99	60		14
Al-Beta (Si/Al = 16)	100	91.6	300 °C, Ethanol solvent, WHSV of 0.33 hr^{-1}, nitrogen carrier gas	18
Al-Beta (Si/Al = 28)	76.5	92.3		18
Al-Beta (Si/Al = 133)	53.8	80.0		18
Al-Beta (Si/Al = 426)	57.6	61.8		18
Nb-MCM-41 (Si/Nb = 16)	100.0	95.2	300 °C, 0.1 bar, 4 hours on stream, oxime 10wt% in ethanol	19
Nb-MCM-41 (Si/Nb = 32)	95.5	98.0		19
Nb-MCM-41 (Si/Nb = 64)	94.0	93.5		19
B-MFI (Si/B = 40)	38.5	81.0	300 °C, 0.1 bar, N_2 carrier, 10wt% oxime in toluene	20
B-MFI (Si/B = 40)	53.3	91.2	300 °C, 0.1 bar, N_2 carrier, 10wt% oxime in methanol	20
B-MFI (Si/B = 40)	94.1	94.0	300 °C, 0.1 bar, N_2 carrier, 10wt% oxime in ethanol	20
ZSM-5 (Si/Al = 8)	62	42	350 °C, WHSV = 3hr^{-1}, Oxime 8wt% in benzene.	21
ZSM-5 (Si/Al = 100)	75	59		21
ZSM-5 (Si/Al = 100,000)	100	80		21

In contrast scarce few studies have been dedicated to the liquid-phase Beckmann rearrangement (see Table 3.2), in which no single system has dominated the field, unlike ZSM-5 in the vapour-phase. Instead the literature focusses far more on the solvent effect (primarily benzonitrile or chlorobenzene)[23] and also the development of new catalysts such as

sulfonated mesoporous silicates[27,28] to try and enhance the rate of reaction of this comparatively slower Beckmann process.

Table 3.2: Summary of the use of aluminosilicates in the liquid-phase Beckmann rearrangement.

Sample	Cyclohexanone oxime conversion/mol%	ε-Caprolactam Selectivity/mol %	Notes	Ref
H-ZSM-5 (Si/Al = 37)	67	95	Chlorobenzene solvent, 24 hours, 130°C	22
H-Beta (Si/Al = 31)	68	81		22
Amorphous SiO_2	0.1	72		22
H-USY (Si/Al = 7)	98.2	75.8	Benzonitrile solvent, anhydrous, 130°C	23
H-USY (Si/Al = 7)	83.6	94.4	Benzonitrile solvent, added water, 130°C	23
H-USY (Si/Al = 7)	16.7	55.8	Chlorobenzene solvent, anhydrous, 130°C	23
H-USY (Si/Al = 7)	13.0	49.8	Chlorobenzene solvent, added water, 130°C	23
H-Beta (Si/Al = 11)	27.3	> 98	Acetronitrile solvent, 5 hours, under N_2, 70°C	24
H-Beta (Si/Al = 11)	19.3	> 98	DMSO solvent, 5 hours, under N_2, 70°C	24
H-Beta (Si/Al = 11)	17.4	> 98	Methyl ethyl ketone solvent, 5 hours, under N_2, 70°C	24
H-Beta (Si/Al = 11)	11.7	> 98	Tetrahydrofuran solvent, 5 hours, under N_2, 70°C	24
H-USY (Si/Al = 11)	80	75.1		25
H-USY (Si/Al = 24)	80	73.0	Benzonitrile solvent, 130°C	25
H-USY (Si/Al = 33)	50	87.2		25
H-USY (Si/Al = 63)	50	85.8		25
Al-MCM-41 (Si/Al = 47)	50.6	89.1	Benzonitrile solvent, 130°C, 5 hours	26
Al-MCM-41 (Si/Al = 47)	28.8	23.3	Chlorobenzene solvent, 130°C, 5 hours	
Al-MCM-41 (Si/Al = 47)	26.5	18.0	Acetophenone solvent, 130°C, 5 hours	26
Al-MCM-41 (Si/Al = 47)	13.0	21.0	Acetonitrile solvent, 130°C, 5 hours	26
Sulfonic acid functionalised SBA-15	49.6	66.5	Toluene solvent, 130 °C, 24 hours	27
SBA-15	5	< 1		28
H-ZSM-5	8	43		28
H-MOR	12	16	Chlorobenzene solvent, 130°C, 24 hours	28
Al-MCM-41	36	12		28
Al-SBA-15	18	17		28
SBA-Ar-SO_3H	44	83		28
SBA-Pr-SO_3H	40	42		28

In an aim to attune these active sites zeolitic analogues, metal-substituted aluminophosphates (AlPOs), have recently been employed to mimic these isolated active species and framework architectures.[29-32] The notion that the alternating Al-O-P framework could subtly modify the structure-property relationships present in the aluminosilicates, offers catalytic benefits over their zeolite counterparts.[33,34] In this pursuit novel synthetic protocols were adroitly designed, in which the necessary active site for each step of ε-caprolactam

production was concurrently incorporated into the same AlPO framework (Figure 3.1C).[35] While desirable, the nature of the one-pot process is insurmountably impeded as the ammoximation intermediate (hydroxylamine) is actively degraded by the Brønsted acid species required for the second step, inhibiting substantial ε-caprolactam production.[35] On account of this paradoxical feature further work on AlPOs for the production of ε-caprolactam has since embraced a more viable two-step process (Figure 3.1D). The synergistic interactions present in bimetallic CoTiAlPO-5 are exploited to facilitate significant quantities of cyclohexanone oxime via an aerobic ammoximation process.[33,36] The second step, the Beckmann rearrangement of the oxime has more recently been performed under sustainable, energy efficient, liquid-phase conditions, achieving near-quantitative yield of ε-caprolactam (> 98 % under optimised conditions) using a silicon-substituted AlPO-37 species; SAPO-37.[37,38] While not as pervasive as their zeolite counterparts, SAPOs play a crucial role in modern society as industrial solid-acid catalysts. Most notably SAPO-34 is still unequivocally associated with the methanol-to-olefin (MTO) process as the industry standard after many decades.[39-41] In analogous fashion to the HZSM-5 species it becomes highly desirable to identify the precise nature of the silicon-species in these SAPO materials, whilst also drawing structure-property correlations that might expedite the formation of such species. As such it is imperative that the propensity of SAPO-37 for the Beckmann rearrangement reaction is probed and contrasted with other SAPO frameworks via a combined multi-technique characterisation and catalysis study, allowing mechanistic insights to be drawn that further the rational-catalytic design of a low-temperature Beckmann rearrangement catalysis.

This chapter begins by initially contrasting the effect of different SAPO framework architectures. With specific focus on the types of silicon substitution mechanisms involved and the acid sites created as a result.The activity of the different framework species is investigated for both the liqud and vapour phase Beckmann rearrangement with an aim to find a suitable framework to optimise for the low-temperature liquid phase Beckmann rearrangement of cyclohexanone oxime to ε-Caprolactam. On selecting a suitable framework synthesis conditions will be modified to optimise the catalytic activity.

3.2 Results and discussions – Screening SAPO frameworks

A specific range of SAPO architectures were purposefully chosen owing to their differing framework motifs, presenting with a range of distinctive and characteristic micropores (Figure 3.2). The dimensions of the nanoporous cavities present in AlPOs play a prominent role in catalytic activity,[42,43] further the precise geometry and orientations of these pores is highly influential in many processes, specifically diffusion of substrates.[44] While the properties of the crystalline host-framework are of exceptional significance, their influence over active site formation is also of paramount importance. A range of silicon environments are possible upon incorporating silicon into an AlPO framework, each accompanied with distinct acidic properties. The specific synthetic protocols for each framework require subtle differences in synthesis conditions and crystallisation kinetics, ultimately leading to each framework favouring a specific silicon site.[45,46] As such it is necessary to consider a range of SAPO-architectures if one is to differentiate between the effects of the framework architecture and the precise nature of the silicon active site. The frameworks chosen are detailed below (figure 3.2). This subsection selected represents a range of pore-sizes, from the smaller AlPO-34 (3.8 Å), which is widely used industrially, to the larger faujasitic analogue, AlPO-37 (7.4 Å). AlPO-5 has been chosen to contrast the SAPO-37 system, given that it has a similar pore aperture, though is a 1D channel structure, unlike the SAPO-37 (and SAPO-34 species) which both have 3D cage structures, allowing a direct contrast between the different framework topologies. SAPO-41 has been included as a second 1D channel structure, though with smaller channel dimensions, thus bridging the gap between the larger SAPO-37 and SAPO-5 systems and the smaller SAPO-34. As a consequence, it is appropriate to employ a wide range of characterisation techniques to simultaneously probe both the active silicon species and the framework topology, before structure-property correlations are determined for this range of species.

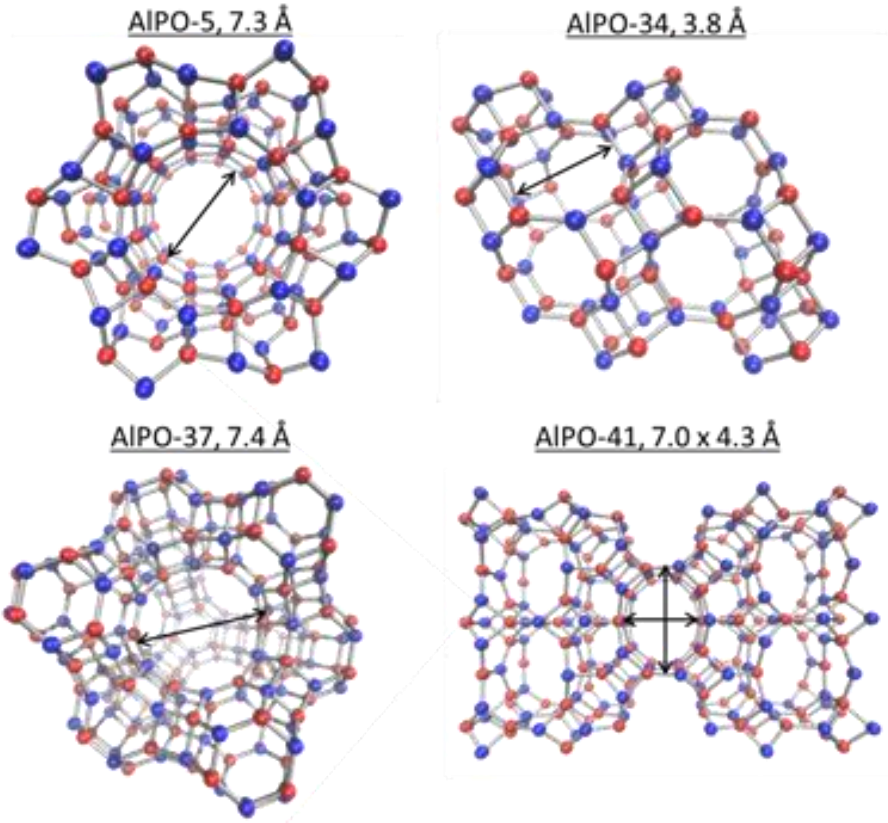

Figure 3.2: Contrasting different SAPO frameworks.

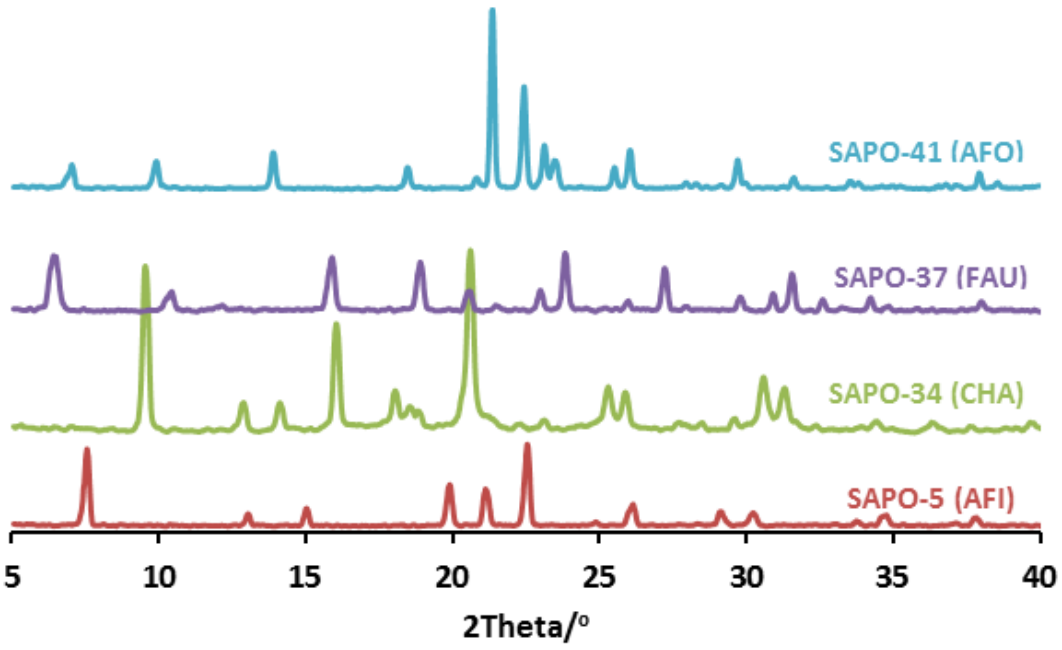

Figure 3.3: Powder XRD confirming structural purity of different SAPO frameworks.

Table 3.3: Fully optimized P1 unit cell parameters for SAPO materials

Material	a / Å	b / Å	c / Å	α / °	β / °	γ / °	Space group
SAPO-5	13.56	13.60	8.39	90.43	89.21	119.32	P6cc
SAPO-34	13.72	13.77	15.01	88.13	90.42	119.77	R-3m
SAPO-37	24.31	24.32	24.32	89.70	90.10	89.98	Fd-3m
SAPO-41	9.57	25.68	8.38	89.61	89.92	89.78	Cmcm

Table 3.4: Full ICP analysis and specific surface area.

Material	Al / wt%	P / wt%	Si / wt%	BET surface area / m^2g^{-1}
SAPO-5	21.7	24.2	1.6	158
SAPO-34	23.1	20.8	3.4	449
SAPO-37	23.5	20.8	3.0	588
SAPO-41	21.6	24.3	1.6	161

The intrinsic structural properties of the distinctive SAPO frameworks were investigated using a range of physico-chemical techniques, designed to probe the specific properties of the different framework motifs. Powder X-ray diffraction (XRD) confirmed that in all cases, after thermal treatment (calcination), the desired framework had been exclusively formed. This presented with no evidence of phase-impurities or extra-framework species (Figure 3.3, Table 3.3). The data was quantitatively analysed (through Reitveld analysis) to yield unit cell parameters for the different frameworks for further insights into silicon incorporation (Table 3.3). All frameworks were in excellent agreement (< 2% deviation) with the expected values derived from the ideal frameworks.[47] Subtle variations from the ideal unit cell parameters are anticipated, given the local structural distortion arising on isomorphously incorporating a heteroatom dopant (silicon) into an AlPO framework. Though such effects are restricted given the comparatively low levels of silicon incorporated, and the comparable size of silicon to the framework Al and P atoms, thus facilitating only slight shifts in expected peak positions.[48] Analysis of the specific quantities of silicon in the SAPO materials confirms the low-levels of silicon present in these materials (Table 3.4). Inspite of the molar gel-

ratios the silicon loadings show good agreement within the two 3-dimensional and the two 1-dimensional structures. With the silicon content following the trend SAPO-34 > SAPO-37 >> SAPO-5 ≈ SAPO-41. The effect of silicon incorporation was investigated using specific surface area measurements to further affirm the formation of the desired nanoporous frameworks. In some cases incorporation of silicon results prompts a disparity from that of the undoped framework, attributed to pore-obstruction, as has been observed in previous work (Table 3.4).[2,32] The faujasite and chabazite frameworks (SAPO-37 & SAPO-34 respectively) showing characteristically superior surface areas, given the intertwining nature of the microporous cavities present in these 3-dimensional structures (Figure 3.4).[49,50] This further suggests the presence of the ordered nanoporous frameworks intended. SEM images provide further information on the location of the silicon species. In all cases there is little evidence of secondary phases or extra-framework species suggesting framework-incorporation of the silicon species. The SAPO species largely show uniform crystalline particles, in accordance with the intended space-groups or previously published work (Figure 3.5 and Table 3.3). This holistically confirms the framework integrity of the synthesised SAPO materials and eludes to the framework substitution of silicon within these the materials.

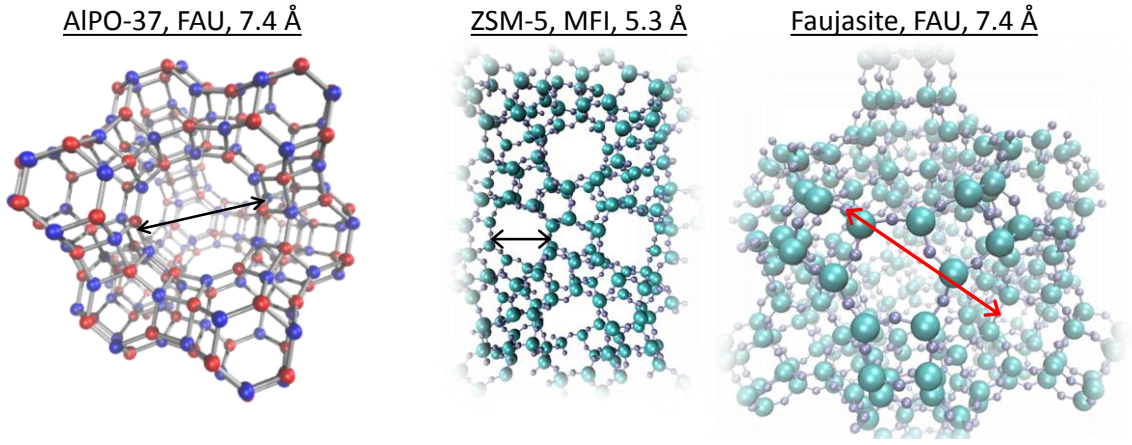

Figure 3.4: Contrasting zeolite and AlPO frameworks

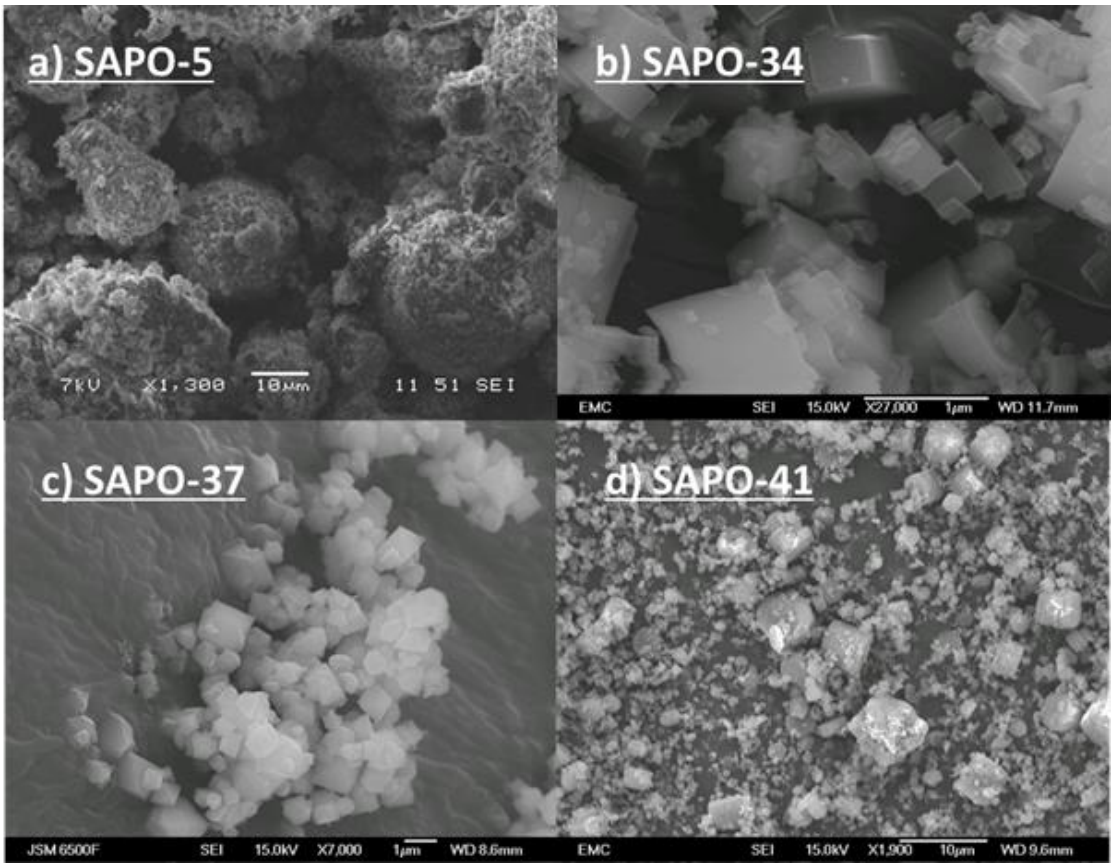

Figure 3.5: Scanning electron microscopy showing particle morphology.

One of the primary challenges afflicting heterogeneous catalysis is the desire to selectively focus on a modest proportion of the catalyst (the active site), while largely excluding the contributions of the vast inorganic host matrix in which it is encapsulated.[51-54] A comprehensive understanding of the active site requires an array of characterisation techniques to be employed to both directly, and indirectly, probe the acidic properties and local environment of the active species. In this vein it is necessary to coalesce findings from magic-angle spinning NMR (MAS NMR), temperature-programmed desorption (TPD) and Fourier-transform infra-red spectroscopy (FT-IR) to uncover the influence of the framework on the formation of the specific active species.

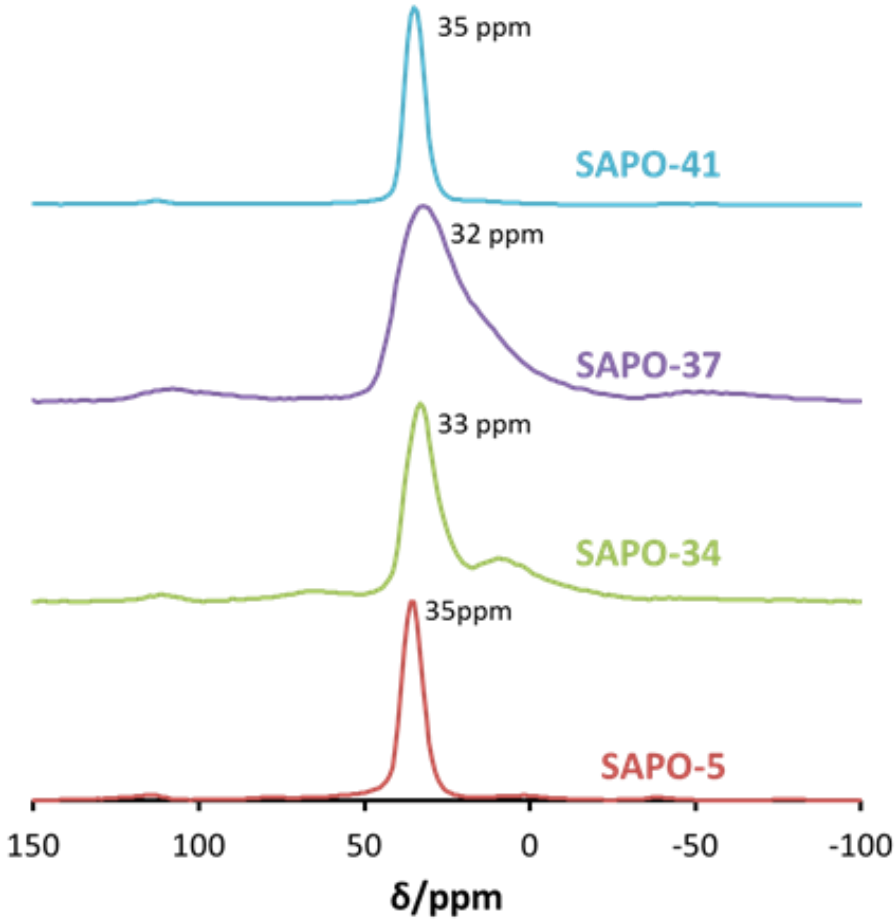

Figure 3.6: ^{27}Al MAS NMR to probe the local aluminium environments, peak maxima shown.

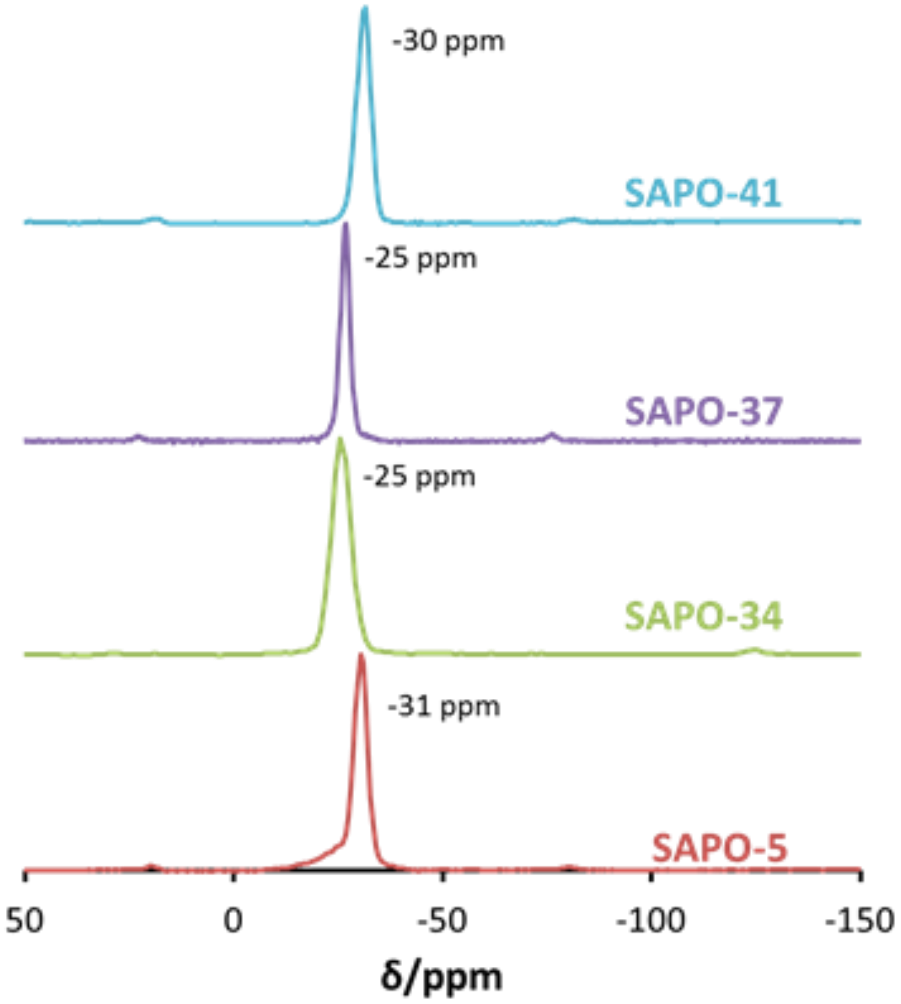

Figure 3.7: ^{31}P MAS NMR to probe the local phosphorus environments, peak maxima shown.

To support our powder-XRD findings the framework integrity is further considered through ^{27}Al and ^{31}P MAS NMR (Figures 3.6 and 3.7). Truly crystalline defect-free species should present a single signal in both of these spectra corresponding to $Al(OP)_4$ and $P(OAl)_4$ species respectively, known to appear between 33 and 48 ppm[55,56] and at -30 ppm in their respective spectra.[57,58] The SAPO materials studied all show one dominant signal in the ^{27}Al spectra, within the region of 33 – 42 ppm, ascribed to tetrahedrally coordinated framework aluminium, indicating the presence of the intended $Al(OP)_4$ species (Figure 3.6). In some cases the signals are broadened owing to the presence of penta-coordinated Al species and hydrated $Al(OP)_4(H_2O)_x$ species.[55,56] The ubiquitous spinning side bands were also present 105 and -50 ppm. ^{31}P NMR provides complementary evidence to the ^{27}Al NMR, with all frameworks showing signals within the -26 to -32 ppm range, attributed to the

primary $P(OAl)_4$ species. Closer inspection of the SAPO-5 spectra shows a shoulder peak at -22 ppm, this is attributed to the presence of $P(OAl)_3(OH)$ defect sites within the framework (Figure 3.7).[57,58]

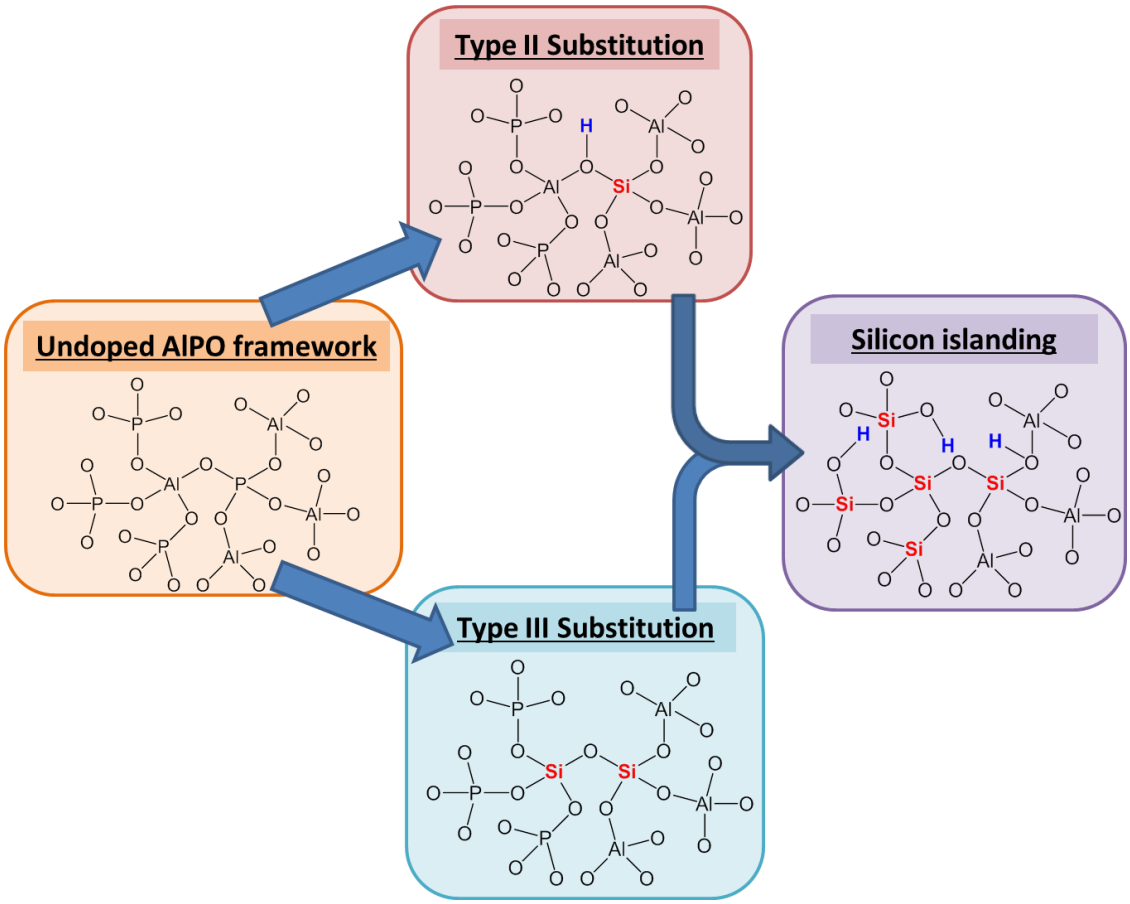

Figure 3.8: Graphical description of different silicon substitution mechanisms.

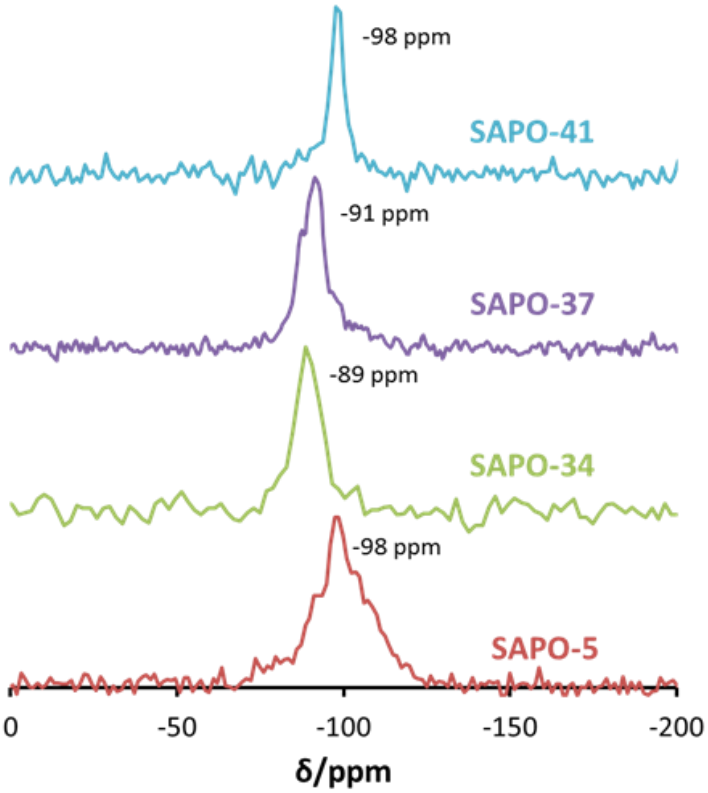

Figure 3.9: ^{29}Si MAS NMR to probe the local silicon environments, peak maxima shown.

Silicon nuclei incorporated into AlPO frameworks are markedly sensitive to the identity of their neighbouring framework tetrahedral atoms. This can be readily interpreted through the conscientious application of ^{29}Si MAS NMR, as each of the possible $Si(OAl)_x(OSi)_{4-x}$ species materialize within a distinctive chemical shift range, allowing NMR signals to be readily attributed to the specific silicon environment.[57-59] Once identified, such species can be perceptively associated with Brønsted acidity. Isolated silicon species ($Si(OAl)_4$) are unequivocally associated with Brønsted acidity. The charge imbalance arising from silicon undergoing type II substitution, is annulled by a proton binding to an apical oxygen atom adjacent to the substituted silicon atom (Figure 3.8). This forms an injective relationship between isolated silicon sites and Brønsted acid species. Other silicon environments may also facilitate Brønsted acidity. A prevalence of non-isolated silicon can be readily attributed to silicon-islanding derived from the combination of type II and type III silicon substitution mechanisms. In this case the extent of Brønsted acidity is wholly dependent on the proportion of type II over type III mechanisms, subsequently smaller silicon islands (possessing mainly $Si(OAl)_3(OSi)$ groups) will produce an substantial

amount of Brønsted acidity per silicon atom more than larger silicon islands (comprised mainly of $Si(OSi)_4$ environments, Figure 3.8). Direct observation of the ^{29}Si nuclei for the SAPO materials reveals that the different framework architectures can categorised according to the degree of silicon islanding (Figure 3.9). The faujasitic SAPO-37 and chabazitic SAPO-34 spectra reveal a strong predisposition for forming isolated active sites, evidenced by a dominant feature between −89 and -91 ppm, corresponding to the $Si(OAl)_4$ environment, directly associated with Brønsted acidity. These two spectra show scarce few other features than this one narrow signal, suggesting a uniformity exists over the framework silicon, favouring type II substitution. In stark contrast the SAPO-5 and SAPO-41 samples show a peak with the apex centred at -98 ppm. Signals in this region signify the presence of Si-O-Si bonds within the sample, attributed to silicon islanding and diminished site isolation.[45,46,57,58]

The silicon-doped AlPO systems presented here show significant differences in both the ^{29}Si and ^{27}Al MAS NMR compared to their zeolite counterparts. Given the majority of the inorganic matrix of a zeolite is comprised of silica there are often substantially more silicon environments present in aluminosilicate materials. Commonly a peak is observed at around -114 ppm, which corresponds to the framework Q^4 site; $Si(OSi)_4$.[60-63] The presence of aluminium can commonly be seen by the appearance of a peak in the range of -107 to -101 ppm, which refers to a $Si(OSi)_3(OAl)$ species. There are subsequently other characteristic peaks that correspond to the $Si(OSi)_2(OAl)_2$, $Si(OSi)(OAl)_3$ and $Si(OAl)_4$ species.[60-63] However these signals are commonly difficult to distinguish and often coalesce. The resolution of these peaks often requires Gaussian curve fittings. It is logical that species with different aluminium contents will also possess different fractions of these sites, and thus different signal intensities. This can be linked back to the aluminium-content of the zeolite using the following formula:[64]

$$(\mathrm{Si/Al})_{NMR} = \frac{I_4+I_3+I_2+I_1+I_0}{I_4+0.75I_3+0.5I_2+0.25I_1} \qquad (3.1)$$

where I_n denotes the intensity of the $Si(OSi)_{4-n}(OAl)_n$ species from the Si NMR.

For zeolite species the interpretation of Si NMR is further complicated by the presence of hydroxyl groups. Many zeolites possess a signal at -103 ppm (though it is commonly masked by the larger $Si(OSi)_3(OAl)$ signal) which

corresponds to the $Si(OSi)_3(OH)$ surface hydroxyl species. This signal becomes particularly prominent when employing $^{1}H \rightarrow {}^{29}Si$ cross-polarization techniques.[61] In these experiments the proton associated with the hydroxyl species drastically increases the intensity of the signal, dwarfing all others.

Finally given the large quantities of silicon that are present in zeolite species (by their very nature) the signal is commonly larger (and thus better resolved) than for SAPO systems. In light of this it is possible to resolve crystallographically inequivalent silicon T-sites, as has been observed in Mordenite (among other species). Given the smaller fraction of silicon present in SAPOs, such observations are far more challenging.

In contrast there is commonly significantly less aluminium present in zeolite species than in SAPOs. This makes the interpretation of the quadrupolar ^{27}Al nuclei much simpler for zeolites. Commonly the primary Al signal in zeolites occurs at 56 ppm, corresponding to $Al(OSi)_4$. It is also possible to see extra-framework octahedral aluminium present at around 0 ppm which is often the result of dealumination. Given that Al-O-Al bonds are forbidden via Loewensteins rule[65] there are scarcely any other features present in the ^{27}Al NMR of zeolitic species.

While MAS NMR is able to unequivocally determine the environment of the substituted silicon species, the details of the active sites are still shrouded. While one can draw subjective correlations between local silicon environments and the nature of the acid sites within the same framework, any conclusions drawn between different SAPO architectures are tenuous at best. Consequently, FT-IR and TPD techniques are employed to accentuate the features of the active species brought about by the differing substitution mechanisms. FT-IR experiments can simultaneously probe the nature, behaviour and location of the acid sites by employing a range of simple probe-molecules including CO and collidine (2,4,6-trimethylpyridine). Initially, the protonic species were observed directly in the hydroxyl-region (3800 – 3500 cm^{-1}, Figure 3.10). Subtle features at 3745 and 3678 cm^{-1} were present in all SAPO catalysts. These features are characteristic of SAPO frameworks and correspond to silanol (Si-OH) and P-OH defect species respectively, that are ubiquitous within this family of frameworks, the latter are also witnessed by ^{31}P NMR (Figure 3.7).[66] The frameworks associated with isolated active sites (SAPO-34 and SAPO-37) both

show two distinct Si-OH-Al signals, further substantiating the notion of isomorphous framework substitution. SAPO-37 shows peaks at 3640 and 3575 cm^{-1}, representing two proton locations. The former (3640 cm^{-1}) corresponds to proton species existing within the supercages of the faujasite framework, whereas the signal at 3575 cm^{-1} represents protons existing within the 6-rings of the apical sodalite cages. The disparity between the two signals can be attributed to the varying degree of hydrogen bonding the proton experiences with the framework oxygens in the two different conformations. Similarly, SAPO-34 exhibits two proton signals for an analogous reason, again referring to framework position. The signal at 3626 cm^{-1} corresponds to protons within the open cages of the SAPO-34 framework, whereas the signal at 3599 cm^{-1} derives from protons existing within the 6-rings of the 6,6 secondary building units. The spectra of the SAPO-5 and SAPO-41 species complements the NMR findings, with the signals corresponding to the framework-substituted silicon species (Si-OH-Al) showing a marked decrease in intensity (Figure 3.10), in good correlation with the lack of site isolation observed in the ^{29}Si MAS NMR (Figure 3.9). Whilst it is not possible to quantitatively analyse these observations (owing to the variance in scattering profile between distinctive structures) it remains clear that these two structures possess comparatively fewer acid sites.

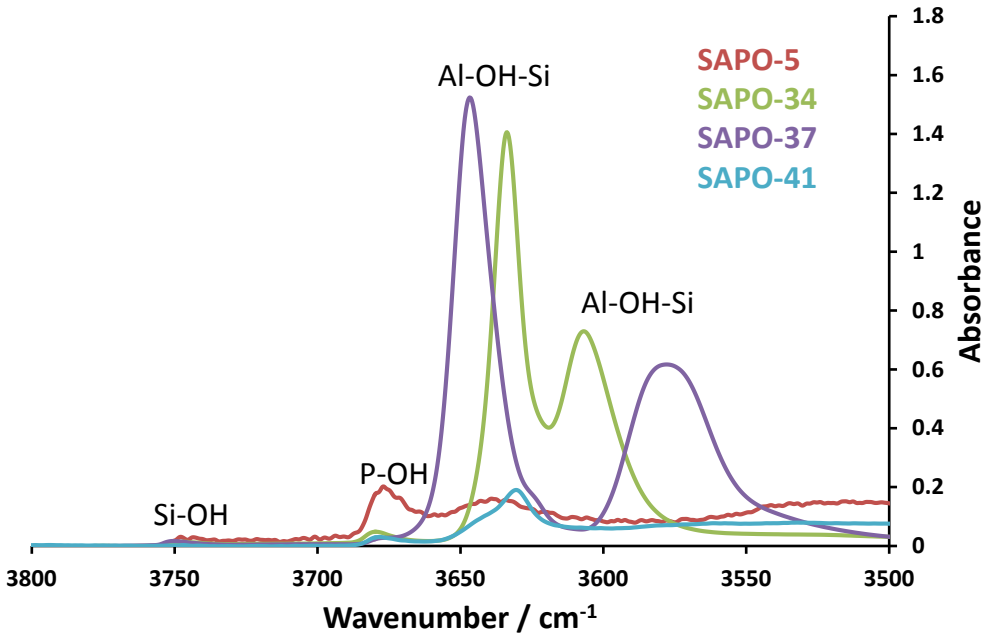

Figure 3.10: FT-IR spectra of the hydroxyl region (3800 – 3500 cm^{-1}) of the different SAPO species.

To gain quantitative insights on both the strength and number of acid sites, CO was employed as a molecular probe. On interacting with the acidic species a decrease in the hydroxyl OH stretches is accompanied by the appearance of a signal in the 3300 – 3500 cm^{-1} region attributed to O-H-CO interactions (Figures 3.11, 3.13 and 3.15).[67-70] Moreover, a signal derived from the CO stretch appears in the 2200 – 2150 cm^{-1} region (Figures 3.12, 3.14 and 3.16). The OH stretch in the smaller pore SAPO-34 framework completely recedes on CO adsorption, indicating that all sites are accessible within the pores. The two signals which appear in the CO region, (2170 and 2140 cm^{-1}) are attributed to CO adsorbed on Brønsted acid sites, and physisorbed CO interacting with the surface respectively,[71] no bands were observed > 2190 cm^{-1}, confirming a lack of Lewis acidity. The different OH species show subtly different behaviour given the disparity between their chemical shifts, suggesting that SAPO-34 possess both medium and strong Brønsted acid species. In SAPO-37, the two different acidic environments also show contrasting behaviour as the signal at 3575 cm^{-1} is preserved on CO adsorption. This suggests that these protonic species are inaccessible even to small molecules such as CO, as such these species will not contribute to catalytic processes. The primary signal at 3641 cm^{-1} significantly diminishes on CO adsorption, showing that a large proportion of the Brønsted acid species in SAPO-37 are still accessible. Quantifying the signal shift confirms that the system possesses significant quantities of medium-strength Brønsted acid species (Table 3.5). In contrast the signal from SAPO-41 shows substantial effects from hydrogen-bonding as witnessed by a broad signal in the 3550 to 3200 cm^{-1} range. The primary proton signal at 3631 cm^{-1} shifts by a value of 261 cm^{-1}, with a smaller contributory peak which shifts by 309 cm^{-1}, indicating the presence of some strong acid species. SAPO-5 shows only one shift due to CO adsorption with a value of 270 cm^{-1}, in a similar region to SAPO-41 (as expected from the MAS NMR, Figure 3.9), though shows significant differences from the isolated sites present in SAPO-34 and SAPO-37. Direct comparison of the integrated CO areas allows further correlations to be made between the two sets of samples (Table 3.5). Both SAPO-34 and SAPO-37 show significant quantities of acid sites, owing to a large proportion of isolated type II silicon species. In contrast the islanding silicon present in SAPO-41 and SAPO-11 results in the formation of significantly fewer acid sites as expected.

Table 3.5: Quantified CO FT-IR data.

Material	Shift 1/cm^{-1}	Shift 2/cm^{-1}	CO area on 0.20 cm^3 of CO added (au)
SAPO-5	270	N/A	0.179
SAPO-34	286	329	1.084
SAPO-37	305	N/A	0.854
SAPO-41	261	309	0.172

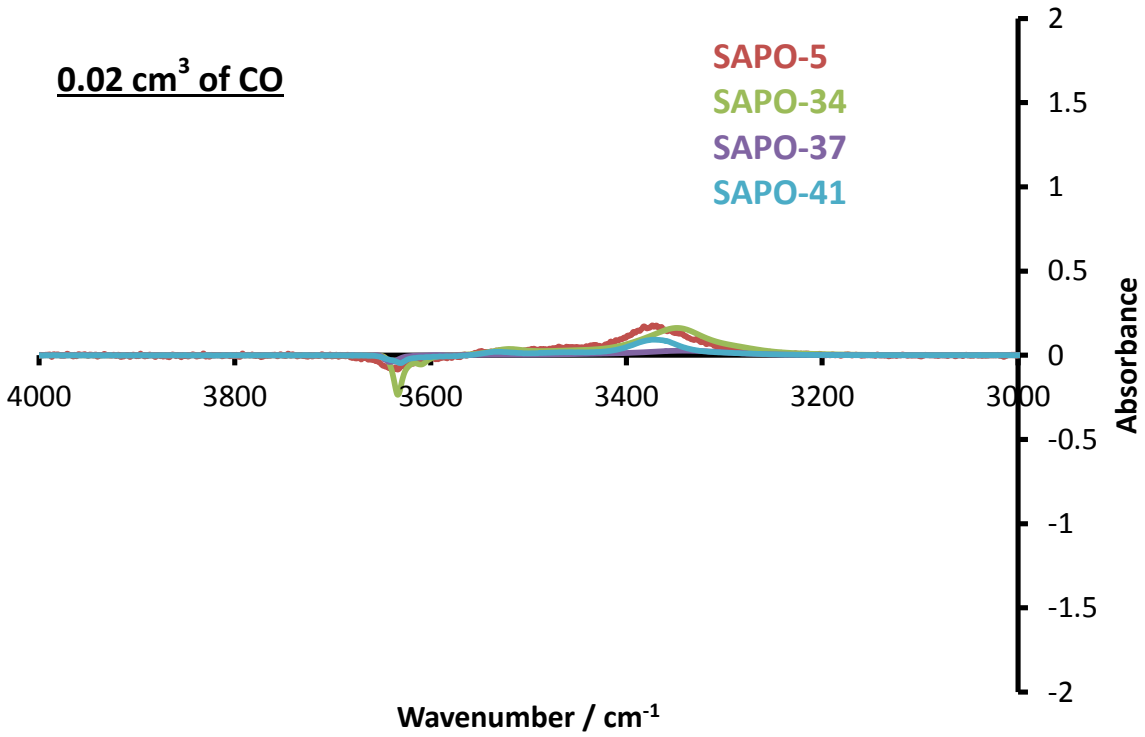

Figure 3.11: FT-IR difference spectra on adsorbing 0.02 cm^3 of CO on SAPO architectures in the hydroxyl region.

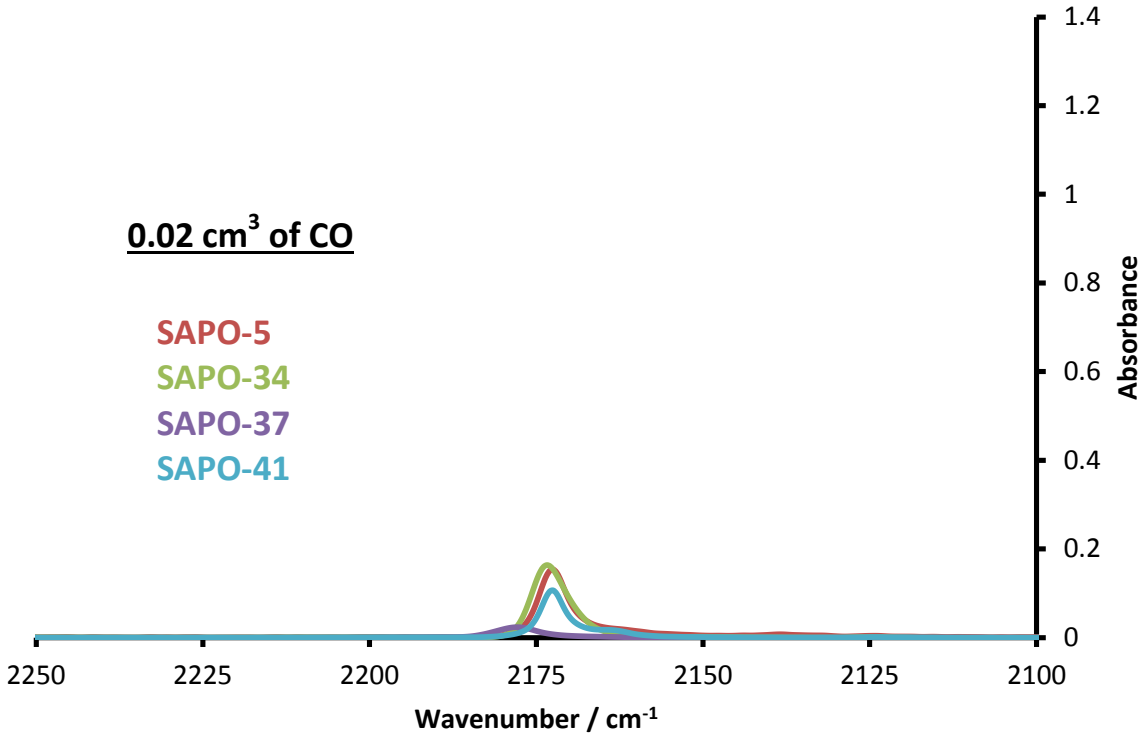

Figure 3.12: FT-IR difference spectra on adsorbing 0.02 cm^3 of CO on SAPO architectures in the CO region.

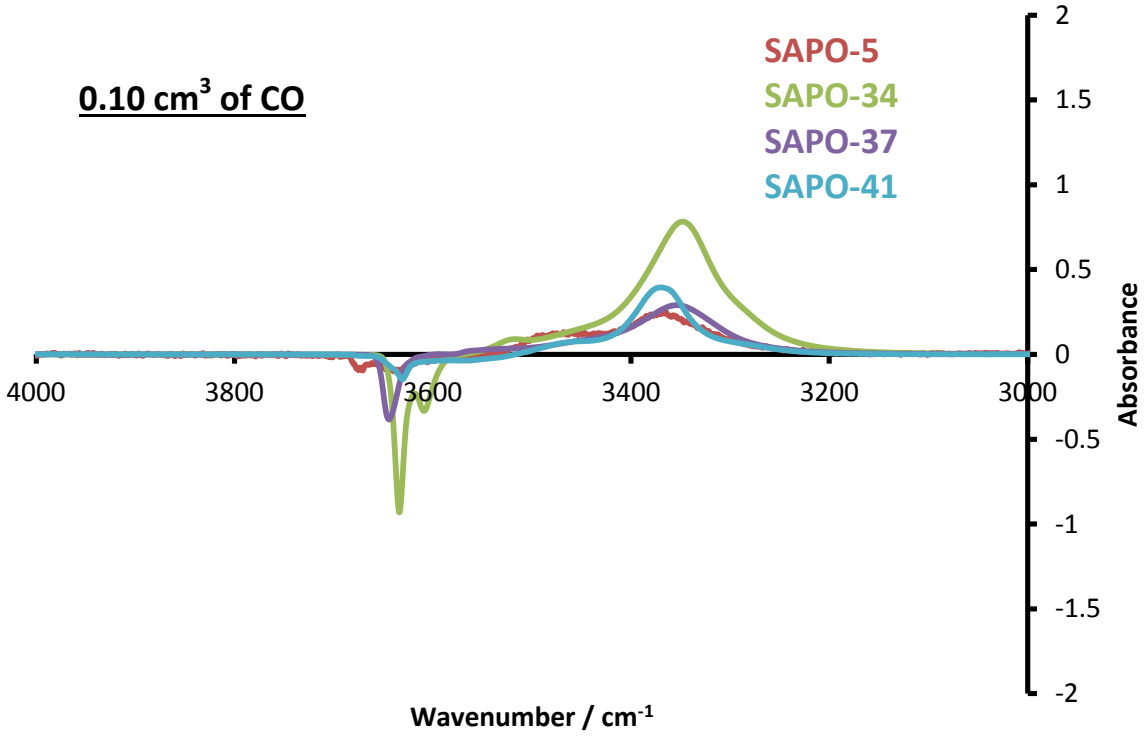

Figure 3.13: FT-IR difference spectra on adsorbing 0.10 cm^3 of CO on SAPO architectures in the hydroxyl region.

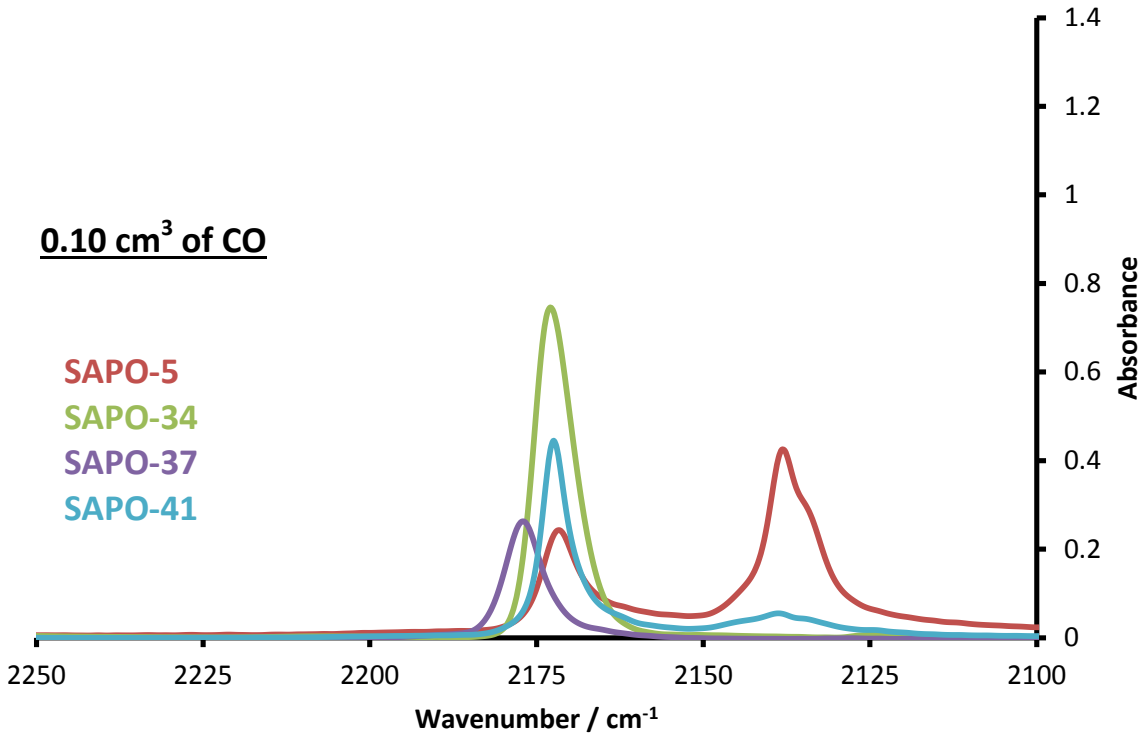

Figure 3.14: FT-IR difference spectra on adsorbing 0.10 cm^3 of CO on SAPO architectures in the CO region.

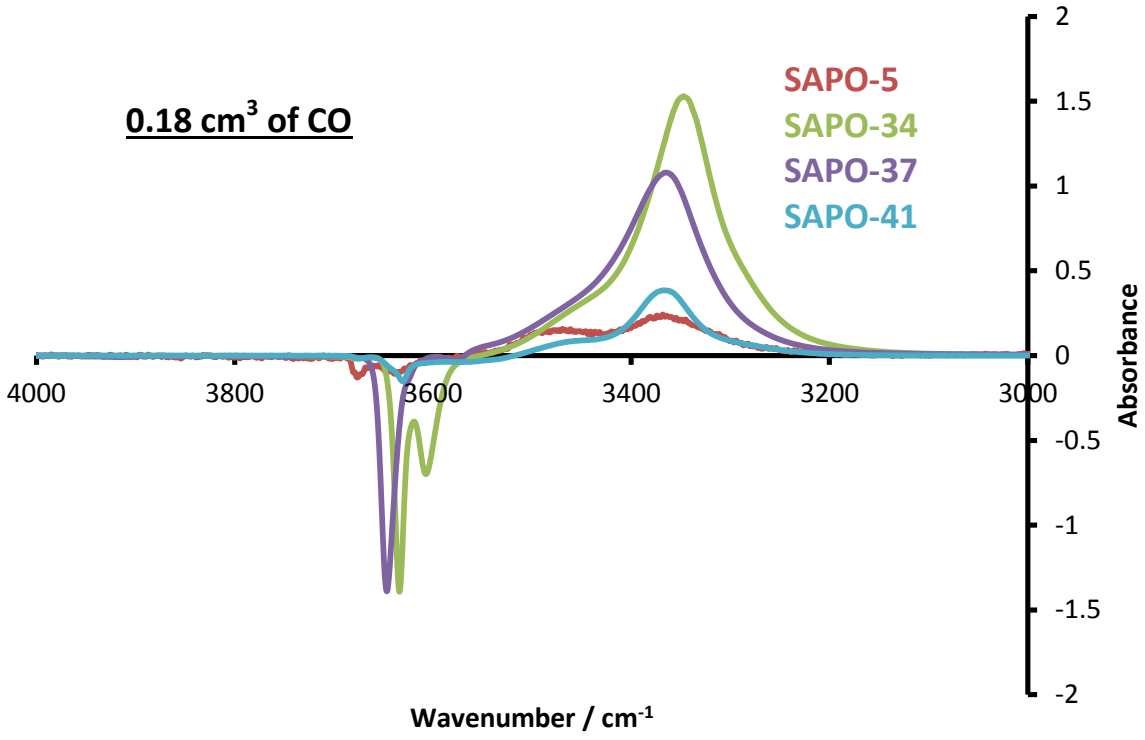

Figure 3.15: FT-IR difference spectra on adsorbing 0.18 cm^3 of CO on SAPO architectures in the hydroxyl region.

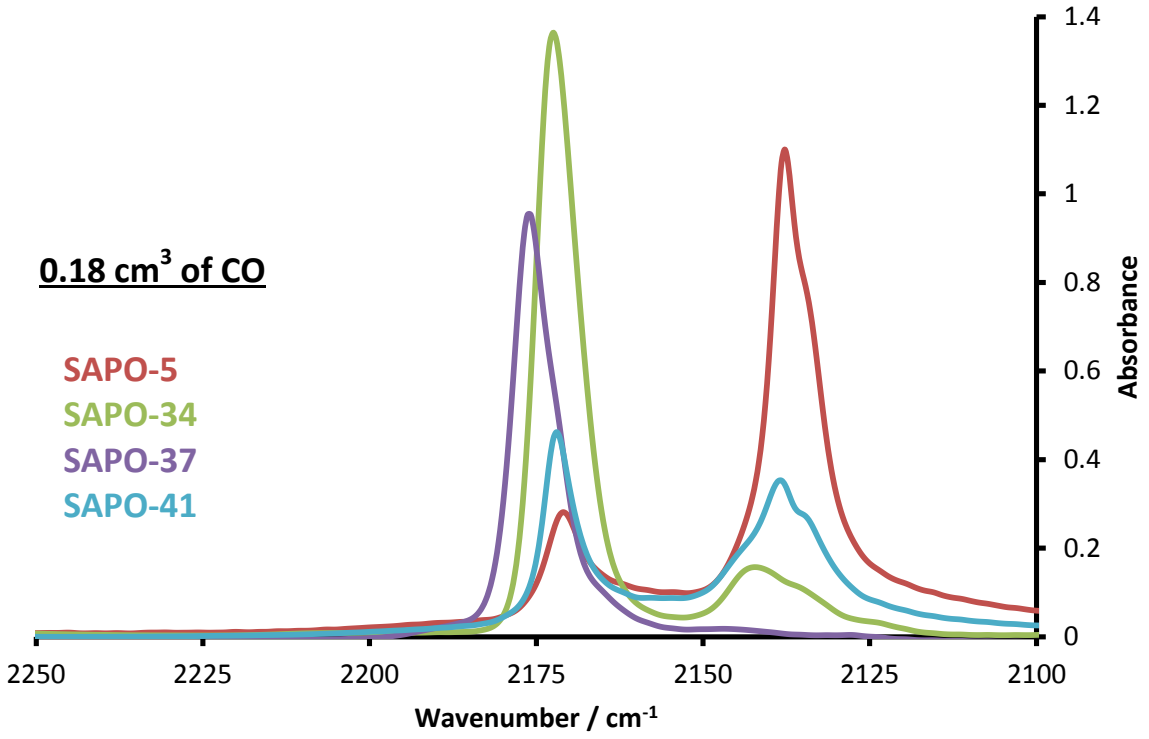

Figure 3.16: FT-IR difference spectra on adsorbing 0.18 cm^3 of CO on SAPO architectures in the CO region.

Table 3.6: Summary of previous CO FT-IR studies on zeolitic species.

Sample	Features of blank framework	Shift on adsorption of CO/cm^{-1}		Ref
		Silanol signal	Al-OH-Si signal	
H-Beta (Si/Al = 20)	**3737 cm^{-1}** Silanol species **3615 cm^{-1}** Al-OH-Si species	82	305	72
H-MOR (Si/Al = 5)	**3746 cm^{-1}** Silanol species **3612 cm^{-1}** Al-OH-Si species in 12-ring channels **3585 cm^{-1}** Al-OH-Si species in 8-ring	86	297	67

	channels			
H-ZSM-5 (Si/Al = 30)	**3746 cm**$^{-1}$ Silanol species **3618 cm**$^{-1}$ Al-OH-Si species	N/A	303	73
H-Y (Si/Al = 5.6)	**3748 cm**$^{-1}$ Silanol species **3648 cm**$^{-1}$ Al-OH-Si species in supercage **3543 cm**$^{-1}$ Al-OH-Si species in sodalite cage	N/A	275	74

The spectra presented share many key features with well-known zeolite systems in the literature (Table 3.6). The silanol (Si-OH) defect sites present in the SAPO-5 catalyst are almost ubiquitous in aluminosilicates materials, given the exceptionally high silicon content, though this feature is commonly more intense in zeolite materials. The Al-OH-Si bands also occupy similar positions (spanning the 3650 – 3500 cm^{-1} range).[67,72-74] These systems also show similar CO shifts to the analogous SAPO systems, particularly good agreement is seen between the SAPO-37 and H-Y system, with the signal also being split to represent the presence of proton environments in supercages and sodalite cages.[74]

Further insights on the acidic properties of these SAPO materials can be gained through ammonia-TPD, as a complementary tool to CO FT-IR (Figure 3.17 & Table 3.7). TPD data further accentuates the trends witnessed above, with the SAPO-37 and SAPO-34 showing similar quantities of acid sites, yet SAPO-34 possessing significantly stronger acid sites. In contrast the SAPO-5 and SAPO-41 species possess a much lower quantity of acid sites. Further, these sites are weaker strength acid sites than those present in either the SAPO-34 or SAPO-37 systems. It follows that to generate significant quantities of Brønsted acidity within an AlPO framework, targeted type II substitution is required. Despite identical substitution processes the strength of the acid sites generated is a function of the specific framework. In contrast silicon islanding leads to a

lower incorporation of silicon into the framework (Table 3.4). The combination of silicon islanding and a reduced quantity of framework silicon leads to the formation of substantially fewer acid sites with weaker acidity.[69]

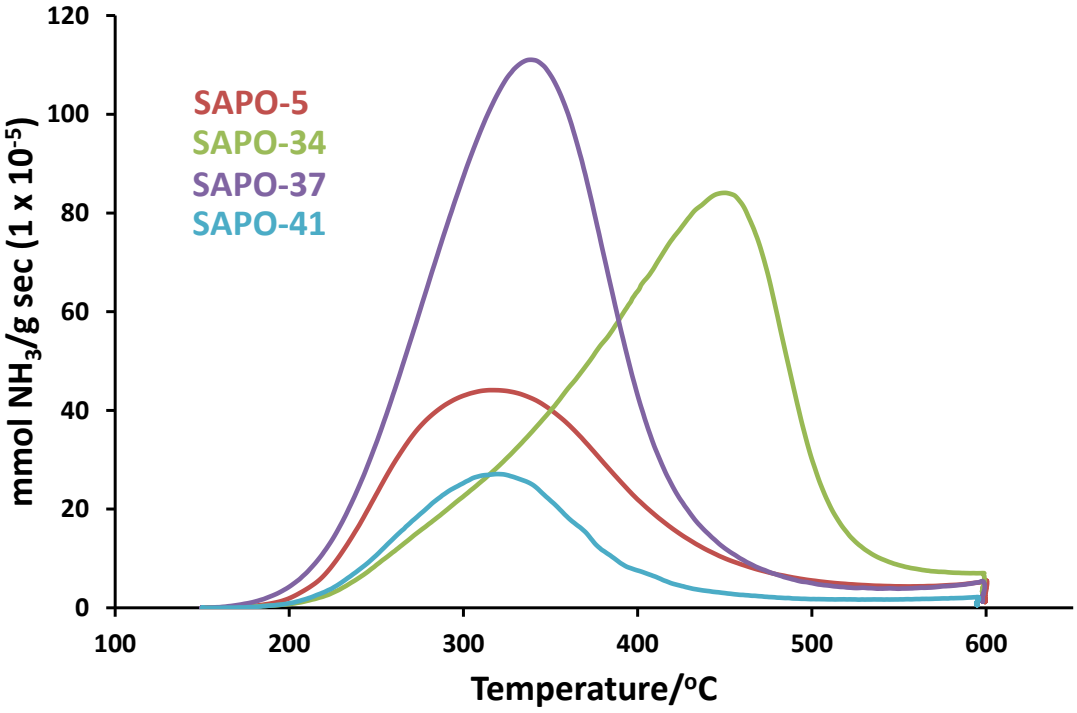

Figure 3.17: NH_3-TPD plots of SAPO architectures.

Table 3.7: Quantified peak areas for NH_3-TPD on various SAPO architectures.

Material	Peak area (mmol / g)						Peak maximum
	150 – 200/°C	200 – 300/°C	300 – 400/°C	400 – 500/°C	500 – 600/°C	Total	
SAPO-5	0.0014	0.1390	0.2274	0.0679	0.0293	0.47	313
SAPO-34	0.0008	0.0602	0.2533	0.4268	0.0811	0.82	447
SAPO-37	0.0000	0.2370	0.5630	0.0940	0.0330	0.93	340
SAPO-41	0.0007	0.0721	0.1205	0.0223	0.0134	0.23	313

The NH_3-TPD presented emphasises the subtle differences between the SAPOs and zeolites. In many cases zeolites boast stronger acid sites than SAPOs. An

in-depth analysis of the NH_3-TPD data of H-ZSM-5 and H-Mordenite catalysts revealed that on evacuation at a sufficiently high temperature only one signal at 542 °C remained on the MFI framework, whereas the MOR framework showed a solitary signal at 639 °C.[75] This confirms the superior acid strength of these materials. However the acid strength of zeolitic species is heavily influenced by the Si/Al ratio, as has been observed in ultrastable-zeolite-Y (H-USY).[16] Initially a Si/Al ratio of 6.3 produced a high density of weak acid sites, with the signal maxima at 175°C. On reducing the Si/Al ratio to 27 by steaming, the signal intensity decreased at the profile resolved into two peaks at 163 °C and the stronger acid species at 330 °C. It was the latter that was found to be catalytically active for the vapour-phase Beckmann rearrangement of cyclohexanone oxime. Similarly the acid properties of zeolite Beta have also been shown to be influenced greatly by the Si/Al ratios. H-Beta was found to contain peaks at 250 and 420 °C, corresponding to weak and strong acid sites respectively.[76] Reducing the aluminium content greatly reduced the quantity of the weaker sites, whilst the majority of the strong sites remained, though the peak maxima in both cases was found to shift to a lower value, indicating a weakening of the acid sites as the Si/Al ratio increased.

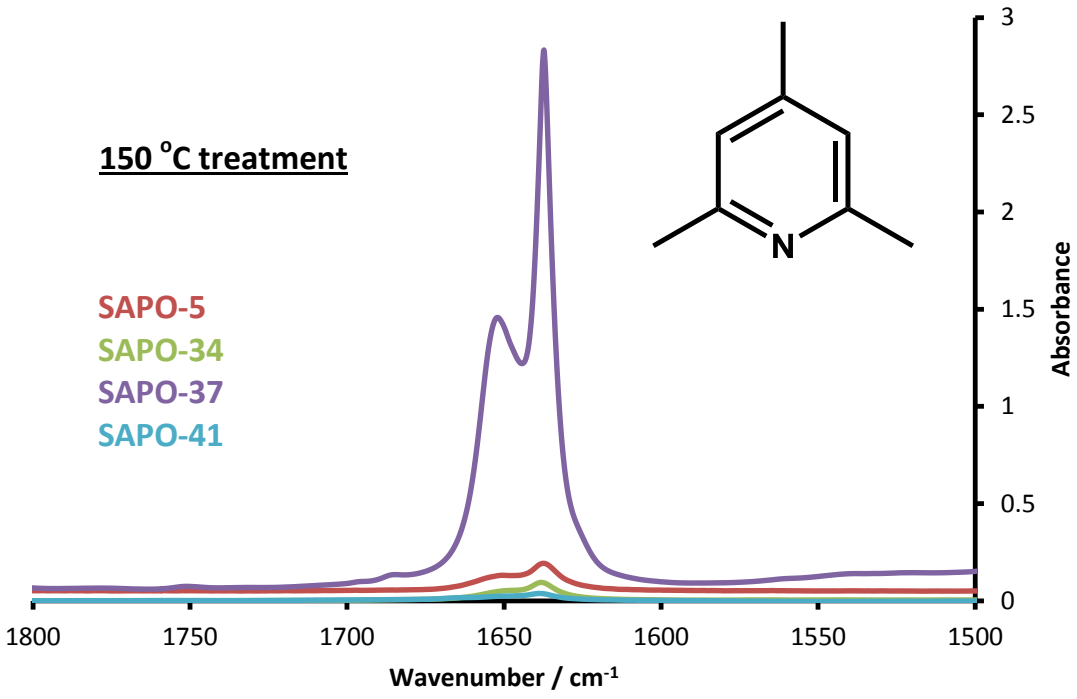

Figure 3.18: Collidine probed FT-IR spectra showing accessible active sites after treatment at 150 °C.

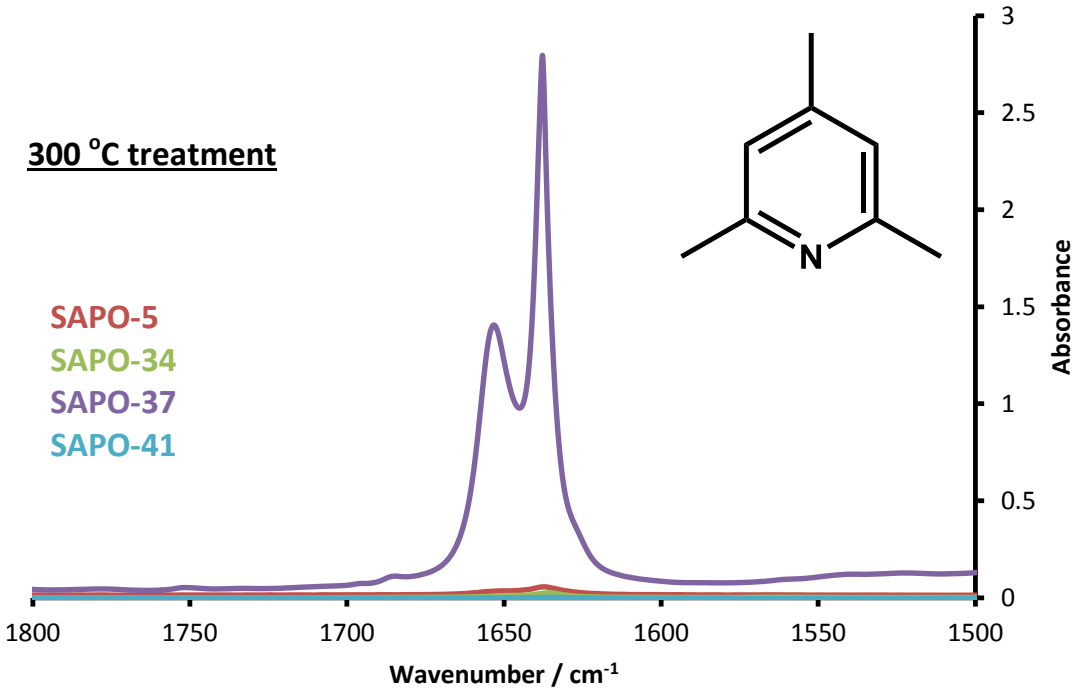

Figure 3.19: Collidine probed FT-IR spectra showing accessible active sites after treatment at 300 °C.

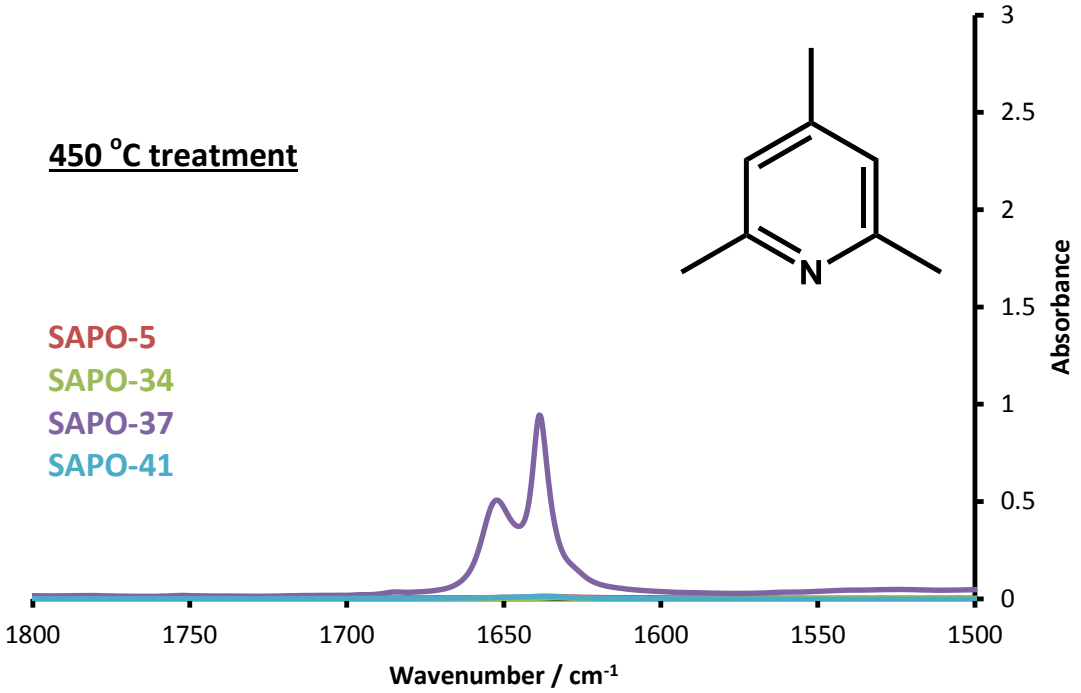

Figure 3.20: Collidine probed FT-IR spectra showing accessible active sites after treatment at 450 °C.

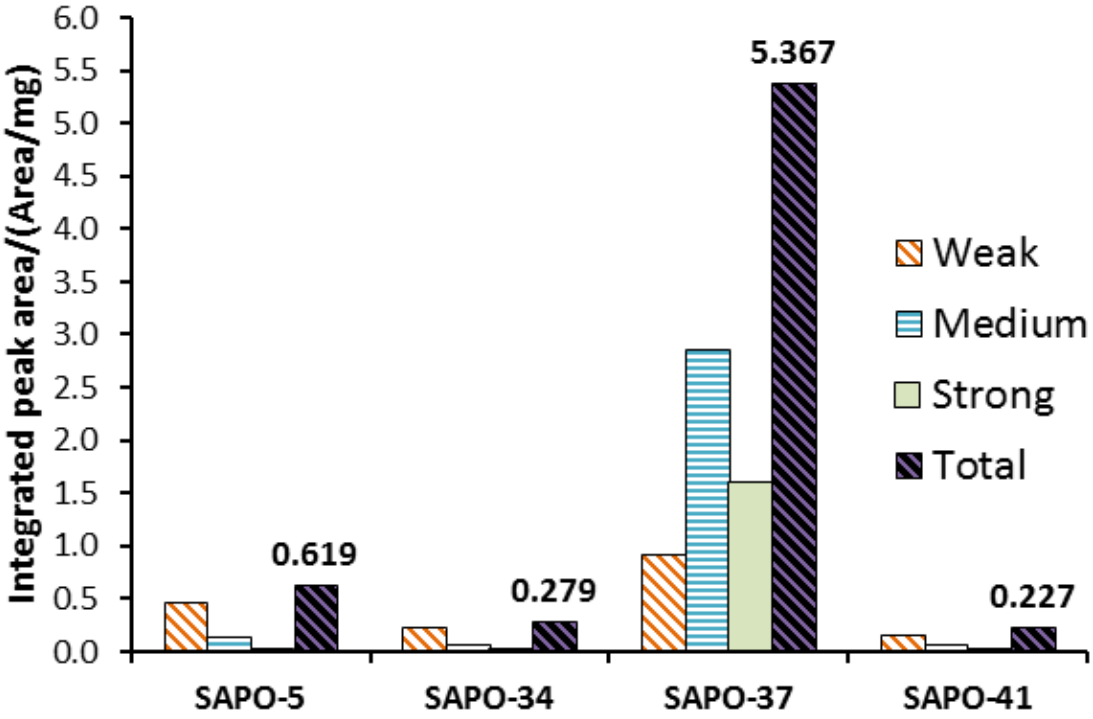

Figure 3.21: Quantitative analysis of accessible acid site from collidine-probed FT-IR.

Table 3.8: Quantified peak areas for the collidine probed FT-IR.

Material	Acid sites / (au / mg)			
	Weak (150 – 300 °C)	Medium (300 – 450 °C)	Strong (> 450 °C)	Total
SAPO-5	0.451	0.137	0.031	0.619
SAPO-34	0.215	0.056	0.008	0.279
SAPO-37	0.913	2.845	1.609	5.367
SAPO-41	0.150	0.059	0.018	0.227

Despite yielding significant information on the nature of the acid sites neither CO nor ammonia bears any resemblance to the larger cyclohexanone oxime reagent. Therefore, to gain a full understanding of the chemical potential for

the Beckmann rearrangement process the use of a more discerning probe molecule is necessary. To gain a more realistic understanding of reactant diffusion, collidine is purposefully used as a probe to mimic cyclohexanone oxime (Figures 3.18-3.21 and Table 3.8). Once adsorbed the uptake of collidine was monitored by quantifying the areas of the 1652 and 1637 cm^{-1} signals upon heating over a range of temperatures. Of the four samples the larger-pored SAPO-37 species was the only sample to show significant collidine uptake, with SAPO-5 showing only a slight affinity for collidine. Despite other contrasting behaviour, the quantity of collidine absorbed by SAPO-41 and SAPO-34 was comparable. These observations can be rationalised in terms of the framework motifs and pore geometries. The SAPO-37 system, possessing the largest micropores (7.4 Å), is too large to impede the diffusion of the probe molecule into the nanoporous framework, permitting access to the internal acid sites within the microporous network. SAPO-5, which while also possessing a comparatively large micropore (7.3 Å), will show subtle differences in diffusion behaviour to the comparably sized SAPO-37 material owing to the fundamental differences in framework topology. Being a 1-dimensional framework AlPO-5 (AFI) materials are more prone to factors such as pore-blockage. In contrast the 3-dimensional SAPO-37, possessing interlocking micropores, will not be afflicted to the same magnitude, hence allowing greater uptake of large molecules. Further, the distinction in total collidine adsorption between the two samples (5.37 for SAPO-37 and 0.62 for SAPO-5) is also the result of the total number of acid sites present as seen by CO-probed FT-IR. The similarity between the SAPO-41 and SAPO-34 species, despite differing in other factors, is indicative of a lack of internal diffusion, as in both materials collidine only adsorbs on the materials surface. In both these cases the micropores are sufficiently small (SAPO-34: 3.8 Å and SAPO-41: 7.0 x 4.3 Å) to prevent the probe from accessing the internal active sites. By comparing the total number of acid sites calculated through CO and collidine FT-IR studies it becomes possible to calculate the proportion of active sites available to larger probe molecules (in this case collidine, Table 3.9). By assuming that all active sites are accessible to collidine in the SAPO-37 framework (100 % of sites are accessible) it is possible to scale the values accordingly for each framework thus:

The proportion of available acid sites can be normalised with respect to SAPO-37, thus it was assumed that 100 % of acid sites were accessible in SAPO-37. This means that an area of 5.367 au/mg on adsorption of collidine, corresponds to 0.854 au for the CO probed FT-IR. Given that both are FT-IR based techniques this is a reasonable assumption. A sample calculation is presented below for SAPO-5:

SAPO-5 gave a collidine area of just 0.619 au/mg, this is just:

$$\frac{100\ \% \times 0.619\ au}{5.367\ au} = 11.5\ \% \qquad (3.2)$$

SAPO-5 only possesses 11.5 % of accessible sites that SAPO-37 has. However CO FT-IR showed that SAPO-5 also had a lesser amount of total acidity, only:

$$\frac{100\ \% \times 0.179\ au}{0.854\ au} = 21.0\ \% \qquad (3.3)$$

SAPO-5 only possesses 21.0 % of the acid sites which SAPO-37 has. Thus SAPO-5 has only 21.0 % of the total acidity of SAPO-37, but only 11.5 % of the accessible sites of SAPO-37, therefore the proportion of accessible active sites in SAPO-5 is:

$$\frac{100\ \% \times 11.5\%}{21.0\%} = 55.0\ \% \qquad (3.4)$$

Table 3.9: Proportion of acid sites which are accessible in each SAPO-material.

Material	Proportion of active sites which are accessible / %
SAPO-5	55.0
SAPO-34	4.1
SAPO-37	100.0
SAPO-41	21.0

In doing so it can be shown that a significant number of active sites are available in SAPO-5 (55 %), whereas in the smaller pore SAPO-41 only 21 % are accessible. Finally it is shown that only a fraction of the acid sites in SAPO-34 (4 %) are on the surface and therefore accessible to larger molecules. It should

be emphasised that while collidine more closely resembles the oxime reagent they are not identical in their molecular dimensions, and as such some subtle disparities may exist between the two, however the underlying trend of SAPO-37 > SAPO-5 > SAPO-41 ≈ SAPO-34 will still apply. The subject of internal diffusion is currently of considerable debate with regard to the use of ZSM-5 for the vapour-phase Beckmann rearrangement. At this time it is not conclusive whether the oxime reagent can penetrate into the MFI framework and access the internal sites, or whether the reaction occurs on the surface. As such the subject of active-site accessibility is fundamental in determining reaction kinetics and optimising catalyst performance.[77,78]

Given the diverse range of nanoporous frameworks examined, and on exploring the active sites therein, these frameworks are deemed as suitable for performing acid-catalysed reactions, with differences in catalytic behaviour being fundamentally linked to at least one of these two attributes. As such the production of ε-caprolactam using these heterogeneous solid-acid nanoporous materials above was investigated. Both their activity for liquid (130 °C) and vapour phase (≥ 300 °C) Beckmann rearrangement processes was evaluated. The liquid phase method, while traditionally less active and requiring higher substrate-to-catalyst ratios, offers the advantage of being less energy intensive given the lower temperatures required.[26,28] Under identical conditions significant differences in both activity and product specificity were observed between the four different frameworks.

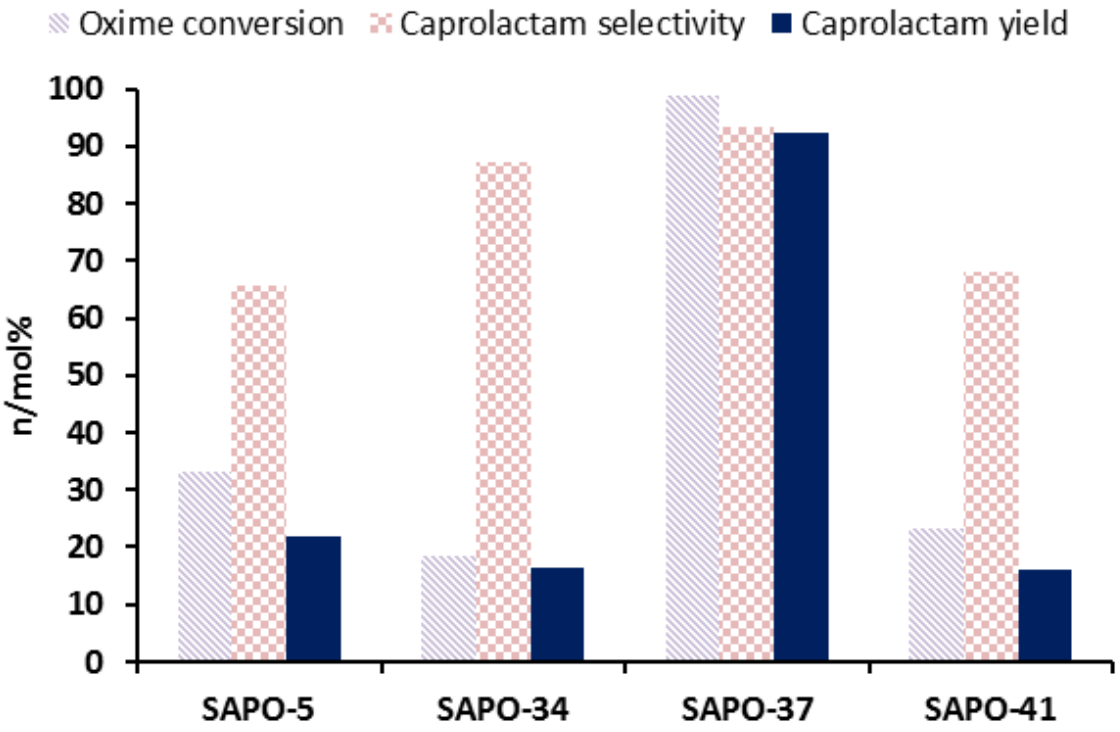

Figure 3.22: Catalytic data from the liquid-phase Beckmann rearrangement, emphasising the influence of framework topology. Conditions: 130 °C, 7 hours, 20 ml benzonitrile, 100 mg of cyclohexanone oxime, 100 mg of catalyst.

Clear trends are evident in both conversion and selectivity for this process (Figure 3.22). We note that the conversion does not correlate with any of the insights on the precise nature of the active site witnessed from ICP, NH_3-TPD, CO FT-IR or MAS NMR. Instead a more intuitive relationship exists between pore size (framework topology) and catalyst efficacy, thus mirroring the trend seen in the collidine adsorption FT-IR (Figures 3.18-3.21 and Table 3.8). The larger pore SAPO-37 will not supress internal diffusion of the oxime reactant (as seen by enhanced total acidity for collidine adsorption), thus allowing it to access the many available internal active acid species. Simultaneously the faujasitic supercages (~ 13 Å) will not impede the formation of bulky transition states or the diffusion of the larger ε-caprolactam product away from the active species, thereby limiting over-activation and coking. Similarly, the 1-dimensional SAPO-5 material (possessing a pore diameter of 7.3 Å), in which a proportion of the internal active sites are accessible, out-performs both the SAPO-34 and SAPO-41 species. SAPO-41 shows an astute increase in activity over the SAPO-34, this is also attributable to the framework dimensions. In the

SAPO-34 system the reaction must almost exclusively occur on the surface, as internal diffusion is infeasible, given the discrepancy in pore size and the kinetic diameter of the reactant. Despite the larger collidine probe being principally unable to access the SAPO-41 micropores, the smaller oxime molecule may still achieve limited diffusion, facilitating interactions with a proportion of the internal active species. It is prudent at this point to consider not just the number of available acid sites, but also the nature of these sites. The collidine adsorption on the SAPO-5, -34 and -41 species reveals that the available sites present are primarily weaker acid sites residing on the surface, in contrast the available acid sites in SAPO-37 are stronger (Figure 3.21, Table 3.8). This suggests that not only is the diffusion into the faujasitic framework vital, but the stronger acid sites within are adroitly suited to activating this particular process. This hypothesis is furthered by the selectivity profiles. The SAPO-5 and SAPO-41 show significantly lower specificity for ε-caprolactam (both ~ 65 mol%) compared to SAPO-34 and SAPO-37 (both ~ 90 mol%). It is known that microporous materials are able to supress the formation of ε-caprolactam, as the constricting micropores instead favour the formation of linear ring-opening products.[79] However reactions occurring inside the larger-pore SAPO-37, and the surface of the SAPO-34, will not be sterically hindered in such a way, promoting the formation of the caprolactam product. While any reactions occurring in the micropores of SAPO-5 and SAPO-41 will facilitate the formation of ring-opening by-products, lowering the selectivity. These results firmly suggest that the weaker surface species are ineffective for activating the oxime molecule under these conditions. As such access to active acid sites is fundamental to the design of successful catalysts for the liquid-phase process. Without internal diffusion a large proportion of the stronger acid sites are inaccessible and therefore ineffective, thus access to the micropores is imperative in optimising this process, as reflected in the collidine adsorption data (Figures 3.18-3.21 and Table 3.8).

Table 3.10: Vapour-phase Beckmann rearrangement data

Material	300°C		350°C		400°C	
	Conv/mol%[a]	Sel/mol%[b]	Conv/mol%[a]	Sel[b]/mol%[b]	Conv/mol%[a]	Sel/mol%[b]
SAPO-5	63.3	81.4	83.6	82.7	96.4	84.9
SAPO-34	36.3	75.5	87.1	48.6	100.0	94.7
SAPO-37	92.6	95.1	99.7	91.2	100.0	76.1
SAPO-41	98.5	76.8	99.8	77.2	99.8	65.2

a) Conversion of cyclohexanone oxime, b) Selectivity to ε-caprolactam.

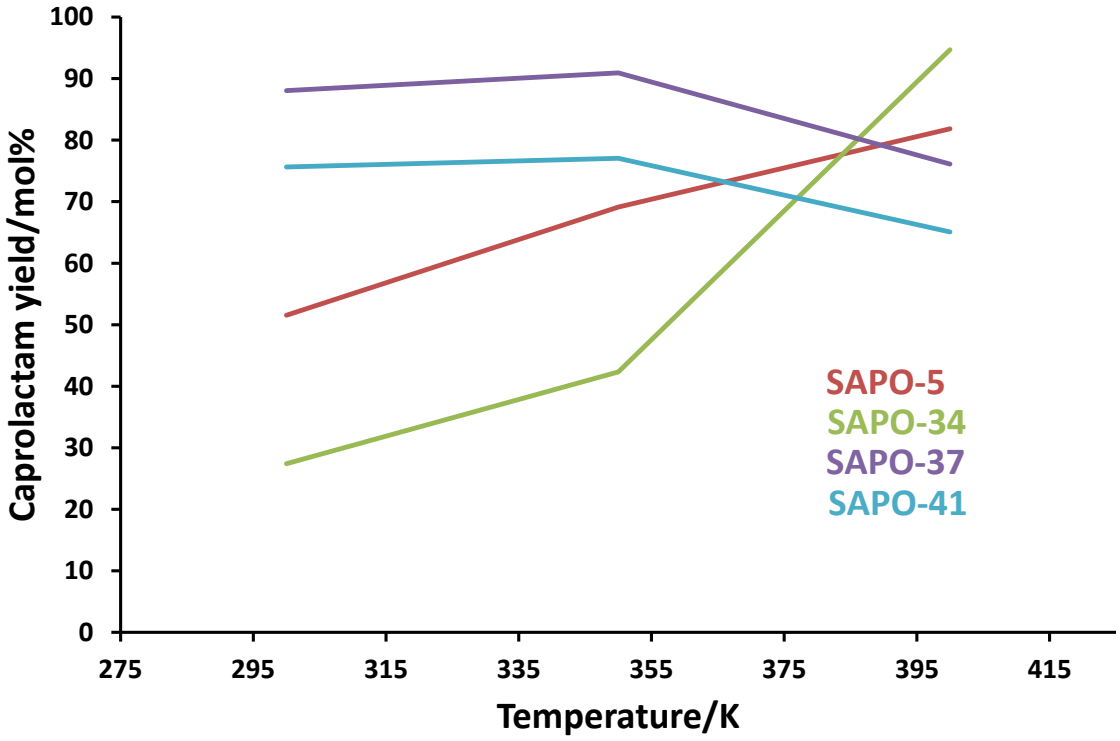

Figure 3.23: The influence of framework architecture on the vapour-phase Beckmann rearrangement. Conditions: Liquid feed of 10 wt% cyclohexanone oxime in ethanol, WHSV of 0.4 hr^{-1}, 33.3 ml of He carrier gas, 1 hour on stream.

The vapour-phase process, while requiring higher temperatures, utilises lesser quantities of a more common solvent (ethanol) than the liquid-phase process

(which uses benzonitrile). Further the higher temperature often leads to a greater catalyst efficiency and lifetime, as such a greater body of work has been dedicated to the vapour-phase process in both the academic and patent literature.[7,9-13] Given the industrial implementation of the medium-pore HZSM-5 catalyst (5.4 Å, Figure 3.1B) it is possible that internal diffusion is not as significant in the vapour-phase as in the liquid-phase process.[80,81] The vapour-phase process was studied over a range of temperatures to be comparable to current literature methods (Table 3.10, Figure 3.23).[7,9-13] Initially at the lower temperature (300 °C) the trend in caprolactam yield resembles that of the liquid phase process (Table 3.10 and Figures 3.22 and 3.23), the larger pore SAPO-37 show better activity than the SAPO-5 and SAPO-41, both of which outperformed the smaller-pored SAPO-34 material. Similar arguments can therefore be made with regard to diffusion kinetics and the nature of the specific active species under these conditions. When considering the activity at 400 °C a significant difference is observed, whereby the smaller-pore SAPO-34 species is the most efficient catalyst for this process, followed by the SAPO-5. The heightened activity of SAPO-34 suggests that the rate of reaction is no longer dominated by the kinetics of internal diffusion. It is conspicuous that there will be marked differences in diffusion behaviour between the 130 °C liquid phase and 400 °C vapour phase processes, though despite this internal diffusion is still implausible. As such, given the increased activity, it must be concluded that the active sites for this reaction are located on the surface or at the pore-mouth of the SAPO-34 catalyst. Therefore the higher temperature (400 °C) allows a greater range of acid sites to catalyse the Beckmann rearrangement reaction. This occurs to the extent that the surface species are now active, accounting for the unanimous increase in conversion witnessed among all samples. A decrease in lactam yield was witnessed in both SAPO-37 and SAPO-41, despite increased conversion. Similar arguments can be applied to explain this behaviour. Whilst increased temperature supplies sufficient energy to allow previously inactive acid sites to perform the desired Beckmann rearrangement, it also allows already-active sites to access a range of higher energy reaction pathways. Therefore promoting the formation of by-products and lowering the selectivity. The behaviour of all four of the catalysts at 350 °C appears to be intermediary between the behaviours at 300 and 400 °C, showing a gradual transition from the behaviour seen at the liquid phase (and at 300 °C) to the more active conditions of 400 °C.

It becomes clear that, while the mechanism for the Beckmann rearrangement is well known (Figure 3.24), that subtle differences in behaviour can be witnessed depending on the reaction temperatures used. While diffusion dictates the reaction rate in the liquid phase, the higher temperatures of the vapour-phase activate the surface species of the catalysts present, negating the need for internal diffusion, allowing the reaction to happen on the surface. It is hypothesised therefore that liquid-phase reactions primarily occur on medium and strong internal acid species, whilst the vapour-phase process instead occurs on the weaker external surface species, as witnessed in other reactions.

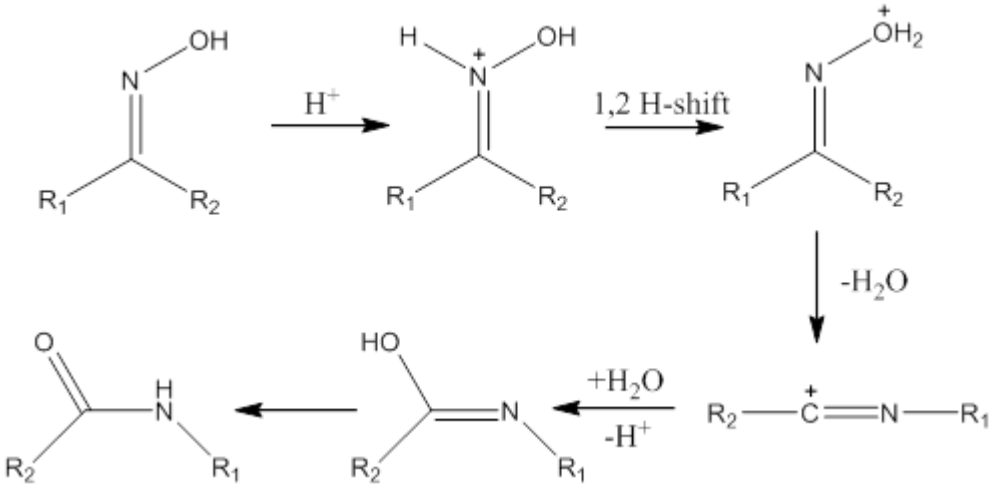

Figure 3.24: The Beckmann Rearrangement mechanism.

The influence of framework topology has been explored with reference to silicon-substitution mechanisms. By doping silicon into an AlPO framework (generating a SAPO species) one can induce an array of different acid active species within the nanoporous framework. The exact nature, location and strength of these active species has been explored using a combination of structural, physico-chemical and *in situ* spectroscopy designed to correlate the exact nature of the Brønsted acid active species to the framework-specific substitution mechanism. The paramount influence of the specific framework topology and these distinctive acid properties has also been described. Such species have been found to be highly active for both the sustainable low-temperature liquid-phase and the industrial vapour-phase Beckmann rearrangement of cyclohexanone oxime. Furthermore differences in catalytic profiles have been allied with the multi-technique characterisation study to infer the nature of the active species. These studies also revealed contrasting

behaviour between the liquid and vapour-phase processes which lead to significant mechanistic insights on the location of the active species. The framework-acidity correlations afforded in this work have been significant with regards to the future modification and design of SAPO catalysts for industrial applications.[82-84] The catalytic activity of different framework SAPO materials has shown that SAPO-37 is best suited to both the liquid and vapour-phase Beckmann rearrangement of cyclohexanone oxime to ε-Caprolactam, given the combination of the 3D-cage framework and the isolated active sites within. Given the high yields of caprolactam obtained this system is of considerable interest.

3.3 Results and discussions – Optimising SAPO-37

Given the exceptional activity of SAPO-37 in the low-temperature liquid-phase Beckmann rearrangement, a further study was performed with the aim to optimise the synthetic protocols, by which SAPO-37 is formed. Adroit design of the active sites was performed by modifying the silicon loadings and observing the effect this had on the catalytic activity of the system. To optimise the catalytic activity of the SAPO-37 system the silicon content used during synthesis was systematically varied to further enhance the production of ε-caprolactam to near quantitative yields. Three further SAPO-37 systems were synthesised with varying silicon loadings. These samples are labelled according to their silicon loadings, with the original SAPO-37 sample now being called SAPO-37(0.21), in addition to this SAPO-37(0.11), SAPO-37(0.42) and SAPO-37(0.63) were synthesised. All of the samples were found to have exclusively formed the faujasitic framework with the exception of SAPO-37(0.11). The SAPO-37(0.11) sample was found to contain a significant AlPO-5 (AFI) phase impurity (see figue 3.25). It is known that the AlPO-37 framework requires a certain level of silicon to form, to the extent that undoped AlPO-37 has never been successfully synthesised. If insufficient amounts of silica are present in the synthesis the formation of the more thermodynamically stable AFI phase is heavily promoted. The three remaining phase-pure systems (SAPO-37(0.21), SAPO-37(0.42) and SAPO-37(0.63)) showed consistent powder-XRD patterns with similar levels of intensity confirming both the crystallinity and phase-

purity of the materials (Figure 3.25). After Reitveld analysis of the three systems it was found that the unit cell parameters of the three systems systematically increased with increased silicon-content. This finding is consistent with previous observations as the incorporation of heteroatoms into an AlPO framework distorts the local environment of the structure around the dopant.[85] This effect is particularly pronounced when creating Brønsted acid sites. The framework-bound charge-balancing proton is known to create a heavily-distorted tridentate oxygen ion, which provokes a significant expansion of the M-OH bond.[86] From this it can be inferred that increased levels of silicon incorporation would facilitate a more significant expansion of the average bond lengths in the unit cell, and therefore an overall increase in the unit cell parameter. The size and morphology of the particles of the three different systems were congruent. All samples exclusively exhibited uniform octahedral particles ranging from 0.5 – 1.0 µm in size and were free of any visible extra phases (Figures 3.26-3.28). Further, the surface area of the three samples confirmed their porous nature and are in good agreement with the literature values and each other.[87]

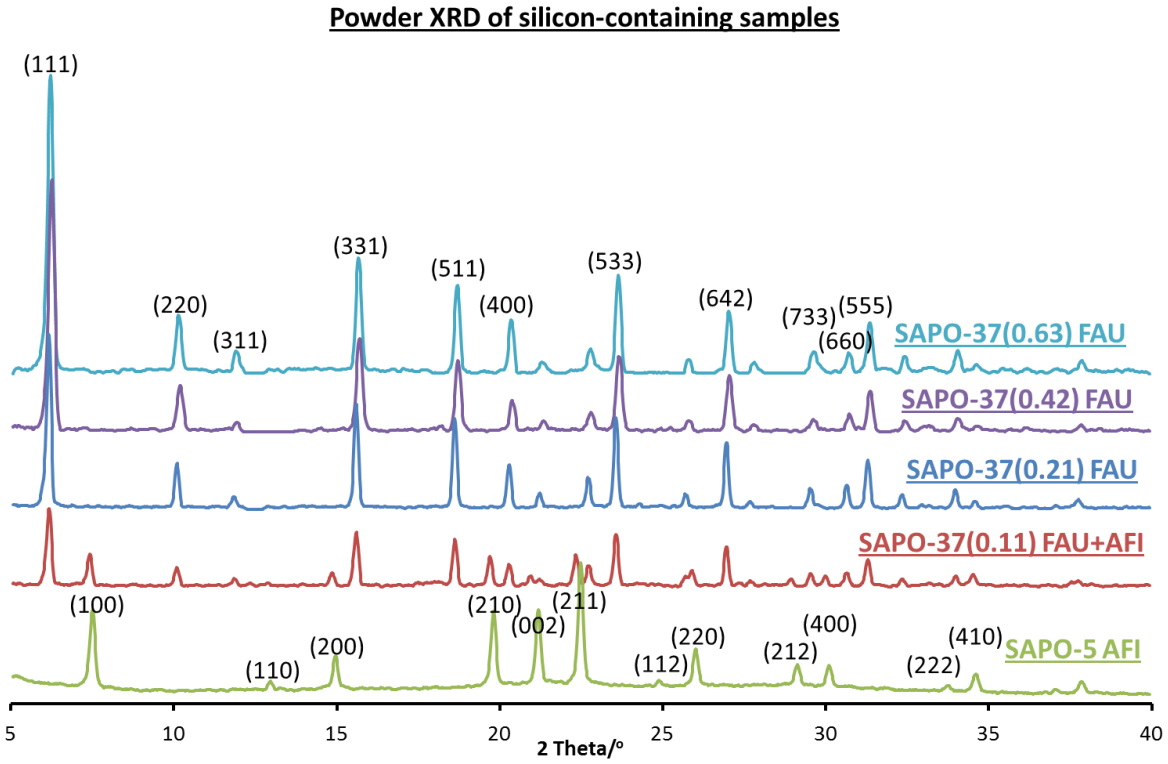

Figure 3.25: Powder XRD patterns of different SAPO-37 systems.

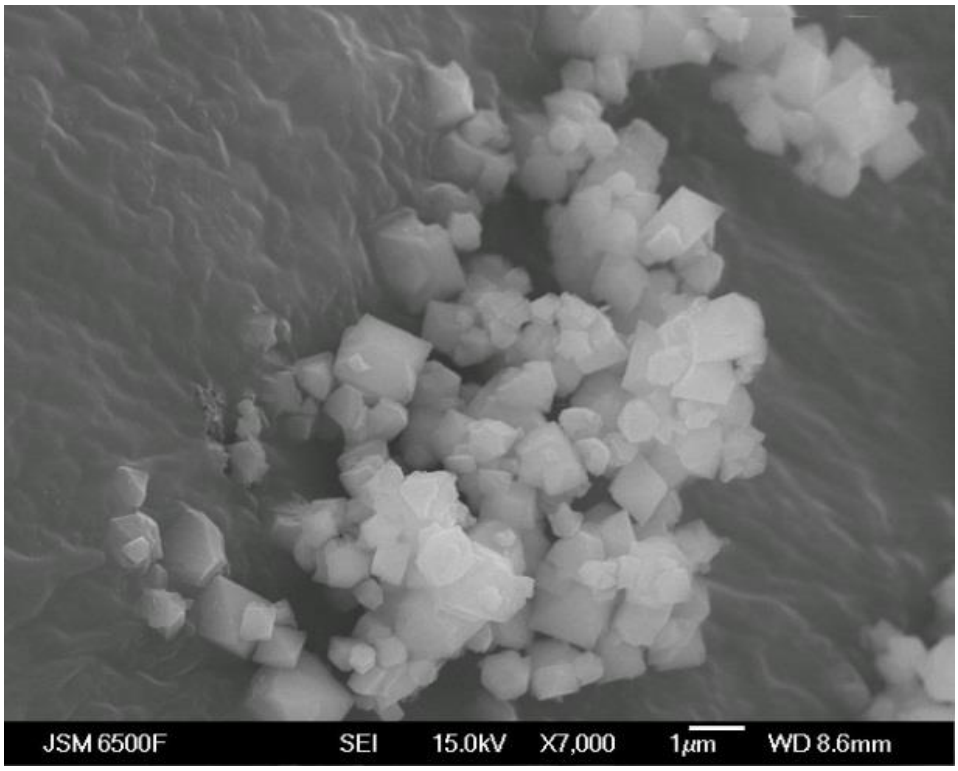

Figure 3.26: SEM image of SAPO-37(0.21).

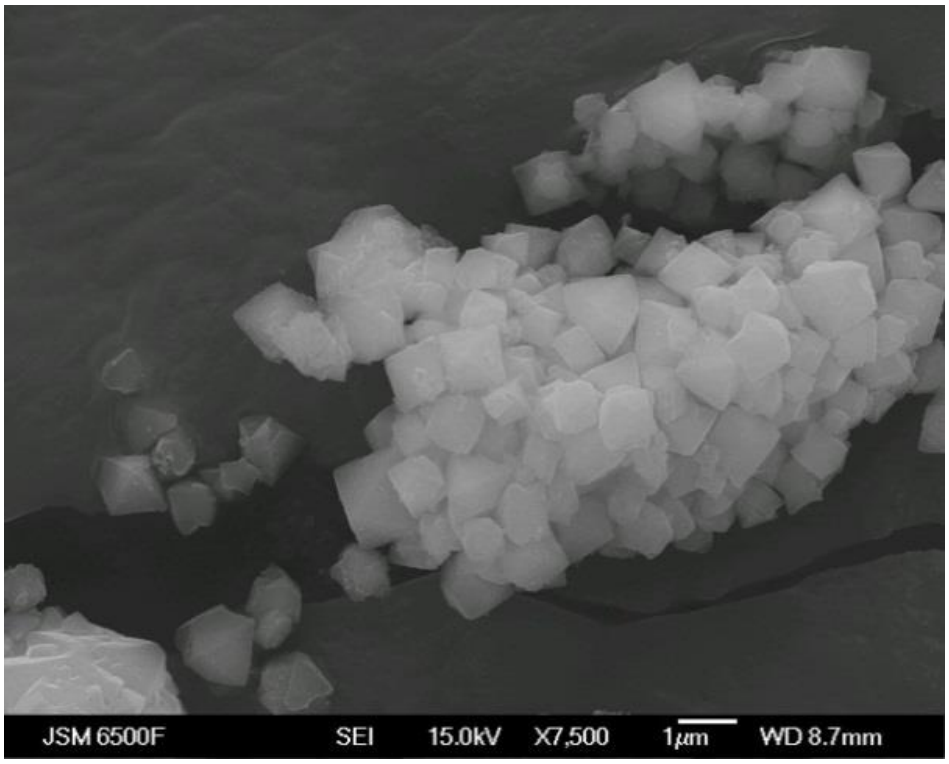

Figure 3.27: SEM image of SAPO-37(0.42)

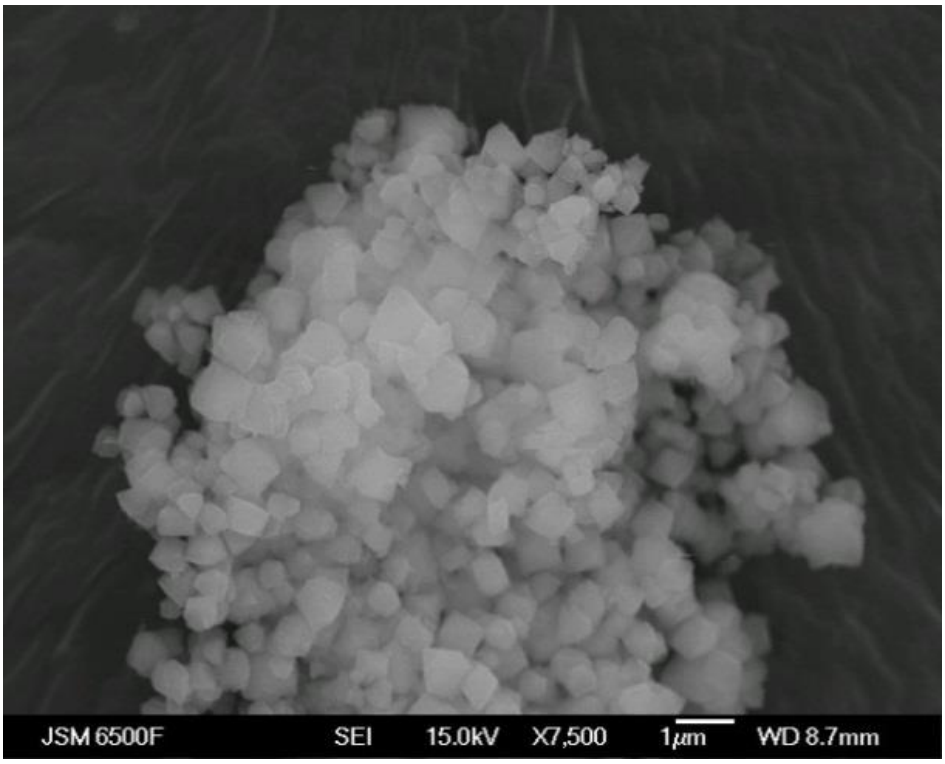

Figure 3.28: SEM image of SAPO-37(0.63)

Despite the physical similarities of the three samples, further use of MAS ^{29}Si NMR revealed the influence of varying the silicon loading had on incorporation mechanisms and the distribution of silicon environments in the SAPO-37 materials (Figures 3.29-3.31). In order to probe the individual type II and type III environments the experiments were performed under a constant flow of dry nitrogen to improve the signal quality. The benefits of this method are evident as the two individual environments are readily resolved and easily observable as individual peaks at -98.0 ppm and -93.4 ppm respectively. The previous NMR spectra collected under air (Figure 3.9) exclusively shows isolated framework incorporated sites with a single peak at -91 ppm. As a result these two peaks are labelled as -93.4 ppm being $Si(OAl)_4$ and -98.0 ppm as $Si(OAl)_3(OSi)$. It is clear that there has been a shift in peak position, this is attributed to the anhydrous nature of the experiment preventing water adsorption on the silicon sites of the material, thus shifting the peak position. By comparing the intensities of the two peaks we conclude that increasing the silica-gel ratio facilitated an increase in silicon-clustering and reduced the proportion of well-isolated silicon sites. This is demonstrated through the prominent increase in the intensity of the -98.0 ppm signal, attributed to the $Si(OAl)_3(OSi)$ signal in calcined SAPO-37,[88] relative to the -93.4 ppm signal. This

finding represents an increasing quantity of silicon isomorphously substituted into the nanoporous framework through type III substitution (forming of Si-O-Si bonds) at the expense of single well-isolated silicon sites. Further evidence for increased silicon clustering can be seen through resolving the spectra and reveals other signals at -101.0, -104.0 and -108.0 ppm in the SAPO-37(0.42) and SAPO-37(0.63) spectra, which correspond to $Si(OSi)_2(OAl)_2$, $Si(OSi)_3(OAl)$ and $Si(OSi)_4$ species respectively in both the 1D and 2D NMR spectra,[58] indicative of silicon clusters forming. These findings conclude that increasing the silicon content forces a reduction in site-isolation while subsequently promoting the formation of silicon clusters. Through further analysis of the 1D NMR it is also apparent that lower silicon loadings are necessary to construct a material in which the silicon exclusively occupies a $Si(OAl)_4$ environment, thus achieving consummate site-isolation. Despite the difference in ^{29}Si NMR, both the ^{27}Al and ^{31}P NMR signals were in excellent agreement showing predominantly $Al(OP)_4$ and $P(OAl)_4$ exclusively (Figures 3.32 and 3.33).

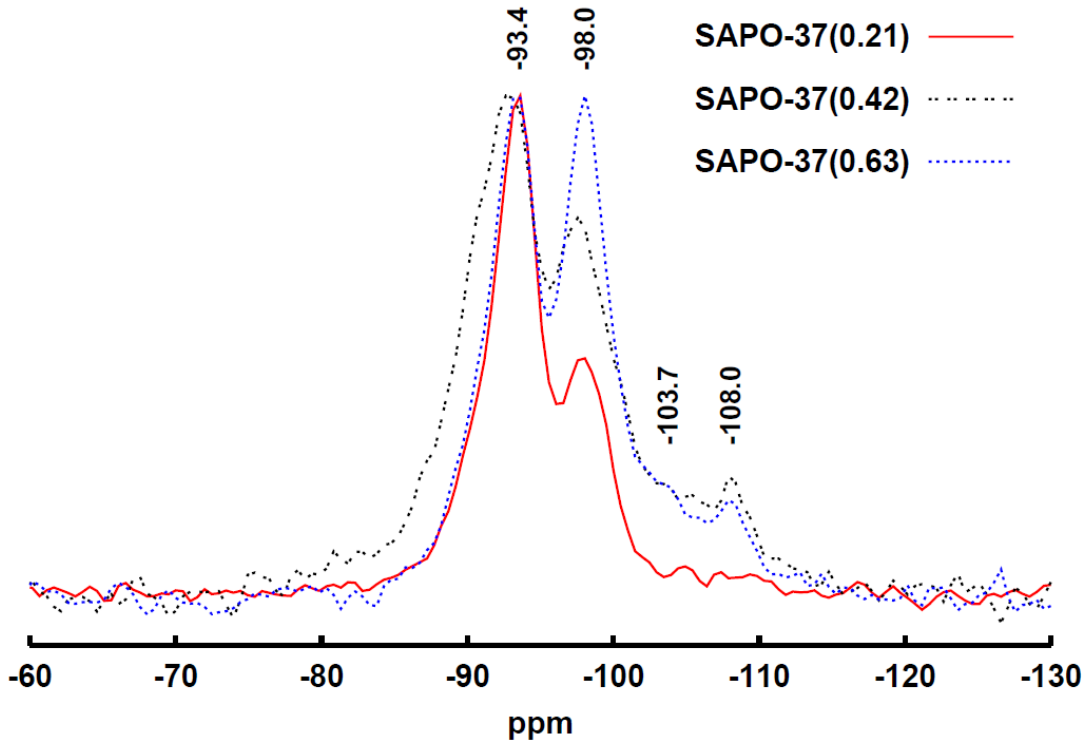

Figure 3.29: Comparison of CP ^{29}Si MAS NMR spectrum for SAPO-37 samples.

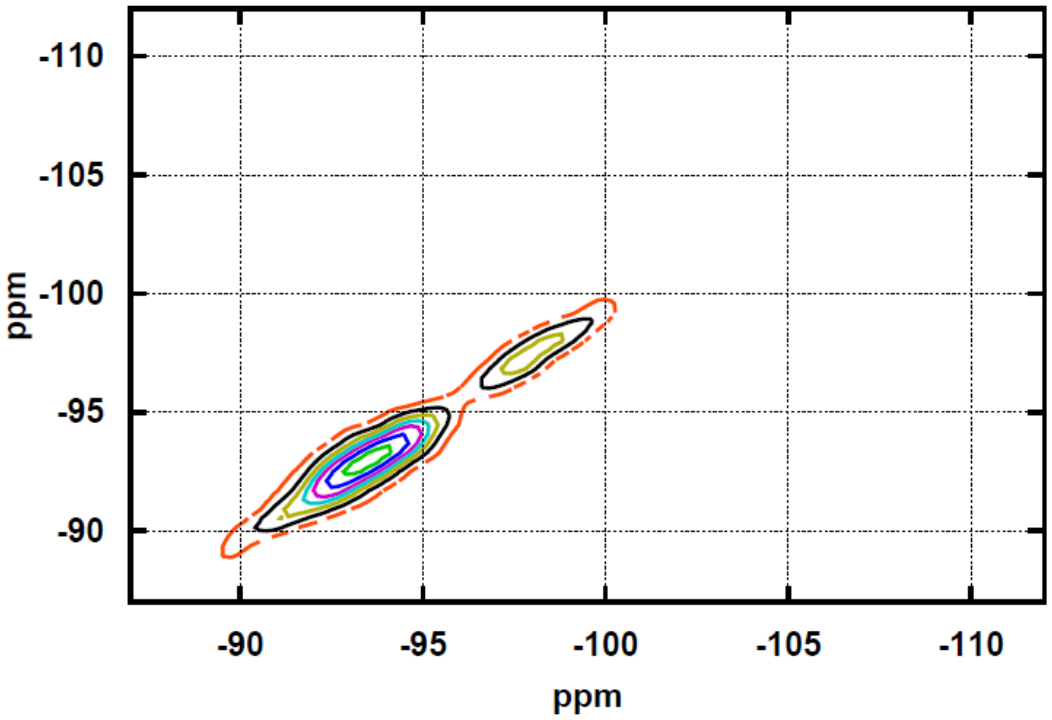

Figure 3.30: 2D CP ^{29}Si MAS NMR spectrum of SAPO-37(0.21).

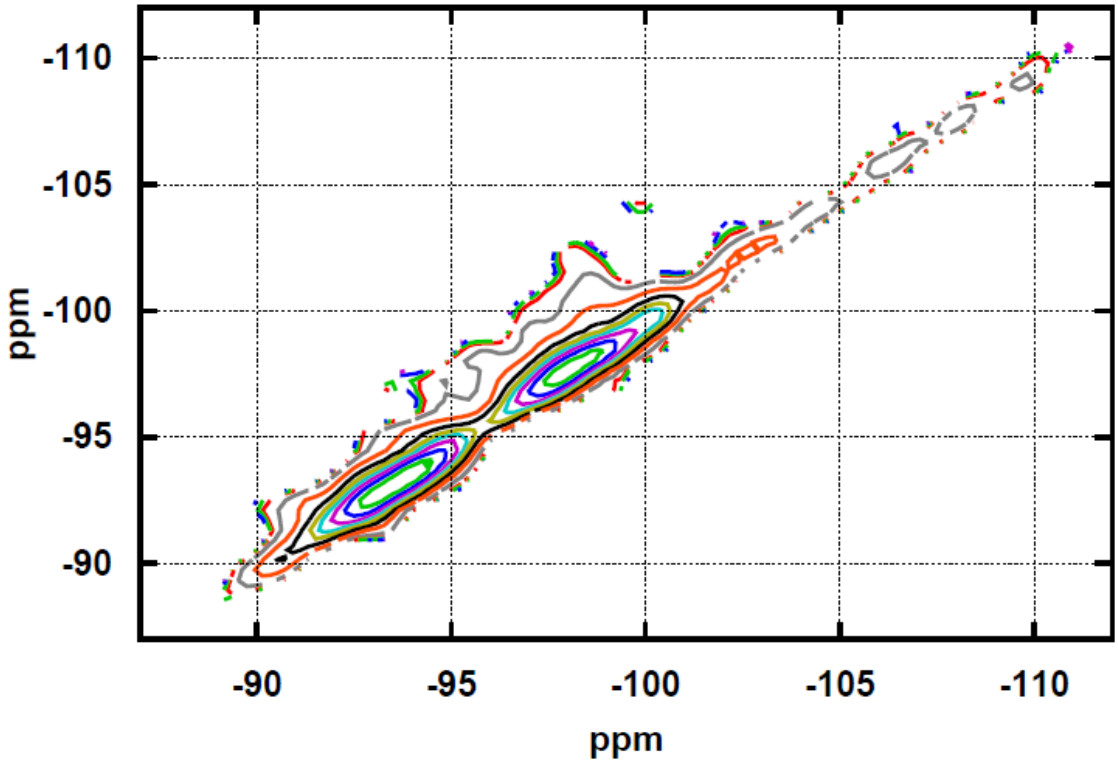

Figure 3.31: 2D CP ^{29}Si MAS NMR spectrum of SAPO-37(0.63)

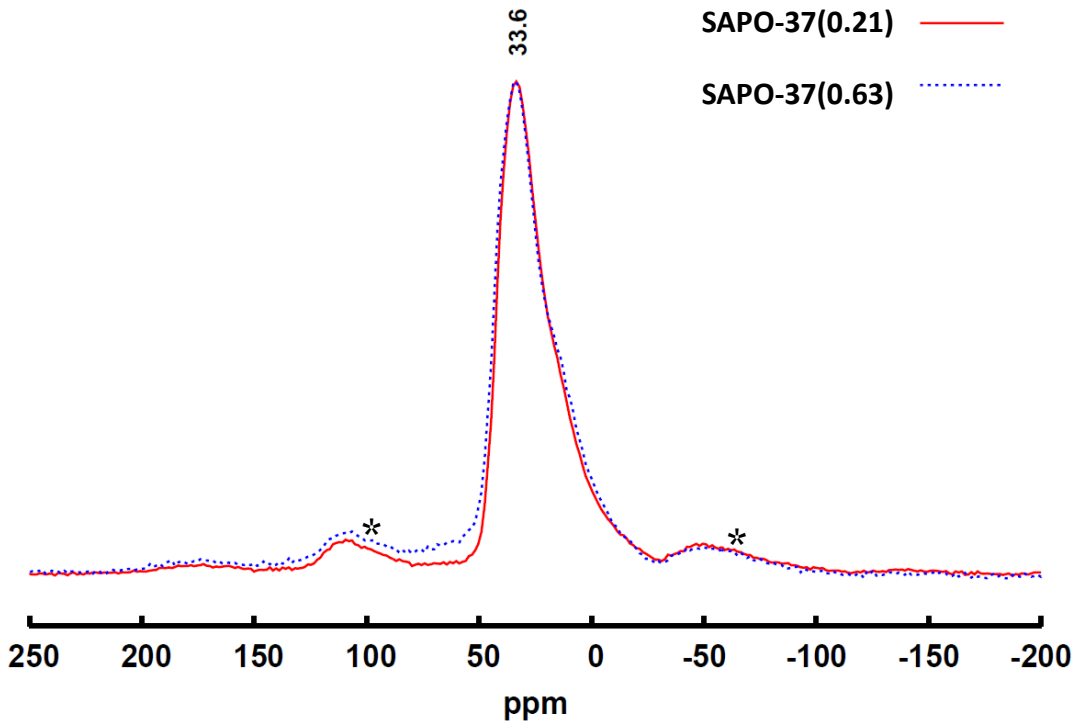

Figure 3.32: 1D ^{27}Al MAS NMR spectra comparing SAPO-37(0.21) and SAPO-37(0.63), * mark the peaks due to spinning side-bands.

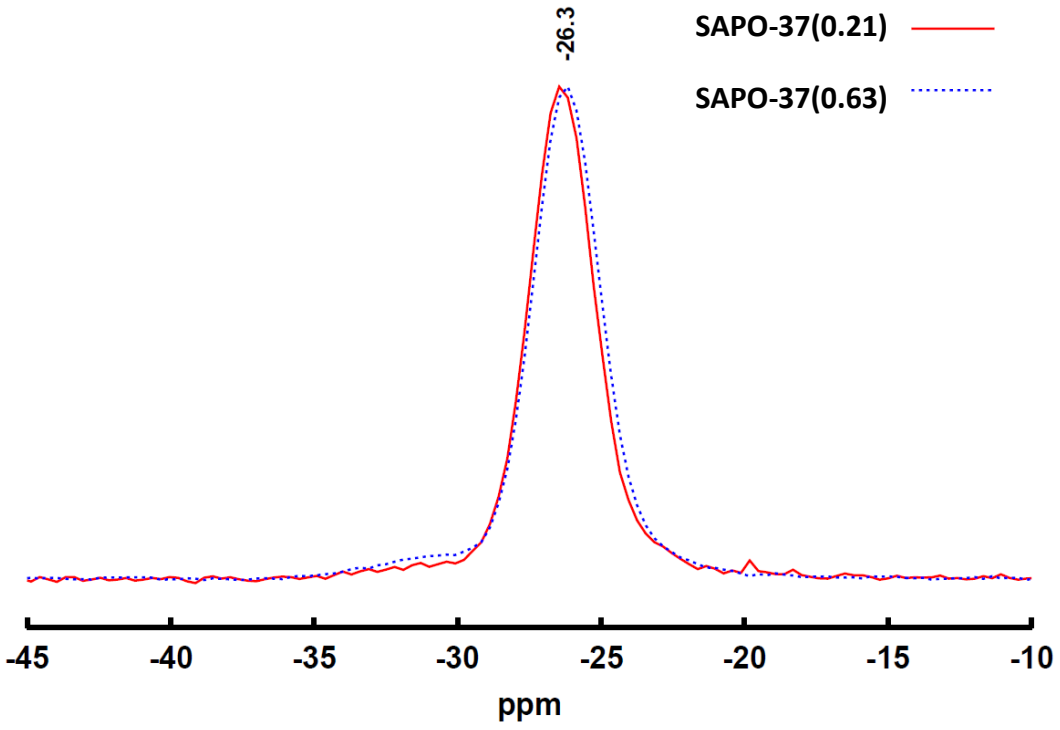

Figure 3.33: 1D ^{31}P MAS NMR spectra comparing SAPO-37(0.21) and SAPO-37(0.63).

While the NMR findings provide fundamental information on the location of the silicon species, TPD and FT-IR techniques are expedient for probing both the acid strength and the total acidity of the different systems. TPD experiments provide compelling evidence that increased silicon content reduces the total acidity as it was found that while SAPO-37(0.21) and SAPO-37(0.42) possess similar numbers of acid sites (0.927 and 0.873 mmol/g respectively) which is consistent with similar SAPO materials.[89,90] In contrast the higher loading SAPO-37(0.63) system had significantly less acid sites (0.765 mmol/g, Figure 3.34) Analysis of the individual peak shapes and areas yields further information on the strength of the acid sites present. The observed increase in the areas for both the 200-300 °C and 300-400 °C sections suggests that lowering the silicon loading increases the quantity of weaker acid sites. Conversely increasing the silicon loading was found to increase the number of strong acid sites as the 400-500 °C area was found to increase with the silicon loading. While the exact areas for these sections are dependent on a great many factors, it is clear from figure 3.34 that a significant relationship between peak shapes (for higher temperatures, thus stronger acid sites) exists within the three SAPO-37 species. These observations reinforce the NMR findings above as type III substitution does not lead to the exact formation of isolated weak acid sites. Therefore it would be expected that increased type III substitution would result in lower acidity, as observed. Furthermore, it is known that silicon islanding can produce strong acid sites on the periphery of such zones.[45] Therefore increased silicon clustering (as seen by the appearance of -103 and -108 ppm signals) would be accompanied by the presence of stronger acid sites, as witnessed in the TPD.

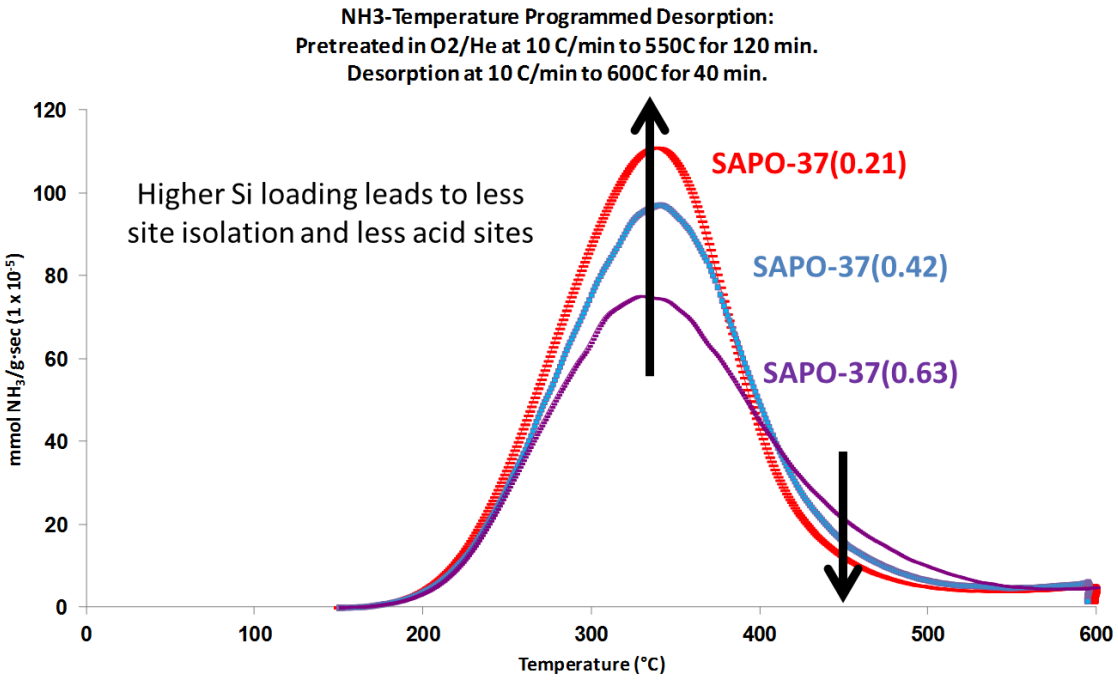

	Integration Results/(mmol/g)					Total
System	150-200°C	200-300°C	300-400°C	400-500°C	500-600°C	mmol/g
SAPO-37(0.21)	0.004	0.233 ↑	0.563 ↑	0.094 ↓	0.033	0.927 ↑
SAPO-37(0.42)	0.004	0.206	0.503	0.122	0.039	0.873
SAPO-37(0.63)	0.003	0.182	0.406	0.139	0.035	0.765

Figure 3.34: NH_3-TPD analysis of SAPO-37 samples with varying silicon loadings.

The TPD values obtained for the SAPO-37(0.21) correlate well with the expected values based on NMR and ICP findings (0.98 mmol/g), this can be calculated thus:

Initially it is assumed that in low-silicon environments only one of two sites produce acid sites (Figures 3.35 and 3.36). Further we assume that the peak at -93 ppm accurately quantifies the number of $Si(OAl)_4$ species, whilst the peak at -98 ppm accurately quantifies the number of $Si(OAl)_3(OSi)$ species which comes from the periphery of small silicon islands, constituting 4 $Si(OAl)_3(OSi)$ species and one $Si(OSi)_4$ species, which is attributed to the peak at -108 ppm.

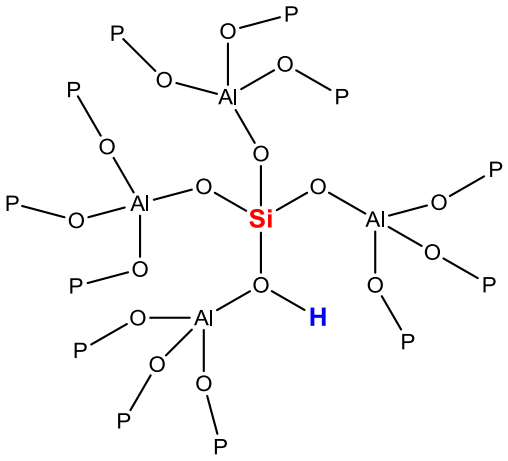

Figure 3.35: Detailing the isolated acid site at -93 ppm. Red silicon atoms represent silicons incorporated through a type II mechanism, blue protons are the generated acid sites. From this we see that one silicon at -93 ppm forms one acid site.

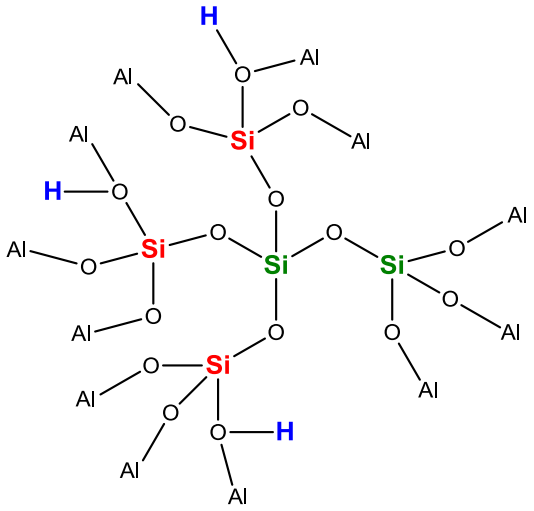

Figure 3.36: Detailing the 5-silicon islands. The central silicon atom is the $Si(OSi)_4$ peak at -108 ppm. The green silicon atoms are incorporated through type III substitution, therefore do not generate a proton. The red silicon atoms are incorporated through type II substitution and generate acid sites.

From this we see that five silicons form three acid sites. Therefore for every 4 silicons at -98 ppm we expect three acid sites, thus each silicon at -98 ppm is responsible for ¾ of an acid site. The ICP shows that SAPO-37(0.21) contains 2.95 wt% of Si (Table 3.4). The ^{29}Si NMR of SAPO-37(0.21) gives the following distribution:

Table 3.11: Calculation of the number of acid sites in SAPO-37(0.21)

Observable peaks/ppm	Relative area	Moles of silicon per gram of SAPO-37(0.21) / mmol g^{-1}
-93	0.71	0.748
-98	0.29	0.305

From figures 3.35 and 3.36 it is known one mole of silicon from the peak at -93 ppm forms one acid site. One mole of silicon from the peak at -98 ppm forms 0.75 moles of an acid site. Therefore the total moles of acid are:

$$(0.748 \times 1) + (0.305 \times 0.75) = 0.977\ mmol\ g^{-1} \qquad (3.5)$$

This agrees well with the NH_3-TPD value of 0.927 mmol g^{-1} from figure 3.34.

This calculation has not been attempted for the SAPO-37(0.42) and SAPO-37(0.63) as it is believed that the significant amount of clustering will mean there are a greater variety of silicon islands than those assumed, as such the calculation will be inaccurate and non-representative.

These findings are also consistent with the FT-IR analysis (figure 3.37). Analysis of the hydroxyl region (3800 – 3400 cm^{-1}) reveals two separate bands at 3641 and 3575 cm^{-1} representing accessible hydroxyl groups in the supercage and inaccessible hydroxyl groups in the sodalite cages of the faujasitic framework respectively (Figure 3.37). The SAPO-37 system matches the data from its zeolite analogue in this respect as zeolite-Y shows a 1:1 ratio of these two bands, owing to the energetic infeasibility of two of the oxygen atoms in the supercage. Comparing the intensity of the 3641 cm^{-1} band in the three different samples confirms that the SAPO-37(0.21) and SAPO-37(0.42) possess similar quantities of acid sites while the SAPO-37(0.63) contains dramatically fewer acid sites (Figures 3.38-3.40, Table 3.12). Low temperature CO adsorption confirmed the identification of the two bands, as the 3575 cm^{-1} remained unchanged but the intensity of the 3641 cm^{-1} band dropped dramatically as a new band appeared in the 3330 cm^{-1} region, indicative of hydroxyl-groups interacting with the CO probe. The new band at 3330 cm^{-1} is visibly broader than that at 3641 cm^{-1} as expected given the different hydrogen

bonding possible between the CO probe and the OH site. It is also noted on closer inspection that the band at 3330 cm^{-1} is subtly distorted with a shoulder at 3450 cm^{-1}, this is attributed to the CO binding to available P-OH bonds and also to the migration of a small proportion of protons from the sodalite cages. The magnitude of the shift of the supercage hydroxyl band due to CO adsorption can be directly linked to the average acid-strength of the material, which is also found to increase as the silicon loading increases in agreement with the TPD data (Figure 3.34, Table 3.12). By employing CO as a probe it is possible to gain information on the total number of acid sites by analysing the area of the C-O stretching band in the 2180-2160 cm^{-1} region. This supported the TPD findings that the total acidity of SAPO-37(0.21) and SAPO-37(0.42) were similar, while SAPO-37(0.63) possessed far fewer acid sites. It has previously been shown that a direct link exists between the shift of the OH band on adsorption of CO and the proton affinity, which for the SAPO-37(0.21), SAPO-37(0.42) and SAPO-37(0.63) systems was calculated as per ref 91 as being 1155, 1152 and 1146 kJ mol^{-1} respectively, this is again in good agreement with values previously obtained for the SAPO-5 and SAPO-34 systems (1172 kJ mol^{-1} and 1168 kJ mol^{-1} respectively).[91]

Table 3.12: Summary of FT-IR data on SAPO-37 samples using a CO probe.

Sample	Bridging OH band position/cm^{-1}			CO Area (AU)
	Before CO	After CO	Shift	(0.18 cc add)
SAPO-37(0.21)	3646.8	3342.1	305	0.854
SAPO-37(0.42)	3646.7	3335.4	311	0.856
SAPO-37(0.63)	3646.1	3325.0	321	0.582

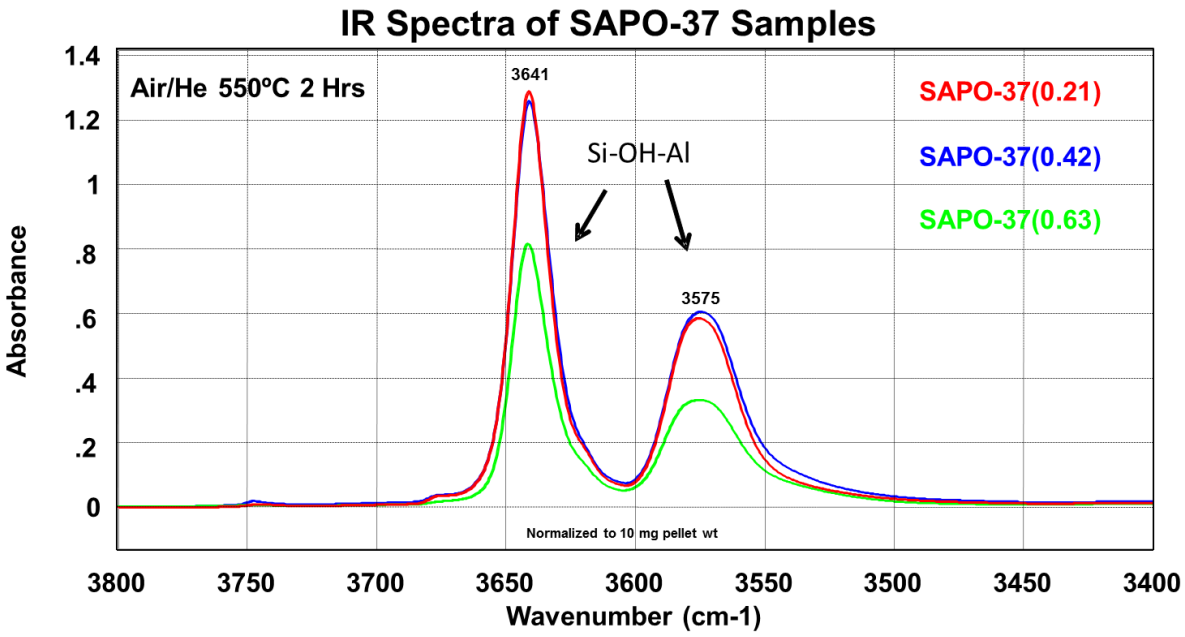

Figure 3.37: FT-IR spectra of the hydroxyl region of various SAPO-37 systems.

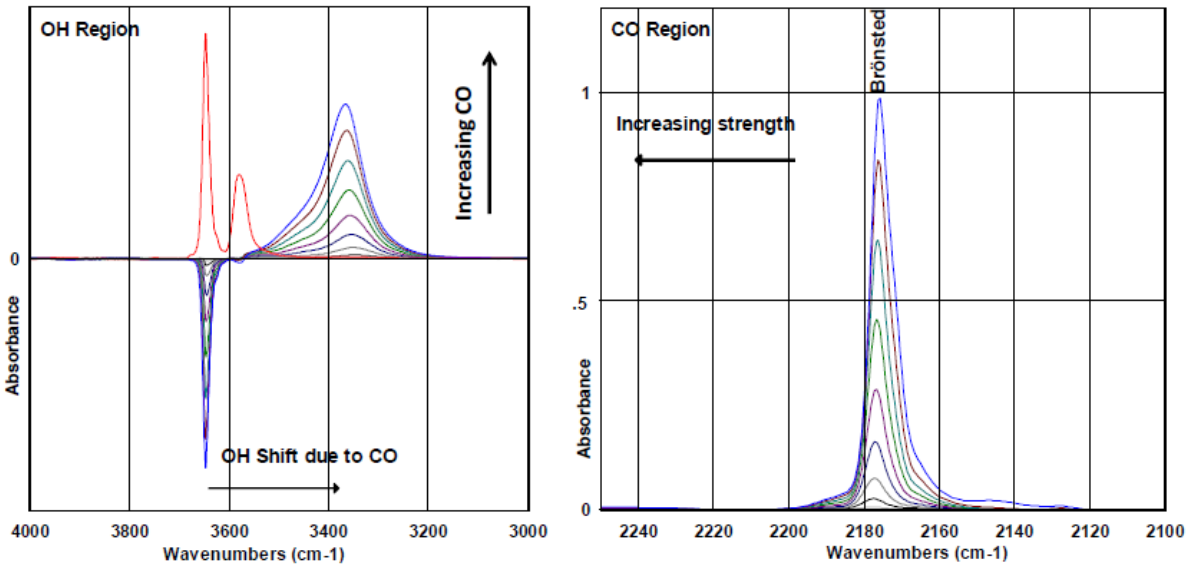

Figure 3.38: Difference FT-IR spectra of SAPO-37(0.21) with varying CO loadings.

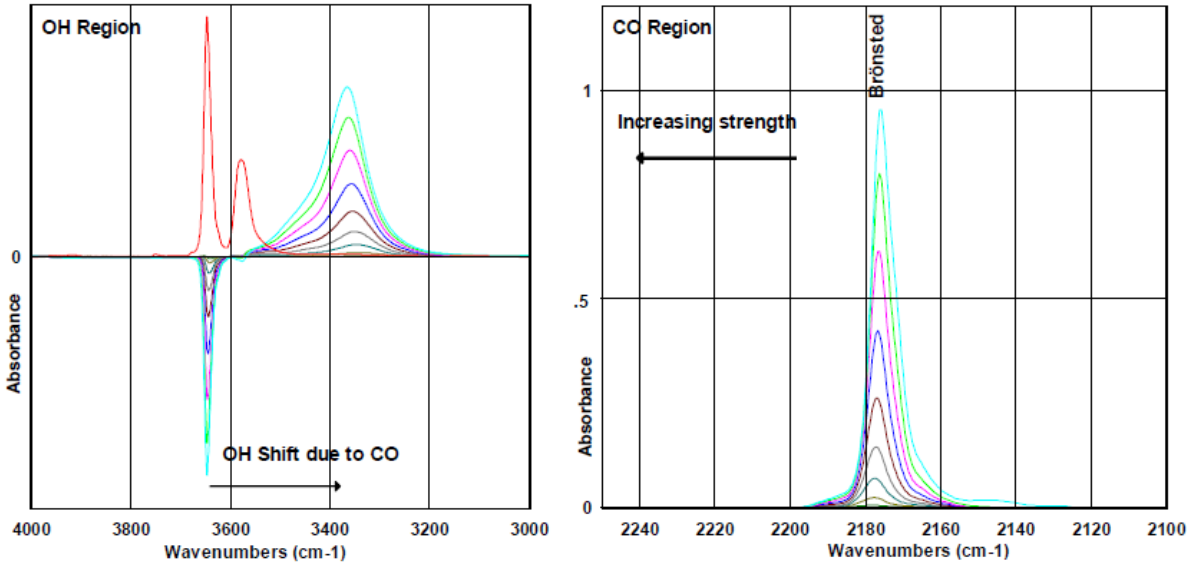

Figure 3.39: Difference FT-IR spectra of SAPO-37(0.42) with varying CO loadings.

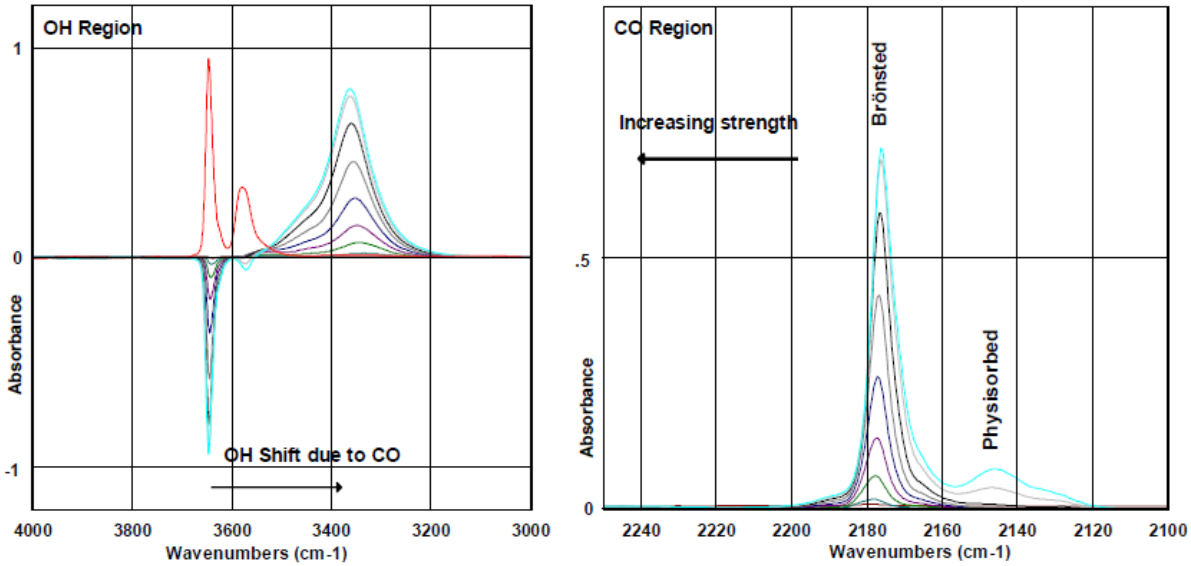

Figure 3.40: Difference FT-IR spectra of SAPO-37(0.63) with varying CO loadings.

Finally collidine was used as a probe to further evaluate the acid strength of the three SAPO-37 samples (Figures 3.41-3.43 and Table 3.13). By quantifying the areas of the 1652 and 1637 cm^{-1} bands after a series of desorption temperatures one can observe the strength of O-H···N interactions and label them as weak or strong in a similar process to TPD (Figure 3.43). This data

further substantiated the claim that lower silicon content facilitates the formation of increased quantities of acid sites from which collidine desorbs by 300°C. These are designated as weak acid sites, which again correlates well with observations from the other techniques. This behaviour is commonly attributed to the need to have an acid site which is sufficiently strong to form the caprolactam, yet weak enough to release the caprolactam afterwards. Too weak an acid site hinders the formation of the product, while too strong a site will block active sites for further reaction cycles and promote the formation of by-products. Further analysis of the collidine data reveals further insight into the nature and the location of some active species. On inspection the degree of attenuation of the hydroxyl band does not follow the silicon content trend, instead it follows SAPO-37(0.63) > SAPO-37(0.21) > SAPO-37(0.42), with only the former achieving complete attenuation. This behaviour contrasts the CO adsorption where complete attenuation was achieved in all samples, as such any differences observed are attributable to the differences between the two probes. The complete attenuation of SAPO-37(0.63) sample is a result of the significantly lower acid site density, thus the acid sites are not blocked by neighbouring collidine molecules. In contrast the acid sites appear less accessible in the SAPO-37(0.42) sample, this is believed to be the combined effect of a higher acid site density and also due to the presence of stronger acid sites around the mouth of the faujasitic pores, thereby blocking the passage for other molecules. Through the stringent use of a variety of characterisation techniques we believe we have conclusively shown that the three samples are crystalline and free of secondary phases, and that while the three samples possess equivalent physical characteristics, the increased silicon content facilitates a reduction in site-isolation through increased type III substitution and silicon zoning, which results in fewer, stronger acid sites. Only by adroitly reducing the silicon content can one enhance the number of sites created through type II substitution, thereby generating the desired well-isolated weak acid sites.

Table 3.13: Summary of FT-IR data using collidene as a probe on SAPO-37 samples.

Sample	Weak sites[a] (au/mg)	Medium sites[b] (au/mg)
SAPO-37(0.21)	0.913	2.845
SAPO-37(0.42)	0.389	2.722
SAPO-37(0.63)	0.382	2.420

a) Collidine band area after 150°C – 300°C desorption b) Collidine band area after 300°C – 450°C desorption.

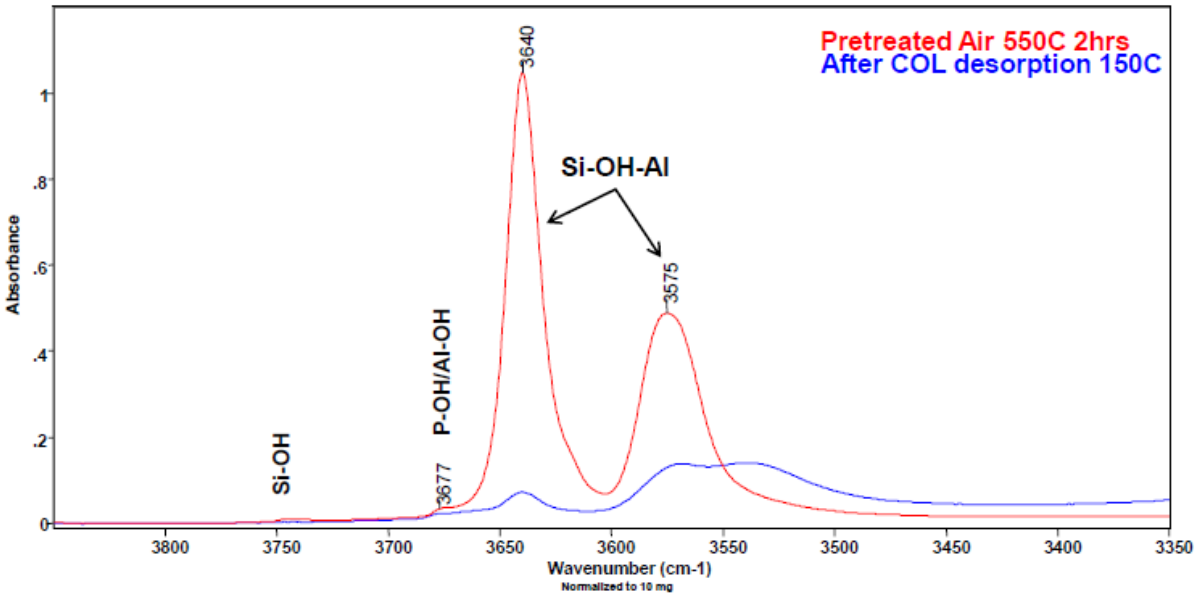

Figure 3.41: FT-IR spectra of SAPO-37(0.21) using collidene as a probe.

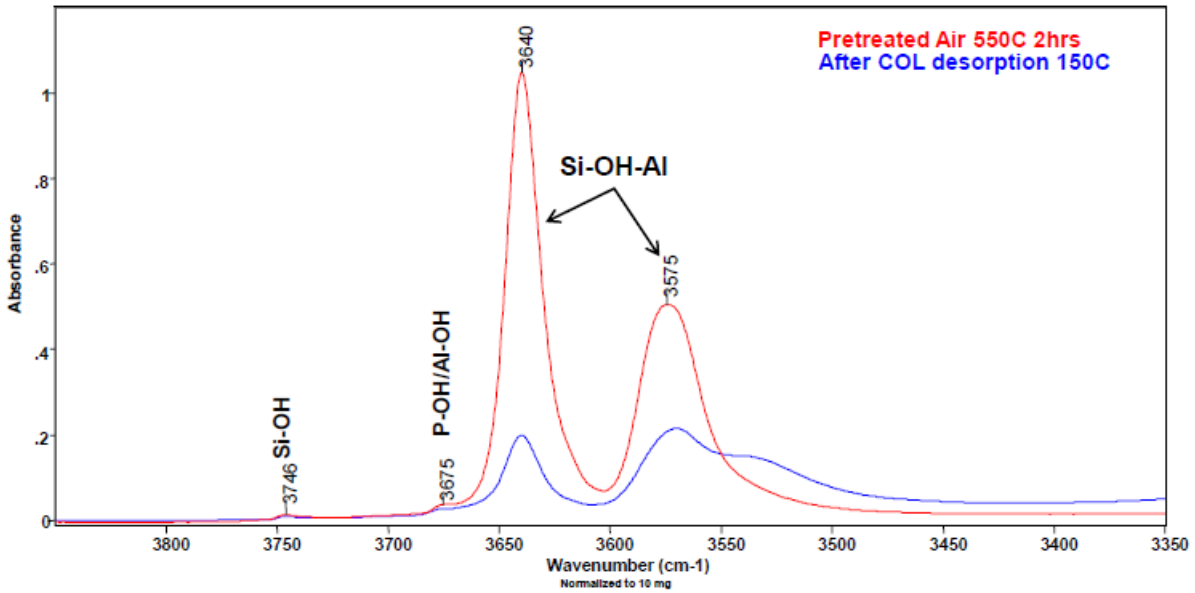

Figure 3.42: FT-IR spectra of SAPO-37(0.42) using collidene as a probe.

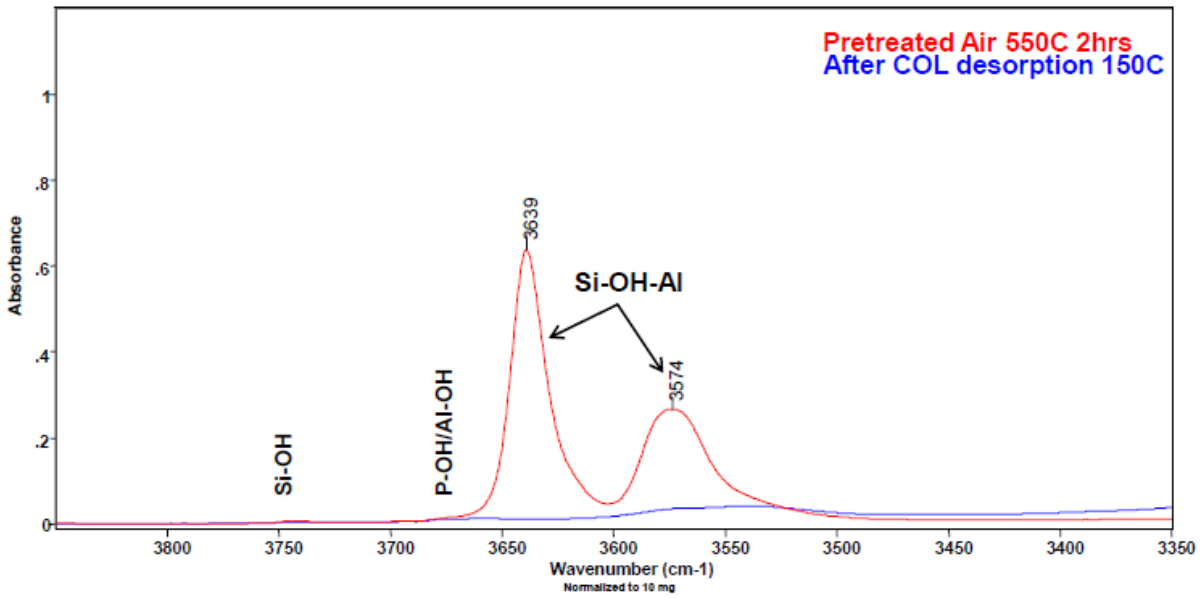

Figure 3.43: FT-IR spectra of SAPO-37(0.63) using collidene as a probe

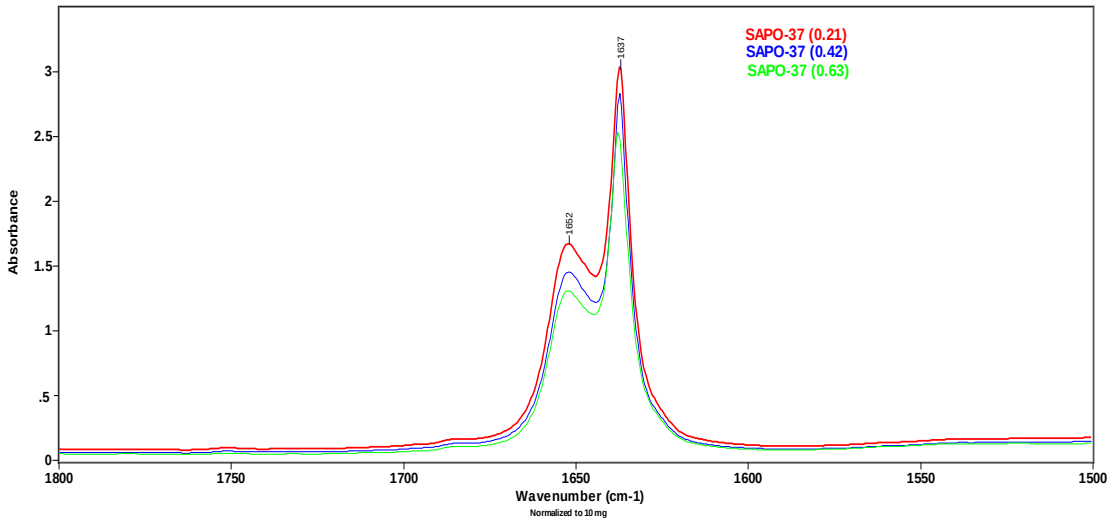

Figure 3.44: Difference FT-IR spectra of various SAPO-37 samples after collidene adsorption/desorption at 150°C.

The catalytic data emphasises the variations found in the acid sites of the three different SAPO-37 samples (Table 3.14). The most striking trend is the effect of silicon loading on the specificity for the ε-caprolactam product. It is evident over a range of temperatures that the lower-loading SAPO-37(0.21) sample consistently displays an improved selectivity for ε-caprolactam over the SAPO-37(0.42) species despite both systems containing a similar number of acid sites. This effect is attributed to the increased presence of stronger acid sites in the SAPO-37(0.42) sample, as observed through TPD and FT-IR spectroscopy. This represents a deviation away from the formation of the targeted isolated weak-acid sites by promoting alternate reaction pathways to form high-boiling by-products. This trend extends to the SAPO-37(0.63) system which possesses the greatest number of strong acid sites (and average acid strength) and consistently exhibits the lowest selectivity over the whole range of temperatures examined. From this we confirm that the presence of strong acid sites from silicon clustering is responsible for the formation of the unwanted by-products. Another notable trend is that while all systems reach complete conversion, the lower loading SAPO-37(0.21) also appears more active than the other two systems, in most cases showing either comparable or superior conversions at identical times and temperatures to the other two systems. It has previously been established that the isolated silicon sites enhance the activity, and further that the stronger acid sites promote the formation of by-products. It can then be rationally inferred that the weaker acid sites, formed

by type II substitution favour the formation of the ε-caprolactam product. By combining the information from the FT-IR and TPD techniques we also propose that the increased number of weak acid sites that the SAPO-37(0.21) system possesses, enhances the rate of ε-caprolactam production. Again, it is important to note that these trends are not based on total acidity but on the individual number of weak and strong acid sites, as evidenced by the SAPO-37(0.21) and SAPO-37(0.42) systems, which despite possessing equivalent numbers of acid sites display conflicting behaviour. This behaviour is also consistent with the collidine FT-IR findings, in which the acid sites of the SAPO-37(0.42) species were shown to be less accessible than the SAPO-37(0.21), further explaining the enhanced activity of the SAPO-37(0.21) system.

Table 3.14: Summary of catalytic results for the low-temperature Beckmann rearrangement of cyclohexanone oxime to ε-caprolactam

Temp/°C	System	Time/mins	Conversion/mol%	ε-caprolactam selectivity/mol%[a]
130	SAPO-37(0.21)	180	89.3	96.0
		420	98.9	93.5
	SAPO-37(0.42)	180	89.8	93.3
		420	98.8	90.3
	SAPO-37(0.63)	180	90.4	90.9
		420	99.8	88.4
150	SAPO-37(0.21)	90	98.7	93.7
		240	100.0	90.8
	SAPO-37(0.42)	90	95.2	91.1
		240	99.9	88.7
	SAPO-37(0.63)	90	92.1	85.0
		240	99.7	84.1

170	SAPO-37(0.21)	40	98.6	90.4
		60	99.8	90.1
	SAPO-37(0.42)	40	95.5	88.8
		60	98.9	89.9
	SAPO-37(0.63)	40	93.5	82.3
		60	97.6	83.9
190	SAPO-37(0.21)	40	99.5	90.1
		60	99.9	89.8
	SAPO-37(0.42)	40	99.7	86.2
		60	100.0	85.4
	SAPO-37(0.63)	40	98.7	78.9
		60	99.7	79.5

Conditions: Catalyst:Cyclohexanone oxime:Benzonitrile ratio 1:1:200, 0.1 g of cyclohexanone oxime. a) Other products include cyclohexanone and products arising from solvent-oxime interactions.

The three SAPO-37 systems display consistent behaviour on variation of temperature, with each catalyst showing increased activity and reduced selectivity with increasing temperature. The enhanced rate of reaction is attributed to the improved rate of diffusion of the oxime molecule to, and through, the SAPO-37 catalyst. This facilitated more interactions between the available acid sites and the reactant thereby enhancing the reaction rate. Furthermore an increased temperature will bestow a greater energy to the reactant molecules, such that they have sufficient energy to overcome the activation energy of the system. The reduction in selectivity is also attributed to an increased diffusion rate and the promotion of more energetically demanding pathways, thereby enhancing the rate of by-product formation. It is noted that the variation in temperature has little effect on the rate of reaction

above 170 °C, however such behaviour is not the result of the system being mass-transfer limited, given the linear behaviour of the rate constants and the activation energies calculated. Kinetic analysis was performed for each catalyst, revealing that the production of ε-caprolactam was a first-order process (within experimental limits) as expected, this finding is in agreement with the postulated catalytic mechanism for the Beckmann rearrangement which shows that the 1,2-hydride shift from the N to OH group is the rate determining step for the reaction, similar to that in the vapour phase. This analysis also yielded rate constants for each system at the four different temperatures examined. Further calculation, through manipulation of the Arrenhius equation, confirmed the lower silicon loading systems, with greater quantities of weak acid sites, facilitated the faster rate of reactions and overcame the lower activation energies (Figure 3.45, Table 3.15). The value obtained for SAPO-37(0.21) of 50 kJ mol^{-1} is in good agreement with both theoretical and experimental work performed in the vapour-phase,[92] (Figure 3.23) further confirming that the reaction proceeds via a similar reaction pathway. It is further found that a linear trend exists between the silicon gel ratios and the calculated activation energies. This observation further affirms that it is explicitly the weak acid sites that lead to the production of ε-caprolactam for this process.

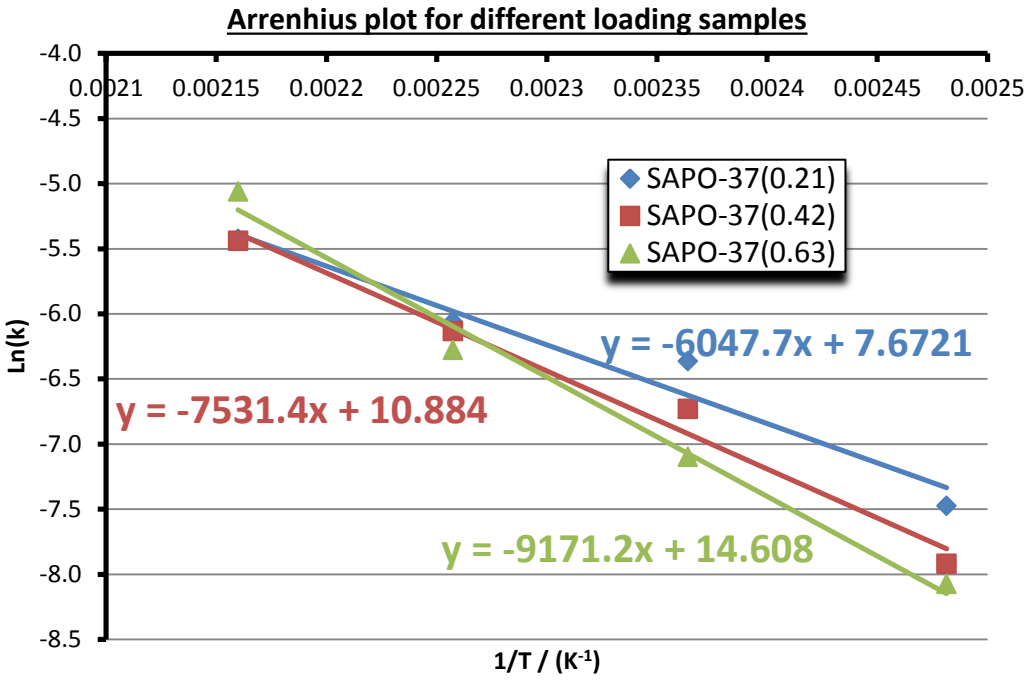

Figure 3.45: Arrenhius plot giving information on the activation energies of various SAPO-37 samples.

Table 3.15: Calculating of activation energy from the gradients obtained in Figure 3.45.

Sample	**$-E_a/R$**	**E_a/ kJ mol^{-1}**	**E_a/ kCal**
SAPO-37(0.21)	-6047.7	50.3	12.0
SAPO-37(0.42)	-7531.4	62.6	15.0
SAPO-37(0.63)	-9171.2	76.2	18.2

The presence of water is known to hinder the Beckmann rearrangement of cyclohexanone oxime through gradual deactivation of the active sites and by facilitating the production of the cyclohexanone by-product.[25] In view of this the reactivity of the system was contrasted with that of a comparatively 'water-free' system under inert conditions with anhydrous benzonitrile as a solvent (Table 3.16). The specificity for ε-caprolactam of both the SAPO-37(0.21) system at 130 °C and the higher-loading SAPO-37(0.63) at 190 °C were both

found to improve significantly, while improvements in conversion were also observed. It is noted that under the conditions below an almost quantitative yield of ε-caprolactam is obtained after 7 hours at 130 °C, using the SAPO-37(0.21) catalyst. To explore this result further a variety of anhydrous solvents were tested and compared but, only benzonitrile and chlorobenzene showed any significant reactivity (Figure 3.46). This effect is partially attributed to the combination of a polar-group protruding from a non-polar ring which provokes a high solvent boiling point (191 and 131 °C respectively) that maintains the solvent in the liquid-phase for the temperatures required for this system. We finally confirmed the heteroegenous nature of the catalyst through recyclability studies under optimised conditions; we showed that the catalytic activity of the material was retained on reactivation, thus confirming its reusability (Figure 3.47).

Table 3.16: Comparison of anhydrous and wet systems for the low temperature rearrangement of cyclohexanone oxime to ε-caprolactam.

Temp/°C	Sample	Time/mins	Conversion/mol%	ε-caprolactam selectivity/mol%[a]
130	SAPO-37(0.21) Anhydrous	120	82.5	99.0
		180	93.4	97.8
		420	99.8	97.8
	SAPO-37(0.21) Wet	120	78.1	96.1
		180	89.3	96.0
		420	98.9	93.5
190	SAPO-37(0.63) Anhydrous	20	92.1	94.7
		40	99.4	92.3
		60	99.9	91.6
	SAPO-37(0.63)	20	92.2	80.8

	Wet	40	98.7	78.9
		60	99.7	79.5

Conditions: Catalyst:Cyclohexanone oxime:Benzonitrile ratio 1:1:200, 0.1 g of cyclohexanone oxime. a) Other products include cyclohexanone and products arising from solvent-oxime interactions.

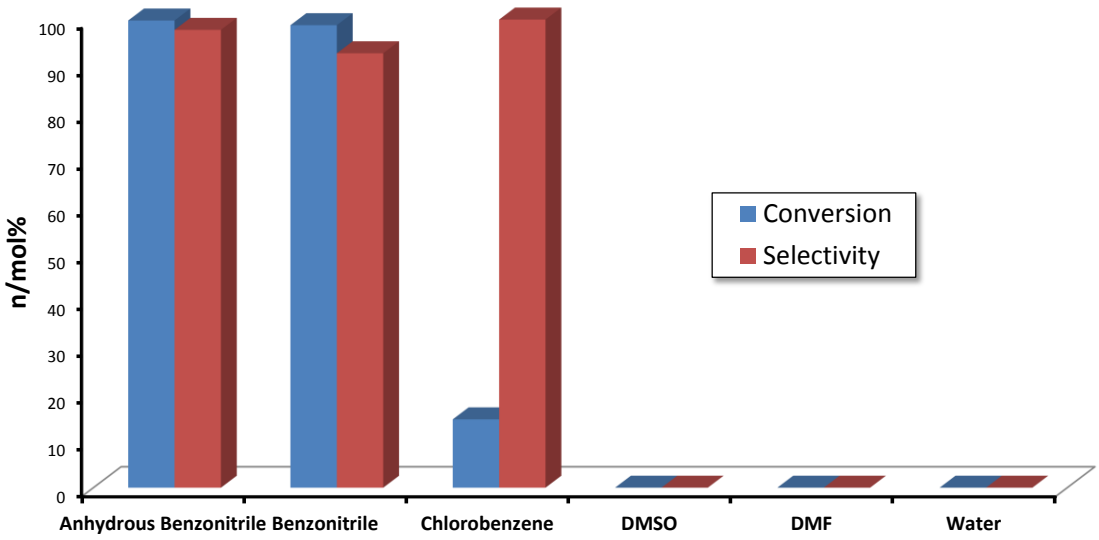

Figure 3.46: Contrasting the reactivity of SAPO-37(0.21) under a range of solvents.

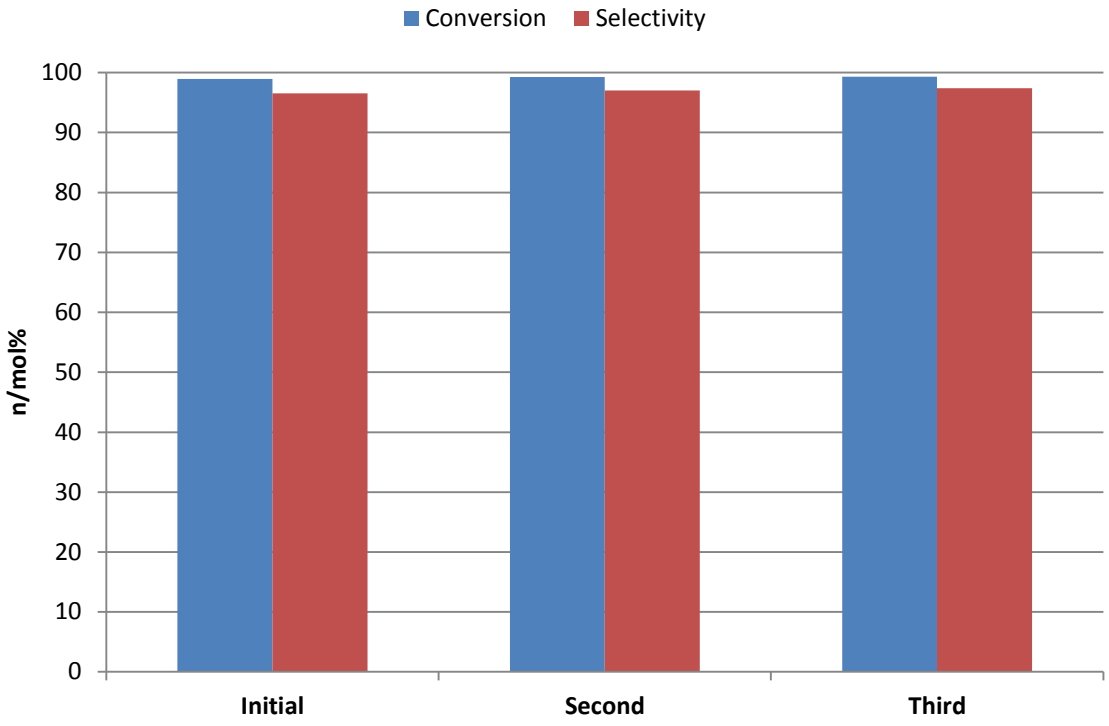

Figure 3.47: Plot detailing the recyclability of the SAPO-37(0.21) for the conversion of cyclohexanone oxime to ε-caprolactam at 130 °C under anhydrous conditions after reactivation cycles.

3.4 Conclusions

Given the commercial interest in an efficient process to form ε-caprolactam a range of SAPO-based materials were investigated for their suitability to this reaction. A multi-technique characterisation study was performed to assess the influence of the framework, the active site, and the complex relationship between the two.

SAPO-5, SAPO-34, SAPO-37 and SAPO-41 were chosen given their contrasting framework topologies. On confirming the integrity of the individual framework via a range of techniques (powder-XRD, BET etc.) the location of the specific active sites was probed by observing a range of NMR active nuclei. This revealed that a range of different silicon species were present among the four frameworks, with SAPO-34 and SAPO-37 primarily forming isolated silicon species through type II substitution, whereas SAPO-5 and SAPO-41 formed

silicon islands. The properties of the different acid sites were then investigated using a combined probe-based FT-IR and NH_3-TPD study. The latter study showed further similarities between the SAPO-5 and SAPO-41 species by revealing similar strength acid sites were present in significantly smaller quantities than the other SAPO species. Despite both frameworks possessing isolated silicon species, the acid sites in SAPO-34 and SAPO-37 were found to significantly different. With SAPO-34 possessing stronger acid sites than SAPO-37.

The accessibility of these systems was then assessed by the use of a collidine FT-IR probe. It was found that among the four systems only the faujasitic SAPO-37 framework could adsorb significant amounts of the bulkier probe, allowing it to diffuse through the pores. The combination of the larger-pored framework architecture and weaker acid sites meant that the SAPO-37 framework excelled at the Beckmann rearrangement in both the vapour-phase (300 °C) and in the liquid-phase (130 °C). As such the silicon loading of this system was varied to optimise the catalytic system.

It was concluded that by limiting the silicon content of this species the acid site could be controlled, by lowering the acid strength and maintaining site isolation to increase the total quantity of acid sites. This facilitated an enhancement in both catalytic activity, and the selectivity to ε-caprolactam, in the liquid-phase Beckmann rearrangement. After sufficient optimisation a near quantitative process was found (97.8% yield) to produce the coveted lactam monomer.

3.5 Experimental section

Synthesis details

SAPO materials were synthesised according to previous reported literature protocols, the details of which are outlined below:

SAPO-5 and -41 were hydrothermally synthesized by the method reported by Meriaudeau et al.[59] Aluminium source was added to the mixture of phosphoric acid and water that was then stirred for 4 h until homogeneous gel was achieved. After addition of the template (dipropylamine for SAPO-11 and triethylamine for SAPO-5) and the silica sol, the mixture was stirred for 2 h and transferred to a Teflon-lined steel autoclave and heated in the oven at 200˚C for 24 h. The autoclave contents were filtered, washed with deionized water, left drying at room temperature, followed by calcination at 600 ˚C for 40 h in air.

SAPO-34 synthesis involved initially adding 31.10 g of tetraethyl ammonium hydroxide (35 % in H_2O, Aldrich) to 15.10 g aluminium isopropoxide (Aldrich) and allowing the mixture to stir for 1.5 h. 0.66 g of fumed silica (Aldrich) was added to the above solution, which was stirred for a further 30 minutes. A homogeneous solution of 8.52 g of phosphoric acid (85 % in H_2O, Aldrich) in 12.2 mL of water was added to the above solution which was stirred for a further 2 h to obtain a gel with the composition 1.0Al:1.0P:0.15:Si:1.0TEAOH:50H_2O. The contents of the gel were sealed in 2 Teflon-lined stainless-steel autoclaves, which were then transferred to a pre-heated, fan-assisted oven (WF-30 Lenton) that was set to the desired temperature of 200 ˚C, prior to the onset of the crystallization. The autoclave was heated at 200 ˚C under autogeneous pressure for 60 h. The white solid product was collected by centrifuge, washed with approx. 100 mL deionised water, and dried in air (60 ˚C) overnight. The as-prepared sample was calcined in a tube furnace under a flow of air at 575 ºC for 16 h yielding a white solid.

The exact gel ratios are given below:

Table 3.17: Molar gel compositions for synthesis of SAPO materials.

Material	Molar gel composition				
	H_3PO_4	Al_2O_3	SDA	SiO_2	H_2O
SAPO-5	2.0	1.0	0.4	2.0	50.0
SAPO-34	1.0	1.0	1.0	0.15	50.0
SAPO-37(0.21)	2.0	0.67	0.97 & 0.025	0.21	50.0
SAPO-41	2.0	0.85	3.0	0.1	50.0
SAPO-37(0.11)	1.0	0.67	0.97 & 0.025	0.11	50.0
SAPO-37(0.42)	1.0	0.67	0.97 & 0.025	0.42	50.0
SAPO-37(0.63)	1.0	0.67	0.97 & 0.025	0.63	50.0

The standard synthesis procedure for SAPO-37 is outlined below and is typical for all samples examined in this study as per reference 93. Table 17 shows the variation in gel composition for the 4 different samples. Pseudo-boehmite was slowly added to a diluted solution of phosphoric acid (85 wt%) and left to stir for 7 hours. A second solution of tetramethylammonium hydroxide pentahydrate dissolved in tetrapropylammonium hydroxide (40 wt%) was prepared to which fumed silica was slowly added. This was left to stir for 2 hours and was then added dropwise to the stirred Al/P gel. The mixture stirred for 68 hours and was then transferred to an autoclave. The solution was heated under autogeneous pressure at 200°C for 24 hours. On removal the gel was centrifuged, filtered and washed. The material was then dried overnight at room temperature. The white solid was then calcined at 550°C for 16 hours and kept in an inert atmosphere.

ICP analysis

A Perkin-Elmer Optimum 3000 DV was used for ICP analyses with calcined samples prepared and fully digested in 10ml of deionised water and 10ml of

ACS Plus Certified H_2SO_4 (Fisher Scientific). Solutions of standard concentrations were used for calibration.

BET surface area measurements

BET surface area measurements were performed using a Micromeritics Gemini 2375 surface area analyser and prepared using flow gas preparation.

Scanning electron microscopy

Scanning electron microscopy images were obtained using a JOEL-JSM5910 microscope with accelerating voltage of 0.3-30 kV. The samples were prepared by carbon coating.

Powder X-ray diffraction

Powder X-Ray diffraction patterns were obtained using a Siemens D5000 diffractometer using Cu K_{α_1} radiation, whereby λ = 1.54056 Å. Unit cell parameters were obtained using the Celref package. This initially used 'ideal' unit cell parameters and space groups taken from reference 47, and was solved iteritivally until variation in parameters was no longer seen.

NMR measurements

All NMR measurements were performed on a Chemagnetics Infinity 400 spectrometer on a 4mm MAS double-resonance probe. For all samples, approximately 100 mg of material was quickly transferred in a thin wall zirconium oxide rotor and then spun at 8kHz using compressed nitrogen, in order to prevent sample degradation in air, for bearing, drive and purge. The nitrogen gas was generated in-house from evaporation of liquid nitrogen in high pressure 1300 litre tanks suitably connected to the NMR facility. ^{27}Al NMR experiments were performed using direct acquisition (128 scans with and a pulse delay of 2s between scans). ^{31}P NMR data were acquired both with direct acquisition (4 scans and 120s delay between scans) and with ramped cross-

polarization[94] (2s delay between scans), but only the direct acquisition data are shown in Fig.S18. ^{29}Si NMR data for all 1D experiments were performed using cross-polarization and SPINAL64 decoupling.[95] Typical spectra were acquired with 8192 scans and 2s between scans. Two dimensional experiments were performed using proton-driven spin diffusion (PDSD)[96] with a mixing time of 5ms and 160 t_1 increments of 62.5μs, for a total acquisition time of 23 hours. Phase sensitive spectra were obtained using the TPPI approach. The chemical shift axes in the ^{27}Al, ^{31}P and ^{29}Si spectra were referenced using 1M $AlCl_3$ aqueous solution (0ppm), 85% H_3PO_4 (0ppm) and silicon rubber (-22.42ppm) respectively, following the convention described in ref 97. The NMR data was processed using matNMR.[98]

Temperature-programmed-desorption

All TPD measurements were performed on a custom built system using TCD detectors to monitor ammonia concentration. As-synthesised materials were pretreated by heating at 10°C/min to 550°C in a 20% O_2/ helium mixture [Matheson UHP grade passed through a Drierite/molecular sieve gas purifier (Alltech Associates)] and held for 2 hours. The samples were exposed to ammonia and allowed to equilibrate at 150°C for 8 hours. Desorption was performed in flowing helium [Matheson UHP grade further purified with an Oxy-Trap (Alltech Associates) and an indicating OMI-1 purifier (Supelco)] at 10°C/min to 600°C and held for 40 minutes at 600°C.

Low temperature CO adsorption FT-IR

As-synthesised samples were ground and pressed into 13mm diameter self-supporting pellets (~8 mg/cm^2) and heated at 10 °C/min to 550 °C in a mixture of 20 % O_2 in N_2 [Matheson UHP grade further purified using a P400 air purifier(VICI)] and held for 1 hour. The flow was then switched to helium[Matheson UHP grade further purified using a P-100 helium purifier(VICI) and an indicating OMI-1 purifier(Supelco)] and held for an additional hour.

All IR experiments were performed in a custom designed IR flow cell that allowed for sample heating and cryogenic cooling. The system was then cooled

to ~-175°C and a spectrum recorded. Nine 0.02 cm^3 injections of CO (Matheson research purity) were added to the system followed by a final injection of 0.20 cm^3. After each injection, the system was equilibrated for 3 minutes and a spectrum recorded. All spectra were collected on a Nicolet Nexus 870 FT-IR spectrometer using a cooled MCT detector. Each spectrum was obtained by co-adding 128 scans at a resolution of 2 cm^{-1}. All spectral processing was done using the GRAMS/AI 9 software (Thermo Scientific). All spectra are normalized to a 10 mg pellet weight. Difference spectra were obtained by subtracting the spectrum of the sample before adsorption of the probe molecule.

Collidine adsorption FT-IR

As-synthesised samples were ground and pressed into 13mm diameter self-supporting pellets (~8 mg/cm^2) and heated at 10 °C/min to 550 °C in a mixture of 20 % O_2 in N_2[Matheson UHP grade further purified using a P400 air purifier(VICI)] and held for 2 hours. The system was then cooled to 30 °C and a spectrum recorded. The sample was equilibrated with collidine (helium saturated with collidine vapor at 7 °C) for 1 hour at 150 °C. Stepwise desorption of collidine was done at 150, 300 and 450 °C. After an hour hold at desorption temperature, the sample was cooled to room temperature and a spectrum recorded. All spectra were collected on a Nicolet Nexus 870 FT-IR spectrometer using a cooled MCT detector. Each spectrum was obtained by co-adding 128 scans at a resolution of 2 cm^{-1}. All spectral processing was performed using the GRAMS/AI 9 software (Thermo Scientific). All spectra were normalized to a 10 mg pellet weight. Difference spectra were obtained by subtracting the spectrum of the sample before adsorption of the probe molecule.

Catalysis reaction – Liquid phase

100 mg of cyclohexanone oxime, 100 mg of catalyst and 20 ml of benzonitrile (Aldrich) were put into a glass reactor and stirred at 500 rpm at the appropriate temperature (130, 150, 170 and 190 °C) under reflux. Samples were taken at appropriate intervals (30, 15, 5 and 5 minutes respectively).

For anhydrous conditions a nitrogen bubbler was attached to the top of the condenser. A glass reactor containing cyclohexanone oxime and the catalyst was purged with nitrogen for five minutes before 20 ml of anhydrous benzonitrile (Aldrich) was injected through into the vessel using a dry needle and syringe. The system was then lowered into the pre-heated oil-bath and stirred at 500 rpm under a steady flow of nitrogen. Samples were taken at appropriate intervals (30 minutes for 130 °C, 5 minutes for 190 °C) via a clean, dry needle and syringe. Samples were analysed as above.

All samples were analysed on a Varian Star 3400CX gas chromatogram with flame ionization detector (FID). Samples were injected into a Perkin Elmer a HP1 cross linked methylsiloxane (30 m x 0.32 mm x 1 μm film thickness) column. The samples were mass balanced using chlorobenzene as an internal standard. The following GC method was used:

Start at 120 °C, Hold 2 minutes, Ramp at 15 °C/min up to 220 °C, Hold for 5 minutes at 220 °C. The method is 13 minutes and 40 seconds long in total. The benzonitrile solvent peak is a large peak at 3.5 minutes, the cyclohexanone oxime is at 4.0 minutes, ε-caprolactam peak is at 5.8 minutes, the by product is at 6.6 minutes.

The injector port is set to 220 °C, the detector is set to 250 °C. The carrier pressure (Helium) is at 14 psig. The method is given 1 minute to equilibrate before injection. Typically 5 μl of centrifuged sample is injected.

The samples were calibrated using a relative response factor of ε-caprolactam relative to cyclohexanone oxime, this was found to be 1.119. The samples were calibrated to an internal standard of chlorobenzene for the mass balance. Cyclohexnaone oxime was found to have a relative response factor of 1.2972 relative to chlorobenzene, and ε-caprolactam was found to have a response factor of 1.4516, the mass balance at 130 °C was found to be 106 % after 6 hours.

The response factors were used to calculate the moles of cyclohexanone oxime, ε-caprolactam and by-products (response factor assumed to be 1.00). The conversion is calculated as:

$$Conversion = \frac{100 \times (Initial\ Moles\ of\ Oxime - Moles\ of\ Oxime\ Detected)}{Initial\ Moles\ of\ Oxime} \qquad (2.6)$$

$$Selectivity = \frac{100 \times (Moles\ of\ Caprolactam)}{Moles\ of\ products\ detected} \quad (2.7)$$

Kinetics and derivations

The rate of the reaction at time t was calculated by comparing the concentrations and times with that of the previous sample thus:

$$Rate_t = \frac{[Cyclohexanone\ oxime]_t - [Cyclohexanone\ oxime]_{t-1}}{Time_t - Time_{t-1}} \quad (2.8)$$

The order and rate constant of the reaction were then found through manipulation of the equation below:

$$Rate_t = k \times [Cyclohexanone\ oxime]^n \quad (2.9)$$

where k is the rate constant and n is the order of the reaction:

$$Ln|Rate_t| = Ln|k \times [Cyclohexanone\ oxime]^n| \quad (2.10)$$

$$Ln|Rate_t| = Ln|k| + Ln|[Cyclohexanone\ oxime]^n| \quad (2.11)$$

$$Ln|Rate_t| = Ln|k| + (n \times Ln|[Cyclohexanone\ oxime]|) \quad (2.12)$$

$$y = Ln|k| + n \times x \quad (2.13)$$

By plotting Ln|Rate| v Ln|[Cyclohexanone oxime]| the Ln|k| and the order of the reaction are shown as the y-intercept and gradient respectively.

The activation energies were calculated through manipulation of the Arrenhius equation:

$$k = A \times \exp\left(\frac{-E_a}{RT}\right) \quad (2.14)$$

where k is the rate constant, A is the pre-exponential factor, E_a is the activation energy in kJ mol^{-1}, R is the perfect gas constant (8.314 J K^{-1} mol^{-1}) and T is the temperature in Kelvin.

$$Ln|k| = Ln|A \times exp\left(\frac{-E_a}{RT}\right)| \quad (2.15)$$

$$Ln|k| = Ln|A| + Ln|exp\left(\frac{-E_a}{RT}\right)| \quad (2.16)$$

$$Ln|k| = Ln|A| - \frac{Ea}{RT} \quad (2.17)$$

$$y = Ln|A| - \left(\frac{E_a}{R}\right)x \quad (2.18)$$

By plotting Ln|k| against 1/T the activation energy is found by multiplying the gradient by -8.314 J K^{-} mol^{-1}.

Recycles

After a reaction the catalyst was collected via filtration, washed with fresh benzonitrile (~20 ml) and distilled water (~50 ml) and dried at 80 °C overnight. The material was then reactivated through calcination and re-run as above.

Catalysis Reaction – Vapour phase

The vapour-phase Beckmann rearrangement of cyclohexanone oxime was performed in a fixed-bed, quartz reactor (4 mm in diameter) with a glass frit, in which a layer of pelletized catalyst (0.25 g) was packed between two layers of glass beads. This was pre-heated by a jacket in the flow-reactor to 673 K under a 20 mL/min flow of helium gas for 1 h. The temperature was reduced to 573 K and a liquid feed of 10 wt% of cyclohexanone oxime in ethanol was fed into the reactor, maintaining a WHSV of 0.4 hr^{-1}, with samples being analysed on an hourly basis (under steady-state conditions). The temperature was then increased to the desired value (623 and 673) and samples were taken at each temperature after being allowed to equilibrate for 1 h.

3.6 Kinetic analysis

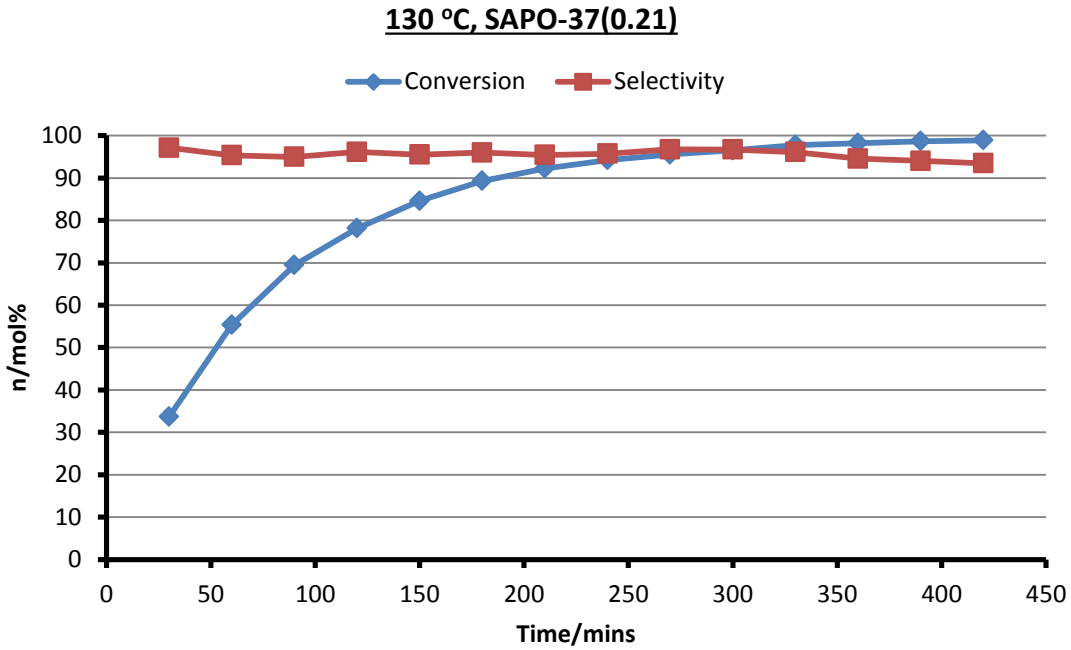

Figure 3.48: Catalytic data for the conversion of cyclohexanone oxime to ε-caprolactam with SAPO-37(0.21) at 130°C

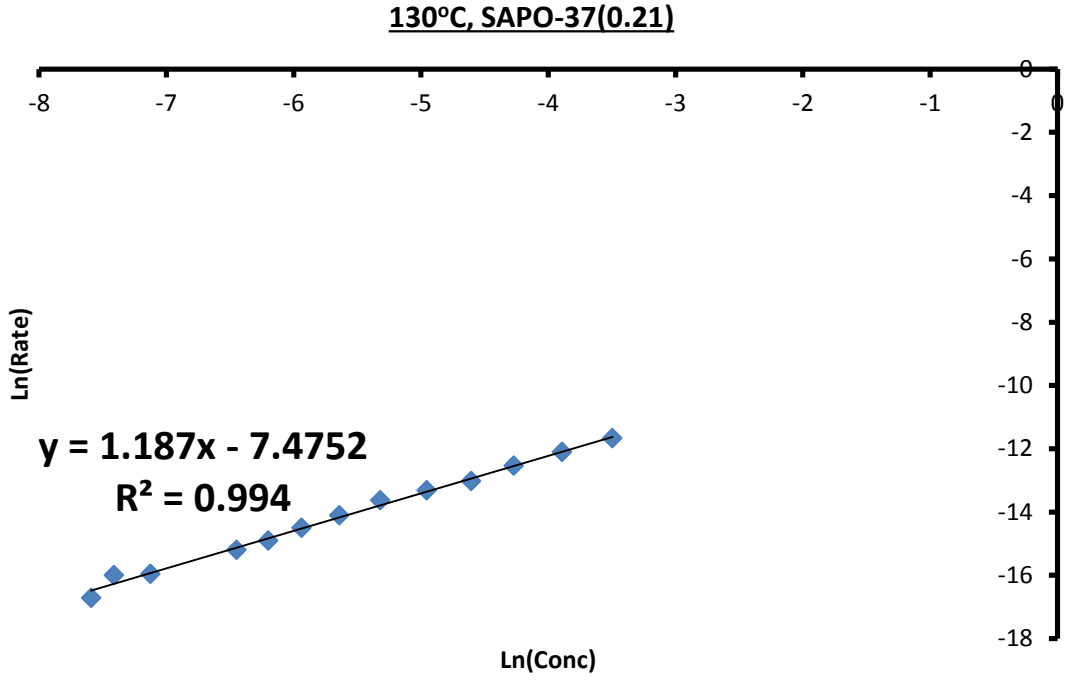

Figure 3.49: Graph detailing kinetic analysis of cyclohexanone oxime to ε-caprolactam with SAPO-37(0.21) at 130 °C

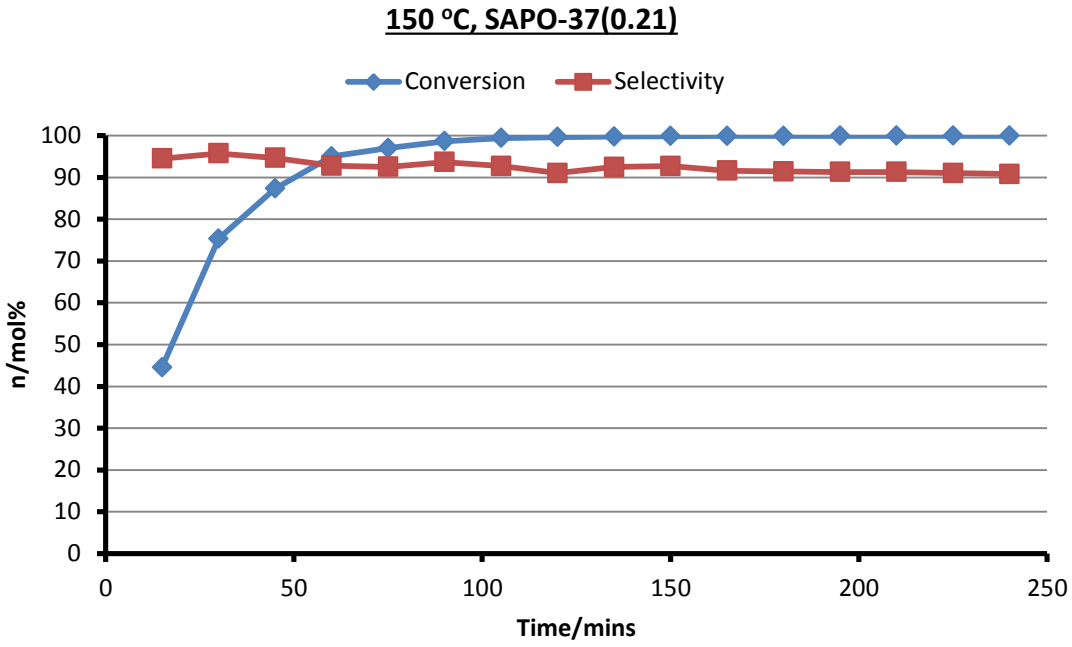

Figure 3.50: Catalytic data for the conversion of cyclohexanone oxime to ε-caprolactam with SAPO-37(0.21) at 150°C

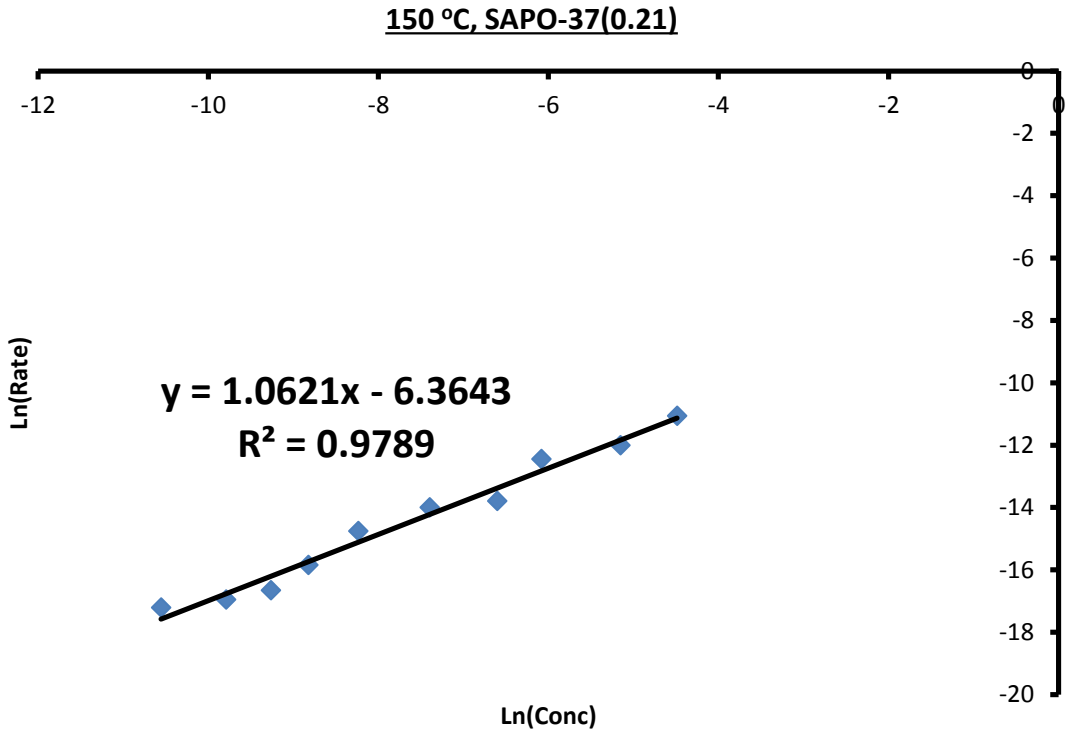

Figure 3.51: Graph detailing kinetic analysis of cyclohexanone oxime to ε-caprolactam with SAPO-37(0.21) at 150 °C

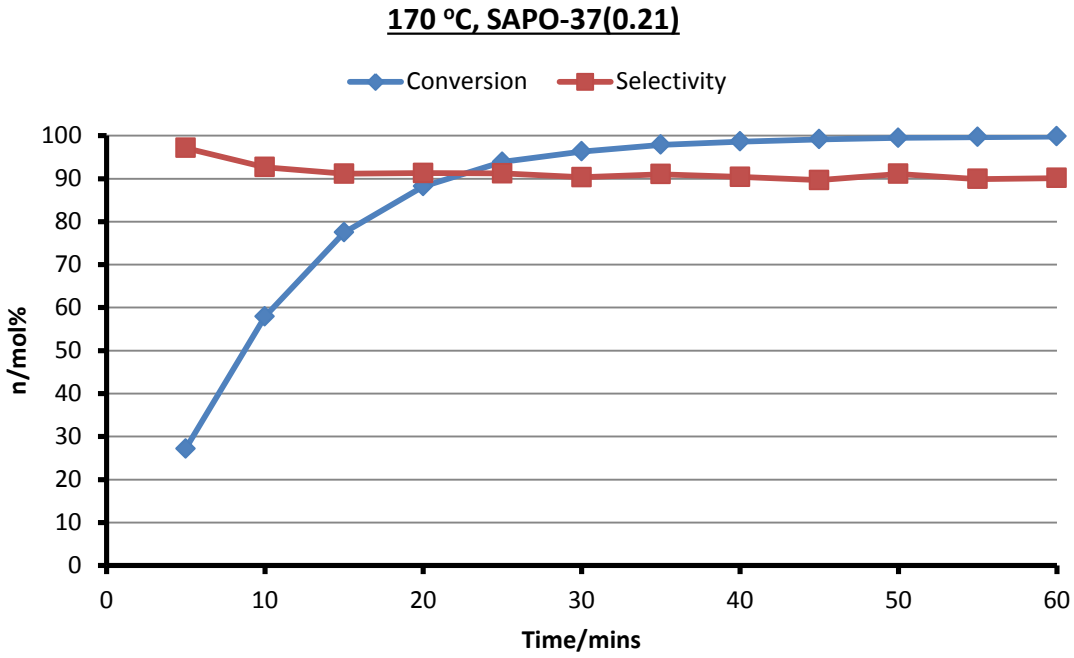

Figure 3.52: Catalytic data for the conversion of cyclohexanone oxime to ε-caprolactam with SAPO-37(0.21) at 170°C

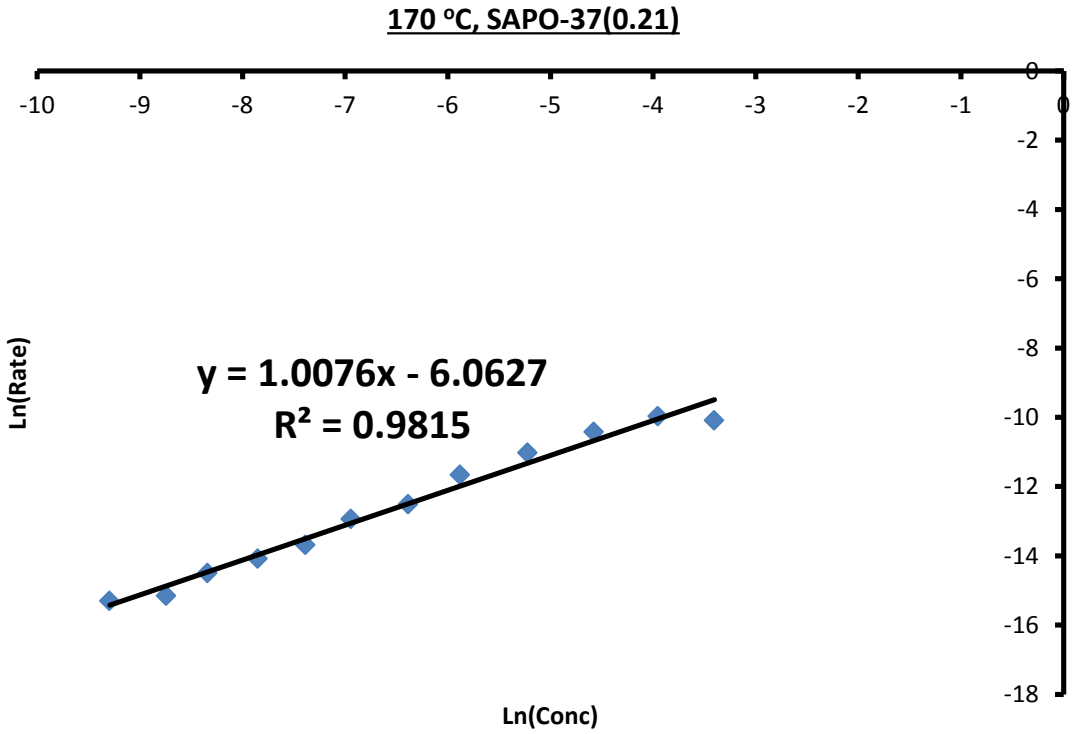

Figure 3.53: Graph detailing kinetic analysis of cyclohexanone oxime to ε-caprolactam with SAPO-37(0.21) at 170 °C

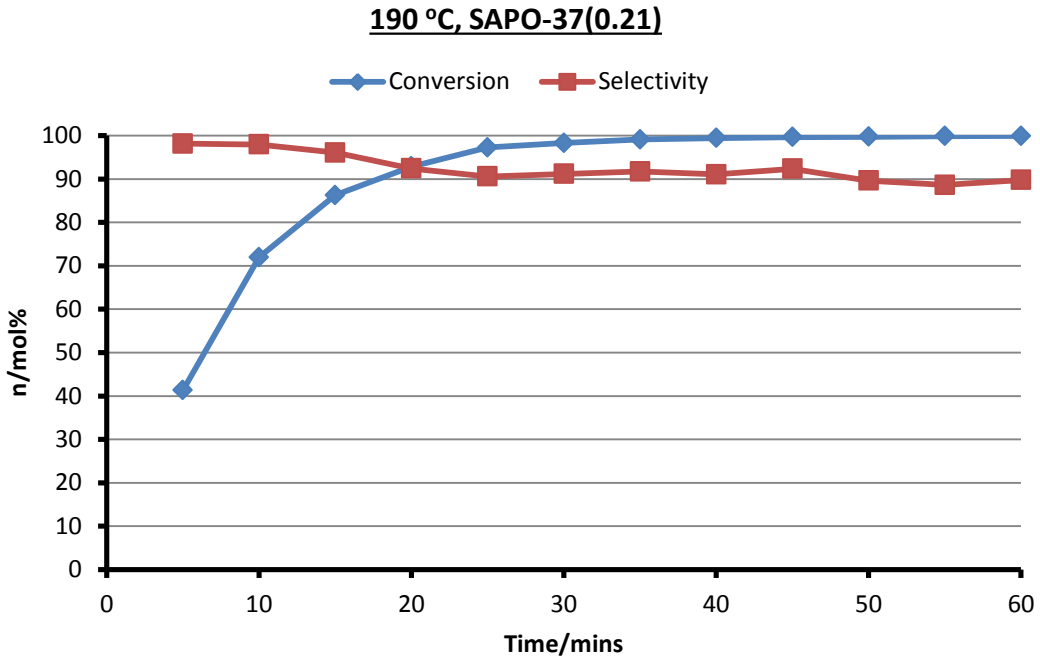

Figure 3.54: Catalytic data for the conversion of cyclohexanone oxime to ε-caprolactam with SAPO-37(0.21) at 190°C

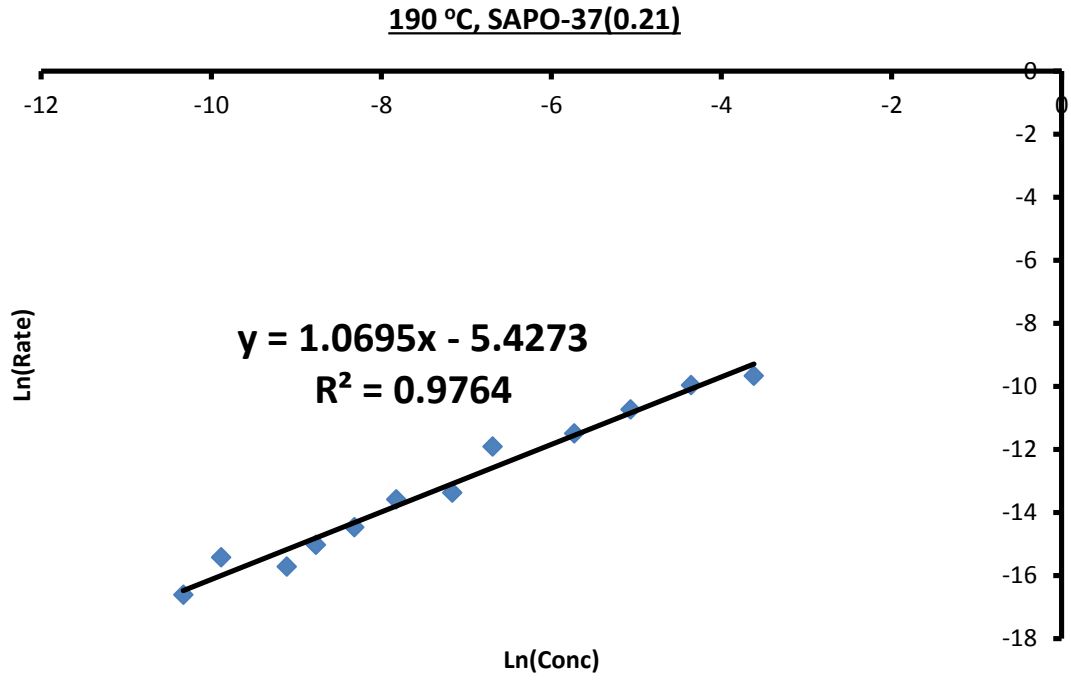

Figure 3.55: Graph detailing kinetic analysis of cyclohexanone oxime to ε-caprolactam with SAPO-37(0.21) at 190 °C

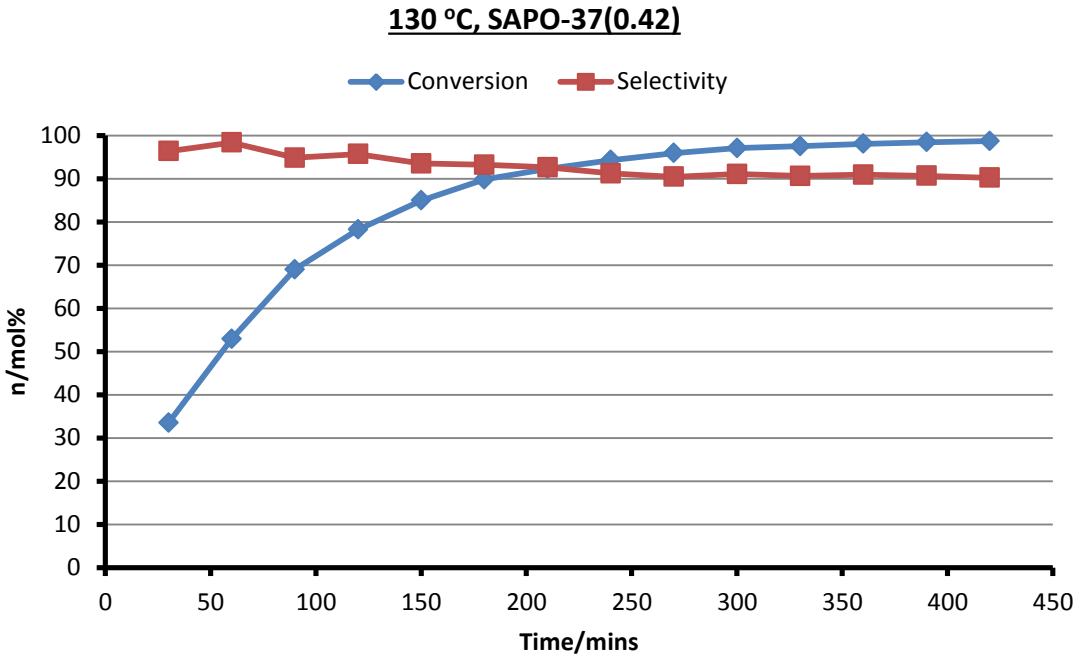

Figure 3.56: Catalytic data for the conversion of cyclohexanone oxime to ε-caprolactam with SAPO-37(0.42) at 130°C

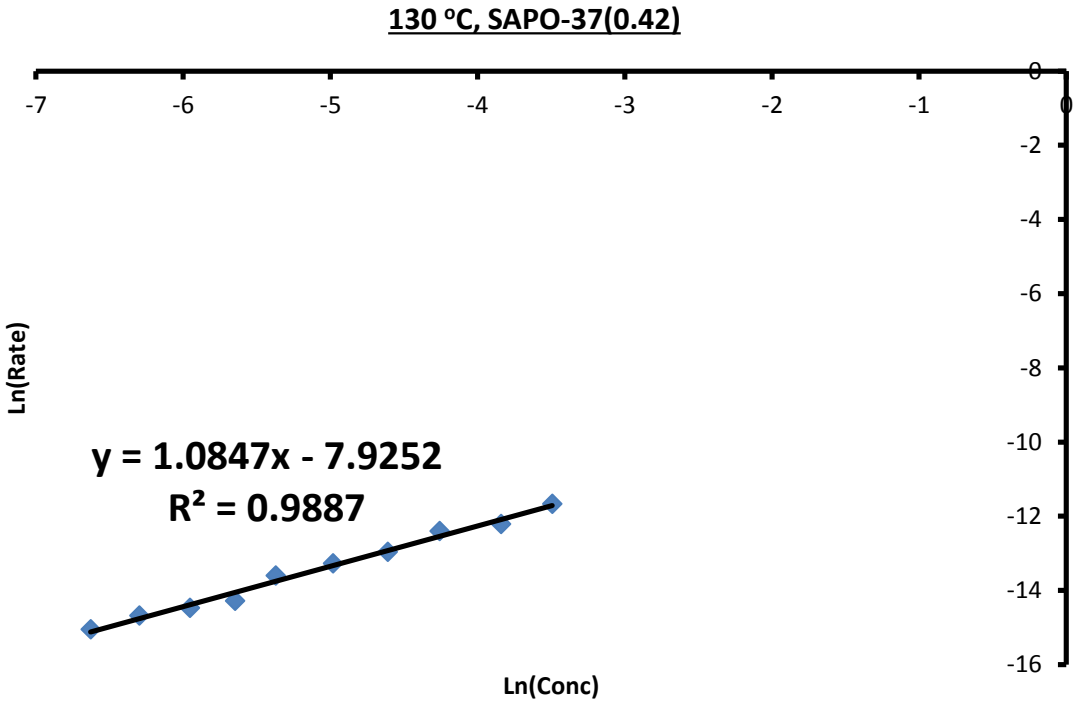

Figure 3.57: Graph detailing kinetic analysis of cyclohexanone oxime to ε-caprolactam with SAPO-37(0.42) at 130 °C

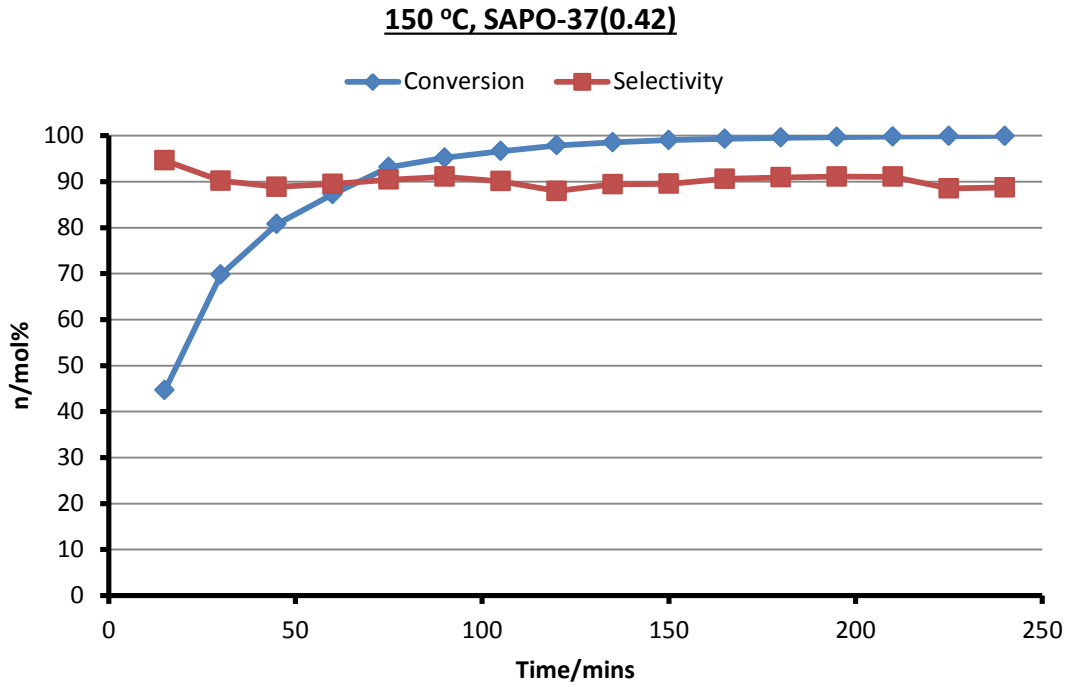

Figure 3.58: Catalytic data for the conversion of cyclohexanone oxime to ε-caprolactam with SAPO-37(0.42) at 150°C

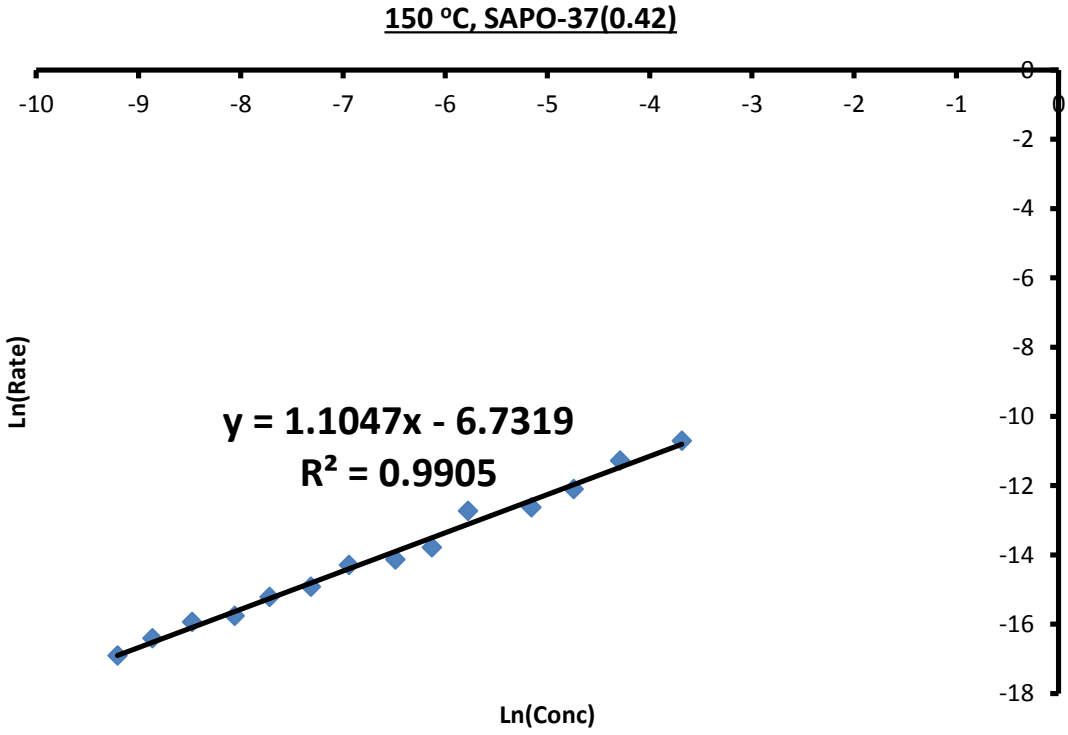

Figure 3.59: Graph detailing kinetic analysis of cyclohexanone oxime to ε-caprolactam with SAPO-37(0.42) at 150 °C

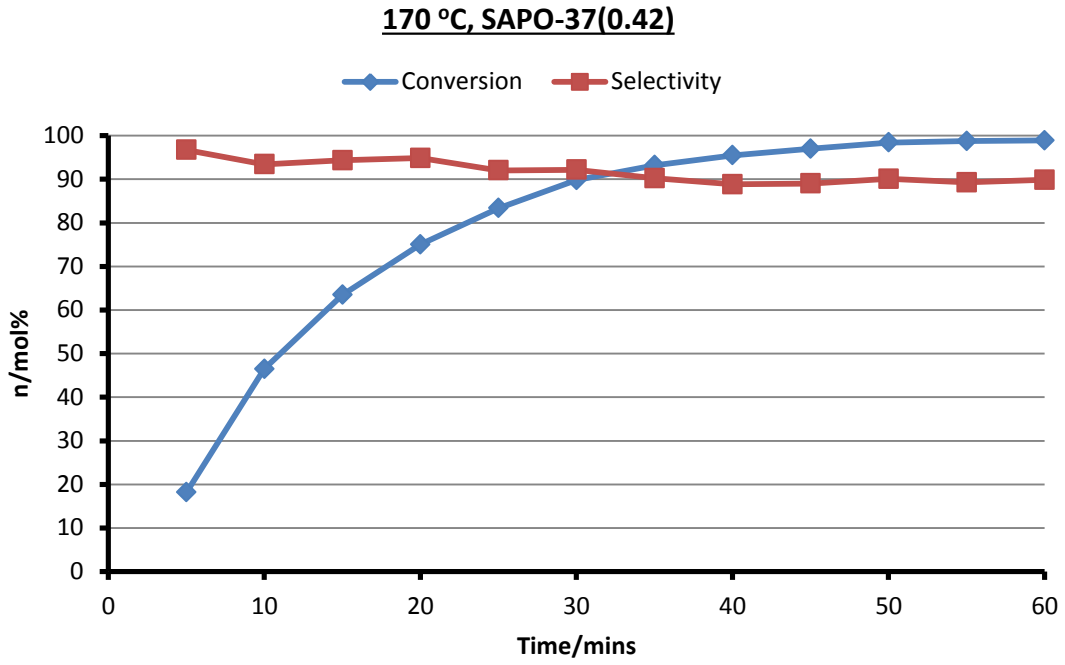

Figure 3.60: Catalytic data for the conversion of cyclohexanone oxime to ε-caprolactam with SAPO-37(0.42) at 170°C

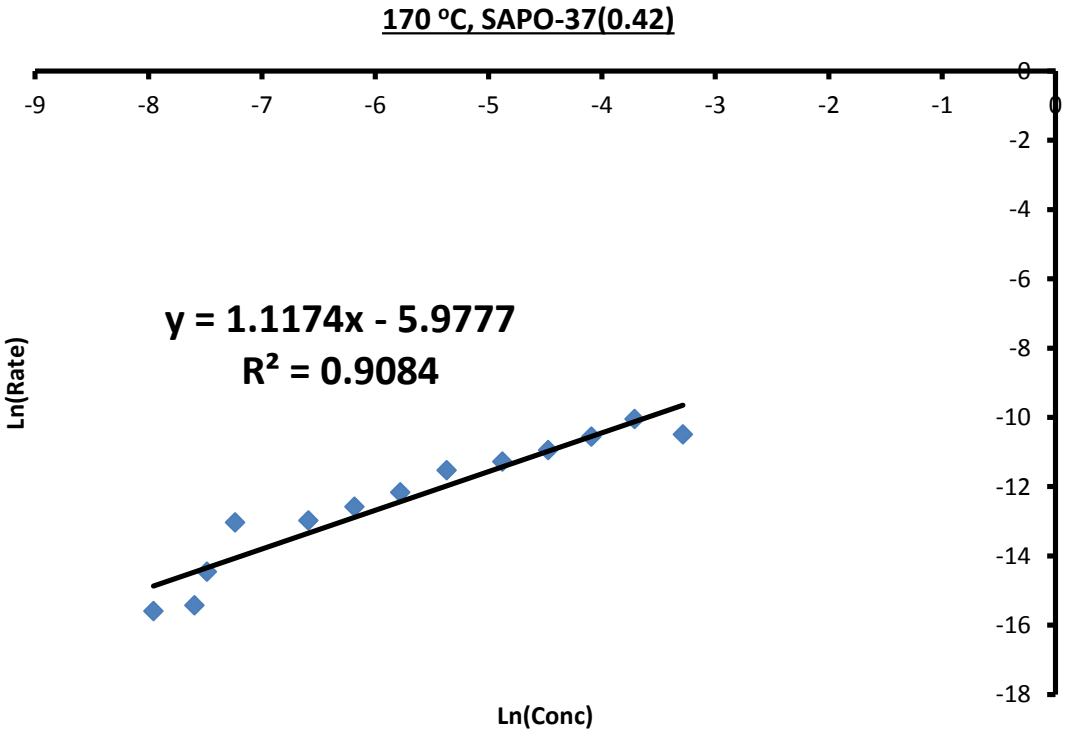

Figure 3.61: Graph detailing kinetic analysis of cyclohexanone oxime to ε-caprolactam with SAPO-37(0.42) at 170 °C

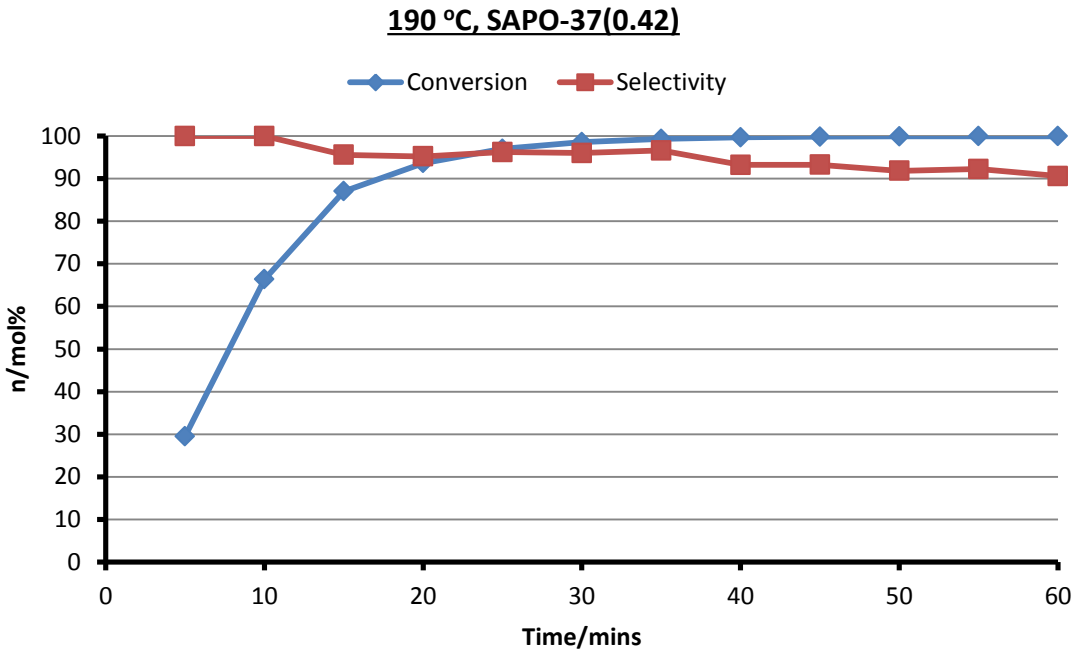

Figure 3.62: Catalytic data for the conversion of cyclohexanone oxime to ε-caprolactam with SAPO-37(0.42) at 190°C

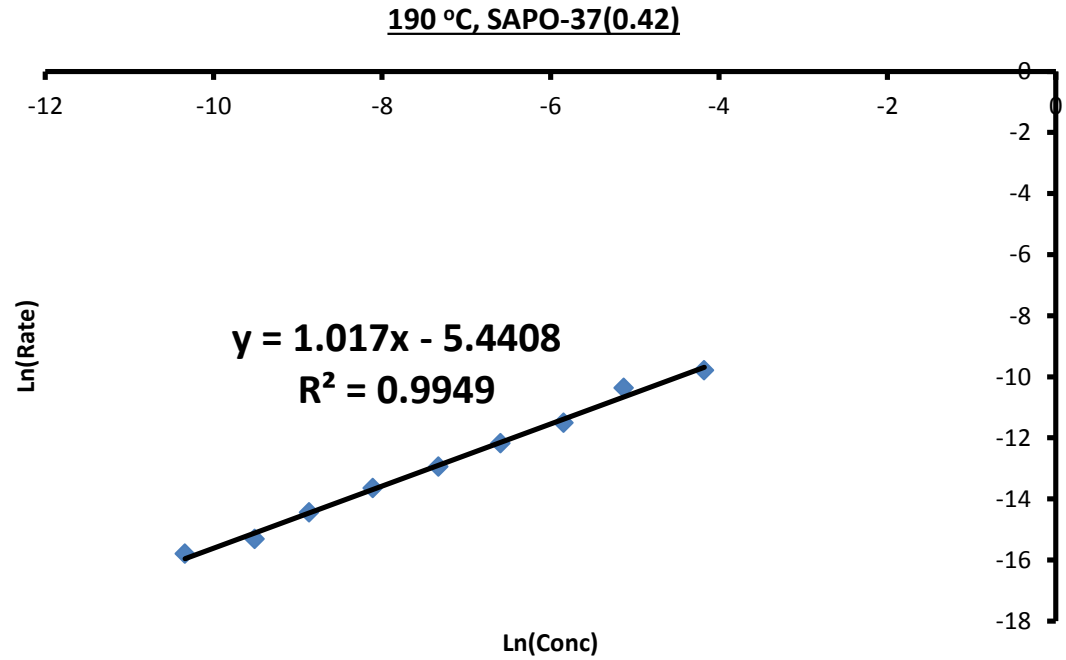

Figure 3.63: Graph detailing kinetic analysis of cyclohexanone oxime to ε-caprolactam with SAPO-37(0.42) at 190 °C

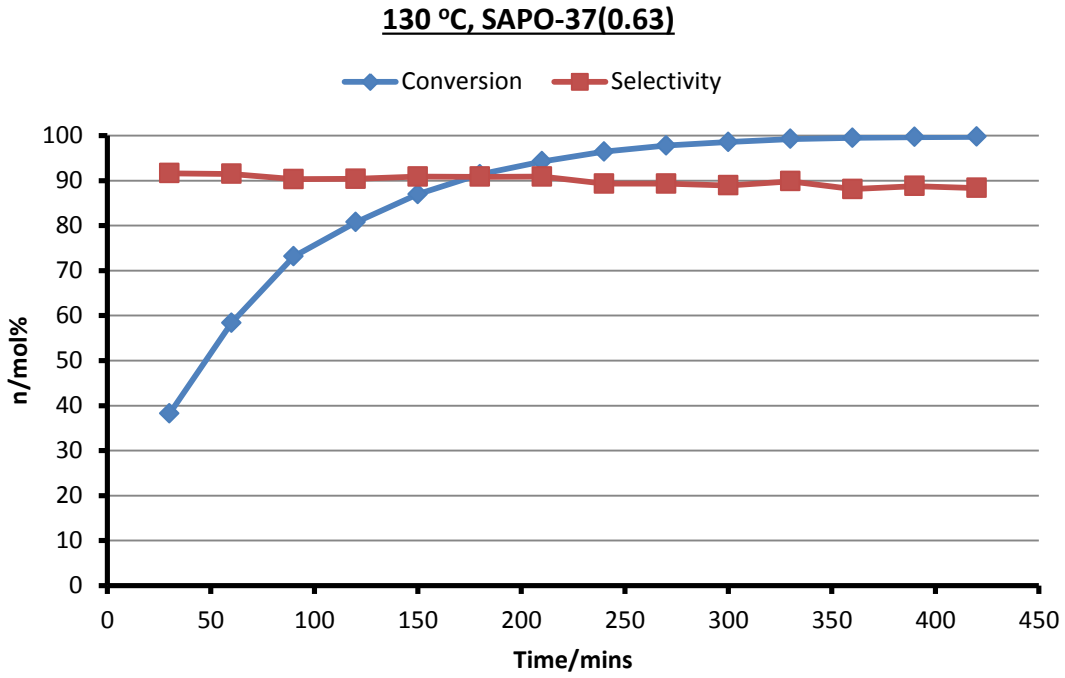

Figure 3.64: Catalytic data for the conversion of cyclohexanone oxime to ε-caprolactam with SAPO-37(0.63) at 130°C

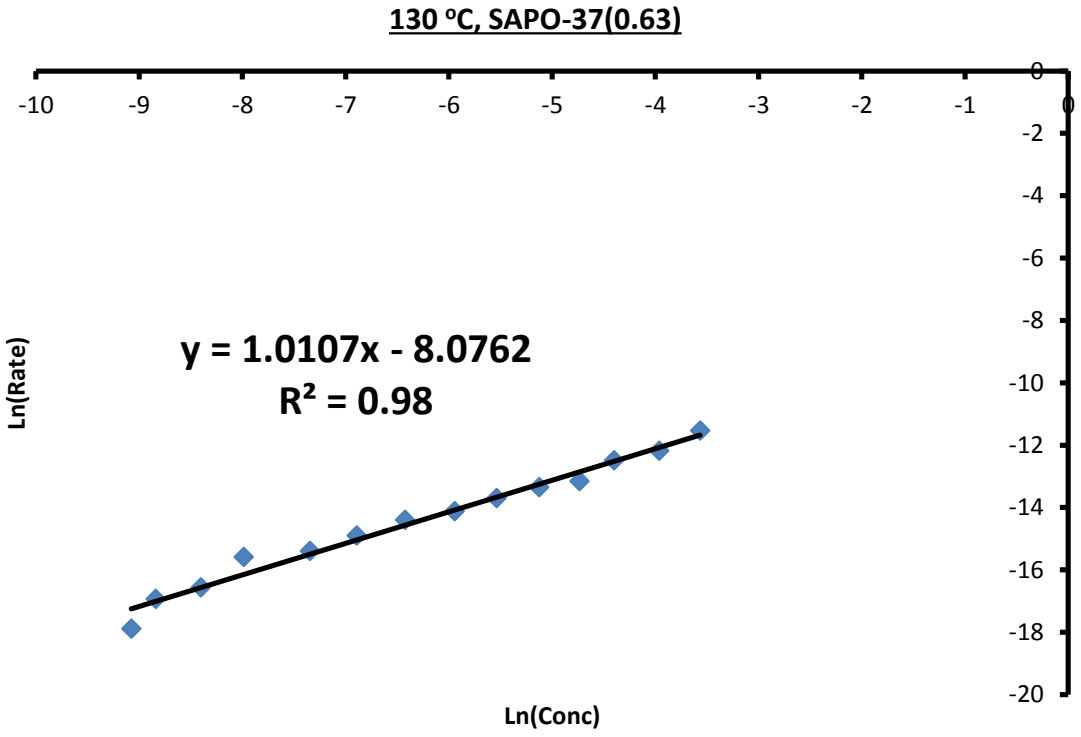

Figure 3.65: Graph detailing kinetic analysis of cyclohexanone oxime to ε-caprolactam with SAPO-37(0.63) at 130 °C

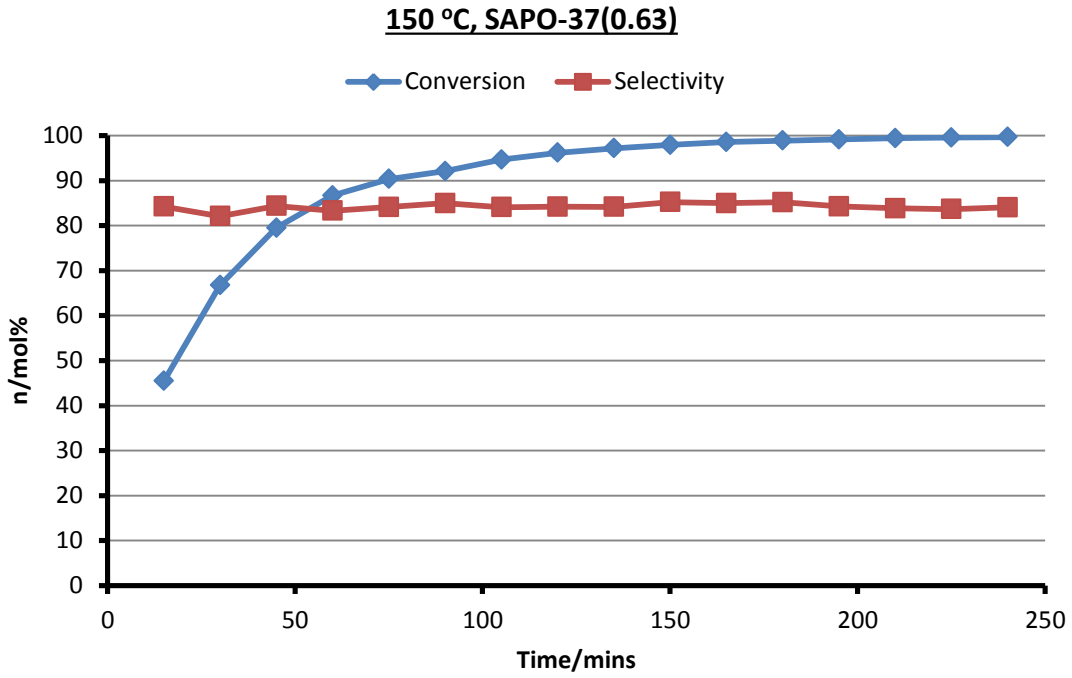

Figure 3.66: Catalytic data for the conversion of cyclohexanone oxime to ε-caprolactam with SAPO-37(0.63) at 150°C

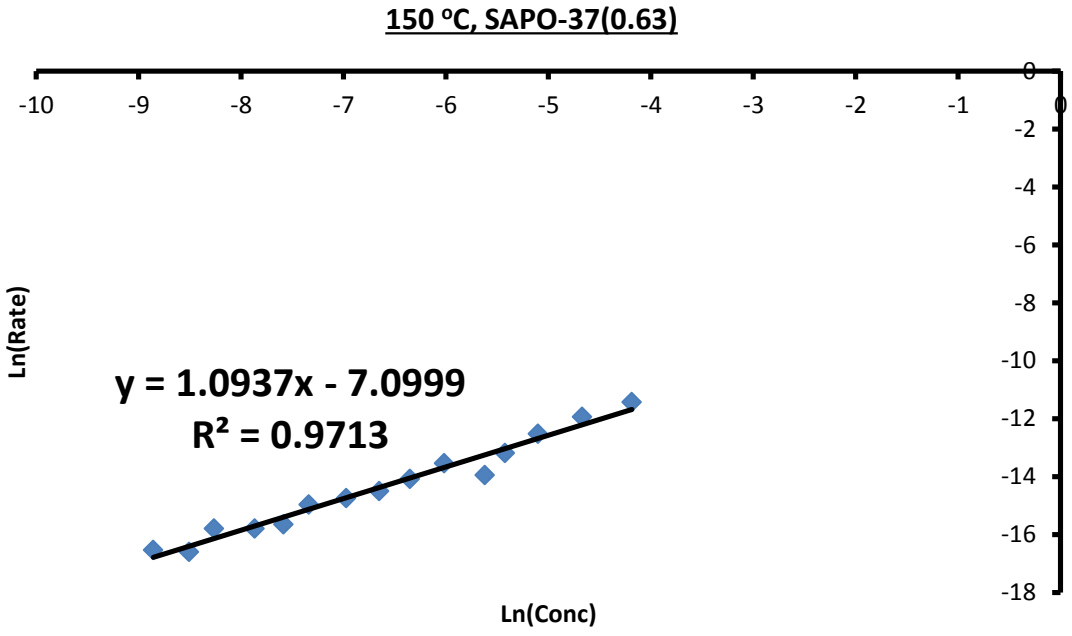

Figure 3.67: Graph detailing kinetic analysis of cyclohexanone oxime to ε-caprolactam with SAPO-37(0.63) at 150 °C

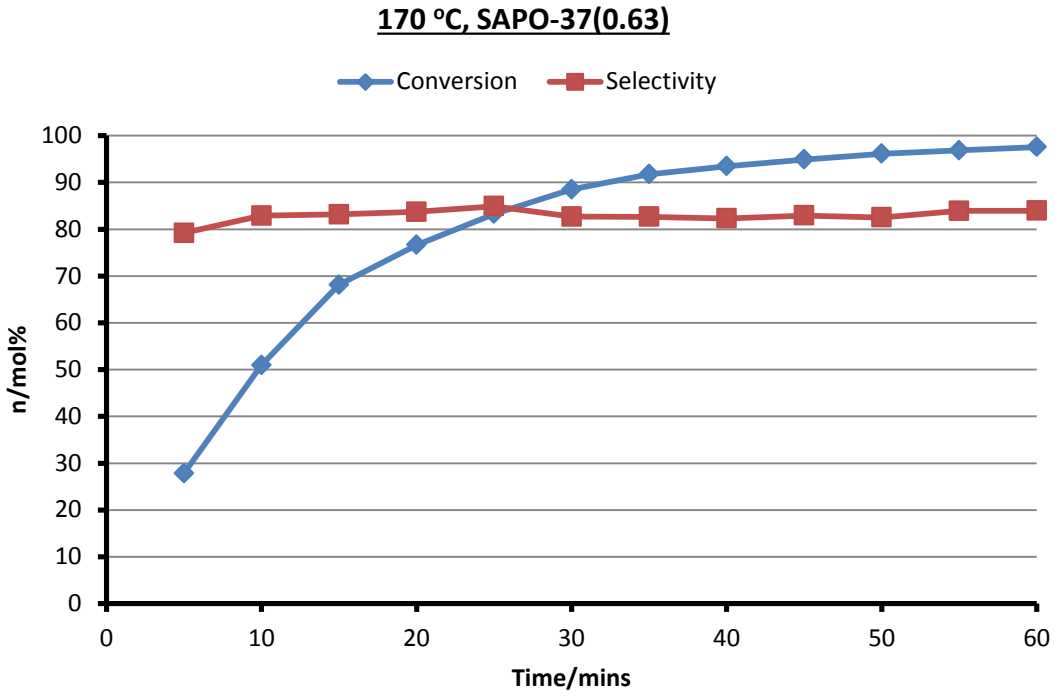

Figure 3.68: Catalytic data for the conversion of cyclohexanone oxime to ε-caprolactam with SAPO-37(0.63) at 170°C

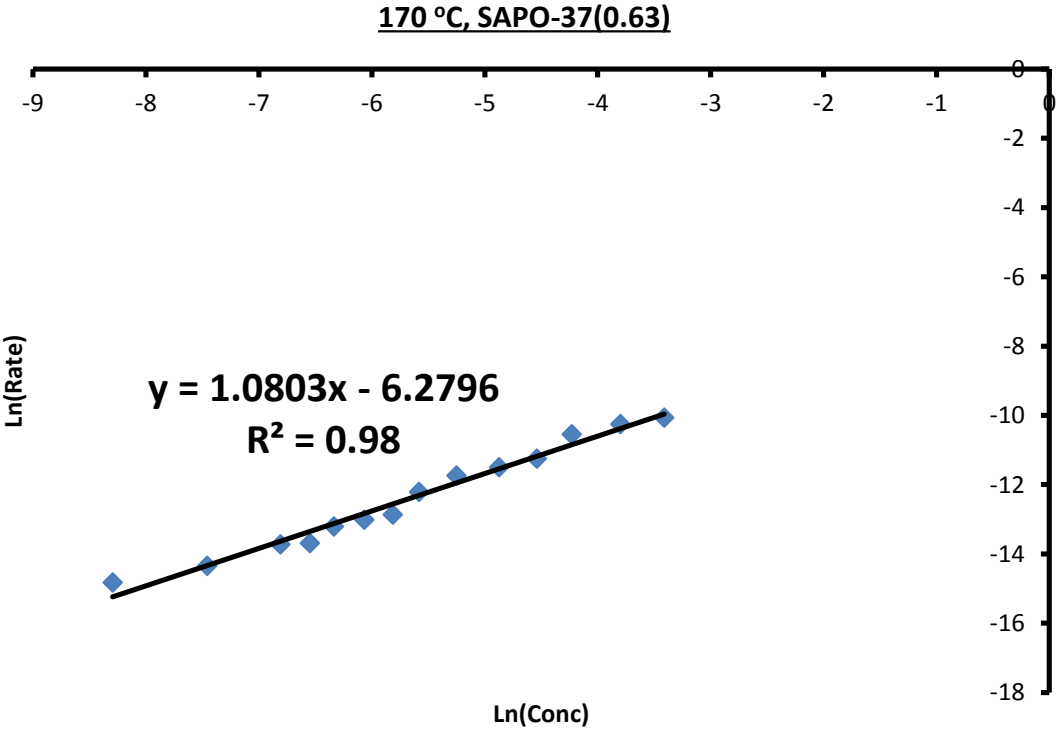

Figure 3.69: Graph detailing kinetic analysis of cyclohexanone oxime to ε-caprolactam with SAPO-37(0.63) at 170 °C

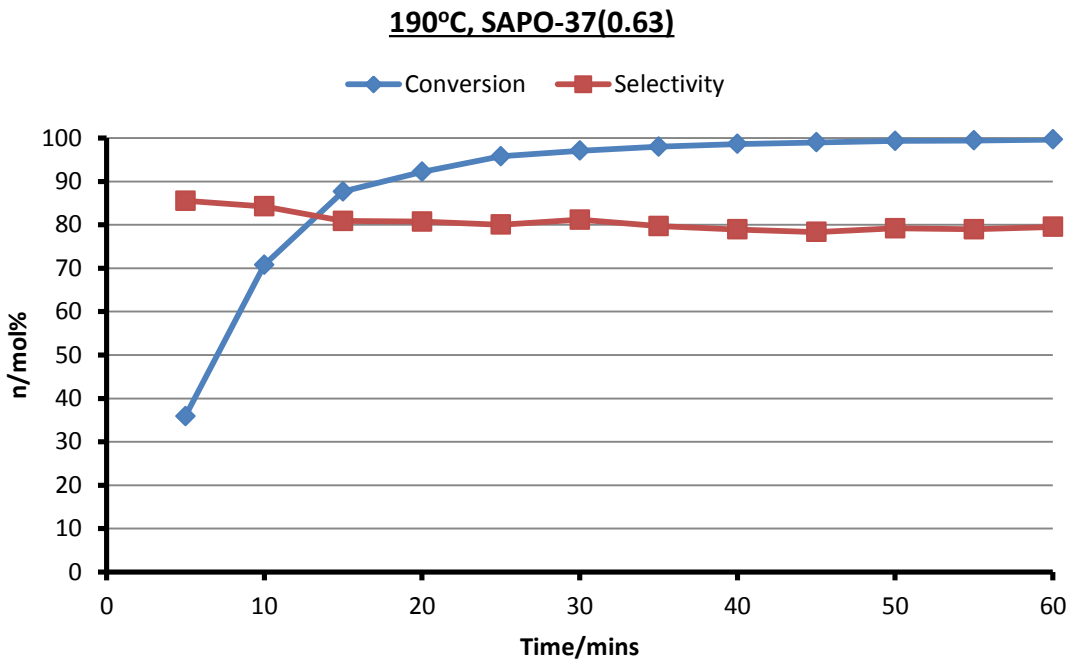

Figure 3.70: Catalytic data for the conversion of cyclohexanone oxime to ε-caprolactam with SAPO-37(0.63) at 190ºC

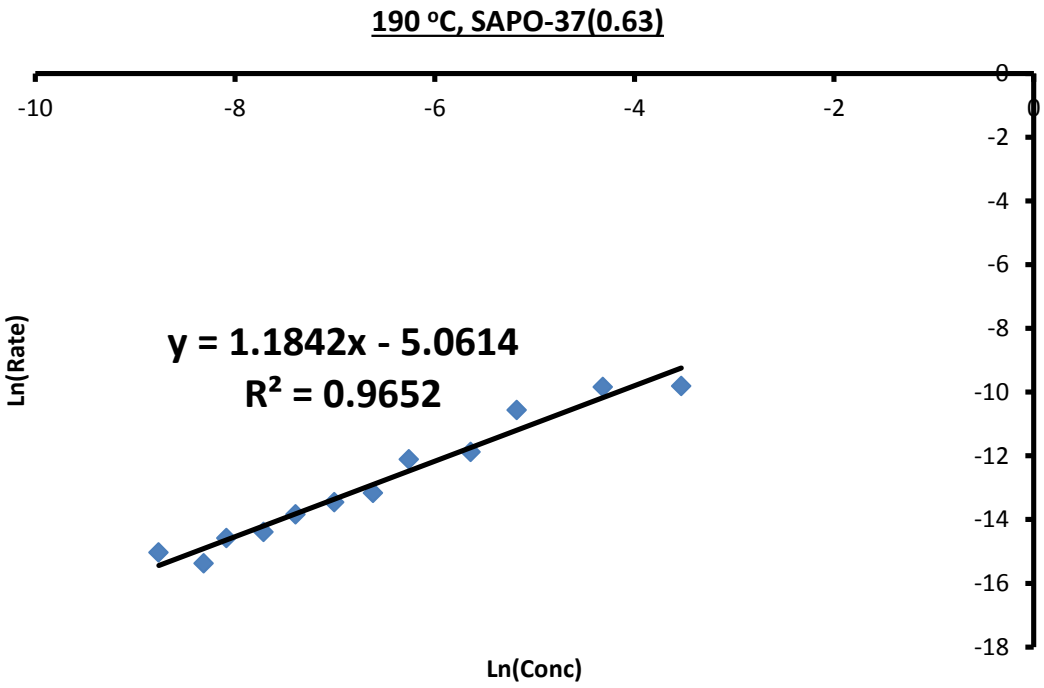

Figure 3.71: Graph detailing kinetic analysis of cyclohexanone oxime to ε-caprolactam with SAPO-37(0.63) at 190 ºC

3.7 References

1. R. Raja, M. E. Potter and S. H. Newland, *Chem. Commun.*, **2014**, *50*, 5940-5957.
2. E. Gianotti, M. Manzoli, M. E. Potter, V. N. Shetti, D. Sun, J. Paterson, T. M. Mezza, A. Levy and R. Raja, *Chem. Sci.*, **2014**, *5*, 1810-1819.
3. R. D. Oldroyd, J. M. Thomas and G. Sankar, *Chem. Commun.*, **1997**, *21*, 2025-2056.
4. C. O. Arean, B. M. Weckhuysen and A. Zecchina, *Phys. Chem. Chem. Phys.*, **2012**, *14*, 2125-2127.
5. "Nylon – A global strategic business report" Global industry analysts inc., **2010.**
6. G. Bellussi and C. Perego, *CATTECH*, **2000**, *4*, 4-16.
7. H. Ichihashi and H. Sato, *Appl. Catal. A: Gen.*, **2001**, *221*, 359-366.
8. M. Mantegazza and G. Petrini, US Patent, **1996**, US 5498793 A.
9. H. Kajikuri, M. Kitamura and Y. Higashio, US Patent, **1994**, US 5304643 A.
10. G. P. Heitmann, G. Dahlhoff and W. F. Hoelderich, *J. Catal.*, **1999**, *186*, 12-19.
11. Y. Izumi, H. Ichihashi, Y. Shimazu, M. Kitamura and H. Sato, *Bull. Chem. Soc. Jpn.*, **2007**, *80*, 1280-1287.
12. A. B. Fernandez, I. Lezcano-Gonzalez, M. Boronat, T. Blasco and A. Corma, *J. Catal.*, **2007**, *249*, 116-119.
13. H. Kath, R. Glaser and J. Weitkamp, *Chem. Eng. Tech.*, **2001**, *24*, 150-153.
14. L. Forni, C. Tosi, G. Fornasari, F. Trifiro, A. Vaccari and J. B. Nagy, *J. Mol. Catal. A: Chem.*, **2004**, *221*, 97-103.
15. A. Cesana, S. Palmery, R. Buzzoni, G. Spano, F. Rivetti and L. Carnelli, *Catal. Today*, **2010**, *154*, 264-270.
16. L. X. Dai, K. Koyama, M. Miyamoto and T. Tatsumi, *Appl. Catal. A: Gen.,* **1999**, *189*, 237-242.
17. R. Anand, R. B. Khomane, B. S. Rao and B. D. Kulkarni, *Catal. Lett.*, **2002**, *78*, 189-194.
18. G. P. Heitmann, G. Dahlhoff and W. F. Holderich, *Appl. Catal. A:Gen.*, **1999**, *185*, 99-108.
19. M. Anilkumar and W. F. Holderich, *J. Catal.*, **2008**, *260*, 17-29.

20. J. Roseler, G. Heitmann and W. F. Holderich, *Appl. Catal. A: Gen.*, **1996**, *144*, 319-333.
21. H. Ichihashi and M. Kitamura, *Catal. Today*, **2002**, *73*, 23-28.
22. M. A. Camblor, A. Corma, H. Garcia, V. Semmer-Herledan and S. Valencia, *J. Catal.*, **1998**, *177*, 267-272.
23. C. Ngamcharussrivichai, P. Wu and T. Tatsumi, *Appl. Catal. A: Gen.*, **2005**, *288*, 158-168.
24. Y. M. Chung and H. K. Rhee, *J. Mol. Catal. A: Chem.*, **2001**, *175*, 249-257.
25. C. Ngamcharussrivichai, P. Wu and T. Tatsumi, *J. Catal.*, **2005**, *235*, 139-149.
26. C. Ngamcharussrivichai, P. Wu and T. Tatsumi, *J. Catal.*, **2004**, *227*, 448-458.
27. W. Zhao, P. Salame, F. Launay, A. Gedeon and Z. Hao, *J. Porous Mater.*, **2008**, *15*, 139-143.
28. X. Wang, C. C. Chen, S. Y. Chen, Y. Mou and S. Cheng, *Appl. Catal. A: Gen.*, **2005**, *281*, 47-54.
29. M. Hartmann and L. Kevan, *Chem. Rev.*, **1999**, *99*, 635-664.
30. R. M. Leithall, V. N. Shetti, S. Maurelli, M. Chiesa, E. Gianotti and R. Raja, *J. Am. Chem. Soc.*, **2013**, *135*, 2915-2918.
31. L. Gomez-Hortiguela, F. Cora, G. Sankar, C. M. Zicovich-Wilson and C. R. A. Catlow, *Chem. Eur J.*, **2010**, *16*, 13638-13645.
32. M. E. Potter, D. Sun, E. Gianotti, M. Manzoli and R. Raja, *Phys. Chem. Chem. Phys.*, **2013**, *15*, 13288-13295.
33. J. Paterson, M. E. Potter, E. Gianotti and R. Raja, *Chem. Commun.*, **2010**, *47*, 517-519.
34. J. M. Thomas, R. Raja and D. W. Lewis, *Angew. Chem., Int. Ed.*, **2005**, *44*, 6456-6482.
35. J. M. Thomas and R. Raja, *Proc. Natl. Acad. Sci.*, **2005**, *39*, 13732-13736.
36. R. Raja and A. J. Paterson, US Patent, **2013**, US 8444917 B2.
37. A. B. Levy, R. Raja and M. E. Potter, US Patent, **2013**, US 20130109851 A1.
38. A. B. Levy, R. Raja and M. E. Potter, WO Patent, **2013**, WO 2013063244 A1.
39. S. Wilson and P. Barger, *Micropor. Mesopor. Mater.*, **1999**, *29*, 117-126.

40. B. P. C. Hereijgers, F. Bleken, M. H. Nilsen, S. Svelle, K. P. Lilerud, M. Bjorgen, M. M. Weckhuysen and U. Olsbye, *J. Catal.*, **2009**, *264*, 77-87.
41. P. T. Barger, US Patent, **1992**, US5095163 A.
42. M. Dugal, G. Sankar, R. Raja and J. M. Thomas, *Angew. Chem. Int. Ed.*, **2000**, *39*, 2310-2313.
43. J. M. Thomas, R. Raja, G. Sankar and R. G. Bell, *Nature*, **1999**, *398*, 227-230.
44. R. W. Dorner, M. Deifallah, C. R. A. Catlow, F. Cora, S. P. Elangovan, T. Okubo and G. Sankar, *J. Phys. Chem. C*, **2008**, *112*, 4187-4194.
45. G. Sastre, D. W. Lewis and C. R. A. Catlow, *J. Phys. Chem. B*, **1997**, *101*, 5249-5262.
46. G. Sastre, D. W. Lewis and C. R. A. Catlow, *J. Phys. Chem.*, **1996**, *100*, 6722-6730.
47. "Collection of simulated XRD powder patterns for zeolites" M. M. J. Treacy and J. B. Higgins, Elsevier, 5th edition.
48. M. E. Potter, A. J. Paterson and R. Raja, *ACS Catal.*, **2012**, *2*, 2446-2451.
49. B. M. Lok, C. A .Messina, R. L. Patton, R. T. Gajek, T. R. Cannan and E. M. Flanigen, *J. Am. Chem. Soc.*, **1984**, *106*, 6092-6903.
50. R. B. Borade and A. Clearfield, *J. Mol. Catal.*, **1994**, *88*, 249-265.
51. S. Maurelli, M. Chiesa, E. Giamello, R. M. Leithall and R. Raja, *Chem. Commun.* , **2012**, *48*, 8700-8702.
52. S. A. Bartlett, P. P. Wells, M. Nachtegaal, A. J. Dent, G. Cibin, G. Reid, J. Evans and M. Tromp, *J. Catal.*, **2011**, *284*, 247-258.
53. E. Gianotti, V. N. Shetti, M. Manzoli, J. A. L. Blaine, W. C. Pearl Jr., R. D. Adams, S. Coluccia and R. Raja, *Chem. Eur. J.*, **2010**, *16*, 8202-8209.
54. D. I. Enache, J. K. Edwards, P. Landon, B. Solsona-Espiru, A. F. Carley, A. A. Herzing, M. Watanabe, C. J. Kiely, D. W. Knight and G. J. Hutchings, *Science*, **2006**, *311*, 362-365.
55. W. Shen, X. Li, Y. Wei, P. Tian, F. Deng, X. Han and X. Bao, *Micropor. Mesopor. Mater.*, **2012**, *158*, 19-25.
56. E. Lippmaa, A. Samoson and M. Magi, *J. Am. Chem. Soc.*, **1986**, *108*, 1730-1735.
57. C. S. Blackwell and R. L. Patton, *J. Phys. Chem.*, **1984**, *88*, 6135-6139.
58. C. S. Blackwell and R. L. Patton, *J. Phys. Chem.*, **1988**, *92*, 3965-3970.

59. P. Meriaudeau, V. A. Taun, V. T. Ngheim, S. Y. Lai, L. N. Hung and C. Naccache, *J. Catal.*, **1997**, *169*, 55-66.
60. J. Barras, J. Klinowski and D. W. McComb, *J. Chem. Soc. Faraday Trans.*, **1994**, *90*, 3719-3723.
61. C. Jia, P. Massiani and D. Barthomeuf, *J. Chem. Soc. Faraday Trans.*, **1993**, *89*, 3659-3665.
62. J. A. van Bokhoven, A. L. Roest, D. C. Koningsberger, J. T. Miller, G. H. Nachtegaal and A. P. M. Kentgens, *J. Phys. Chem. B*, **2000**, *104*, 6743-6754.
63. W. Zhang, X. Bao, X. Guo and X. Wang, *Catal. Lett.*, **1999**, *60*, 89-94.
64. G. Engelhardt and D. Michel, *High Resolution Solid State NMR Spectroscopy of Silicates and Zeolites,* Wiley, New York, **1987**.
65. W. Loewenstein, *Am. Mineral.*, **1954**, *39*, 92-96.
66. L. Marchese, J. Chen, J. M. Thomas, S. Coluccia and A. Zecchina, *J. Phys. Chem.*, **1994**, *98*, 13350-13356.
67. S. Bordiga, C. Lamberti, F. Geobaldo, A. Zecchina, G. Turnes Palomino and C. Otero Arean, *Langmuir*, **1995**, *11*, 527-533.
68. O. Cairon, T. Chevreau and J. C. Lavalley, *J. Chem. Soc., Faraday Trans.*, **1988**, *94*, 3039-3047.
69. K. G. V. A. Martins, G. Berlier, C. Bisio, S. Collucia, H. O. Pastore and L. Marchese, *J. Phys. Chem. C*, **2008**, *112*, 7193-7200.
70. K. Chakarova and K. Hadjiivanov, *J. Phys. Chem. C*, **2011**, *115*, 4806-4817.
71. G. E. Ewing, *J. Chem. Phys.*, **1962**, *37*, 2250-2256.
72. M. R. Delgado and C. O. Arean, *Energy*, **2011**, *36*, 5286-5291.
73. C. O. Arean, *J. Mol. Struct.*, **2008**, *880*, 31-37.
74. C. O. Arean, O. V. Manoilova, A. A. Tsyganenko, G. T. Palomino, M. P. Mentruit, F. Geobaldo and E. Garrone, *Eur. J. Inorg. Chem.*, **2001**, *7*, 1739-1743.
75. F. Lonyi and J. Valyon, *Micropor. Mesopor. Mater.*, **2001**, *47*, 293-301.
76. H. Wang and W. Xin, *Catal. Lett.*, **2001**, *76*, 225-229.
77. C. Flego and L. Dalloro, *Micropor. Mesopor. Mater.*, **2003**, *60*, 263-271.
78. T. Yashima, K. Miura and T. Komatsu, *Stud. Surf. Sci. Catal.*, **1994**, *84*, 1897-1904.
79. T. Takahashi, M. N. A. Nasution and T. Kai, *Appl. Catal. A: Gen.*, **2001**, *210*, 339-344.

80. M. Anilkumar and W. F. Hoelderich, *Catal. Today*, **2012**, *198*, 289-299.
81. I. Lezcano-Gonzales, A. Vidal-Moya, M. Boronat, T. Blasco and A. Corma, *Phys. Chem. Chem. Phys.*, **2010**, *12*, 6396-6403.
82. M. Lefenfeld, R. Raja, A. J. Paterson and M. E. Potter, US Patent, **2010**, US 20100249476.
83. M. Lefenfeld, R. Raja, A. J. Paterson and M. E. Potter, EU Patent, **2010**, EP 2389245 A2.
84. M. Lefenfeld, R. Raja, A. J. Paterson and M. E. Potter, WO Patent, **2010**, WO 2010085708 A2.
85. C. Zenonos, G. Sankar, F. Cora, D. W. Lewis, Q. A. Pankhurst, C. R. A. Catlow and J. M. Thomas, *Phys. Chem. Chem. Phys.*, **2002**, *4*, 5421-5429.
86. G. Sankar, J. M. Thomas and C. R. A. Catlow, *Top. Catal.*, **2000**, *10*, 255-264.
87. H. B. Mostad, M. Stocker, A. Karlsson and T. Rorvik, *Appl. Catal. A: Gen.*, **1996**, *144*, 305-317.
88. M. J. Peltre, P. P. Man, M. Briend, M. Derewinski and D. Barthomeuf, *Catal. Lett.*, **1992**, *16*, 123-128.
89. R. Wendelbo, D. Akporiaye, A. Andersen, I. M. Dahl and H. B. Mostad, *Appl. Catal. A:Gen.*, **1996**, *142*, L197-L207
90. Y-J. Lee, S-C. Baek and K-W. Jun, *Appl. Catal. A:Gen.*, **2007**, *329*, 130-136.
91. S. Coluccia, L. Marchese and G. Martra, *Micropor. Mesopor. Mater.*, **1999**, *30*, 43-56.
92. T. Bucko, J. Hafner and L. J. Benco, *Phys. Chem. A*, **2004**, *108*, 11388-11397.
93. N. Jappar, Y. Tanaka, S. Nakata and T. Tatsumi, *Micro. Meso. Mater.*, **1998**, *23*, 169-178.
94. G. Metz, X. Wu and S. O. Smith, *J. Magn. Reson. A,* **1994**, *110*, 219-227.
95. B. M. Fung, A. K. Khitrin and K. J. Ermolaev, *J. Magn. Reson.*, **2000**, *142*, 97-101.
96. N. M. Szeverenyi, M. J. Sullivan and G. E. Maciel, *J. Magn. Reson.* **1982**, *47*, 462-475.
97. S. Hayashi and K. Hayamizu *Bull. Chem. Soc. Jpn,* **1989**, *62*, 2429-2430.
98. J. D. van Beek, *J. Magn. Reson.*, **2007**, *187*, 19-26.

Chapter 4: Modifying the nature of acid sites through the bimetallic substitution of nanoporous frameworks

The following people have contributed to the work in this chapter:

Enrica Gianotti of Dipartimento di Scienze e Innovazione Tecnologica, Alessandria and Maela Manzoli of the University and Diparmento di Chimica e NIS-Centro di Eccellenza, Torino, Italy (respectively) obtained all the FT-IR data in this chapter.

Danni Sun of the Unviersity of Southampton helped to obtain the isopropylation catalytic data.

4.1 Tailoring acid-sites in AlPOs

In the modern era the ever-growing global population places increasingly stringent demands on energy production. As a result the requirement for cleaner and more sustainable technology is becoming progressively more urgent. Advances in catalysis are attempting to meet these demands on multiple fronts, some by employing more sustainable feedstocks, while others seek to improve existing chemical routes through the use of more effective catalytic materials. Despite the diverse expansion of modern catalysis, it is clear that any significant advances in sustainability will require the new and inspired development of new catalytic systems. This subsequently places significant importance on the design and creation of catalytic materials with increasingly intricate active sites, with the aim of optimising product yields.[1-5]

In the last decade the need to adroitly construct precise active species has prompted a surge in the development of multimetallic systems.[6-9] A growing number of examples in the literature describe how the proficient cooperation of different metals may influence the structure-property correlations between the active site, the support and the reactants, ultimately achieving catalytic benefits.[10-12] Such notions are already well-understood in the field of nanoparticle chemistry, where complete control of particle placement and morphology is the definitive goal. While several synthetic protocols are already

well-established to modulate such properties, the possible combinations are limited in monometallic species. However, the introduction of a second metal offers a plethora of new synthetic possibilities towards optimising catalyst performance.[6,10]

While such systems are still under-development, current synthetic techniques to engineer such species are reliant on precise and delicate synthetic conditions[6] or increasingly sensitive and expensive precursors.[12,13] Therefore in-order to increase industrial feasibility, and be applicable to a wider-range of processes, more robust and versatile synthetic strategies need to be established. Previously the benefits of bimetallic substitution have been shown through the synthesis of novel bifunctional nanoporous aluminophosphate (AlPO) systems. By introducing two discrete active sites into the same microporous framework it was shown that one could perform multi-step reactions, such as the sustainable production of ε-caprolactam from cyclohexanone, in a one-pot method.[14-16] This circumvented the need for caustic reagents such as oleum, whilst generating minimal waste. This was achieved by simultaneously incorporating a redox-active cobalt[17] and a silicon brønsted acid site,[18] into the same framework. The initial step, the ammoximation of cyclohexanone to the oxime, was performed by the cobalt species, whilst the subsequent Beckmann rearrangement of oxime to ε-caprolactam occurred at the silicon site.[14-16]

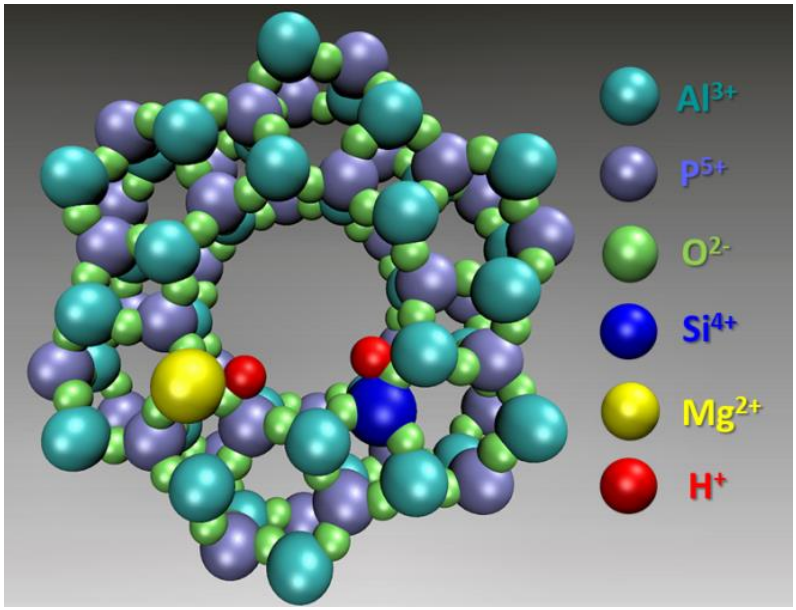

Figure 4.1: Schematic detailing bimetallic metal substitution in MgSiAlPO-5

More recently it has been shown that the potential of this synthetic strategy extends beyond bifunctionality. Through careful and considered synthesis techniques it is possible to engineer novel synergistic interactions between metal sites. By controlling the relative proximity and location of the two individual species[19,20] one can prompt metal-metal interactions (when the two are sufficiently close) which subtly alter the local environment of the two species, enhancing their catalytic potential.[20] While such enhancement requires precise and careful planning it is not unique to specific metal combinations, and has to date been shown in a range of bimetallic AlPO species for both acid-catalysed (Figure 4.1) and oxidation reactions.[19-22]

In this chapter it is demonstrated how induced site-specific interactions can be tailored between different metal active species for acid-catalysed hydrocarbon transformations using Mg, Zn and Si-containing AlPO catalysts. The effects of bimetallic substitution are investigated through a combined multi-reaction catalytic study, demonstrating the advantages of the novel bimetallic catalysts for the vapour-phase Beckmann rearrangement of cyclohexanone oxime to ε-caprolactam, and also the isopropylation of benzene to cumene. These reactions are of great significance in the polymer and fine-chemical industry,[23-25] whilst also showing efficacy for contrasting Brønsted acid sites, yielding valuable diagnostic information on the nature of the acid site. The former reaction (Beckmann rearrangement) shows a preference for weak acid sites, with stronger sites facilitating the formation of coking and ring-opening by-products.[26,27] In stark contrast the isopropylation reaction requires strong acid sites to active propan-2-ol, with weak sites proving insufficient for this process.[28] By contrasting the behaviour of the novel bimetallic catalysts for these diagnostic reactions we are able to gain significant insights into the nature and specific acid strength of the active sites within these heterogeneous catalysts.

Despite being basic in its bulk oxidic form, magnesium has been used to great extent as a dopant in microporous materials, particularly in zeolites and AlPOs, primarily in acid catalysis (Table 4.1). The use of magnesium-incorporated zeotype species can be primarily be divided into three sections; Magnesium-AlPOs for use as acid catalysts, Magnesium-AlPOs as acidifed supports for heavy-metal dopants and magnesium as a dopant to pacify strong-acid sites in zeolites. In AlPO chemistry magnesium has been repeatedly shown to generate

the strongest Brønsted acid sites of all divalent dopants within an AlPO framework,[29] this is attributed to a range of factors including M-OH bond and dopant size.[29] In stark contrast magnesium is used more as a pacifying agent in zeolitic frameworks to control and limit both the acid strength and the density of acid sites (Figure 4.2). This behaviour is attributed to the different environment of the magnesium dopant, in AlPOs the magnesium is isomorphously substituted into the framework to generate a charge imbalance (2+ dopant substituting a 3+ dopant), which is annulled by the proton. In zeolites magnesium acts instead as the charge balancing cation, which will displace the protons in the framework.

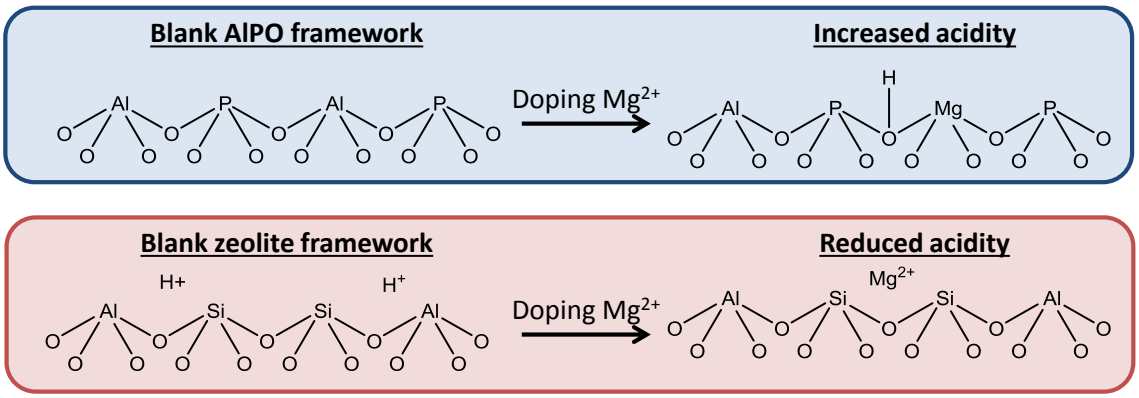

Figure 4.2: Scheme outlining the effect of adding magnesium into AlPO and zeolite frameworks.

Table 4.1: Summarising the use of magnesium in solid-state catalysis.

System	Reaction	Product yield	Ref
MgAlPO-18	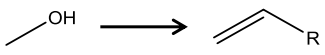	96 wt%	30
MgAlPO-5	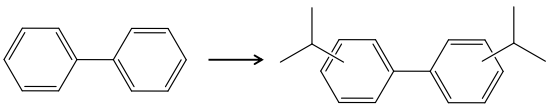	42 mol%	31
MgAlPO-5	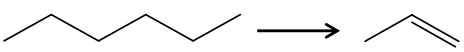	36 mol%	32

Pt/MgAlPO-11	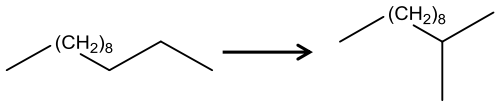	76 wt%	33
Pt/MgAlPO-5	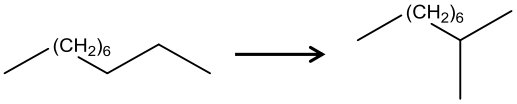	> 99 mol%	34
Pt-Pb/MgAlPO-5	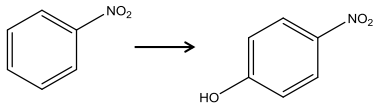	71 mol%	35
Mg/HZSM-5	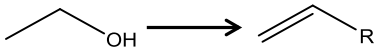	97.0 mol%	36
Mg-Pt/ZSM-23	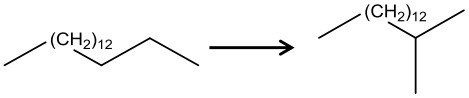	71 wt%	37
Mg-Si-P/ZSM-5	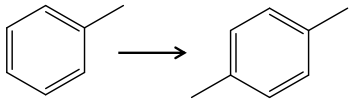	22 mol%	38
Mg-Zn/ZSM-5/Al_2O_3	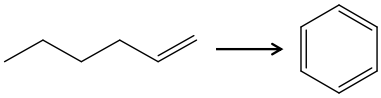	30 wt%	39

In contrast zinc-substituted AlPOs have been limited purely to acid catalysis, given their weaker acid strength they have not attracted the same attention as MgAlPOs as acidifed supports. As a result of this there are comparatively fewer reports of ZnAlPOs as acid catalysts. There has been an increased interest in zinc as a dopant for zeolites, as it has been shown to be a useful Lewis acid for a range of reactions (Table 4.2).

Table 4.2: Summarising the use of zinc in solid-state catalysis.

System	Reaction	Product yield	Ref
ZnAlPO-5	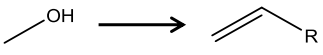	38.7 wt%	40
ZnAlPO-5	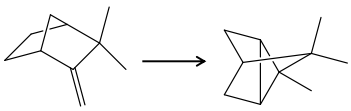	35.1 wt%	41

Modifying the nature of acid sites through the bimetallic substitution of nanoporous frameworks

ZnAlPO-11	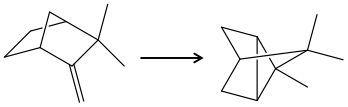	40.2 wt%	41
ZnAlPO-5	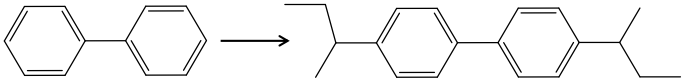	55 wt%	42
ZnAlPO-40	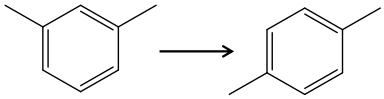	58 wt%	43
Zn/SiO_2	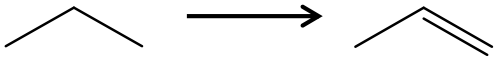	TOF 0.772 hr^{-1}	44
Zn/HZSM-5	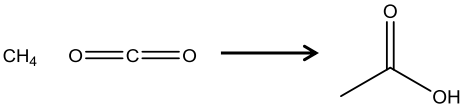	N/A	45
Zn/H-Beta	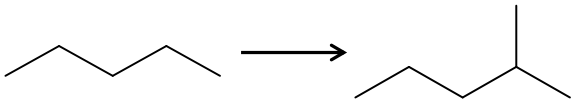	28.9 mol%	46

As a result, the contrasting Brønsted acid centres which are engineered on incorporation of Mg^{2+} and Zn^{2+} ions, make them excellent candidates for engineering optimising the chemical activity of the Beckmann rearrangement of cyclohexanone oxime and the isopropylation of benzene. Both of these processes are known to require contrasting Brønsted acid sites to proceed (Figure 4.3).[26-28] The combination of these two dopants with silicon (the use of which has been extensively discussed in the Beckmann rearrangement in the previous chapter) offers a range of possibilities for complementary acid sites to enhance these particular acid catalysed reactions.

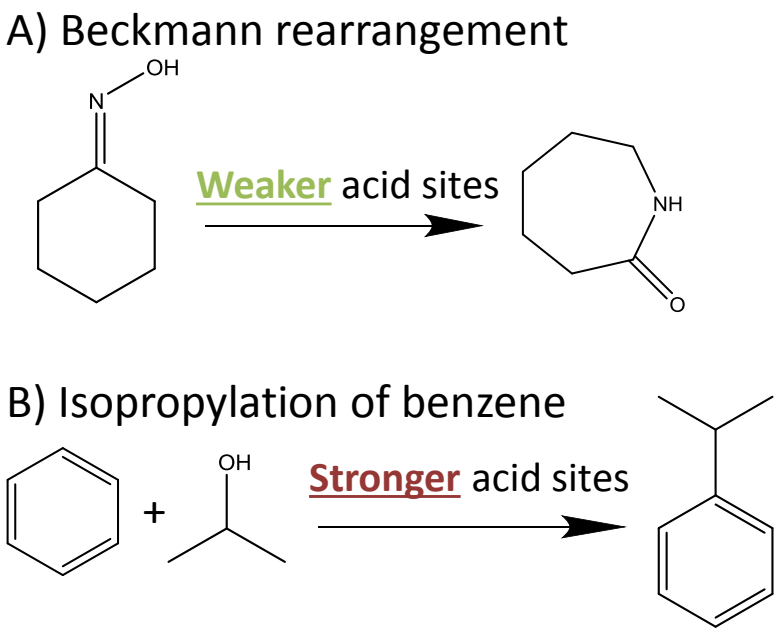

Figure 4.3: Schematic of A) Beckmann rearrangement of cyclohexanone oxime and B) Isopropylation of benzene.

4.2 Results and discussion – Synthesis and structural characterisation

With an aim to generate Brønsted acid species inside the AlPO-5 framework the structural integrity of the targeted mono- and bi-metallic samples was confirmed using a range of physico-chemical characterisation techniques. In all samples the intended AFI (AlPO-5) phase was the only AlPO phase present, confirming the success of the synthetic procedure, despite the metal incorporation (Figures 4.4, 4.5 & Table 4.3). The characteristic AFI patterns were examined though Reitveld analysis, which subsequently confirmed that only minimal distortion of the unit cell had occurred. The deviation was quantified as being less than 1% of the undoped-framework parameters in all cases, in concurrence with the small quantities of metal incorporated into the systems (Table 4.4). While subtle, these slight changes in the unit cell parameters account for the shifts in peak position between the different samples. On closer inspection of the 30-55° range the Zn-containing systems show trace amounts of ZnO within the pores of the AlPO framework, however, given the low intensity of the pattern in this range it is not possibly to quantify

the total fraction of the zinc in this state (Figure 4.5).

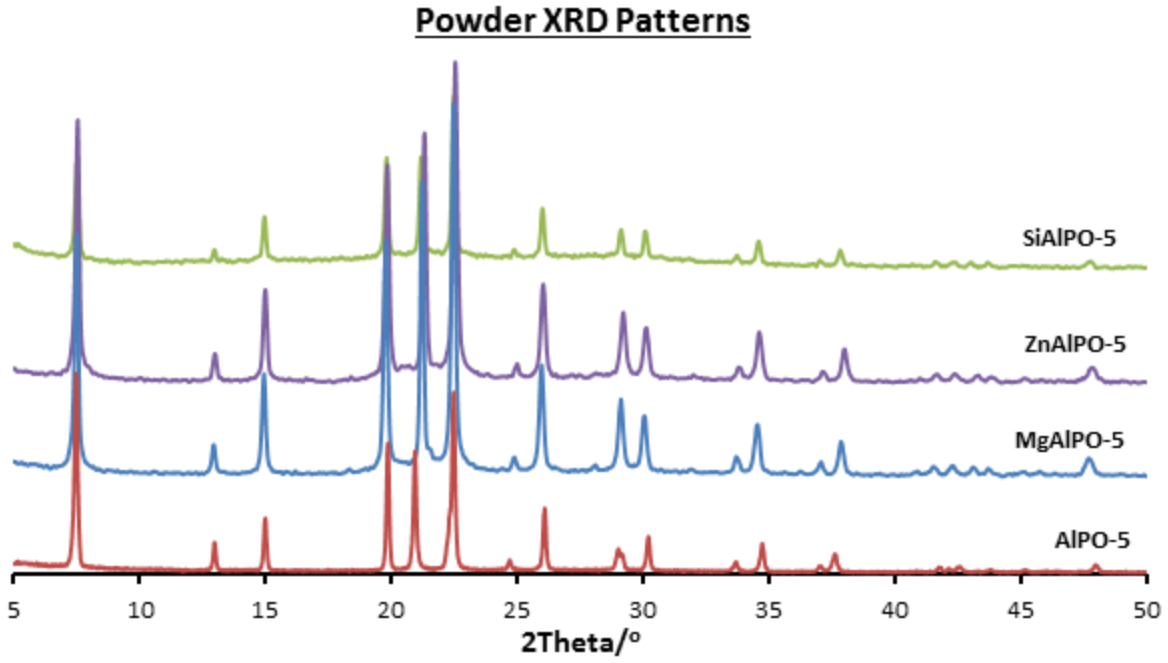

Figure 4.4: Powder X-ray diffraction pattern of monometallic AlPO-5 systems

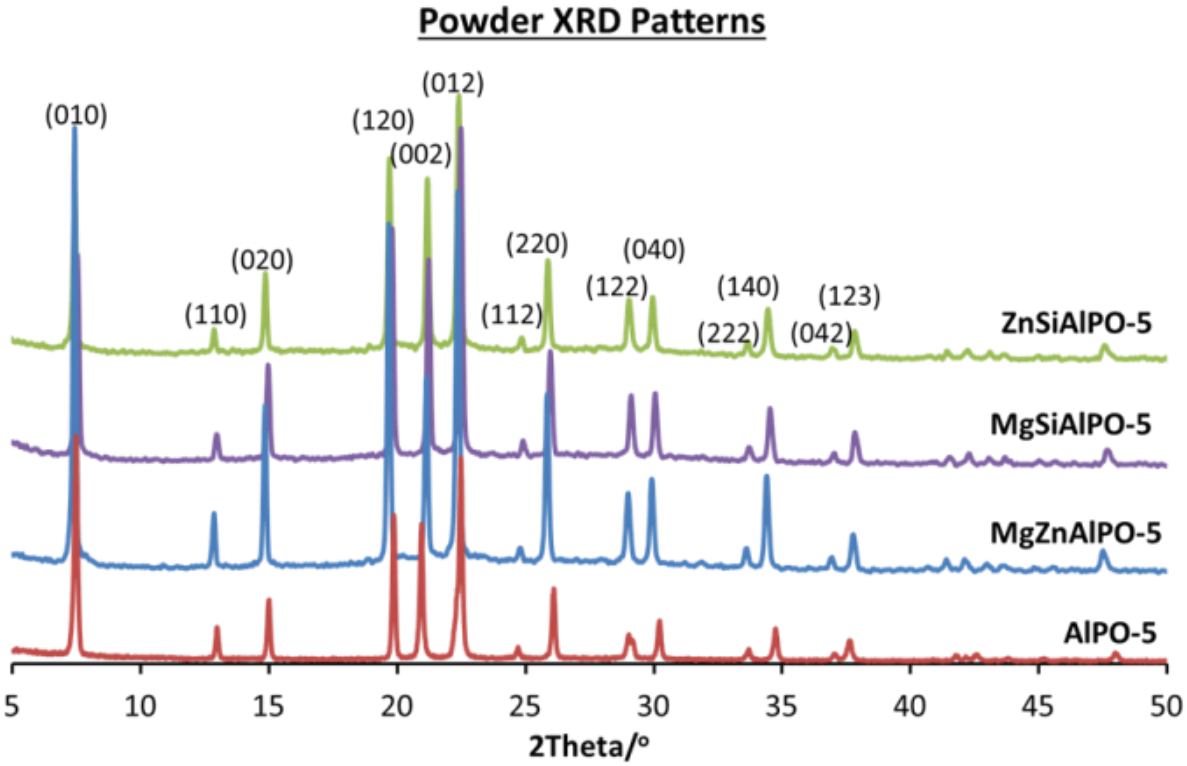

Figure 4.5: Powder XRD patterns of the novel bimetallic Mg, Zn and Si-containing AlPO-5 catalysts

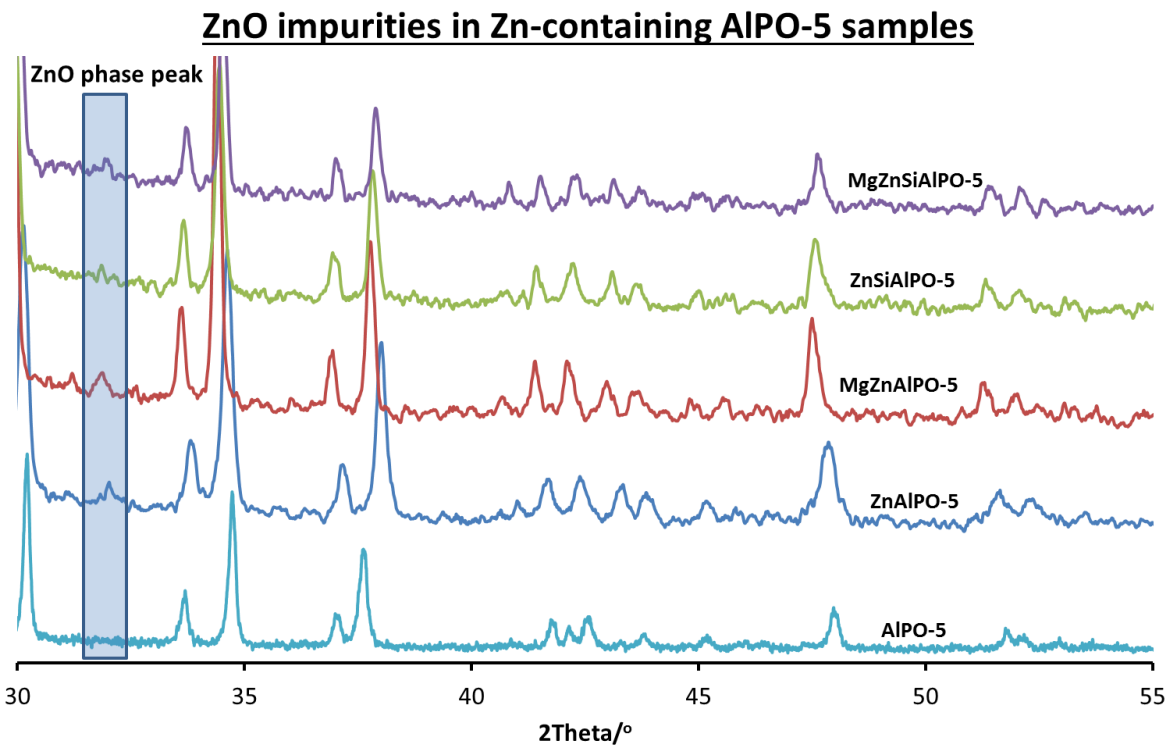

Figure 4.6: Zoomed XRD pattern of Zn-containing species revealing trace quantities of ZnO hexagonal phase.

Table 4.3: XRD parameters, particle size and surface area summary

System	Optimized XRD parameters for P6cc		Particle size/nm	BET SSA/m^2 g^{-1}
	a/Å	c/Å		
AlPO-5	13.69	8.43	56.5	295.1
ZnAlPO-5	13.68	8.34	55.5	165.4
MgAlPO-5	13.71	8.40	55.5	193.3
SiAlPO-5	13.70	8.39	54.8	181.9
MgZnAlPO-5	13.80	8.41	66.3	283.3
MgSiAlPO-5	13.71	8.39	52.6	168.1
ZnSiAlPO-5	13.76	8.40	64.2	236.2

Table 4.4: Full ICP data

System	Al/wt%	P/wt%	Zn/wt%	Mg/wt%	Si/wt%
AlPO-5	18.1	16.7	-	-	-
MgAlPO-5	15.9	20.6	-	0.85	-
ZnAlPO-5	16.4	21.2	2.11	-	-
SiAlPO-5	19.8	14.7	-	-	1.69
MgZnAlPO-5	17.0	22.9	1.86	0.72	-
MgSiAlPO-5	18.0	14.6	-	0.89	1.70
ZnSiAlPO-5	18.7	15.9	1.33	-	1.66

The porous nature of the catalytic frameworks was confirmed through volumetric BET analysis, with some systems displaying a prominent derivation from the undoped AlPO-5 system (295.1 to 165.4 m^2 g^{-1}, Table 4.3). The reduction in surface area is attributed to the addition of metal dopants modifying the delicate crystallisation kinetics, in some cases forming extra-framework species within the pores, in accordance with powder XRD findings (Figure 4.6). By applying Scherrer's equation on the 7.4° peak the uniformity of particle sizes was confirmed, as all systems fell within a narrow range of 52-66 nm (Table 4.3). This was confirmed through SEM, whereby all systems contained spherical particles of comparable size (10-20 μm) with no visible extra phases present (Figures 4.7-4.9). ICP analysis confirmed that the bimetallic samples contain similar metal loadings to the analogous monometallic systems allowing direct comparisons to be made between the catalytic behaviour of the different systems (Table 4.4).

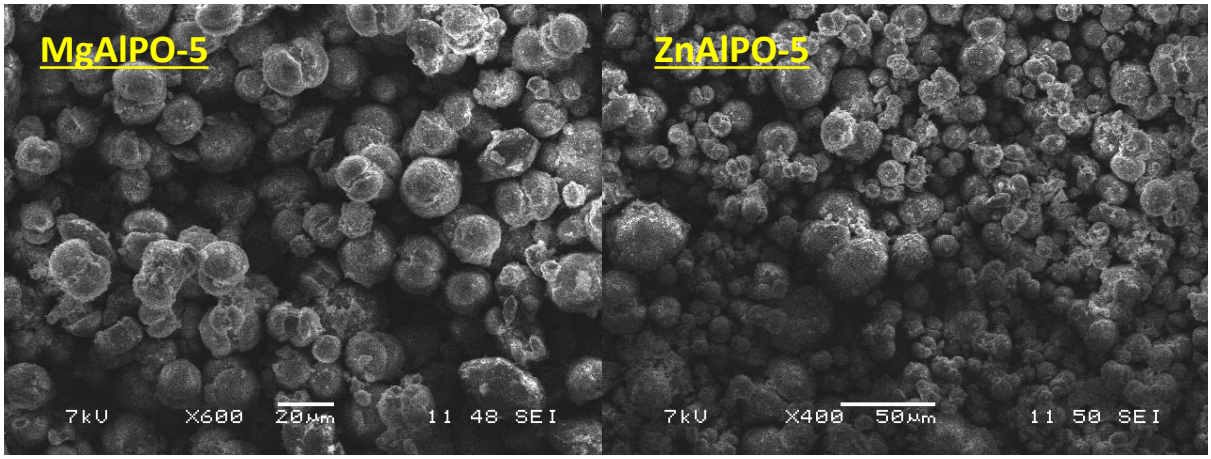

Figure 4.7: SEM image of monometallic MgAlPO-5 and ZnAlPO-5.

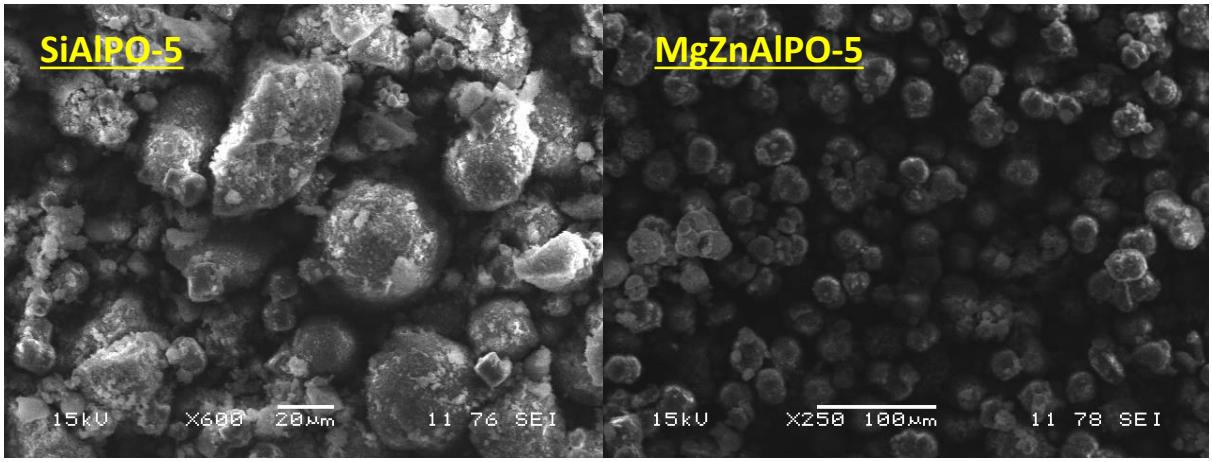

Figure 4.8: SEM image of monometallic SiAlPO-5 and MgZnAlPO-5.

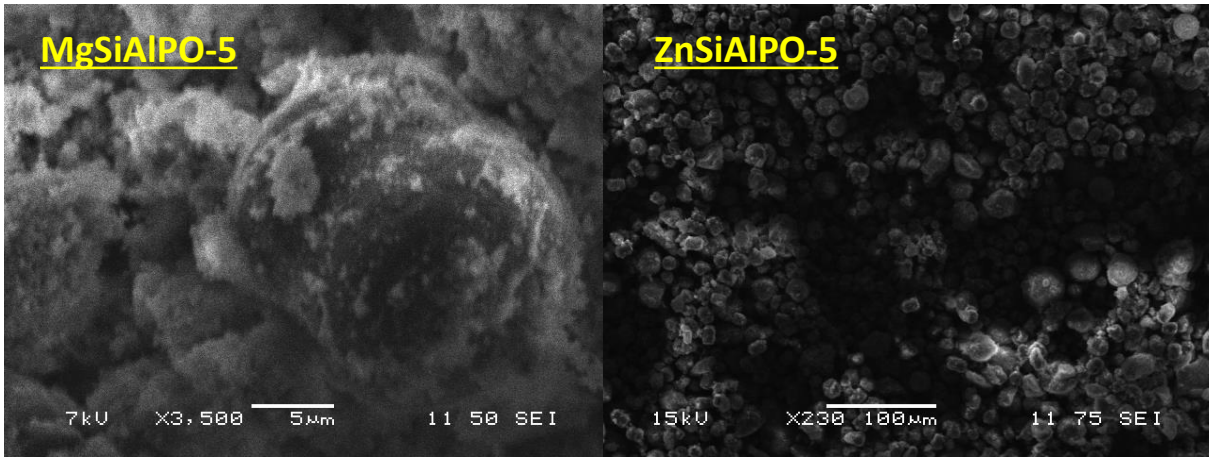

Figure 4.9: SEM image of monometallic MgSiAlPO-5 and ZnSiAlPO-5.

4.3 Results and discussion – Exploring the acid sites of the monometallic AlPOs

Given the contrasting nature of the acidic active site required to perform the isopropylation and the Beckmann rearrangement reactions, the differences in catalytic performance for these reactions is symptomatic of the acid site strength in the metal-doped AlPO catalysts. The concurrence in physical characterisation properties between the different Mg, Zn and Si-containing

Modifying the nature of acid sites through the bimetallic substitution of nanoporous frameworks catalysts allows any differences in catalytic activity to be attributed to the direct influence of the individual acid sites.

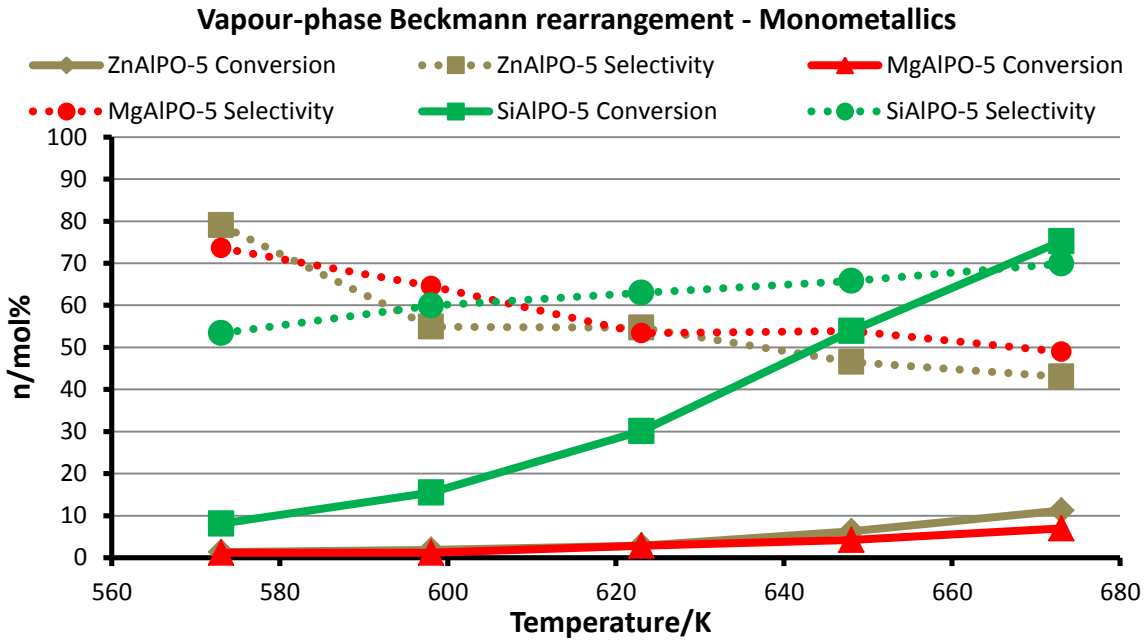

Figure 4.10: Full catalytic data for the vapour-phase Beckmann rearrangement of cyclohexanone oxime using monometallic AlPO-5 systems. Reaction conditions: WHSV 3.3 hr^{-1}, Helium carrier gas flow 20 ml/min, 0.3 g of catalyst, liquid feed 300g/l of oxime in methanol, temperature as shown.

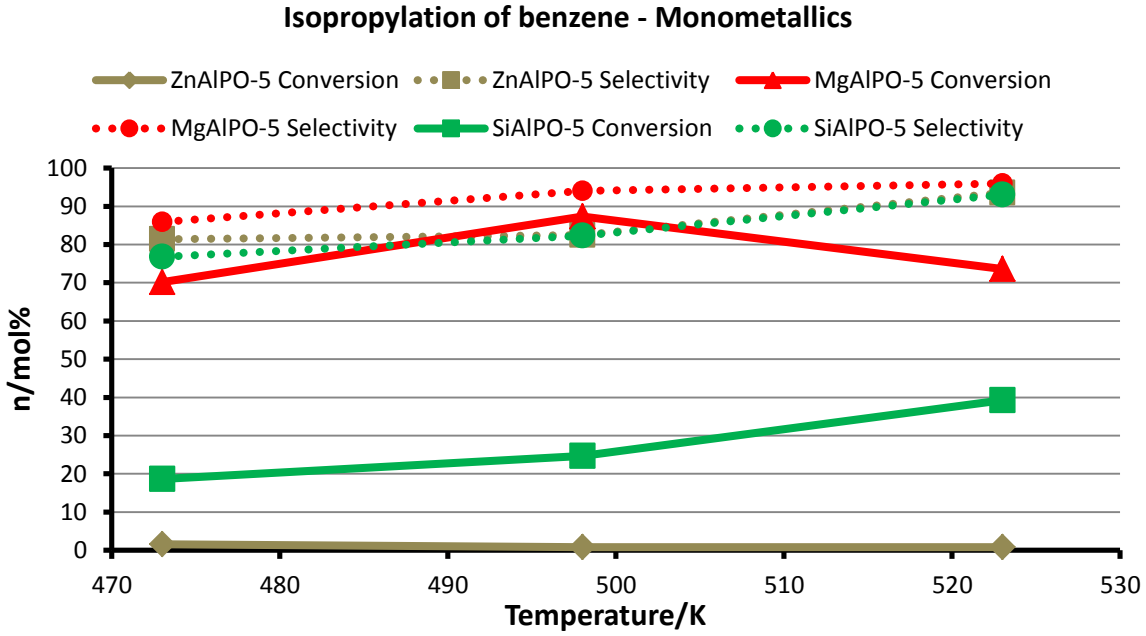

Figure 4.11: Full catalytic data for the isopropylation of benzene using monometallic AlPO-5 systems. Reaction conditions: WHSV of 3.5 hr^{-1}, Helium

carrier gas of 10 ml/min, feed 6:1 mole ratio of benzene:isopropanol, temperature as shown.

The differing catalytic activity between the MgAlPO-5 and SiAlPO-5 catalysts can be directly correlated to the precise nature of the individual active sites. MgAlPO-5 displays enhanced activity for the isopropylation of benzene (Figure 4.11), whilst SiAlPO-5 shows increased specificity for ε-caprolactam in the Beckmann rearrangement (Figure 4.10). These observations are consistent with literature findings, confirming that the Brønsted acid sites generated by the inclusion of Mg^{2+} ions into the AlPO framework are strong, whereas those formed by the isomorphous substitution of Si^{4+} are weaker.[47] The activity demonstrated by both of catalysts in their respective reactions confirms the presence of Brønsted acidity within these catalysts. A clear indication that isomorphous framework substitution of the Mg^{2+} and Si^{4+} dopants has occurred in the nanoporous architecture of the monometallic species. In stark contrast, the ZnAlPO-5 catalyst appears to be relatively inactive for both reactions suggesting little to no Brønsted acid sites are present in this material. Given the significant Zn content of the monometallic ZnAlPO-5 species and the relative inert catalytic performance of the system it must be concluded that unlike the Mg^{2+} and Si^{4+} species the Zn^{2+} ions has not undergone framework substitution, instead forms extra-framework species. It is therefore concluded that the strength of the framework acid site formed is strongly dependent on the metal dopant. Further, it is noted that despite the similar valency and size of the Mg^{2+} and Zn^{2+} the nature of the metal strongly influences the crystallisation kinetics that determines whether the dopant is isomorphously substituted into the framework, or instead, exists as an extra framework site.

To further enhance these findings probe based FT-IR was used to investigate the quantity and nature of the Brønsted acid sites present in the catalysts. Due to the high scattering profile of the AlPO-5 catalysts in the characteristic Brønsted acid site region (typically 3600-3500 cm^{-1} in the IR spectrum), the use of probe molecules is necessary to gain a more detailed understanding of the Brønsted acid sites present in metal-substituted AlPO-5 catalysts. CO was adsorbed at 80 K on the undoped and monometallic species, in order to specifically observe and decipher its interaction with the OH groups (Figure 4.12). (Note that CO is only able to interact, via H-bonding with hydroxyl groups, at low temperatures). The hydrogen-bonded C-O stretching mode

emerges in the 2155-2175 cm^{-1} range, whereas the peak at 2138 cm^{-1} is attributed to liquid-like CO,[48] with the latter being particularly pronounced on adsorption of 5 mbar of CO. The spectrum of undoped AlPO-5 exhibits a band at 2165 cm^{-1}, which increases with increased CO pressure (grey curve); and in conjunction with the band at 2138 cm^{-1} (that has been previously attributed to liquid-like CO). The band at 2165 cm^{-1} is assigned to CO interacting exclusively with P-OH groups,[49,50] as these are the only hydroxyl groups present in the undoped AlPO-5 catalyst, owing to the lack of dopant atoms. The metal-substituted AlPO-5 catalysts show a component at 2171 cm^{-1}, which can be assigned to the stretching mode of the CO, interacting via H-bonding, with the more acidic hydroxyl groups that can be attributed to the presence of Brønsted acid centres.[51-54] It is indeed noteworthy that the increased intensity for MgAlPO-5 and SiAlPO-5, relative to the undoped AlPO-5 species, at 2171 cm^{-1} provides strong evidence for framework incorporation of the Mg^{2+} and Si^{4+} ions into the AlPO-5 architecture. As is evidenced by the creation of the associated Brønsted acid sites (Figure 12). In stark contrast it is noted that ZnAlPO-5 shows no increased intensity relative to the undoped AlPO-5 species. This suggests that the incorporation of zinc into the material has not lead to the formation of Brønsted acid sites as expected, thus it has not undergone isomorphous framework substitution. This observation is in good agreement with the poor catalytic performance seen by the monometallic ZnAlPO-5 for both the weak-acid Beckmann rearrangement and the strong acid isopropylation reactions.

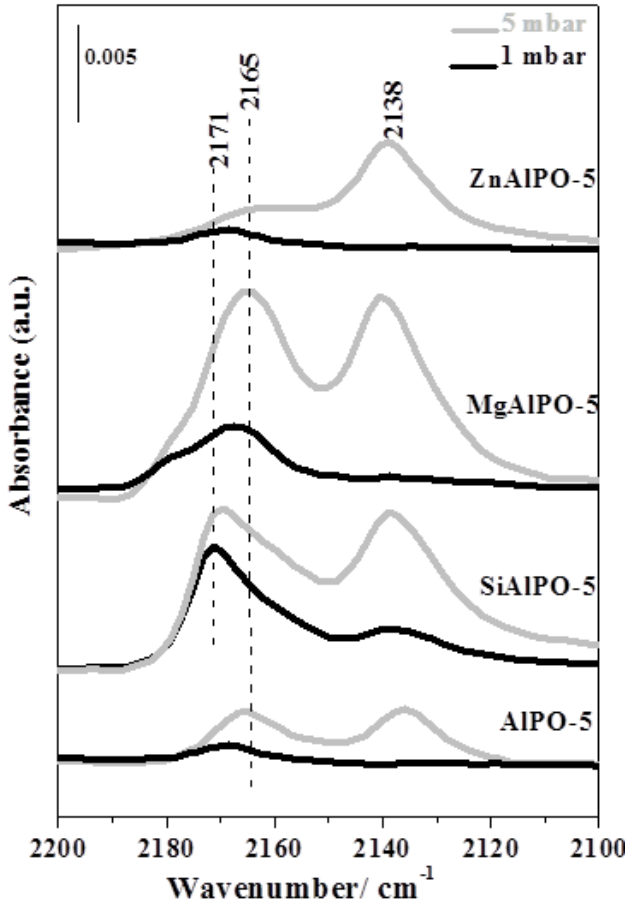

Figure 4.12: CO-probed FT-IR of the monometallic AlPO-5 species.

In order to further elucidate the nature and the strength of the Brønsted acid sites, a stronger base such as 2,6-DMP is required. Compared to pyridine, 2,6-DMP yields the protonated species more readily, due to its stronger basicity[55,56] and its weaker affinity for Lewis acid sites, owing to the steric hindrance induced by the methyl groups.[57] In Figure 4.13, the IR active modes of liquid and adsorbed 2,6-DMP are highlighted. In particular, the ν_{8a} mode, which in the liquid-phase appears at 1594 cm^{-1}, is very sensitive and allows the identification of different types of 2,6-DMP adsorption on solid catalysts. It is also striking that when the ν_{8a} wavenumber is higher than 1625 cm^{-1}, it characterises the presence of protonated species (2,6-$DMPH^+$), whereas lower wavenumbers correspond to coordinated or H-bonded species (DMPL, Figure 4.13).

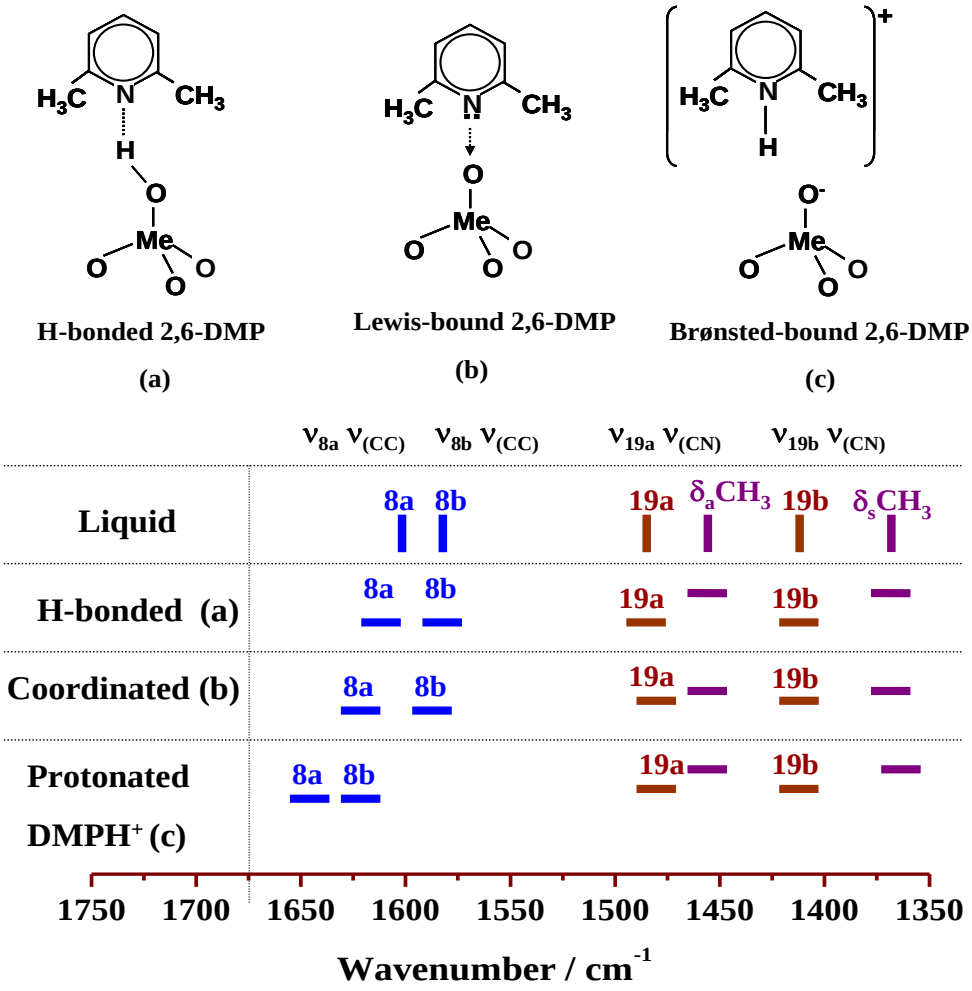

Figure 4.13: Interpreting lutidine (2,6-DMP) peak positions.

In Figure 4.14, the FT-IR spectra collected after adsorption of 2,6-DMP at 4 mbar at different contact times on the nanoporous AlPO-5 catalysts are presented. Bands at 1595 and 1582 cm^{-1}, due to the ν_{8a} and ν_{8b} of liquid-like 2,6-DMP, are visible together with complex bands in the 1650-1600 cm^{-1} range, assigned to the ν_{8a} and ν_{8b} modes of coordinated, protonated and H-bonded 2,6-DMP species (as shown in Figure 4.13). Bands in the 1500-1450 cm^{-1} range are also present: these are due to the ν_{19a} and ν_{19b} modes and can also be attributed to the bending modes of the $-CH_3$ groups. It should however be noted that the peaks in this region (1500-1450 cm^{-1}) are quite insensitive to the different coordination environments and yield very little in terms of valuable information pertaining to the nature of acid sites present in these catalysts. In the un-doped AlPO-5 catalyst, in which only P-OH groups are present (as evidenced earlier by CO adsorption studies; Figure 4.12), the bands in the 1650-1600 cm^{-1} range can be assigned to 2,6-DMP, interacting via H-bonding,

with the P-OH sites that are generated immediately after short exposure (2 minutes); and as expected, do not increase after prolonged contact times.

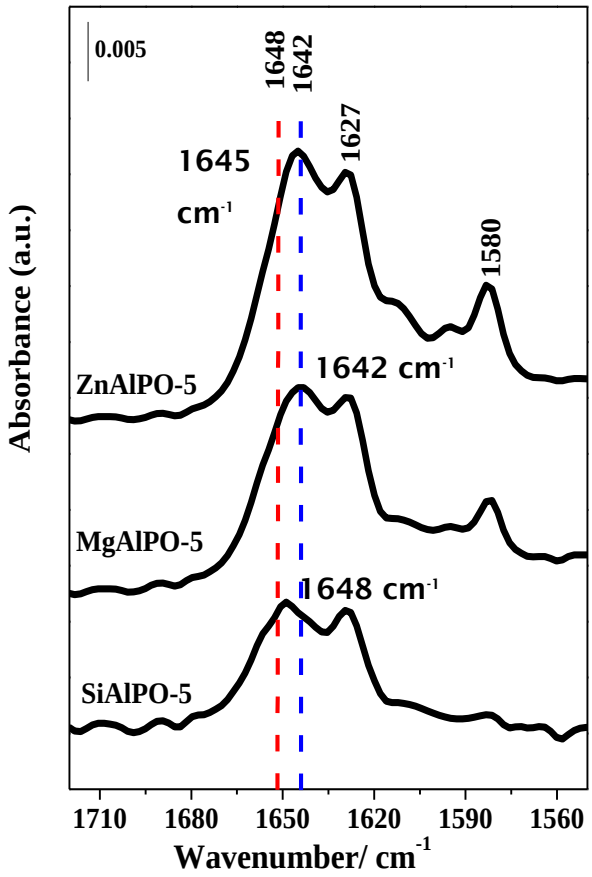

Figure 4.14: FT-IR spectra of outgassed 2,6-DMP at 298K on calcined SiAlPO-5, MgAlPO-5 and ZnAlPO-5, with peak maxima labelled.

The ν_{8a} mode of the protonated 2,6-DMP is present in all three catalysts (1655-1640 cm^{-1} range) and, from the analysis of their relative peak positions, it is possible to deduce information on the nature and strength of the Brønsted acid sites[58]: the stronger the Brønsted acidity, the lower is the position of the ν_{8a} band. With a view to clarifying further the position of this ν_{8a} band, the FT-IR spectra of the catalysts, outgassed at 298 K after 2,6-DMP adsorption, have been examined (Figure 4.14). It was noted that by outgassing the catalysts, the spectra shows only spectroscopic features of the irreversibly adsorbed 2,6-DMP species. In particular, it was noted that the position of the peak maxima of the ν_{8a} band was markedly different (Figure 4.14) in the four catalysts used in this study and this could be used to differentiate the nature and strength of their Brønsted acid sites. By combining the spectroscopic information outlined in Figures 4.14 and 4.12, it has been possible to contrast the relative acid

strengths of the undoped, mono-substituted and bi-substituted catalysts and categorise the degree of their Brønsted acidity in the following order: MgAlPO-5 > ZnAlPO-5 > SiAlPO-5 > AlPO-5; with MgAlPO-5 possessing a greater fraction of the *strong* Brønsted acid sites, whilst the undoped and mono-substituted Si-analogues exhibit a greater proclivity for *weak* Brønsted acid sites.

Through a careful marriage of the catalysis data and FT-IR it becomes apparent that both Mg^{2+} and Si^{4+} ions readily undergo framework substitution to generate brønsted acid centres in the AlPO-5 framework. By considering the spectra from the 2,6-DMP probe it is concluded that MgAlPO-5 possesses stronger acid sites whilst silicon possesses weaker acid sites, explaining their preference for the various catalytic reactions. In stark contrast Zn^{2+} formed extra framework species which did not facilitate the formation of Brønsted acid sites. In light of this it can be concluded that the three dopants are capable of producing unique catalytic environments, and as such make prime candidates for combining together to make novel bimetallic solid-acid catalysts.

4.4 Results and discussions – The introduction of zinc to form novel bimetallic species

Given the comparatively inert behaviour of ZnAlPO-5 it was of interest to observe the effect of introducing extra-framework zinc species to the already active MgAlPO-5 and SiAlPO-5 to create the novel bimetallic MgZnAlPO-5 and ZnSiAlPO-5 species. As shown previously the two novel bimetallic samples were synthesised to yield crystalline and phase-pure samples. In the synthesis procedure the amount of silicon and magnesium was purposefully kept the same as the monometallic samples. This is so that any catalytic differences can be attributed to the presence of zinc, and is therefore not a result of changes in metal loadings. As such, the behaviour of the bimetallic systems was contrasted with the analogous monometallic systems, via identical catalytic testing.

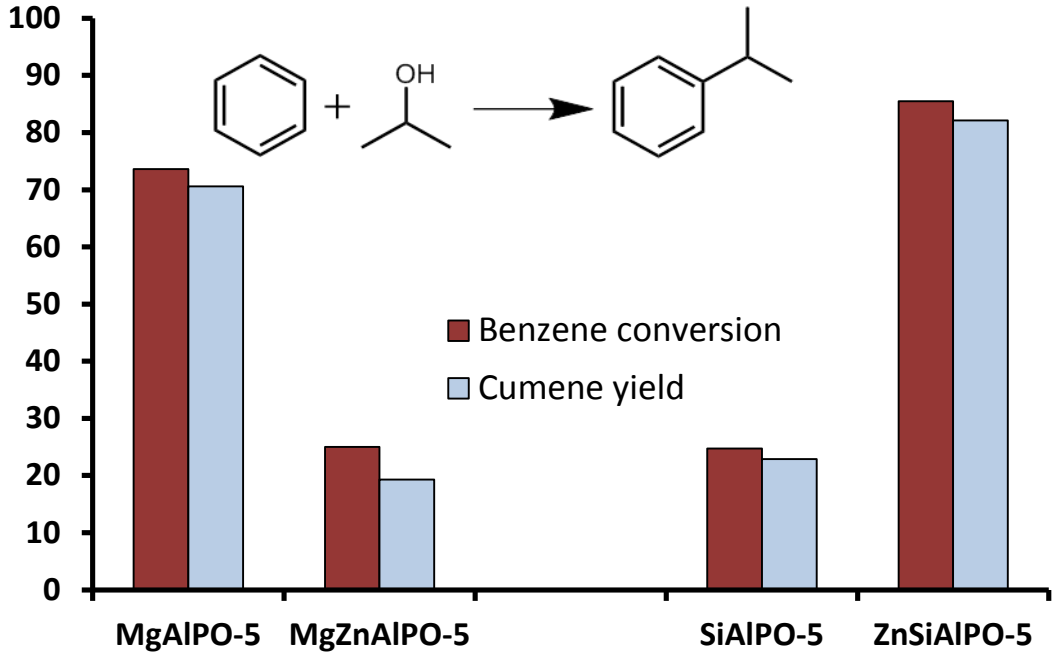

Figure 4.15: Effects of adding zinc on the isopropylation of benzene. Reaction conditions: WHSV of 3.5 hr^{-1}, Helium carrier gas of 10 ml/min, feed 6:1 mole ratio of benzene:isopropanol, temperature 523 K.

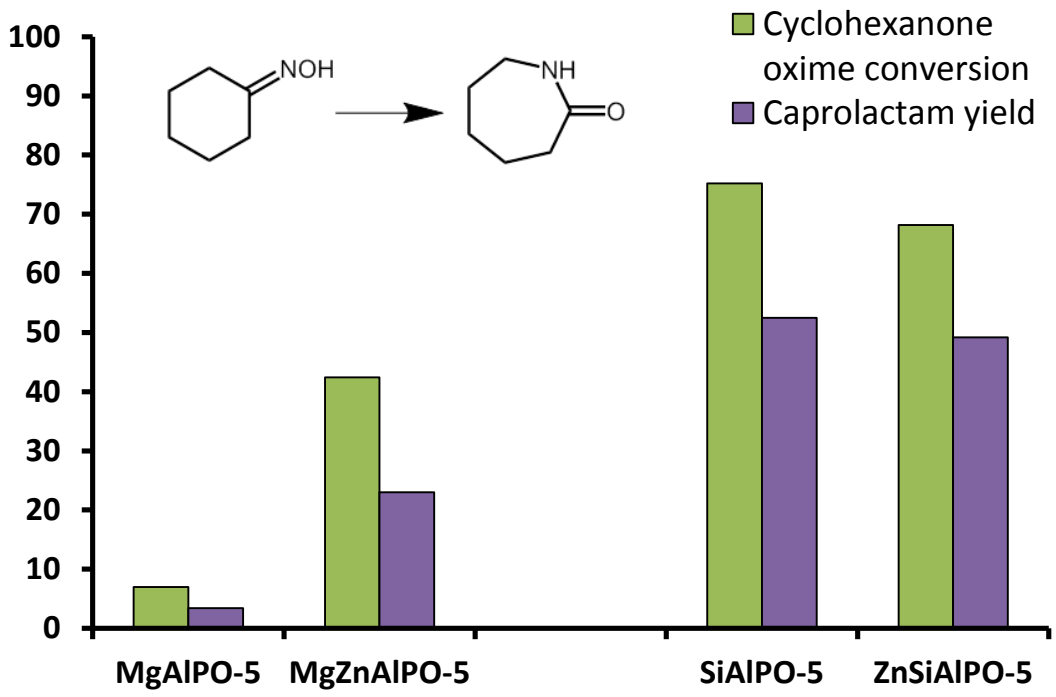

Figure 4.16: Effects of alloying zinc on the Beckmann rearrangement of cyclohexanone oxime. Reaction conditions: WHSV 3.3 hr^{-1}, Helium carrier gas flow 20 ml/min, 0.3 g of catalyst, liquid feed 300g/l of cyclohexanone oxime in methanol, temperature 673 K.

It is clear that the addition of zinc to form bimetallic species is influencing the two systems, despite the relative inactivity of zinc in the monometallic form; ZnAlPO-5. It is noted that zinc has curiously different effects on each system for each reaction. Contrasting MgZnAlPO-5 with MgAlPO-5 reveals that the cumene yield is significantly reduced by the addition of zinc (Figure 4.15), though the yield of caprolactam is greatly improved (Figure 4.16). This result shows that zinc is not acting as a simple poison, as this would result in a reduction in catalytic potential in both reactions. Similarly zinc is also not acting as a promoter, as this would instead improve both reactions. As such it is suggested that zinc is actually modulating the active site and tuning the acidic properties, tailoring them towards one reaction over another. Similar behaviour is observed for the addition of zinc to form ZnSiAlPO-5, one reaction is improved while the other is hindered, again suggesting modulatory behaviour. However, we observe opposite behaviour between the ZnSiAlPO-5 and MgZnAlPO-5, suggesting that zinc is undergoing metal-specific interactions with the different active sites, which is then promoting unique catalytic behaviour. In order to gain a greater understanding of the active species and the acid-site behaviour FT-IR spectroscopy was used to gain further insight into the systems.

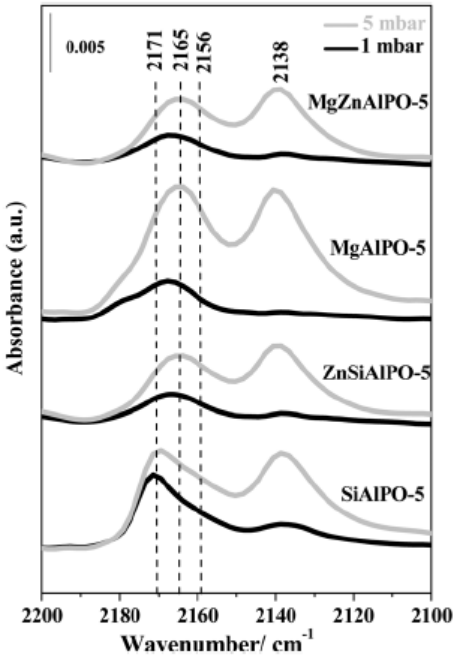

Figure 4.17: CO-probed FT-IR of zinc-containing species in the C-O stretch region.

Recall from previous FT-IR that zinc does not undergo framework substitution, as witnessed by the comparable intensity of the 2165 cm^{-1} peak to the undoped AlPO-5 system (Figure 4.12). Given that zinc does not undergo framework substitution, and that similar levels of magnesium were incorporated into the monometallic and bimetallic systems, then the intensity of the 2165 cm^{-1} signal should be similar in the monometallic and bimetallic species. This is however not the case, and it can be seen that the presence of zinc is actively supressing the formation of available acid sites (Figure 4.17). In both cases the total acidity is reduced as a result of zinc being present, this behaviour would be typical of a poison, and explains the reduction of cumene yield for the MgZnAlPO-5 and the caprolactam yield for ZnSiAlPO-5. This decrease in acidity is attributed to the formation of ZnO species on the acidic regions. It is believed that the Brønsted acid species are acting as nucleation points for the ZnO particles, thus blocking the acid sites from the CO probe molecule. To explain any improvements in product yield we must also look to the strength of the Brønsted acid sites using the 2,6-DMP probe.

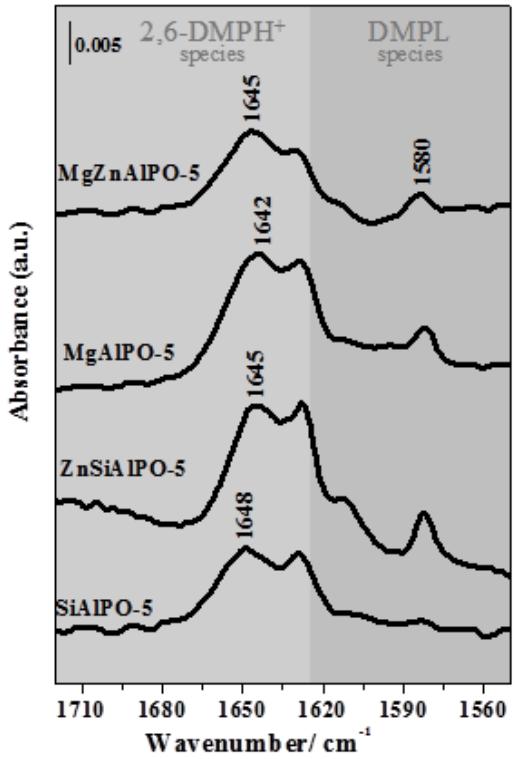

Figure 4.18: 2,6-DMP probed FT-IR to investigate the effect of zinc.

Table 4.5: Position of the v_{8a}(CC) band in the mono and bimetallic AlPO-5 catalysts.

Catalyst	v_{8a}(CC) / cm^{-1}
MgAlPO-5	1642
MgZnAlPO-5	1645
SiAlPO-5	1648
ZnSiAlPO-5	1645
ZnAlPO-5	1645
AlPO-5	1650

From the above findings, it can be inferred that the addition of Zn provokes contrasting behaviour in the various monometallic catalysts. Mg^{2+} ions are known to induce the strongest Brønsted acid sites in AlPO species; which is concurrent with our findings above, as the MgAlPO-5 catalyst yields the lowest v_{8a}(CC) band position (1642 cm^{-1}, Figure 4.18 and Table 4.5). The incorporation of zinc into the MgAlPO-5 catalyst inherently weakens these acid sites, as noted from the increase of the v_{8a}(CC) band (1645 cm^{-1}). The curious influence of the zinc species is further accentuated, as it induces the opposite effect on the Si^{4+} sites, where the acid site strength is relatively increased, as the v_{8a}(CC) band is lowered from 1648 cm^{-1} in SiAlPO-5 to 1645 cm^{-1} in ZnSiAlPO-5. This rather peculiar behaviour confirms that zinc does not have a uniform effect on active sites that are isomorphously incorporated into AlPO frameworks. On the other hand, it forms extra-framework species capable of forming specific and site-selective interactions with different metal cations in the AlPO-5 framework. These findings are in good agreement with the catalytic data seen and confirm that zinc is undergoing a unique interaction with the different metal sites. This shows that the addition of extra framework species can selectively modulate acid sites, thus acting as a new tool in the rational design of active sites.

4.5 Results and discussions – Catalytic synergy within MgSiAlPO-5

The ability of magnesium and silicon to independently undergo framework substitution, using contrasting substitution mechanisms offers exciting possibilities by combining the two to make a bimetallic MgSiAlPO-5 species. This is particularly of interest when considering the different active acid species that can be created. In the previous sections we have already shown that such a species has been synthesised in a phase-pure manner to make a crystalline AlPO-5 material. Note, as before, the metal loadings were purposefully kept the same as the bimetallic MgSiAlPO-5 species was contrasted and compared to the MgAlPO-5 and SiAlPO-5 for both the isopropylation and Beckmann rearrangement reactions under identical conditions.

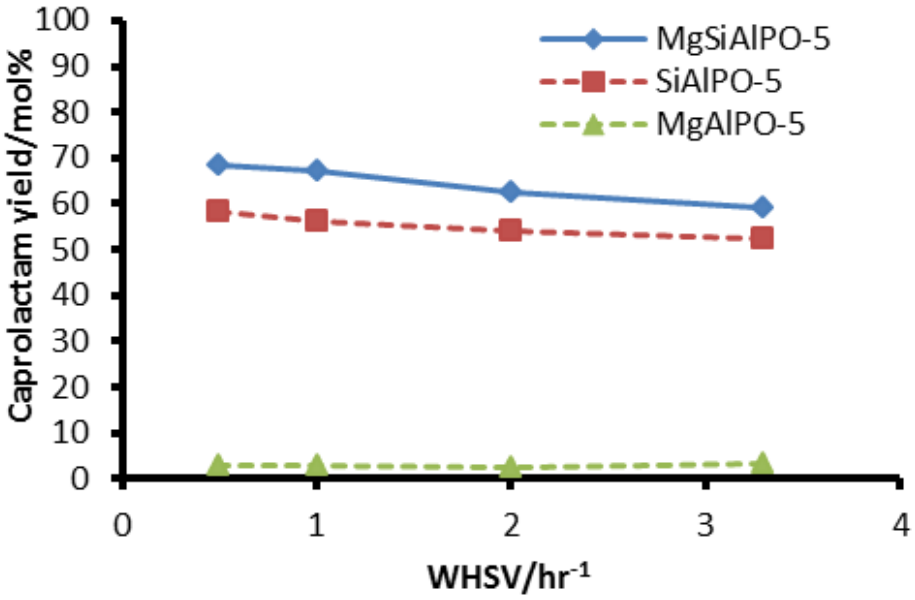

Figure 4.19: Comparing caprolactam yields to investigate the catalytic synergy in MgSiAlPO-5. Reaction conditions: WHSV as shown, Helium carrier gas flow 20 ml/min, 0.3 g of catalyst, liquid feed 300g/l of cyclohexanone oxime in methanol, temperature 673 K.

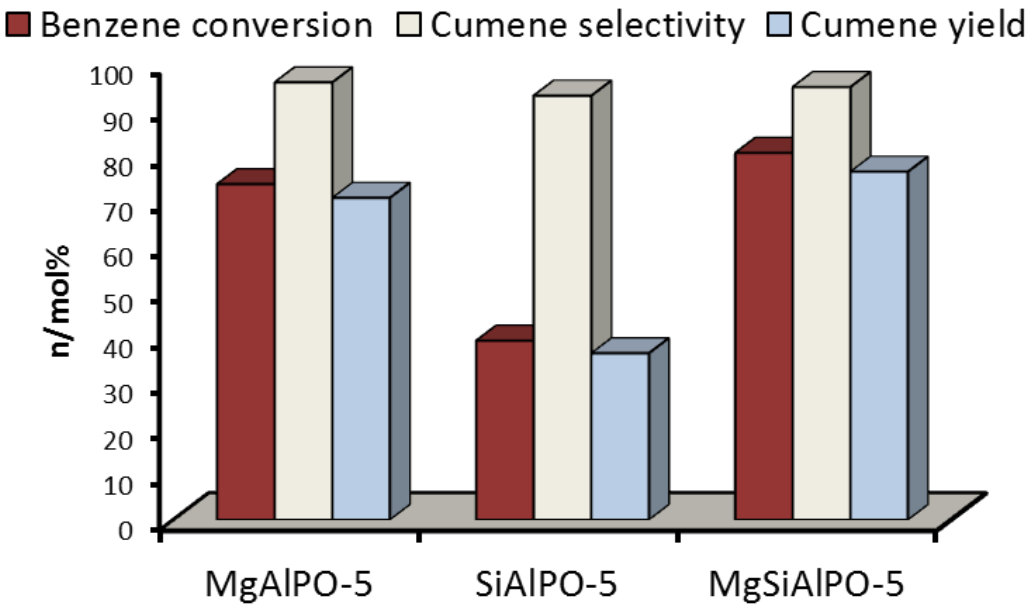

Figure 4.20: Comparing cumene yield to investigate the catalytic synergy in MgSiAlPO-5. Reaction conditions: WHSV of 3.5 hr^{-1}, Helium carrier gas of 10 ml/min, feed 6:1 mole ratio of benzene:isopropanol, temperature 523 K.

In the caprolactam case it is clear that subtle increases in product yield can be achieved by lowering the WHSV. This can be attributed to the inverse relationship between WHSV and contact time, shorter WHSV allows for a longer contact time between reagents and catalyst. This then provides more time to initiate the catalytic cycle, increasing the product yields. It can be seen that in both cases the bimetallic MgSiAlPO-5 system offers catalytic benefits over both the monometallic systems in both reactions (Figures 4.19 & 4.20). In both cases producing notably higher yields of the desired products. Thus the addition of weaker acid sites has improved the catalytic activity in the strong-acid catalysed isopropylation reaction and the inclusion of strong acid sites has improved the activity of the weak-acid catalysed Beckmann rearrangement. To understand the nature of the active species a further CO and 2,6-DMP FT-IR study was performed.

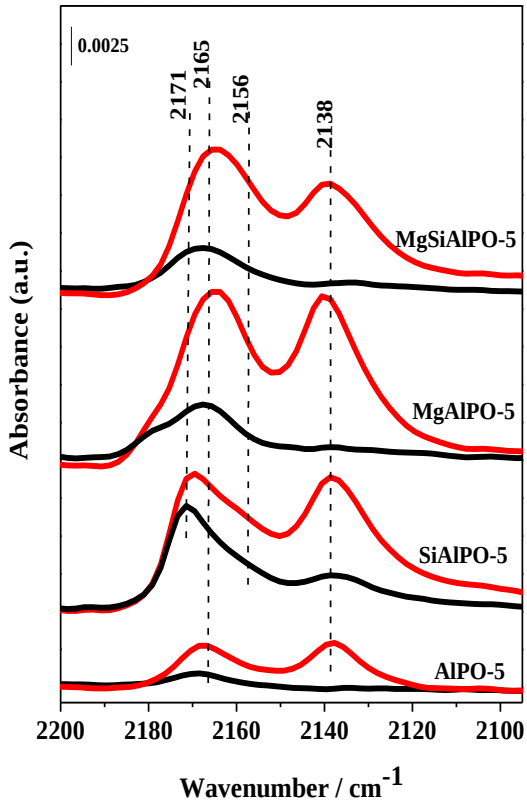

Figure 4.21: CO-probed FT-IR to compare the acidic properties of MgSiAlPO-5.

It can be seen that the CO spectra of MgSiAlPO-5 shows the presence of increased Brønsted acidity compared to the undoped AlPO-5, confirming framework substitution (Figure 4.21). It can also be seen that the shape of the spectra appears to be an average of the MgAlPO-5 and SiAlPO-5 spectra, suggesting an almost intermediate behaviour between the two systems. To gain a further insight into the quantity and strength of acid sites present a quantified FT-IR study of 2,6-DMP was used to further investigate the acidic species (Figures 4.22 & 4.23).

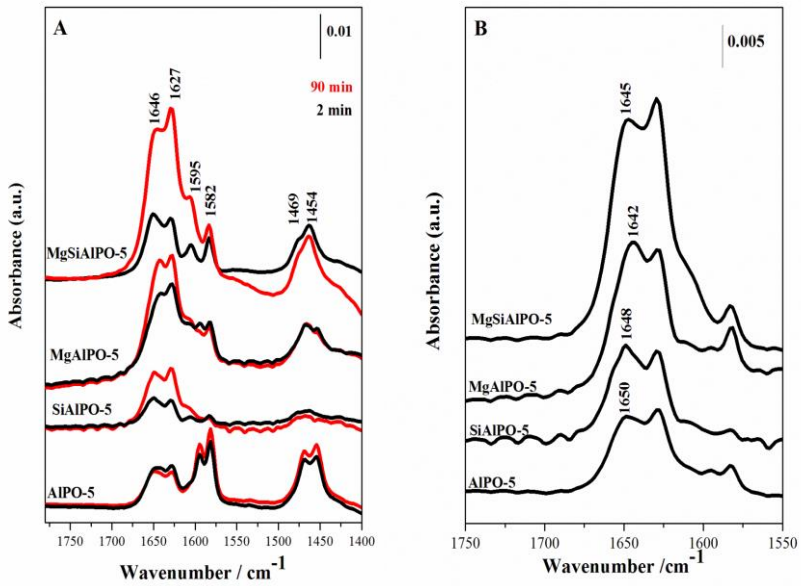

Figure 4.22: A) FT-IR spectra of 2,6-DMP (4 mbar) adsorbed at 298K on mono- and bi-substituted AlPO-5 catalysts; black curve: 2 min contact, red curve: 90 min contact. B) Corresponding FT-IR spectra of outgassed 2,6-DMP at 298K on mono- and bi-substituted AlPO-5 catalysts.

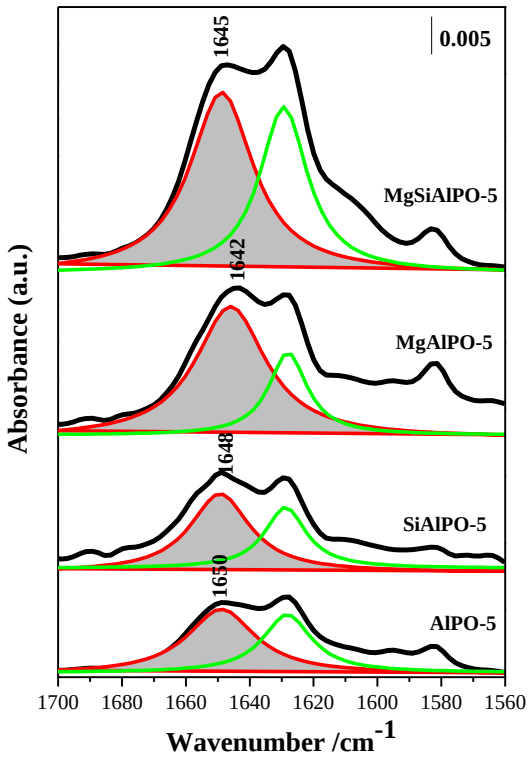

Figure 4.23: FT-IR spectra of outgassed 2,6-DMP at 298K on mono- and bi-substituted AlPO-5 catalysts. Red and green lines: simulated spectra obtained by a curve fitting procedure.

Table 4.6: Comparing the acidic properties of MgSiAlPO-5 with analogous monometallic systems.

Material	**ν_{8a}(CC)/cm^{-1}**	**A/cm^{-1}**	**N/mmol g^{-1}**
MgSiAlPO-5	1645	0.92	230
SiAlPO-5	1648	0.37	92
MgAlPO-5	1642	0.74	185
AlPO-5	1650	0.35	87

By applying the Beer-Lambert law to the 2,6-DMP peak it is also possible to translate the area of the signal to a total quantity of acid sites (Figure 4.23 and Table 4.6). The quantified peak areas confirm the findings from the CO-probed FT-IR that the total acidity of the bimetallic sample is greater than either of the individual monometallics. Further the ν_{8a}(CC) signal shows that the acid strength of the bimetallic system is intermediary between the two monometallic systems. This again is in good agreement with the CO-probed FT-IR as it showed the MgSiAlPO-5 signal displayed characteristics of both the monometallic species. While the characterisation of the acid-site explains the catalytic behaviour it is necessary to consider the mechanisms of both reactions (Figures 4.24 & 4.25):

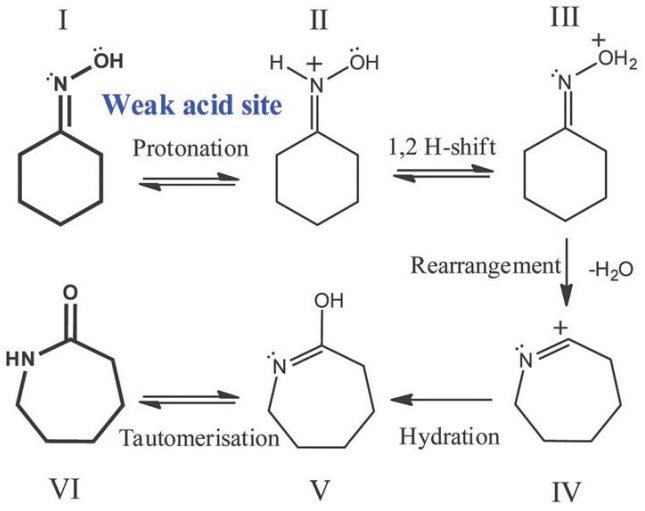

Figure 4.24: Catalytic mechanism of the Beckmann rearrangement of cyclohexanone oxime.

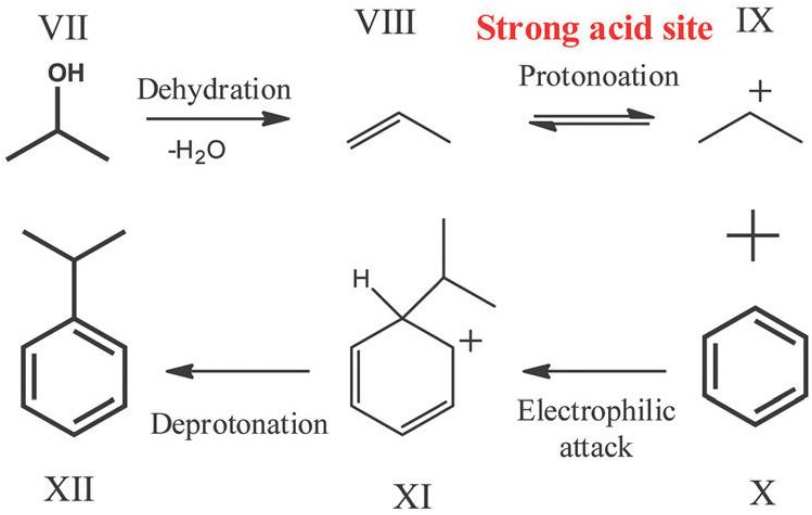

Figure 4.25: Catalytic mechanisms for the isopropylation of benzene.

Given the nature of the acid sites and on the basis of the relative acid strengths (as summarised in Table 4.6), it was to be expected that MgAlPO-5, containing an overwhelming majority of strong Brønsted acid sites, was more active than the SiAlPO-5 analogue for the isopropylation reaction. Contrary to expectations, the bi-substituted MgSiAlPO-5, that possesses intermediate strength Brønsted acid centres, displays superior catalytic properties when compared to its mono-substituted counterparts. In line with our earlier observations, this synergistic enhancement in catalytic activity can be attributed to the presence of both the Mg^{2+} and Si^{4+} ions, the loci of the Mg-OH-P and Si-OH-Al Brønsted acid centres, within the same AlPO framework, and this can be further substantiated by considering the reaction mechanism. The isopropylation reaction is known[59-61] to proceed via a multi-step pathway, comprising of the dehydration of the 2-propanol and subsequent alkylation of benzene. An efficient catalyst should therefore comprise of the requisite active centres that are able to successfully catalyse these individual steps. It has recently emerged[19,62] that Si-containing AlPOs are efficient catalysts for the dehydration of alcohols and we believe that the Si-OH-Al Brønsted acid centres in the bi-substituted catalyst trigger the dehydration of 2-propanol. The subsequent protonation of the olefin requires strong Brønsted acid centres and the ready availability of the Mg-OH-P sites, in close proximity to the Si-OH-Al centres, we believe, is critical for the enhanced performance observed with the bi-substituted MgSiAlPO-5 catalyst. The overall effectiveness in catalysing these tandem reactions is fundamental to the rate-determining step that

involves the electrophilic attack of the protonated olefin and benzene. Thus, whilst the rate-determining step requires a specific acid strength, other subsequent steps may be tailored to different strength acid sites, therefore possession of a multitude of acid sites can facilitate the reaction pathway as a whole, improving catalytic efficiency. Similar arguments can also be applied to the Beckmann rearrangement mechanism (Figure 4.24), this is also a multi-step pathway which may also require a range of different active species to enhance the overall reactivity.

4.6 Conclusions

The ability to modify acid-site strength, to aid the design and engineering of nanoporous architectures for specific catalytic applications, by the incorporation of Zn^{2+} ions, has been demonstrated through a combination of *in situ* FT-IR spectroscopy and detailed complementary catalysis results. The versatility of this design approach has been suitably illustrated with contrasting examples of acid-catalysed transformations (requiring diverse active sites), in which the pairing of inactive substituents has created an active solid-acid catalyst. The findings from this study clearly demonstrate that opportune modulation of the strength of the Brønsted active sites, by insertion of zinc, is fundamental to regulating the activity and selectivity of the catalyst for a particular catalytic transformation. Furthermore, the distinctive influence of extra-framework zinc ions in selectively reducing the acid-strength of magnesium prompted an increased effiency for the Beckmann rearrangement of cyclohexanone oxime; whilst concomitantly improving the cumene yield obtained through the isopropylation of benzene by increasing the acid-strength of silicon sites; as substantiated through this structure-property correlation study, offers adequate scope for the rational design of active sites for targeted acid-catalysed transformations with an extended range of metal pairings.

Further, a resourceful strategy for the design and creation of a novel bi-substituted heterogeneous catalyst comprising of Mg-OH-P and Si-OH-Al species have been introduced through simultaneous isomorphous substitution of the AlO_4 and PO_4 framework tetrahedra. The precise location, geometry,

nature and strength of these active centres has been probed and characterised using a combination of structural, physico-chemical, and *in situ* spectroscopic techniques using molecular probes, with a view to affording structure-property correlations, in two contrasting acid-catalysed transformations that require distinct Brønsted acid centres. In particular, synergistic enhancements in catalytic behaviour have been observed with the bi-substituted catalysts in the industrially significant Beckmann rearrangement of cyclohexanone oxime to ε-caprolactam and in the isopropylation of benzene to cumene.

4.7 Experimental section

Synthetic protocol

The synthetic protocol for the isomorphous substitution of Mg and Si into the AFI framework (MgSiAlPO-5) is described (below); an analogous method was employed for the preparation of the monometallic counterparts, details of which are provided in Table 4.7 (below). The synthesis method to form MgSiAlPO-5 involved initially adding 4.0 g of aluminium hydroxide hydrate (Aldrich) to a homogeneous solution of 5.0 g of phosphoric acid (85% in H_2O, Aldrich) in 20 ml of water and allowing the mixture to stir for 10 minutes. An aqueous homogeneous solutions of 0.33 g of magnesium(II) acetate tetrahydrate (Aldrich) in 10 ml of water and 0.62 g of fumed silica (Aldrich) were added simultaneously to the above solution, which resulted in the formation of a viscous gel, which was stirred for a further 30 minutes in order to obtain a homogeneous gel. N,N-methyldicyclohexylamine (SDA) (Aldrich) (8.0 g) was then added slowly followed by 20 ml of water and underwent vigorous stirring for 60 minutes to obtain a white gel with the composition 1.0Al: 0.85P: 0.80MDCHA: 50H2O: 0.03Mg: 0.20Si.

The contents of the gel were sealed in a Teflon-lined stainless-steel autoclave, which was then transferred to a pre-heated, fan-assisted oven (WF-30 Lenton) that was set to the desired temperature of 190 °C, prior to the onset of the crystallization. The autoclave was heated at 190 °C under autogeneous pressure for 2 hr. The white solid product was collected by filtration, washed with approx. 500 ml deionised water, and dried in air (60 °C) overnight. The as-prepared sample was calcined in a tube furnace under a flow of air at 550 °C for 12 hr yielding a white solid. The synthesis procedures of other samples discussed varied only by crystallization temperature and gel composition, which are shown in Table 4.7.

Table 4.7: Synthetic parameters for the synthesis of Mg, Zn and Si-containing AlPO catalysts.

Sample	Molar gel composition	Crystallisation temperature/°C
AlPO-5	1.00P:1.00Al:0.75TEA:25H_2O	200
MgAlPO-5	1.50P:1.00Al:0.04Mg:0.80MDCHA:60H_2O	200
ZnAlPO-5	1.05P:1.00Al:0.04Zn:0.80MDCHA:65H_2O	190
SiAlPO-5	0.75P:1.00Al:0.25Si:0.65MDCHA:40H_2O	200
MgZnAlPO-5	1.50P:1.00Al:0.03Mg:0.03Zn:0.80MDCHA:50H_2O	180
MgSiAlPO-5	0.85P:1.00Al:0.03Mg:0.20Si:0.80MDCHA:50H_2O	190
ZnSiAlPO-5	0.85P:1.00Al:0.03Zn:0.20Si:0.80MDCHA:50H_2O	190

Structural characterisation

X-Ray powder diffraction patterns were obtained using a Siemens D5000 diffractometer using Cu $K_{\alpha 1}$ radiation, where λ = 1.54056 Å. Scanning electron microscopy images were obtained using a JEOL-JSM5910 microscope with accelerating voltage of 0.3-30 kV. In this case, the samples were prepared by carbon coating. BET surface area measurements were performed using a Micromeritics Gemini 2375 surface area analyser and prepared using flow-gas preparation. A Perkin-Elmer Optimum 3000 DV was used for ICP analyses, with calcined samples prepared and fully digested in 10 ml of deionised water and 10 ml of ACS Plus Certified H_2SO_4 (Fisher Scientific). Solutions of standard concentrations were used for calibration.

Beckmann rearrangement

The Beckmann rearrangement of cyclohexanone oxime was performed in a fixed-bed, quartz reactor (4 mm in diameter) with a glass frit, in which a layer of pelletized catalyst (0.25 g) was packed between two layers of glass beads. This was pre-heated by a jacket in the flow-reactor to 673 K under a 20 ml/min flow of helium gas for 1 hour. The temperature was reduced to 573 K and a liquid feed of 300 g/l of cyclohexanone oxime in methanol was fed into the reactor, maintaining a WHSV of 3.3 hr^{-1}, with samples being analysed on an hourly basis (under steady-state conditions). The temperature was then

increased to the desired value (598, 623, 648 and 673 K) and samples were taken at each temperature after being allowed to equilibrate for an hour. Samples were analysed using a Clarus 400 gas chromatogram with FID and using an Elite 5 column, the peak areas were calibrated using known response factors.

To perform a mass balance an initial stock solution was employed to test the reproducibility and to assess the carbon balance using a chlorobenzene internal standard. This was composed of:

Chlorobenzene: 2.9929 g (0.026589 mol), Cyclohexanone oxime: 15.0088 g (0.132633 mol) and was made up to 50 ml with methanol (solvent).

Response factor for Cyclohexanone oxime relative to Chlorobenzene = 1.2972 (Calibrated)

Response factor for Caprolactam relative to Chlorobenzene = 1.4516 (Calibrated)

Response factor of Others relative to Chlorobenzene = 1 (Assumed)

Performing an identical procedure to the one described the following GC data was obtained at 673 K, WHSV of 3.3 hr^{-1}:

Table 4.8: Raw GC data for the vapour-phase Beckmann rearrangement for MgSiAlPO-5

Time/mins	Molecule	Area
2.7	Chlorobenzene	233780.63
4.1	Cyclohexanone oxime	216732.37
5.9	Caprolactam	489031.09
N/A	Others detected by GC	119505.20

The following calibration equation:

$$\frac{Moles(X)}{Moles(Std)} = \frac{\beta_X}{\beta_{Std}} \times \frac{Area(X)}{Area(Std)} = \gamma_{\frac{X}{Std}} \times \frac{Area(X)}{Area(Std)} \quad (4.1)$$

where $\gamma_{X/Std}$ is the relative response factor of compound X, relative to the standard. Gives:

$$Moles(X) = \gamma_{\frac{X}{Std}} \times Moles(Std) \times \frac{Area(X)}{Area(Std)} \quad (4.2)$$

The moles of internal standard (Chlorobenzene) are constant, so assumed to be 0.026589 moles. Using the equations and response factors above the moles of the remaining molecules can be calculated.

Table 4.9: GC Areas and moles for the mass balance for MgSiAlPO-5, Beckmann rearrangement.

Time/mins	Molecule	Area	Moles
2.7	Chlorobenzene	233780.63	0.026589
4.1	Cyclohexanone oxime	216732.37	0.031976
5.9	Caprolactam	489031.09	0.080739
N/A	Others detected by GC	119505.20	0.013592

Mass balance = 100 x (Moles of [Oxime + Lactam + Others])/Initial moles of oxime

Mass balance = 95.2 mol%

Conversion = 100 x (Initial moles of oxime – Moles of oxime)/Initial moles of oxime

Conversion = 75.9 mol%

Selectivity = 100 x (Moles of Lactam)/Moles of converted oxime

Selectivity = 80.2 mol%

Yield = 100 x (Moles of Lactam)/Initial moles of oxime

Yield = 60.9 mol%

The initial data for this point was:

Conversion = 77.3 mol%

Selectivity = 76.3 mol%

Yield = 59.0 mol%

The yield is very well reproduced. This suggests the highest source of error within these experiments is likely the ±3 % GC error, given the excellent agreement of the Caprolactam yield.

Isopropylation of benzene

An analogous reactor set up and pre-treatment protocol was employed for the isopropylation of benzene. After pre-treatment at 673 K, the temperature was reduced to 523 K and a liquid feed with 6:1 molar ratio of benzene:isopropanol was employed with a WHSV of 3.5 hr^{-1} under a flow of 10 ml/min of helium gas. Samples were analysed and quantified as described above, conversions were normalised with respect to the molar ratio.

Acid site characterisation

FT-IR spectra of self-supporting wafers of the samples (ca. 5 mg cm^{-2}) were recorded with a Bruker IFS88 spectrometer at a resolution of 4 cm^{-1}. All samples were re-calcined at 823K in oxygen to remove the adsorbed species before the FT-IR experiments. CO was adsorbed at 80K and 2,6-DMP was adsorbed at room temperature on the calcined samples, using specially designed cells which were permanently connected to a vacuum line (ultimate pressure $<10^{-5}$ Torr) to perform adsorption-desorption in situ measurements. FT-IR spectra were reported in difference mode by subtracting the spectrum of the sample in vacuo to the spectrum of the adsorbed probe molecules. Multi-peaks fit was performed by employing ORIGIN 6.1 Scientific Graphing and Analysis Software. Lorentzian functions were used and a R^2 =0.99714 was obtained.

4.8 References

1. T. Maschmeyer, F. Rey, G. Sankar and J. M. Thomas, *Nature*, **1995**, *378*, 159-162.
2. A. Thangaraj, R. Kumar and P. Ratsnamay, *J. Catal.*, **1991**, *131*, 294-297.
3. A. T. Bell, *Science*, **2003**, *299*, 1688-1691.
4. L. Li, G. D. Li, C. Yan, X. Y. Mu, X. L. Pan, X. X. Zou, K. X. Wang and J. S. Chen, *Angew. Chem. Int. Ed.*, **2011**, *36*, 8299-8303.
5. J. Lee, O. K. Farha, J. Roberts, K. A. Scheidt, S. T. Nguyen and J. T. Hupp, *Chem. Soc. Rev.*, **2009**, *38*, 1450-1459.
6. J. K. Edwards, B. E. Solsona, P. Landon, A. F. Carley, A. Herzing, C. J. Kiely and G. J. Hutchings, *J. Catal.*, **2005**, *236*, 69-79.
7. S. G. Wettstein, J. Q. Bond, B. M. Alonso, H. N. Pham, A. K. Datye and J. A. Dumesic, *Appl. Catal. B: Environ.*, **2012**, *117*, 321-329.
8. K. Ishii, F. Mizukami, S. Niwa, R. Kutsuzawa, M. Toba and Y. Fujii, *Catal. Lett.*, **1998**, *52*, 49-53.
9. J. Silvestre-Albero, J. C. Serrano-Ruiz, A. Sepulveda-Escribano and F. Rodriguez-Reinoso, *Appl. Catal. A. Gen.*, **2005**, *292*, 244-251.
10. L. Kesavan, R. Tiruvalam, M. H. Ab Rahim, M. I. bin Saiman, D. I. Enache, R. L. Jenkins, N. Dimitratos, J. A. Lopez-Sanchez, S. H. Taylor, D. W. Knight, C. J. Kiely and G. J. Hutchings, *Science*, **2011**, *331*, 195-199.
11. R. D. Adams and B. Captain, *Angew. Chem. Int. Ed.*, **2008**, *47*, 252-257.
12. A. B. Hungaria, R. Raja, R. D. Adams, B. Captain, J. M. Thomas, P. A. Midgley, V. Golovko and B. F. G. Johnson, *Angew. Chem. Int. Ed.*, **2006**, *45*, 4782-4785.
13. E. Gianotti, V. N. Shetti, M. Manzoli, J. A. L. Blaine, W. C. Pearl Jr., R. D. Adams, S. Coluccia and R. Raja, *Chem. Eur. J.*, **2010**, *16*, 8202-8209.
14. R. Raja, G. Sankar and J.M. Thomas, *J. Am. Chem. Soc.,* **2001**, *123*, 8153-8154.
15. R. Raja and J.M. Thomas, *Proc. Natl. Acad. Sci.*, **2005**, *39*, 13732-13736.
16. R. Moyaka and M. Poliakoff, *Nature*, **2005**, *437*, 1243-1244.

17. P. A. Barrett, G. Sankar, C. R. A. Catlow and J. M. Thomas, *J. Phys. Chem.*, **1996**, *100*, 8977-8985.
18. C. S. Blackwell and R. L. Patton, *J. Phys. Chem.*, **1988**, *92*, 3965-3970.
19. M. Lefenfeld, R. Raja, A.J. Paterson and M.E. Potter, US Patent 021882, 2010.
20. J. Paterson, M.E. Potter, E. Gianotti, R. Raja, *Chem Commun.*, **2011**, *47*, 517-519.
21. M. E. Potter, A. J. Paterson and R. Raja, *ACS Catal.*, **2012**, *2*, 2446-2451.
22. R. M. Leithall, V. N. Shetti, S. Maurelli, M. Chiesa, E. Gianotti and R. Raja, *J. Am. Chem. Soc.*, **2013**, *135*, 2915-2918.
23. Product focus, Chem. Week 7, **2007**
24. G. Dahlhoff, J.P.M. Niederer, W.F. Hoelderich, *Catal. Rev. Sci. Eng.*, **2001**, *43*, 381-441.
25. K. S. N. Reddy, B. S. Rao and V. P. Shiralkar, *Appl. Catal. A: Gen.*, **1993**, *95*, 53-63.
26. A. B. Fernandez, M. Boronat, T. Blasco and A. Corma, *Angew. Chem. Int. Ed.*, **2005**, *44*, 2370-2373.
27. I. Lezcano-Gonzales, A. Vidal-Moya, M. Boronat, T. Blasco and A. Corma, *Phys. Chem. Chem. Phys.*, **2009**, *11*, 5134-5141.
28. S. K. Saha, S. B. Waghmode, H. Maekawa, K. Koruma, Y. Kubota, Y. Sugi, Y. Oumi and T. Sano, *Micropor. Mesopor. Mater.*, **2005**, *81*, 289-303.
29. I. Saadoune, F. Cora and C. R. A. Catlow, *J. Phys. Chem. B*, **2003**, *107*, 3003-3011.
30. R. Wendelbo, D. Akporiaye, A. Anderson, I. M. Dahl and H. B. Mostad, *Appl. Catal. A: Gen.*, **1996**, *142*, L197-L207.
31. S. K. Saha, S. B. Waghmode, H. Maekawa, K. Komura, Y. Kubota, Y. Sugi, Y. Oumi and T. Sano, *Micropor. Mesopor. Mater.*, **2005**, *81*, 289-303.
32. L. Feng, X. Qi, J. Li, Y. Zhu and L. Zhu, *React. Kinet. Catal. Lett.*, **2009**, *98*, 327-339.
33. X. Yang, Z. Xu, Z. Tian, H. Ma, Y. Xu, W. Qu and L. Lin, *Catal. Lett.*, **2006**, *109*, 139-145.
34. M. Hartmann and S. P. Elangovan, *Chem. Eng. Technol.*, **2003**, *26*, 1232-1235.

35. S. Wang, B. He, Y. Wang and X. Zhao, *Catal. Commun.*, **2012**, *24*, 109-113.
36. C. Hong, F. Gong, M. Fan, Q. Zhai, W. Huang, T. Wang and Q. Li, *J. Chem. Technol. Biotechnol.*, **2013**, *88*, 109-118.
37. S. W. Lee and S. K. Ihm, *Ind. Eng. Chem. Res.*, **2013**, *52*, 15359-15365.
38. W. Tan, M. Liu, Y. Zhao, K. Hou, H. Wu, A. Zhang, H. Liu, Y. Wang, C. Song and Z. Guo, *Micropor. Mespor. Mater.*, **2014**, *196*, 18-30.
39. X. Li, S. Liu, X. Zhu, Y. Wang, S. Xie, W. Xin, L. Zhang and L. Xu, *Catal. Lett.*, **2011**, *141*, 1498-1505.
40. G. Lischke, B. Parlitz, U. Lohse, E. Schreier and R. Fricke, *Appl. Catal. A: Gen.*, **1998**, *166*, 351-361.
41. S. P. Elangovan, V. Krishnasamy and V. Murugesan, *Catal. Lett.*, **1996**, *36*, 271-277.
42. H. Maekawa, S. K. Saha, S. A. R. Mulla, S. B. Waghmode, K. Komura, Y. Kubota and Y. Sugi, *J. Mol. Catal. A: Chem.*, **2007**, *263*, 238-246.
43. J. P. Lourenco, M. F. Ribeiro, F. R. Ribeiro, J. Rocha, B. Onida, E. Garrone and Z. Gabelica, *Zeolites*, **1997**, *18*, 398-407.
44. N. M. Schweitzer, B. Hu, U. Das, H. Kim, J. Greeley, L. A. Curitss, P. C. Stair, J. T. Miller and A. S. Hock, *ACS Catal.*, **2014**, *4*, 1091-1098.
45. J. F. Wu, S. M. Yu, W. D. Wang, Y. X. Fan, S. Bai, C. W. Zhang, Q. Gao, J. Huang and W. Wang, *J. Am. Chem. Soc.*, **2013**, *135*, 13567-13573.
46. N. H. N. Kamarudin, A. A. Jalil, S. Triwahyono, R. R. Mukti, M. A. A. Aziz, H. D. Setibudi, M. N. M. Muhid and H. Hamdan, *Appl. Catal. A: Gen.*, **2012**, *431-432*, 104-112.
47. F. Cora, M. Alfredsson, C.M. Barker, R.G. Bell, M.D. Foster, I. Saadoune, A. Simplerer, C.R.A. Catlow, *J. Solid State Chem.*, **2003**, *176*, 496-529.
48. G. E. Ewing, *J. Chem. Phys.*, **1962**, *37*, 2250-2256.
49. E. Gianotti, V. Dellarocca, E. C. Oliveira, S. Coluccia, H. O. Pastore and L. Marchese, *Stud. Surf. Sci. Catal.*, **2002**, *142*, 1419-1426.
50. E. Gianotti, C. Bisio, L. Marchese, M. Guidotti, N. Ravasio, R. Psaro and S. Coluccia, *J. Phys. Chem. C*, **2007**, *111*, 5083-5089.
51. S. Bordiga, C. Lamberti, F. Geobaldo, A. Zecchina, G. Turnes Palomino and A. Zecchina, *Langmuir*, **1995**, *11*, 527-533.
52. O. Cairon, T. Chevreau and J-C. Lavalley, *J. Chem. Soc. Faraday Trans.*, **1998**, *94*, 3039-3047.

53. G. V. A. Martins, G. Berlier, C. Bisio, S. Coluccia, H. O. Pastore and L. Marchese, *J. Phys. Chem. C*, **2008**, *112*, 7193-7200.
54. K. Chakarova and K. Hadjiivanov, *J. Phys. Chem. C*, **2011**, *115*, 4806-4817.
55. C. Lahousse, A. Aboulayt, F. Mauge', J. Bachelier and J. C. Lavalley, *J. Mol. Catal.*, **1993**, *84*, 283-297.
56. E. P. Hunter and S. G. Lias, *J. Phys. Chem. Ref. Data*, **1998**, *27*, 413-656.
57. P. A. Jacobs and C. F. Heylen, *J. Catal.*, **1974**, *34*, 267-274.
58. L. Oliviero, A. Vimont, J-C. Lavalley, F. Romero Sarria, M. Gaillard and F. Mauge', *Phys. Chem. Chem. Phys.*, **2005**, *7*, 1861-1869.
59. S. K. Saha, S. B. Waghmode, H. Maekawa, K. Koruma, Y. Kubota, Y. Sugi, Y. Oumi and T. Sano, *Micropor. Mesopor. Mater.*, **2005**, *81*, 277-287.
60. S. Barman, *J. Appl. Sci.*, **2010**, *10*, 2602-2607.
61. J. Joni, M. Haumann and P. Wasserscheid, *Appl. Catal. A: Gen.*, **2010**, *372*, 8-15.
62. J. N. Kondo, K. Ito, E. Yoda, F. Wakabayashi and K. Domen, *J. Phys. Chem. B*, **2005**, *109*, 10969-10972.

Chapter 5: Spectroscopic and theoretical insights on catalyic synergistic interactions in redox catalysts

The following people have contributed to the work in this chapter:

Simon Bare of UOP and Bhoopesh Mishra of Illinois Institute of Technology obtained and analysed the XAS data in this chapter, respectively.

5.1 Introduction into AlPO redox chemistry

Growing global concerns over greenhouse gas emissions and finite energy resources have facilitated growth in many areas of materials science. Catalysis is no exception to this growth. The desire for cheaper, cleaner and more efficient technologies demands that any novel catalytic material possessing distinctive or exceptional structural characteristics be stringently investigated, aiding the understanding and promoting the judicious design of single-site catalysts.[1-3] In order to reach this goal a detailed knowledge of the exact nature of catalytically-active sites at the molecular level and their behaviour is of fundamental importance. Further, a meticulous understanding of structure-property relationships between such sites, and the surrounding inorganic matrix, are necessary before such a catalyst can be rationally designed.[4] In the vast majority of heterogeneous catalysts such tempting notions are far from trivial owing to the difficulties in precise active-site placement, combined with the need for more advanced *in situ* techniques to be developed to specifically probe and engineer active sites, which may constitute only a small fraction of the whole system.[5]

Recent research has witnessed widespread developments in the field of multi-metallic catalysis, with a large proportion exploiting the idea of metal-metal synergy. A number of examples currently exist in the literature whereby the combination of two metal dopants results in a favourable modification of the catalytic profile, highlighting potential benefits for the industrial applicability of such designed catalysts.[6-8] While the notion is undoubtedly appealing, the inclusion of a second metal introduces a further level of complexity in the

design strategy, that demands more stringent control from a synthetic perspective. A more detailed knowledge of the local structural environment and associated structure-property relationships is therefore required, not just between the host and the dopants but also between the different heteroatoms substituents themselves. To quantify such interactions at the molecular level often requires a detailed understanding of the nature of the active sites, and it is necessary to employ a range of physico-chemical, operando and spectroscopic characterisation techniques for achieving the above goal.[9-15]

One area where this is notion is of particular interest is in oxidation catalysis, whereby the exact environment of the metallic dopant heavily influences the redox activity (and thus the catalytic potential) of these materials. A range of metal dopants have been incorporated into AlPOs to induce redox activity. Among the most common are cobalt, manganese, iron, vanadium and titanium. These systems have been of particular interest due to their ability to be isomorphosuly substituted into the framework and induce selective C-H activation under aerobic conditions within the microporous AlPO network.[16,17] Cobalt, manganese and iron are known to undergo type I substitution, in accordance with their $M^{2+/3+}$ chemistry (Figure 5.1). Once incorporated into the framework they are able to alternate between the two states with minimal distortion to the local structure, thereby facilitating redox processes, though despite this the individual preferences of the different metals for specific oxidation states promotes subtle differences in redox chemistry.

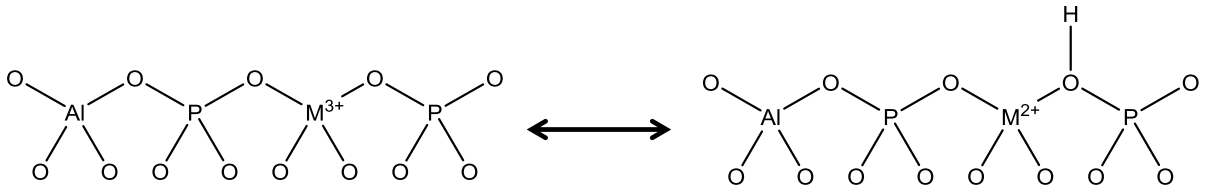

Figure 5.1: Redox transitions of $M^{2+/3+}$ ion dopants such as Co, Mn and Fe.

Iron-containing AlPOs (FeAlPOs) have been stringently investigated owing to their ability to hydroxylated benzene and phenol,[18] and also their ability to form adipic acid from cyclohexane. In light of this many studies have been dedicated to understanding the specific nature of the active site. The effects of different preparation methods have been extensively studied. A study by Zhao *et al*[18] linked the influence of different synthetic protocols (hydrothermal, ionothermal and wet impregnation) on their effects for the hydroxylation of

phenol. Despite the contrasting preparation methods it was found that ~0.4 wt% of Fe was incorporated into each material. The three synthesis protocols showed varying degrees of success in forming the desired material, with the more typical hydrothermal synthesis forming $FeAl_2(PO_4)_2(OH)_2$ as a lesser secondary phase. Despite having fundamentally the same AlPO-5 framework, the surface areas were significantly different. The impregnation method (FeAlPO-5-Imp) lowered the surface area as expected, whilst the ionomethermal method (FeAlPO-5-Iono) resulted in the formation of a significant amount of mesopores. The nature of the active site was probed using UV/Vis spectroscopy and the signals resolved into individual peaks. The hydrothermal method (FeAlPO-5-Hydro), designed to promote isomorphous substitution, showed only two signals at 210 and 270 nm, characteristic of isolated Fe^{3+} ions in tetrahedral and octahedral environments, confirming exclusive framework incorporation. In contrast the other two methods facilitated the formation of Fe_2O_3 nanoparticles and other $Fe^{3+}_xO_y$ clusters as well, to the extent that only 60 % of the Fe was isomorphously substituted in both systems. Initially the FeAlPO-5-Imp and FeAlPO-5-Iono showed improved yields of dihydroxybenzene over the FeAlPO-5-Hydro species, though subsequent recycle tests revealed a significant decrease in the iron content of these two systems and subsequently reduced catalytic performance after 1 hour, whereas the isolated Fe^{3+} species present in the FeAlPO-5-Hydro method did not experience a reduction in activity and the isolated sites were retained (Figure 5.2).[18]

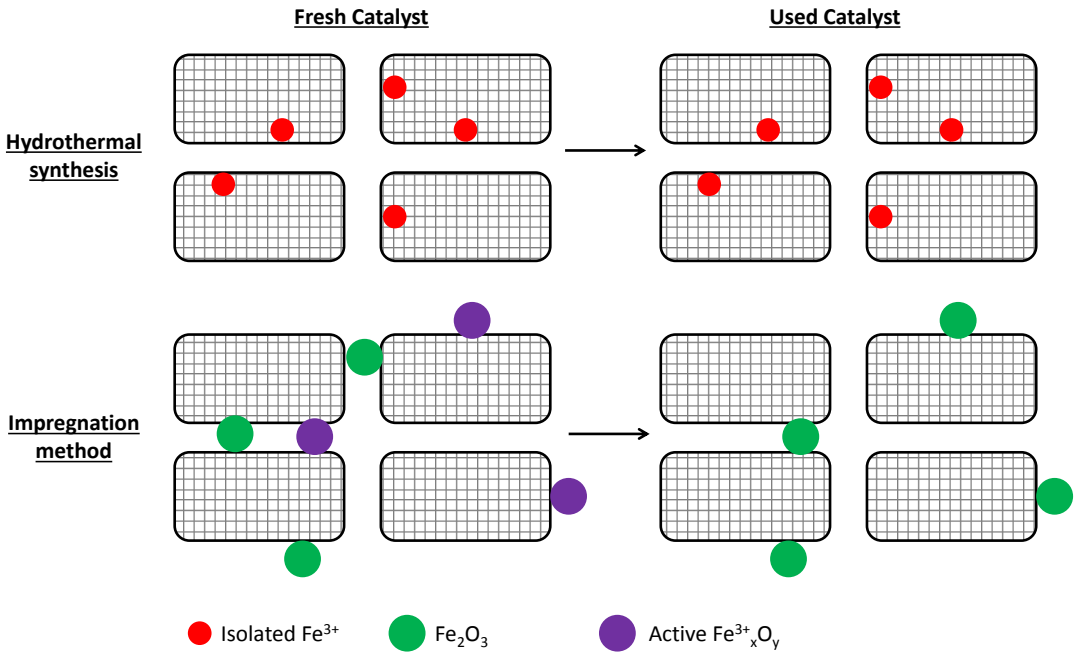

Figure 5.2: Describing the stability of FeAlPO-5.

The recyclability of isolated isomorphously substituted FeAlPO-5 was also witnessed in a study on N_2O reduction.[19] Similarly an impregnated Fe/AlPO-5 species and a hydrothermally synthesised FeAlPO-5 species were contrasted, the UV/Vis confirmed a significantly higher proportion of isolated sites were present in the hydrothermal species (1.2 wt% instead of 0.7 wt%) despite both possessing 1.8 wt% of iron. By contrasting the two species before and after catalysis via H_2-TPR and EPR spectroscopic techniques, the more active hydrothermal species; FeAlPO-5, was found to be significantly more stable. H_2-TPR of the FeAlPO-5 fresh and used showed just one signal at 390 °C, while the EPR showed only two signals, g = 2.0 and g = 4.2, corresponding to isolated Fe^{3+} ions in tetrahedral and octahedral environments. In this case the used and fresh EPR spectra were in excellent agreement showing the stability of such systems. The Fe/AlPO-5 fresh system showed a range of different signals, though post-catalysis the spectra was significantly different, showing just one signal at g = 2.2, assigned to extra-framework Fe_2O_3 species. Again, this shows the merits of isomorphous substitution in terms of the recyclability and the stability of the isolated active sites produced.

The behaviour of iron in the framework on calcination has also been extensively probed in a comprehensive XAS study, in which the influence of different AlPO-5 templating agents was observed on post-synthesis thermal

treatment.[20] It was observed that physical factors such as crystal growth and lattice parameters were subtly influenced by the choice of template. However *in situ* XAS revealed that the behaviour of the Fe atoms on calcination did show subtle variations, but the environment of the Fe post-calcination was in excellent agreement between the samples. In all cases the Fe began in the octahedral geometry, and on removal of the template formed isolated tetrahedral Fe^{3+} species, though subtle changes were also witnessed in the temperatures of the transition between the two states.[20]

The activity of FeAlPOs stems from the Fenton chemistry of Fe - its preference for the Fe^{3+} state, whilst still accessing the Fe^{2+} state. As a result there is also significant interest in manganese-doped AlPOs (MnAlPOs), as Mn displays the opposite behaviour, preferring the Mn^{2+} state but also able to access the Mn^{3+} state. It has been demonstrated that the redox capabilities of MnAlPOs are strongly linked to the topology of the AlPO framework,[21] and because of this behaviour MnAlPOs have been used to great effect in the selective aerobic oxidation of linear alkanes. Inspite of this interest Mn-containing samples offer a range of challenges for various characterisation techniques. UV/Vis spectroscopy can provide useful information on the Mn^{3+} state, however is unable to observe the Mn^{2+} species, as the high-spin d^5 electron configuration means that the vast majority of electronic transitions are spin-forbidden.[22] Conversely EPR is able to probe the Mn^{2+} species, however the Mn^{3+} species is EPR inactive due to fast spin-lattice relaxation times.[23] Given the difficulties in characterising MnAlPOs there has recently been a growing interest in the use of theoretical methods to understand the behaviour of MnAlPOs (This has been discussed in earlier chapters), because of this any study of MnAlPOs commonly employs multiple techniques. A combined EPR and XAS investigation undertaken by Sankar *et al* explored the effect of the framework on MnAlPOs, contrasting the redox behaviour of MnAlPO-5 and MnAlPO-18.[23] EPR spectroscopy showed excellent agreement between the two as-synthesised frameworks, both showing six well-resolved hyperfine splitting lines, within a resonance centred at g = 2.0, this was attributed to tetrahedrally coordinated Mn^{2+} ions. On calcination differences appear between the spectra of the two different systems. In both cases the signal intensity drastically decreases, suggesting there is significantly less Mn^{2+} present, as expected. The signal intensity appears to be weaker for the MnAlPO-18 material suggesting a

greater fraction of the Mn has been oxidised to the unobservable Mn^{3+} species in the AlPO-18 framework than the AlPO-5 framework. Another notable difference is the appearance of a resonance with a g value of 3.20 in the MnAlPO-18 spectra this is assigned to the production of extra-framework Mn^{2+} species, suggesting that some Mn may be leaching out of the framework on calcination, however this is not observed in the case of MnAlPO-5. The XAS analysis confirms that in the as-synthesised state Mn occupies a tetrahedral (framework) site, thus has undergone isomorphous substitution and is initially in the Mn^{2+} state. On calcination Mn retains its framework position (4 Mn-O bonds) though these bonds contract from 2.03 to 1.86 Å, signifying a change in oxidation state from Mn^{2+} to Mn^{3+}. By comparing the XAS and EPR data in the as-synthesised and calcined states the redox capacity of the two different frameworks could be estimated. It was found that 80-100% of the Mn ions in MnAlPO-18 were able to access the Mn^{3+} state on calcination, whereas only 50-58% of those in MnAlPO-5 could, thus highlighting the importance of framework selection in catalyst design.[23] It has been postulated that it is this ability of MnAlPO-18 to undergo near quantitative reduction and oxidation that makes it a more effective oxidation catalyst (Figure 5.3).

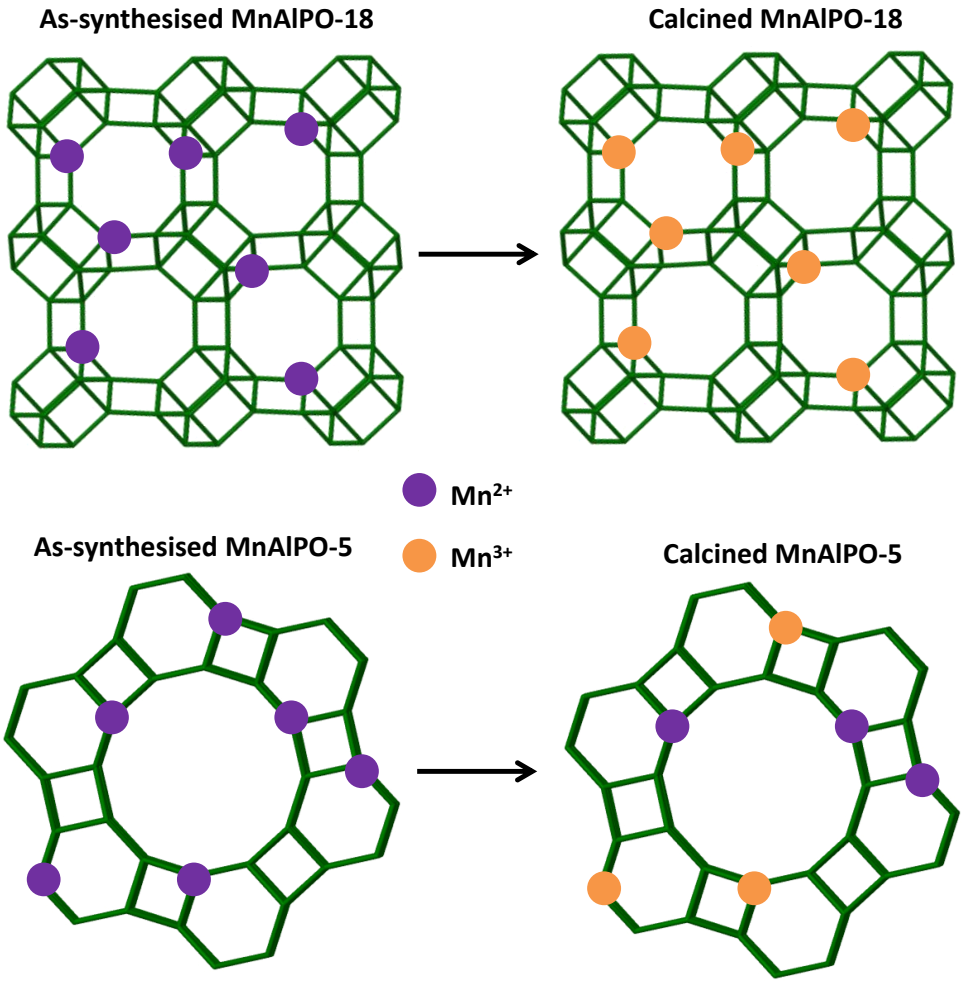

Figure 5.3: Schematic demonstrating the differences in redox fraction between different MnAlPOs.

In a similar study to that performed for FeAlPO-5 (as discussed above) MnAlPO-5 has also been examined to contrast the effects of framework substitution and wet-impregnation methods by Wan *et al*.[22] The substituted MnAlPO-5 and the impregnated Mn/AlPO-5 were examined using a combined UV/Vis, EPR and H_2-TPR study. It was concluded that despite being synthesised hydrothermally the MnAlPO-5 system contained a variety of environments on calcination, including isolated Mn^{2+}, Mn^{3+} and extra framework Mn-oxide species. Little evidence was found of framework Mn-species in the impregnated Mn/AlPO-5, which comprised mostly of Mn_2O_3 and MnO_2.[22] The substituted MnAlPO-5 species was then evaluated for the oxydehydrogenation of ethane to ethylene, however it was observed via H_2-TPR that the quantity of extra-framework species had been drastically decreased post-catalysis.

Cobalt has also been used to great effect as a dopant for inducing redox behaviour in AlPOs. While it shares similar properties to manganese (preferring the Co^{2+} state) it is also more limited in its chemistry, owing to fewer oxidation states, making it an excellent candidate for catalysing a range of aerobic oxidation reactions. The effect of the framework on the redox behaviour of cobalt has also been stringently investigated, contrasting CoAlPO-5, CoAlPO-11, CoAlPO-18 and CoAlPO-36.[24,25] As with the Mn atoms, the specific framework was found to have a significant effect on the redox fraction (and therefore catalytic activity) of the different CoAlPOs. Cobalt has been found to have a lower redox fraction than Mn and Fe AlPOs, and as such an in-depth XAS study has been undertaken to quantify the redox fraction of the cobalt in the system. This value is calculated based on the bond distances. It is known that the tetrahedral Co(II) in the AlPO framework has an average Co-O bond length of 1.94 Å, as this is the value obtained from the as-synthesised materials which exclusively occupy the Co(II) state. The Co(III) average bond distance is larger and is found to be 1.83 Å. The latter value is derived from calcined CoAlPO-18, which undergoes complete oxidation to Co(III) on calcination. As such the redox fraction can then be calculated from the average Co-O bond distance obtained from the calcined samples (which must lie between 1.94 and 1.83 Å) using the following equation:

$$x = \frac{R-1.83}{1.94-1.83} \qquad (5.1)$$

where x is the redox fraction, and R is the average Co-O bond distance.

The redox fraction (x) has been found to be directly linked to the catalytic activity of these materials, as can be seen in Figure 5.4, which contrasts the redox fraction with the TON for the oxidation of n-hexane. In light of this it is of considerable interest to tune the redox fraction of CoAlPOs to enhance their catalytic activity for the oxidation of n-hexane (Figure 5.4).

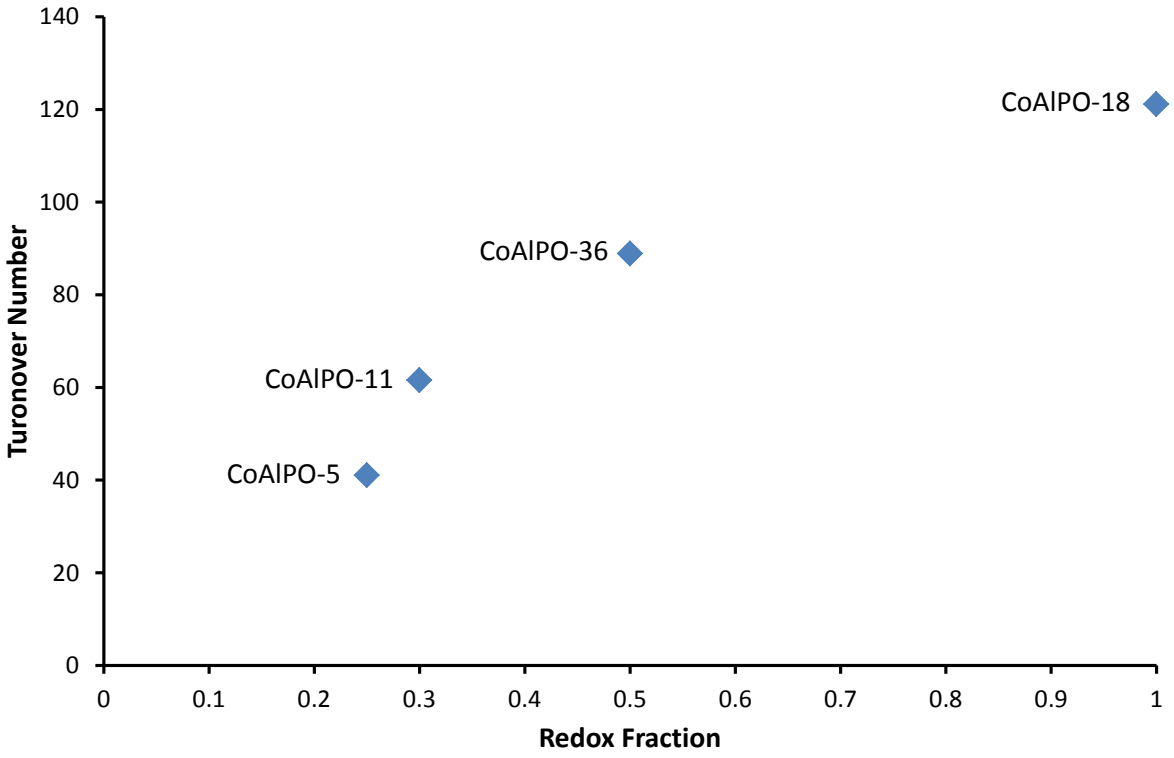

Figure 5.4: The link between redox fraction and catalytic efficiency in CoAlPO frameworks.

Whilst cobalt, manganese and iron AlPO systems have been extensively studied over the years, it is only recently that vanadium systems have been thoroughly investigated. This is because unlike the other atoms mentioned the redox chemistry of vanadium is not a simple tetrahedral $M^{2+/3+}$ system, instead it alternates between $V^{4+/5+}$. These oxidation states make vanadium an excellent candidate to undergo type II substitution (replacing a phosphorus atom). Despite this vanadium instead forms a vanadyl species (V=O), which has an overall charge of 2+/3+, thus still undergoes type I substitution,[9,26] substituting an aluminium ion (Figure 5.5):

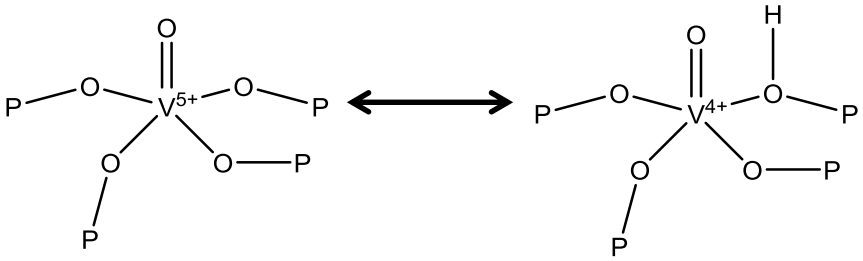

Figure 5.5: Redox chemistry of the isomorphously substituted vanadyl ion incorporated into the AlPO framework.

The nature of this active site has been probed using a combination of in-depth HYSCORE EPR spectroscopy and computational DFT calculations,[27] and the above site has been confirmed. A further active site has also been found, a vanadyl ($V{=}O^{2+}$) species confined within the 6-membered ring of the AlPO-5 framework. Despite both species being observed, the latter is expected to be catalytically inactive, as it resides within the inaccessible 6-membered rings, thus will not be able to interact with reactants. Inspite of this VAlPOs have been found to be active for a range of oxidation reactions, with the activity being linked to the isolated isomorphously substituted vanadium ions and not active extra-framework species.

Given the significant interest in the TS-1 catalyst there have been significant efforts in developing titanium-containing AlPOs to mimic the active site in a range of different frameworks. The use of spectroscopic methods to analyse Ti-containing species and its catalytic activity has already been discussed in previous chapters, though the nature of the active site will now be briefly discussed. Traditionally it was thought that titanium would exclusively undergo type II substitution to form an isolated Brønsted acid site, it would then remain in the Ti^{4+} state, given its lack of redox chemistry. More recently a range of XAS and EPR studies have revealed that under severe reduction conditions a proportion of Ti^{4+} species can be reduced to Ti^{3+} which have also been found to substitute Al not P (roughly 20-25% of the total Ti content).[28-32] Ti-O-Ti species have also been observed using HYSCORE EPR (Figure 5.6). This finding rationalises the existence of the Ti^{3+} species, given that an isolated Ti^{4+} species occupying a Al site would be infeasible, given Loewensteins rules, and the following species have been suggested. It is not yet clear which of these species is the active site for oxidation catalysis, however a range of tests are on-going.[28-32]

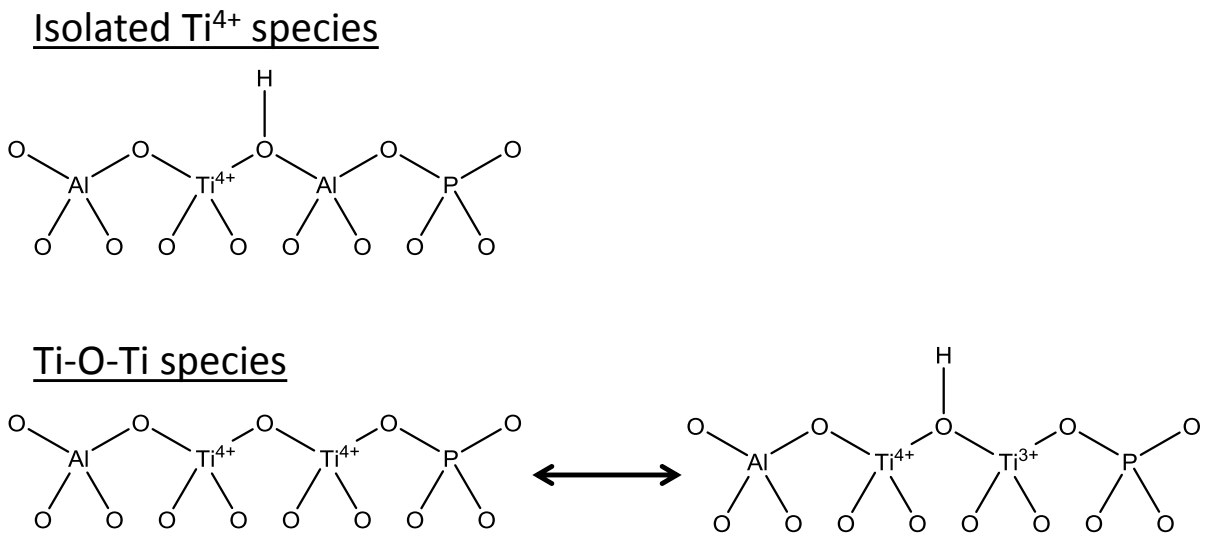

Figure 5.6: Nature of Ti species in TiAlPO-5.

The catalytic activity and the contrasting redox chemistry of these five different metal dopants, when isomorphously substituted into the AlPO framework, offers a range possibilities for multimetallic substitution into the same framework. The influence of combining Co, Mn and Fe into the same framework has already been discussed, along with the synergistic enhancement of combining V and Ti in an AlPO-5 framework. In our recent work[33] we extended our knowledge[10,17,18] on the creation of isolated monometallic active sites within aluminophosphate (AlPO) architectures, to the design of isomorphously incorporated bimetallic active centres that display superior catalytic activity than their monometallic counterparts in oxidation reactions (Figure 5.7).[33] Through a rational selection of appropriate metal combinations, it is possible to engineer and exploit synergistic interactions between individual metal sites that reside within the same framework. By developing novel synthetic strategies we were able to purposefully place two heteroatoms within sufficiently close proximity such that the local geometry of the metals was modified to facilitate catalytic improvements. We have since demonstrated the breadth of this technique by showing that it is possible to engineer this phenomenon not only between different dopants, but also for different industrially relevant catalytic transformations.[9,33,36-38]

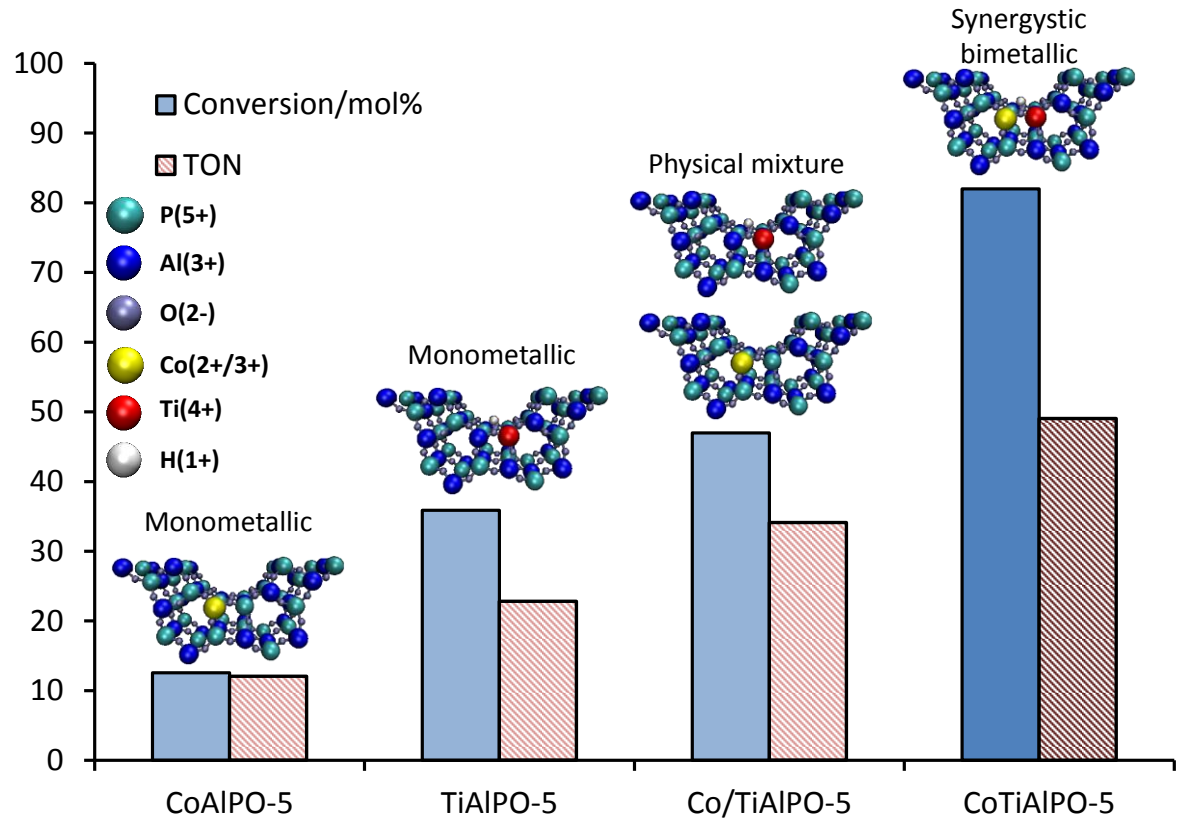

Figure 5.7: Catalytic synergy in the epoxidation of olefins[33] using monometallic and bimetallic Co^{3+} and Ti^{4+} active centers, isomorphously incorporated into the AlPO-5 framework.

In this work the synergistic effects of isomorphously substituting cobalt and titanium ions, simultaneously into the same AlPO framework to yield a bimetallic CoTiAlPO-5 system are discussed (Figure 5.7). It has previously been shown that individually these two metals are capable of catalysing a range of oxidation reactions.[24,39] However the simultaneous incorporation of these two metal ions is paramount in inducing catalytic synergy in sustainable oxidation reactions. Through a comprehensive UV/Vis study it has previously been demonstrated that the local environment around the titanium becomes notably more tetrahedral when cobalt is present in the same framework.[33] It is the increased tetrahedral nature which facilitates more efficient oxidant-activation, promoting the formation of reactive intermediates and increasing product yields. To pursue this work further an in situ X-ray absorption spectroscopy (XAS) study combined with theoretical electronic-structure DFT calculations to elucidate the exact nature of the redox active cobalt site within the previously

published redox-active CoTiAlPO-5 system has been undertaken. By contrast the behaviour of the monometallic CoAlPO-5 and bimetallic CoTiAlPO-5 active species it is possible to uncover the nature of the catalytic synergy in this bimetallic AlPO. Specific emphasis is placed on the cobalt site, to provide complementary data to the previous findings on the local environment of the titanium ions. Further the benefits of simultaneous incorporation of these two ions, regarding their contrasting behaviour in sustainable catalytic applications will be presented.[38]

5.2 Results and discussion – Structural features

Cobalt K-edge XAFS spectra were collected and analysed to determine the local coordination environment of the active site in the calcined (catalytically active) and reduced states (Figure 5.8, Table 5.1). It is known from previous work that not all the cobalt sites in AlPO-5 can be raised to the trivalent oxidation state. Despite calcination some divalent cobalt species still remain.[24] In light of this the data was modelled using a two-shell approach for Co-O (Table 5.1) as the two possible oxidation states of cobalt possess different local environments (tetrahedral and distorted tetrahedral composed of one elongated and three shorter bonds). In both the monometallic (CoAlPO-5) and bimetallic (CoTiAlPO-5) systems the XANES spectra and modelled EXAFS data suggest cobalt exists in a tetrahedral geometry, given that the total coordination number of the Co-O first shell sums to 4.0 Å (Table 5.1). Further, the cobalt atoms have been shown to undergo type I substitution, thereby occupying an aluminum site, owing to the existence of only Co-P distances between 3.0 and 3.1 Å. These bond lengths correspond to the 2nd coordination sphere, in agreement with previously published literature.[24] Both the oxidized and reduced monometallic CoAlPO-5 sample showed two clear environments as expected due to the two possible oxidation states. One environment showed an average Co-O bond length of 1.80 Å, characteristic of the oxidized Co^{3+} state, and the other with an average Co-O length of 1.95 Å, corresponding to the reduced Co^{2+} state. Analysis of the respective coordination numbers for each state reveals that the isomorphously substituted cobalt atoms have a redox fraction of 40 %, in line with previous UV/Vis data.[33] Sigma squared factors were low for this model

indicating that the split shell accounts for the static disorder in the Co-O bond lengths. The coordination environment of the reduced system is in good agreement with that of the oxidized system, with a subtle increase in the fraction of Co^{2+}, as expected. Applying a similar model the bimetallic CoTiAlPO-5 system, the cobalt ions were also found to occupy a tetrahedral environment, having undergone type I substitution methods. The key difference between the two systems is the observation of a Co-O-Ti bridge in the second coordination sphere of the cobalt ion, in addition to the previously observed Co-O-P links. This finding strongly supports the notion of adjacent bimetallic substitution, whereby cobalt has undergone a type I substitution mechanism, whilst simultaneously titanium has undergone a type II substitution to replace an adjacent P^{5+} atom. In doing so, this will lead to a more distorted active species, given that the Ti^{4+} ion will facilitate the formation of a charge-balancing proton and thus another tri-coordinated oxygen species. Further the increased ionic radii of titanium, relative to phosphorus, will require local structural distortion to accommodate the second heteroatom, again increasing the length of any bonds in the local area. Closer inspection of the Co-O bond lengths in CoTiAlPO-5 confirms the above. In both cases (oxidized and reduced) the bimetallic system shows an increase in Co-O bond length over the analogous monometallic system. Further, we note that a higher percentage of Co^{2+} is present on reduction of the bimetallic system, suggesting a greater preference for the divalent state.

Table 5.1. Modelled EXAFS parameters for monometallic CoAlPO-5 and bimetallic CoTiAlPO-5 modelled with a two-shell approach.

Monometallic CoAlPO-5

	Oxidised			Reduced		
Path	CN	R/Å	$\sigma^2/x10^{-3}$ Å^2	CN	R/Å	$\sigma^2/x10^{-3}$ Å^2
Co-O1	1.6 ± 0.1	1.80 ± 0.01	2.0 ± 0.8	1.4 ± 0.1	1.80 ± 0.01	2.0 ± 0.8
Co-O2	2.4 ± 0.3	1.95 ± 0.01	2.0 ± 0.8	2.6 ± 0.3	1.95 ± 0.01	2.0 ± 0.8
Co-P1	1.5 ± 0.4	3.09 ± 0.01	5.9 ± 2.4	1.4 ± 0.4	3.09 ± 0.01	5.9 ± 2.4

Bimetallic CoTiAlPO-5

	Oxidised			Reduced		
Path	CN	R/Å	$\sigma^2/x10^{-3}$ Å^2	CN	R/Å	$\sigma^2/x10^{-3}$ Å^2
Co-O1	1.5 ± 0.1	1.82 ± 0.01	2.0 ± 0.8	1.0 ± 0.1	1.82 ± 0.01	2.0 ± 0.8
Co-O2	2.5 ± 0.3	1.96 ± 0.01	2.0 ± 0.8	3.0 ± 0.3	1.96 ± 0.01	2.0 ± 0.8
Co-P1	1.4 ± 0.4	3.10 ± 0.01	5.9 ± 2.4	1.4 ± 0.4	3.10 ± 0.01	5.9 ± 2.4
Co-Ti1	0.7 ± 0.4	3.20 ± 0.02	9.2 ± 3.0	1.1 ± 0.6	3.20 ± 0.02	9.2 ± 3.0

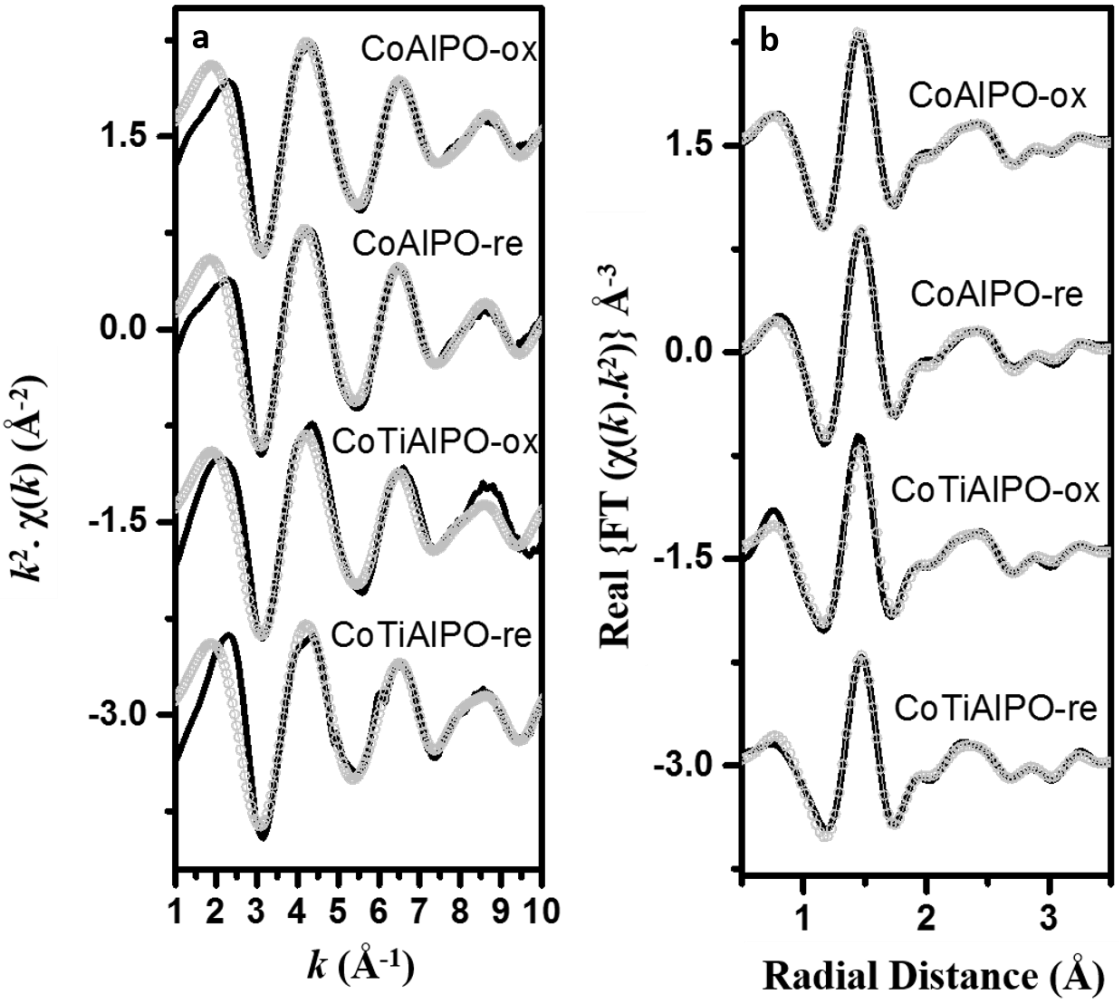

Figure 5.8: EXAFS data (solid) and model (symbol) for oxidized and reduced monoatomic CoAlPO and bimetallic CoTiAlPO samples. A: χ (k)· k^2. B: Real part of the Fourier Transform.

The EXAFS modelling results were then used as the basis to probe the active site directly using theoretical methods. Initially the lowest-energy geometries of monometallic (Co^{2+}, Co^{3+} and Ti^{4+}) and undoped AlPO-5 systems were calculated using electronic-structure periodic DFT calculations. In all cases it was found that the AlPO-5 unit cell remained hexagonal, with unit cell parameters of a = b = 13.75 Å, c = 8.35 Å, α = β = 90° and γ = 120° which varied by less than 1% in all cases. All the bond lengths within the undoped AlPO-5 system were all found to be in good agreement with literature values and showed no significant variation from one-another showing the expected uniformity (Table 5.7).[24,40] Further, no electron spin was observed on any of the atoms and the electron count was also found to show no significant variation between equivalent atoms, again showing uniformity (Table 5.8). On isomorphously substituting a Co^{2+} ion for an Al^{3+} ion (and introducing the appropriate charge-balancing proton) both the high spin and low spin d^7 electron configurations were investigated, the high-spin state was found to be the preferred configuration, as expected for a tetrahedral first row transition element. It was noted that the appropriate bond lengths increased on substituting the cobalt. This showed three longer Co-O bonds and a significantly longer Co-OH bond (Table 5.9). The overall bond-length increase is a direct result of a heteroatom with a larger ionic radii being substituted into an AlPO framework, hence expansion is required to accommodate it. The added expansion of the protonated Co-OH bond is attributed to the increased distortion caused by a tri-coordinated oxygen atom, which also is seen to have a lower electron count, resulting in weaker bonding. Subtle differences in electron count and electron spin were also found as a result of the protonated oxygen (Table 5.10). The three non-protonated oxygens showed a total electron count of around 9.1, whereas the protonated oxygen was found to be just 8.8. This difference in electron count was consistent with the electron spin which was to vary from an average of 0.08 for the three non-protonated oxygens, but was reduced to just 0.02 for the protonated oxygen species. When introducing Co^{3+} into the system for an Al^{3+} ion, again the high-spin (d^6) electronic configuration was favoured. The average bond lengths were found to be larger than the undoped AlPO-5 (Table 5.11), but smaller than those of the Co^{2+} ion. This observation has already been discussed, and has been attributed to the electron count on the cobalt ion. In the Co^{2+} system the electron count (25.4, Table 5.10) is noticeably higher than that of the Co^{3+} (25.1, Table 5.12).

The lower electron count of the Co^{3+} system suggests a greater electron deficiency, which will form stronger (and therefore shorter) ionic bonds with the PO_4^{3-} anions.[40] The uniformity in bond-length, electron count and electron spin returns in the Co^{3+}AlPO-5 system as expected, given that the tetrahedral symmetry is preserved as there is no charge-balancing proton present to break the symmetry. The total electron count of the four oxygen species in Co^{3+}AlPO-5 does not show a significant variation from the electron count seen in the 3 non-protonated oxygen species. However the total electron spin is higher in the trivalent system for all the oxygens, showing an average of 0.21. This is due to the high-spin Co^{3+} ion possessing a greater number of unpaired electrons, therefore a greater amount of spin-leaching is expected on the oxygen atoms. In both cases it was found that the calculated monometallic CoAlPO-5 systems were in good agreement with the experimental XAS results. The average Co-O distances calculated (1.94 and 1.82 Å for Co^{2+} and Co^{3+} respectively) closely match those derived experimentally (1.95 and 1.80 Å, Figure 5.9). Further the calculated average Co-P distances (3.21 and 3.13 Å for Co^{2+} and Co^{3+} respectively) lie well within the range (3.10 and 3.09 Å) found experimentally. It then follows that this is an appropriate computational model to represent the cobalt sites found experimentally (Figure 5.9).

The monometallic Ti^{4+}AlPO-5 system was modelled as having undergone type II substitution, and was found to possess three shorter Ti-O bonds (that are of comparable distance to the P-O bonds of the undoped system) whilst the protonated Ti-OH again shows a significant expansion over the other three bonds (Table 5.13). It is noted that the average Co-O bond-length of the Co^{3+}AlPO-5 system is very similar to the Ti-O bond length Ti^{4+}AlPO-5. This can be directly linked to the electron count of the two metal ions, Ti^{4+} in this case has an electron count of 20.0 (2.0 electrons lower than atomic titanium, Table 5.16) and Co^{3+} has an electron count of 25.1 (1.9 electrons lower than atomic cobalt). It is also revealing that the average electron density for the four oxygens in both cases is 9.03. Similar electron deficiencies on the metal and near identical electron counts on the oxygen atoms would result in similar levels of ionic bonding, and thus similar bond lengths. In this case no electron spin was observed, as expected given that Ti^{4+} possesses no d electrons.

The location of Co^{2+} and Ti^{4+} ions in the bimetallic $Co^{2+}Ti^{4+}$AlPO-5 system provides a valuable insight into the nature of the synergistic enhancement

observed catalytically. To explore this phenomenon a series of calculations were performed to correlate the relative proximity of the two metals with the energetic stability of the system (Table 5.2). In these calculations cobalt was purposefully limited to the divalent "as-synthesised" state to represent the ions during the crystallisation stage, as this is the point at which the final location is determined. The possible positions of the Co^{2+} and Ti^{4+} sites was explored by contrasting the energy of the two monometallic isolated sites with a single bimetallic site by calculating the energy of substitution (E_{Subs}) using equation 5.2.

$$E_{Subs} = E\left[Co^{2+}Ti^{4+}AlPO\text{-}5\right] + E\left[AlPO\text{-}5\right] - E\left[Co^{2+}AlPO\text{-}5\right] - E\left[Ti^{4+}AlPO\text{-}5\right] \quad (5.2)$$

where E_{Subs} is the energy of a specific substitution arrangement, E[$Co^{2+}Ti^{4+}$AlPO-5] is the energy of the bimetallic unit cell ($H_2Co_1Ti_1Al_{11}P_{11}O_{48}$), E[AlPO-5] is the energy of the undoped unit cell ($Al_{12}P_{12}O_{48}$), E[M^{n+}AlPO-5] is the energy of the relevant monometallic unit cell ($H_1Co_1Al_{11}P_{12}O_{48}$ and $H_1Ti_1Al_{12}P_{11}O_{48}$).

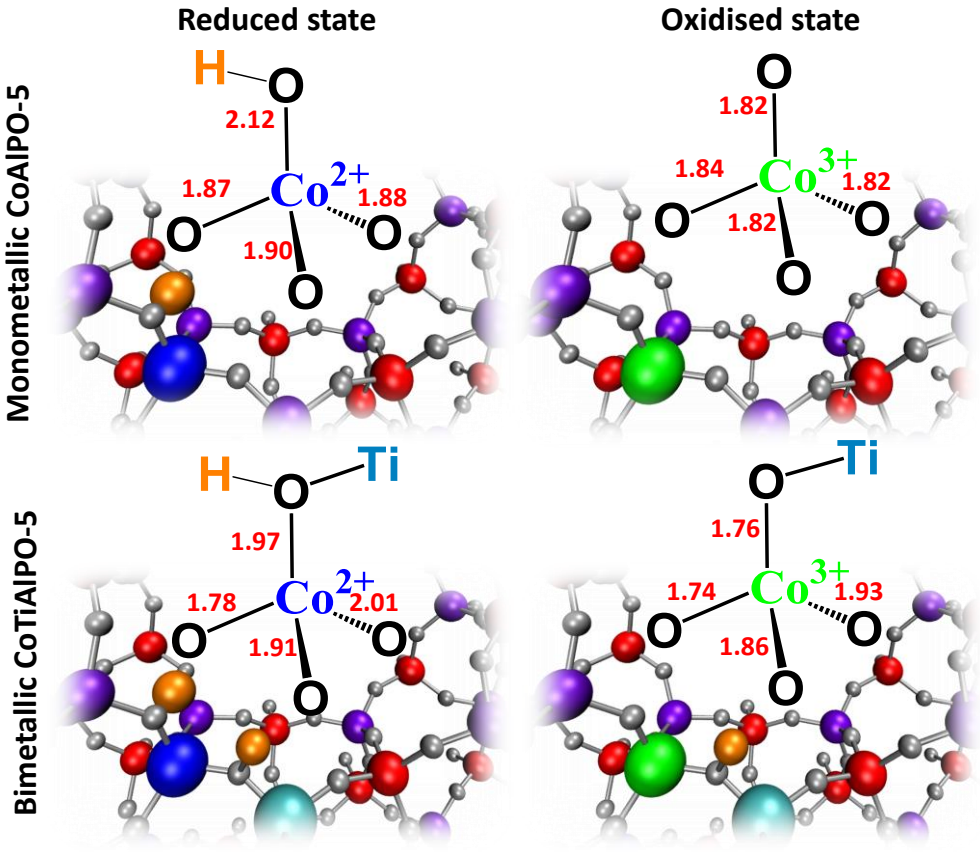

Figure 5.9: Calculated bond distances for mono- and bi-metallic cobalt sites.

All possible proton positions were considered in this system (Table 5.3) and the lowest energy system was selected. The two lowest energy systems possessed comparable energy values, in both of these cases the Co-O-Ti bridge and a Ti-O bond were protonated, creating a O_3Co-OH-Ti(OH)O_2 system. The energy of the most energetically favourable system (containing a bimetallic Co^{2+}-O-Ti^{4+} bridge within the confines of an AlPO-5 framework) was found to be 66.6 kJ mol^{-1} more favourable than the formation of two completely isolated systems (Tables 5.2 and 5.4) and also a unit cell containing two separate ions. This result strongly suggests that adjacent bimetallic substitution of the two elements is preferable to forming two individual active sites, thereby minimising the total distortion of the system and increasing the crystallinity. As such it is expected that during synthesis the formation of a Co-O-Ti bond is more likely than an isolated Co and Ti site during synthesis. Given the lack of migration of these ions during calcination, this will also be true of the catalytically active species, as witnessed through EXAFS analysis. The average Co-O bond length of the bimetallic $Co^{2+}Ti^{4+}$AlPO-5 species showed only a slight (~ 1%) deviation from the monometallic species (Table 5.15), though the presence of titanium and an extra proton species further reduces the similarities in the bond lengths. This is also in good agreement with the EXAFS data. The electron count and electron spin surrounding the cobalt site of the bimetallic $Co^{2+}Ti^{4+}$AlPO-5 species also shows very little variation compared to the monometallic Co^{2+}AlPO-5 system (Table 5.16).

To fully model the range of possibilities for Co^{2+} and Ti^{4+} placement a further set of calculations investigated the possibility of having Co^{2+} and Ti^{4+} in the same unit cell but not adjacent to one another, as a Co^{2+}-O-P-O-Al-O-Ti^{4+} "next-neighbour" system were modelled using eqn. 5.2. It was found that this was more energetically favourable than the isolated system, though less favourable than the adjacent bimetallic system:

Table 5.2: Calculated energy differences for bimetallic $Co^{2+}Ti^{4+}$AlPO-5 unit cells

System	E_{Subs}/kJ mol^{-1}
Isolated	0.0
Adjacent	-66.6
Next-neighbour	-22.8

The possibility of having Co^{2+} and Ti^{4+} separated further was not examined as due to the vast distances between them this would simply count as being two isolated sites.

Table 5.3: Proton positions and energy values in bimetallic $Co^{2+}Ti^{4+}$AlPO-5, with a Co-O-Ti bridge.

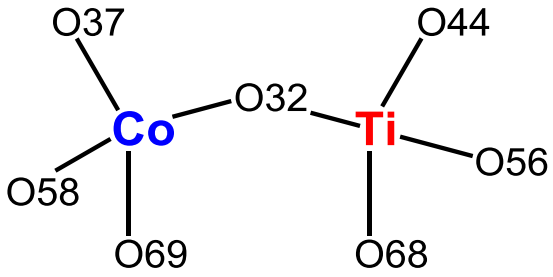

Oxygen attached to H1	Oxygen attached to H2	Relative energy difference/kJ mol^{-1}
32	58	55.2
68	58	84.7
44	58	104.9
56	58	103.7
32	32	89.1
68	32	1.2 (Close in energy)
44	**32**	**0.0 (MINIMUM VALUE)**
56	32	46.6
32	37	85.7
68	37	123.3
44	37	552.3
56	37	135.7
32	69	47.7
68	69	88.9
44	69	99.9
56	69	112.4

Table 5.4: Proton positions and energy values in bimetallic $Co^{2+}Ti^{4+}$AlPO-5, without a Co-O-Ti bridge.

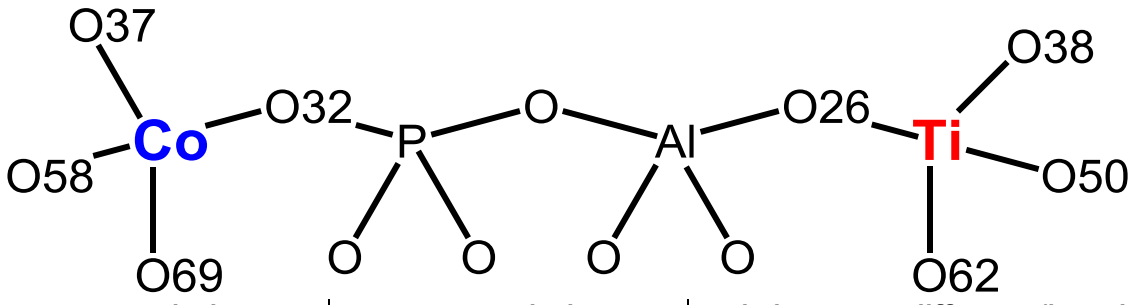

Oxygen attached to H1	Oxygen attached to H2	Relative energy difference/kJ mol^{-1}
38	58	20.0
26	58	19.6
62	58	31.0
50	**58**	**0.0 (MINIMUM VALUE)**
50	32	42.2
62	32	51.3
26	32	67.9
38	32	65.8
38	37	57.2
26	37	49.3
62	37	28.7
50	37	44.8
38	69	41.5
26	69	39.9
62	69	50.2
20	69	19.2

In order to draw meaningful comparisons with the behaviour of the monometallic species the geometry of the $Co^{3+}Ti^{4+}$AlPO-5 species was also calculated, again containing a Co-O-Ti bridge. The geometries were derived from the $Co^{2+}Ti^{4+}$AlPO-5 system, as such two possibilities existed as either of the two protons could be removed in the transition from Co^{2+} to Co^{3+}. The lowest-energy system retained the proton associated with titanium only, removing the proton bound to the oxygen of the Co-O-Ti bridge. The average bond lengths surrounding the cobalt species are also very similar compared to the monometallic Co^{3+}AlPO-5 species (Table 5.17). As with the bimetallic Co^{2+}TiAlPO-5 system there is a greater variation in bond length between the 4 oxygens, again accounting for the disorder and the difficulties modelling the bimetallic XAS data with a two-shell approximation (Table 5.5).

Table 5.5: Comparing calculated and experimental bond lengths for the local environment of oxidised cobalt.

Monometallic CoAlPO-5 distances/Å			
DFT Co^{II}-O	1.94	DFT Co^{III}-O	1.82
EXAFS Co^{II}-O	1.95	EXAFS Co^{III}-O	1.80
Average EXAFS Co-O	1.89		

Bimetallic CoTiAlPO-5 distances/Å			
DFT Co^{II}-O	1.92	DFT Co^{III}-O	1.82
EXAFS Co^{II}-O	1.96	EXAFS Co^{III}-O	1.82
Average EXAFS Co-O	1.91		

It has been previously shown that the ability of a transition-doped AlPO species to initiate oxidation reactions is intrinsically linked to the redox potential of the transition-element within the confines of the framework.[41,42] Based on the calculations above the redox potential of the cobalt site in the monometallic CoAlPO-5 and bimetallic CoTiAlPO-5 system can be quantified using equations 5.3 and 5.4.

$$\Delta E = E\left[Co^{2+}AlPO\text{-}5\right] + E\left[Co^{3+}AlPO\text{-}5\right] - \frac{E[H_2]}{2} \qquad (5.3)$$

$$\Delta E = E\left[Co^{2+}Ti^{4+}AlPO\text{-}5\right] + E\left[Co^{3+}Ti^{4+}AlPO\text{-}5\right] - \frac{E[H_2]}{2} \qquad (5.4)$$

where ΔE is the redox potential, E[Co^{n+}AlPO-5] is the energy of the monometallic Co^{n+}AlPO-5 unit cell, E[$Co^{n+}Ti^{4+}$AlPO-5] is the energy of the bimetallic $Co^{n+}Ti^{4+}$AlPO-5 unit cell and E[H_2] is the energy of an isolated hydrogen molecule.

From equation 5.3 the redox potential of the monometallic CoAlPO-5 species was calculated to be -1.23 eV/ion. Comparing this value with similar CoAlPO materials, calculated by Cora *et al*,[40] shows that this value is lower than other cobalt-substituted AlPO materials. This then represents a greater preference for the divalent state, over the trivalent state. This is in good agreement with

previous studies in which the redox fraction observed in CoAlPO-5 was found to be lower than most other AlPO structures.[24] Using equation 5.3 the redox potential (ΔE) was calculated as being -1.73 eV/ion in the bimetallic CoTiAlPO-5 system, containing the Co-O-Ti bridge. This signifies that the bimetallic species favours the divalent state to an even greater extent than the monometallic species. This correlates well with the EXAFS findings, which showed the average Co-O bond was larger in the bimetallic species, and also a greater preference for the divalent state. Therefore a lower redox fraction is observed as a greater percentage of cobalt remained as Co^{2+} after calcination, due to the lower redox potential. It is important to note at this stage that despite the lower redox fraction a significant amount of cobalt is still raised to the Co^{3+} state during calcination, accounting for the colour change of blue (pre-calcinaton) to green (post-calcination). It is these sites that have been successfully raised to Co^{3+} that account for the catalytic synergy previously seen with these materials.[33] As the rate-determining step of oxidation reactions with these materials has been shown to involve the reduction of M^{3+} to M^{2+}, then a greater preference for the divalent species over the trivalent will lower the activation energy of this step.[41,42] This would then directly translate into improved reactivity and catalytic potential. This finding goes some way to explain the catalytic synergy previously found.[33]

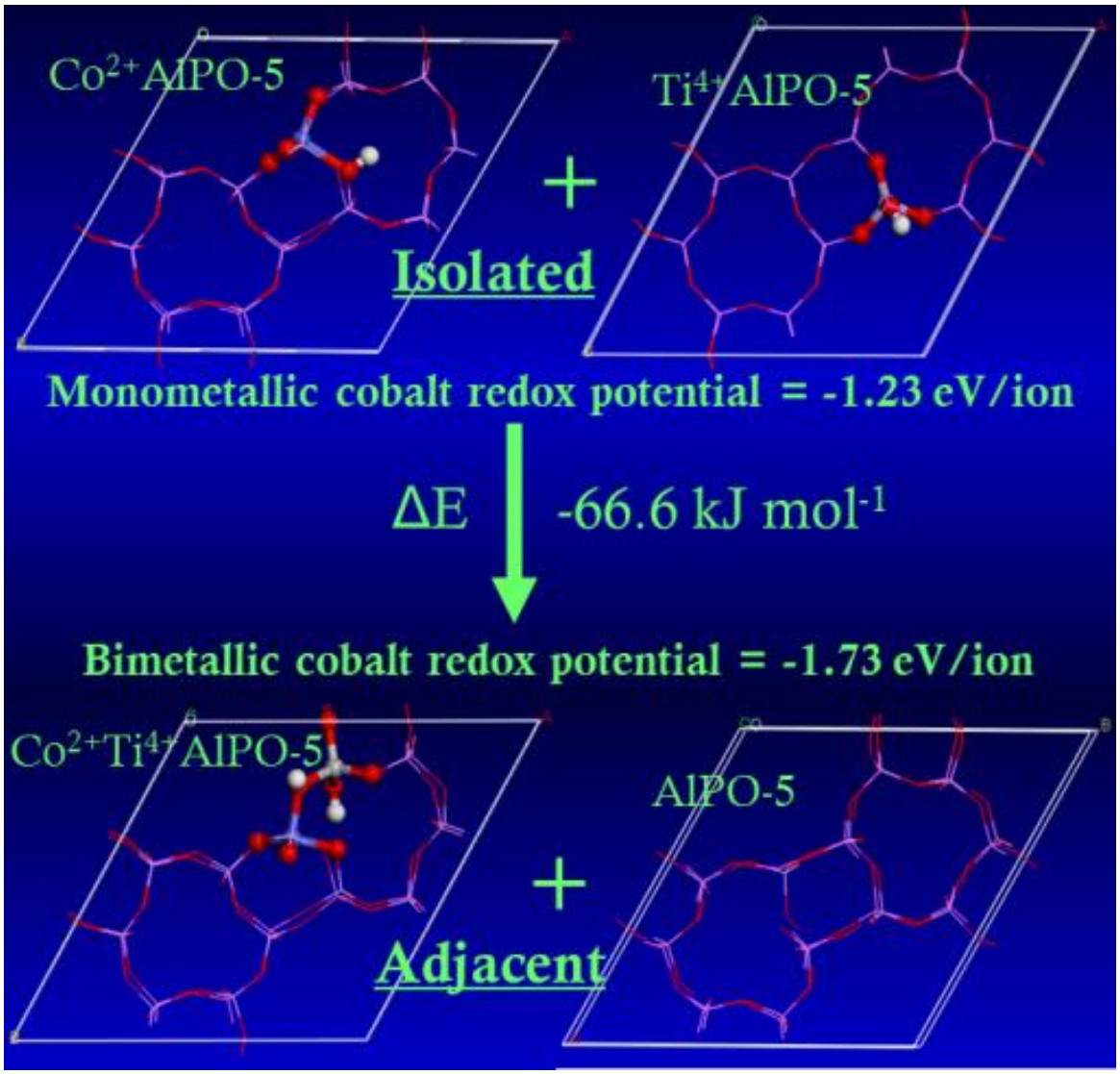

Figure 5.10: Contrasting the redox behaviour of monometallic and bimetallic cobalt sites.

By contrasting the local environment of the cobalt sites it was concluded that the increased preference of the divalent state in the bimetallic species was attributed, not to a stabilisation of the divalent state but, to a destabilisation of the trivalent species. Careful consideration of the electron count and spin values shows that the bimetallic and monometallic Co^{2+} species are consistent with one another (Tables 5.10 and 5.16). In contrast however the two Co^{3+} species show critical variations (Tables 5.12 and 5.18). The average electron spin of the oxygen atoms in the monometallic and bimetallic species are only subtly different (0.21 and 0.23 respectively), however thorough investigation shows that one oxygen in the bimetallic possesses a much higher spin value than the other three (0.42, compared to 0.14, 0.17 and 0.17). While the other

three oxygens are only slightly lower than those in the monometallic species, the fourth is significantly larger. This higher spin density is likely destabilising the trivalent state. Further the oxygen in question is the oxygen involved in the Co-O-Ti, therefore leading to further destabilisation as it introduces a significant amount of electron spin to the titanium environment. By comparing the bimetallic CoTiAlPO-5 unit cells in which the cobalt and titanium are separated with the monometallic unit cells there is very little variation in bond length, electron count or electron spin for either oxidation state (Tables 5.19 to 5.22). This then translates into a redox value that more closely resembles the monometallic species. As such we conclude that the differences in electron spin between the bimetallic (Co-O-Ti) and monometallic systems are responsible for the difference in redox behaviour. This contributes to a destabilisation of the trivalent species over the divalent species, and thus invokes the catalytic synergy observed.

5.3 Results and discussion – Synergy in the formation of hydroxylamine

The sustainable production of NH_2OH is of great interest, as it could circumvent the need for hydroxylamine sulphate in industrial methods. A range of methods have been pursued to replace this caustic reagent, however the ability of cobalt-substituted AlPOs to perform oxidation reactions provides an interesting alternative to more traditional industrial methods. As such the activation of ammonia is of significant interest. Previously, mechanistic studies on activation of hydrocarbons suggest that the initial (and rate-determining) step of the reaction is the activation of the organic substrate to form a radical species.[42] Thus: R-H → R· + H·. Previous work by Cora *et al* on the theoretical activation of ethane suggests that the activation energy for this step is in the region of 135 kJ/mol, with a reaction enthalpy of 93 kJ/mol.[42] By employing a similar methodology we began by investigating the interactions between the appropriate reagents (ammonia and oxygen) for hydroxylamine formation with the different monometallic active species. It was found that neither titanium nor cobalt (in either oxidation state) showed any significant interaction with the oxygen species (see Table 5.6). Instead both oxygen atoms resided at least

3.0 Å away from the metal centre in all three cases. As such the small stabilisation effect on putting oxygen into the framework is not due to any metal-oxygen interaction, but is instead attributed to Van der Waal forces between the oxygen molecule and the pore walls. In contrast all species showed a strong interaction with ammonia (Table 5.6).

Table 5.6: Quantifying the binding energies of ammonia and oxygen with specific metal centres (values in kJ/mol).

System	NH_3	O_2
Co^{2+}AlPO-5	-56.1	-4.7
Co^{3+}AlPO-5	-63.3	-6.0
Ti^{4+}AlPO-5	-107.9	-12.3

In all cases ammonia formed a strong chemical bond between the lone pair of electrons on nitrogen and the electron-deficient metal centre, instead of the charge-balancing protons, behaving in an analogous fashion to that observed in MnAlPO-5 for the activation of ethane.[42] From previous experimental knowledge it is known that this particular isolated titanium site (having exclusively undergone type II substitution) possesses little redox capability. Further, in order to become 'active' cobalt-containing AlPOs must be calcined to access the higher trivalent oxidation state before catalysing oxidation reactions.[33] By combining these two vital factors with the binding energies above (Table 5.6) it follows that the initial step of this reaction involves an interaction between ammonia and a Co^{3+} species. The possibility of O_2 playing a role was also explored through the addition of an oxygen atom to the system. However this only stabilised the system by a further 7.3 kJ/mol, which is a comparable amount to the Van der Waal forces observed on confining the oxygen molecule.

In alignment with the above observations the binding of NH_3 was investigated with the bimetallic $Co^{3+}Ti^{4+}$AlPO-5 system. Despite the monometallic TiAlPO-5 binding more strongly to the NH_3 than the monometallic Co^{3+}AlPO-5 site it was found that in the analogous bimetallic system the NH_3 preferentially bound to the cobalt ion. This is attributed to the subtle differences in geometry and

electron spins that have been found between the two titanium sites. In light of this we therefore suggest the following reaction scheme for both the monometallic CoAlPO-5 and bimetallic CoTiAlPO-5 systems (Figure 5.11).

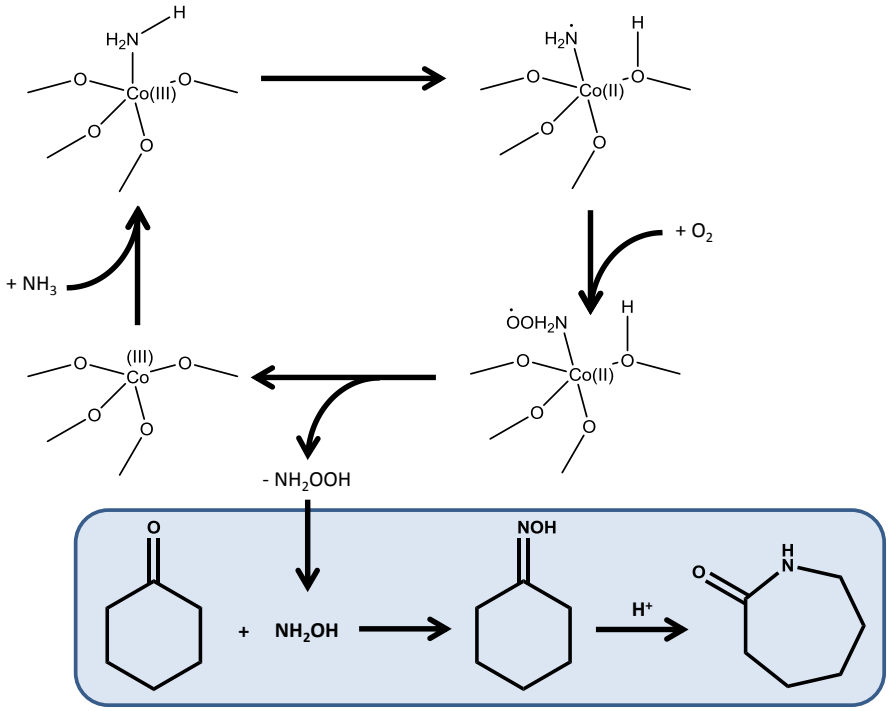

Figure 5.11: Proposed reaction mechanism for the formation of hydroxylamine in the ammoximation of cyclohexanone.

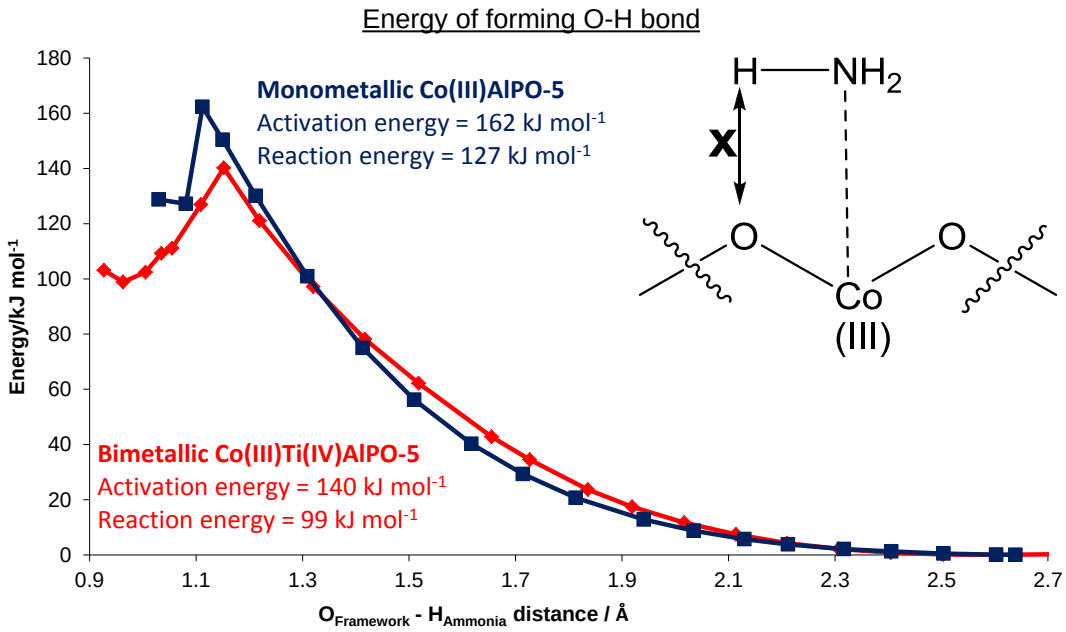

Figure 5.12: Contrasting the energy profile of ammonia activation for monometallic Co^{3+}AlPO-5 and bimetallic $Co^{3+}Ti^{4+}$AlPO-5.

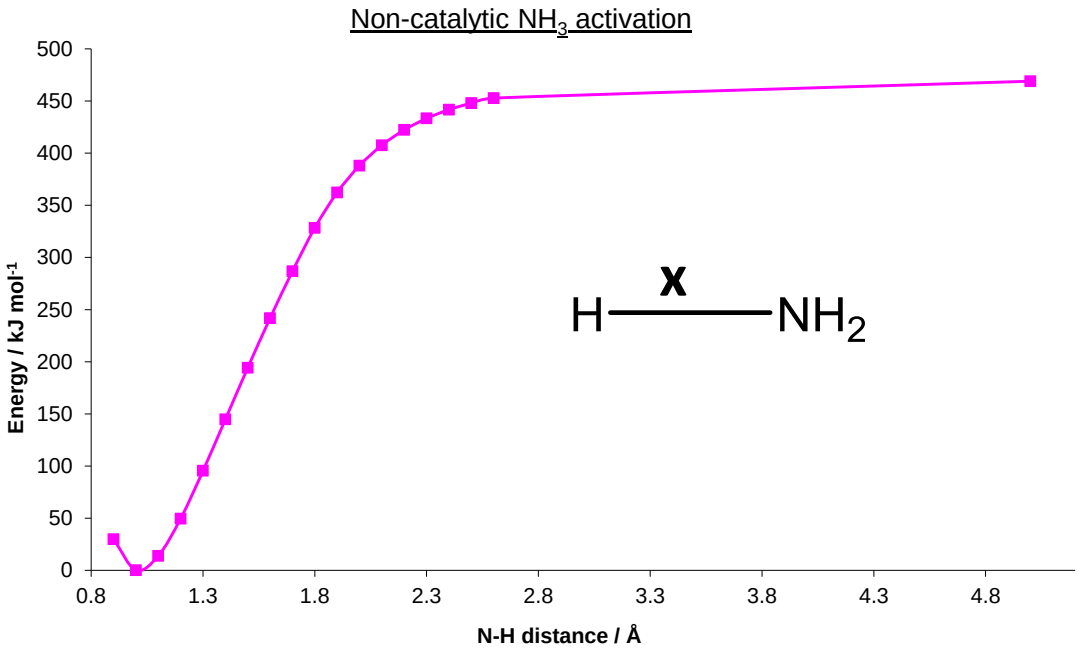

Figure 5.13: Energy profile showing the energy required to break the H—NH_2 bond non-catalytically.

The mechanism proposed is analogous to that embraced by Cora *et al*. We therefore investigate the initial reaction step by monitoring a range of parameters as the reaction coordinate ($O_{Framework}$ – $H_{Ammonia}$ distance) is controlled, resulting in the following energy profiles above. In both cases the framework oxygen of interest was selected by considering the lowest energy proton positions for both the relaxed Co^{3+} and Co^{2+} states where appropriate, in line with previous work. In the monometallic species this encompassed $Co(OP)_4$ becoming $Co(OP)_3(OHP)$ and similarly the bimetallic species transformed from $Co(OP)_3(OTi)$ to $Co(OP)_3(OHTi)$.

It is noted that both the activation energy and reaction energy are lower in the bimetallic ($Co^{3+}Ti^{4+}$AlPO-5) sample than the monometallic (Co^{3+}AlPO-5) species (Figure 5.12). These findings suggest that the bimetallic sample would be the appropriate catalyst for this process, resulting in improved rates of reaction and larger conversions. In accordance with the lower activation energy we also note that the transition state of the bimetallic system occurs at a larger O-H distance than the monometallic system. Again this is in-keeping with the lower activation energy of this process. Further, the final O-H distance is significantly

shorter in the bimetallic system than the monometallic system, this can be attributed to the distorted Co-O-Ti bond forming stronger bonds, something that has been previously observed when contrasting relaxed geometries of Co^{2+}AlPO-5 and $Co^{2+}Ti^{4+}$AlPO-5. These values are both significantly lower than the energy required to perform this reaction step in the absence of a catalyst (460 kJ mol^{-1}, Figure 5.13), thus confirming the necessity for a well-defined isolated active centre to catalyse this reaction.

Closer investigation of the electron spins explains the differing behaviour between the two systems (Figure 5.14 and 5.15). The electron spins varied throughout the reaction step. In both cases the nitrogen initially possesses a slight localised spin (~ 0.1 electrons), while the cobalt starts in the Co^{3+} state with a localised spin of ~ 3.0 electrons, in line with our previous calculations. These spins are constant until the systems reach the transition state, at which point an electron transfer is prompted, whereby the N-H bond breaks homolytically, creating an amide radical and simultaneously reducing Co^{3+} to Co^{2+}. Previous work shows that the divalent Co^{2+} state is stabilised by the presence of an adjacent Ti^{4+} ion. As such the initial ammonia activation step encompasses the reduction of Co^{3+} to Co^{2+} and therefore is likely to be favoured in the bimetallic species. Inspection of the involved oxygen shows in both cases the spin is significantly reduced by the proton binding to it. We note that the binding of ammonia to the cobalt modifies the electron spin of the specific framework oxygen. While this has subtly different effects on the mono- and bi-metallic systems the overall trend is preserved on binding ammonia. The electron spin of the oxygen in the bimetallic system (0.43 electrons) possesses a significantly greater spin than the corresponding oxygen in the monometallic system (0.15 electrons). By examining how the oxygen spin evolves as a function of the reaction parameter we observe a stark contrast to the behaviour of the other spin species. Instead of alternating between two defined states, the oxygen spin shows a significant decrease as the reaction parameter decreases, with a notable jump, coinciding with the transition state. In both cases a significant reduction in the oxygen spin occurs (Figure 5.16), though this occurs to a much greater extent in the bimetallic (0.43 becomes 0.06) than the monometallic (0.15 to 0.03). This significant reduction in spin (in the bimetallic system) which is a contributory factor to the lower activation energy and reaction enthalpy observed in this reaction step.

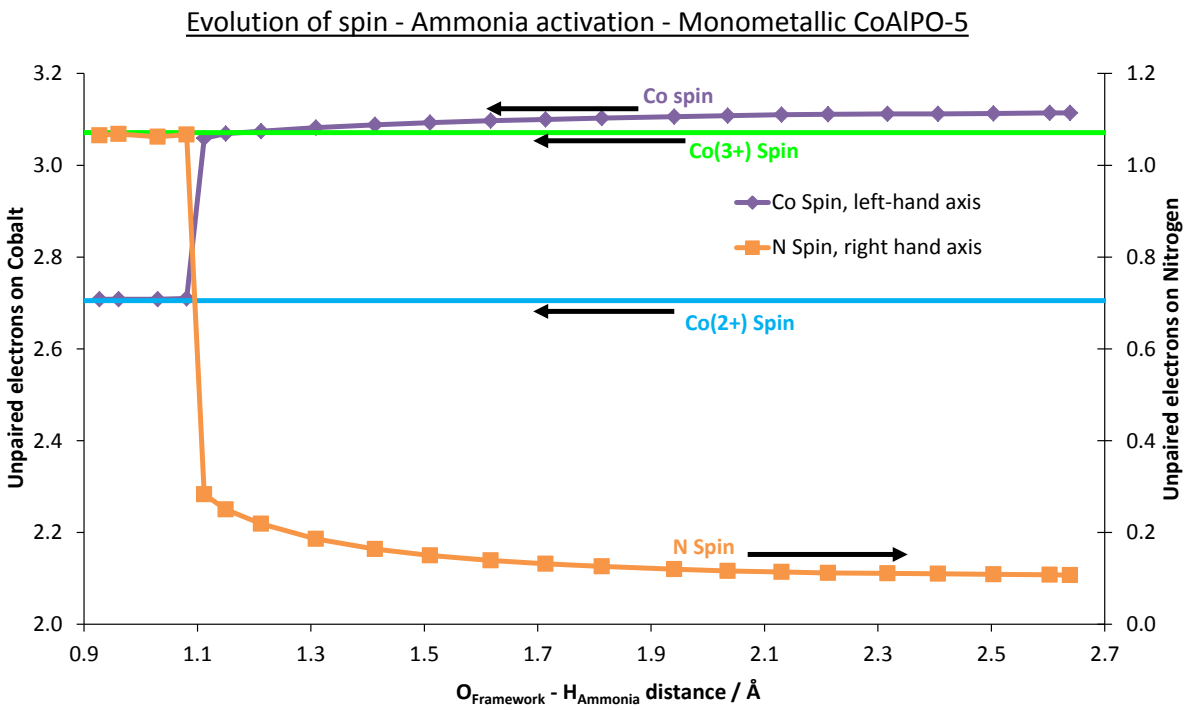

Figure 5.14: Spin evolution of monometallic CoAlPO-5 for the activation of ammonia.

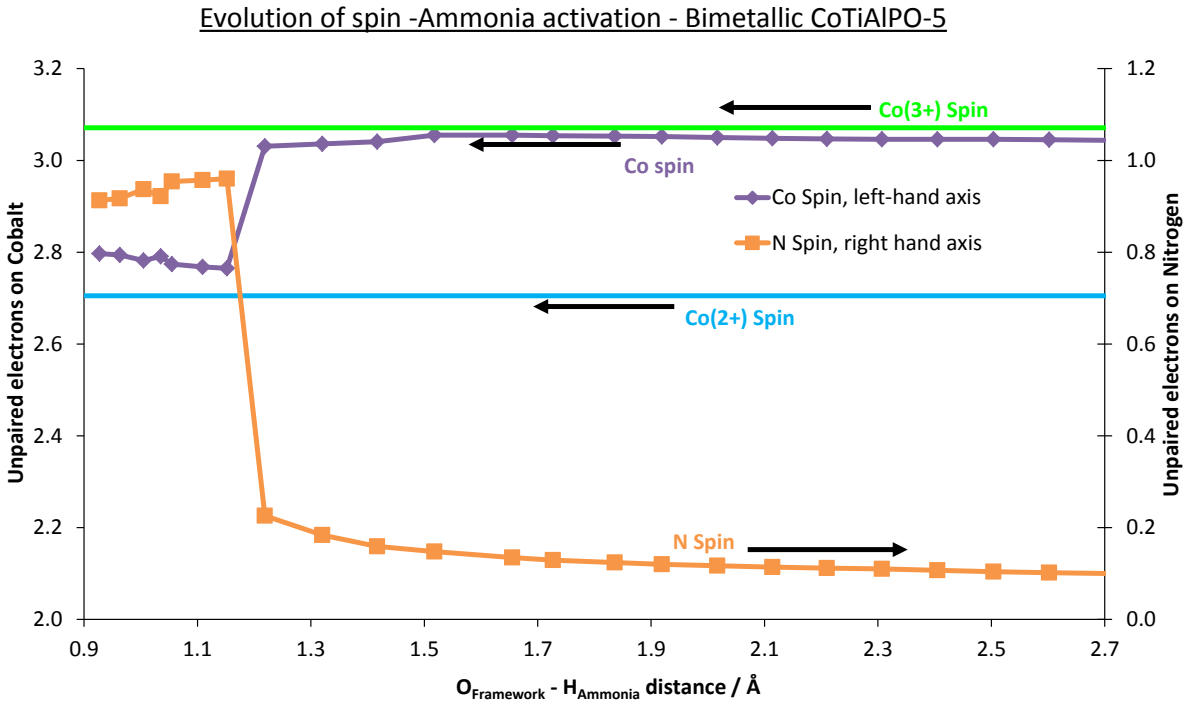

Figure 5.15: Spin evolution of bimetallic CoTiAlPO-5 for the activation of ammonia.

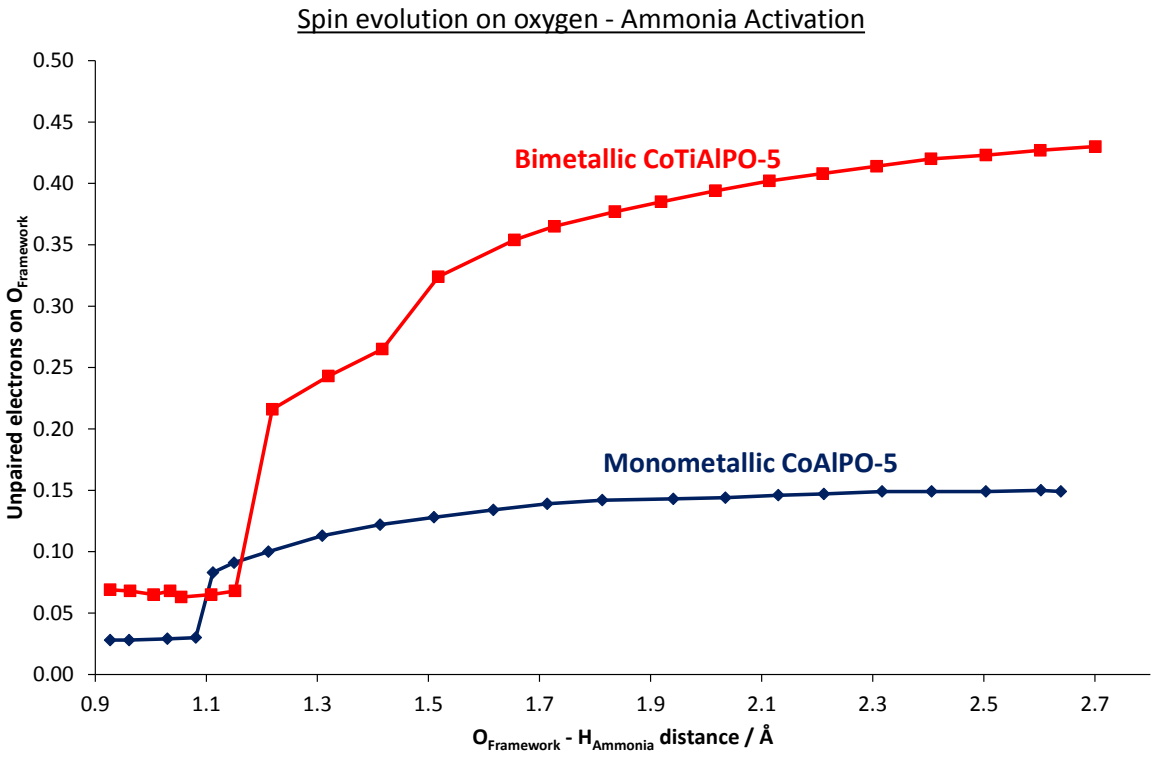

Figure 5.16: Comparison of the spin evolution on the framework oxygen in the monometallic and bimetallic systems.

Careful consideration of the geometries of the two systems (Figures 5.17 and 5.18) reveal fundamental differences in the behaviour of the mono- and bi-metallic systems. Analysis of specific bond lengths (N-H and Co-N) in the monometallic system reveals that the amide radical maintains an interaction with the separated hydrogen atom. As a consequence the amide radical moves away from the cobalt atom, extending the Co-N bond, while maintaining a constant N-H bond distance. In clear contrast the bimetallic system maintains the Co-N bond length and instead breaks the N-H bond. This behaviour is attributed to the enhanced stability and bond strength of the framework-proton bond in the bimetallic system. This increased stability has already been witnessed when considering the shorter O-H bond in the product state of the bimetallic system, which has already been discussed. As a consequence this proton is already stabilised and adopts a geometry which hinders interactions with the amide radical. As such the amide instead maintains the Co-N bond and resides in close proximity to the cobalt ion. We note that as a result of the Co-N bond being maintained in the bimetallic system a proportion of the spin is transferred from the nitrogen to the cobalt atom. In the bimetallic CoTiAlPO-

5 system the nitrogen and cobalt have spins of 2.794 and 0.917 unpaired electrons respectively. Whereas in the monometallic CoAlPO-5 system the amide radical has a higher spin of 1.067 unpaired electrons, while the cobalt possess a spin of 2.710 unpaired electrons. Whilst these differences may appear only subtle, the instability of the amide radical means any spin leaching away from the nitrogen will significantly stabilise the system. Thus the retention of the Co-N bond in the bimetallic system will stabilise the newly formed amide radical, further accounting for the lower reaction enthalpy and activation energy. Therefore it is believed that lower reaction enthalpy and activation energy for this rate determining reaction step are due to a combination of factors. These include the bimetallic system favouring the Co^{2+} state more than the monometallic, the increased spin stabilisation of the framework oxygen and the transfer of spin from the nitrogen to the cobalt.

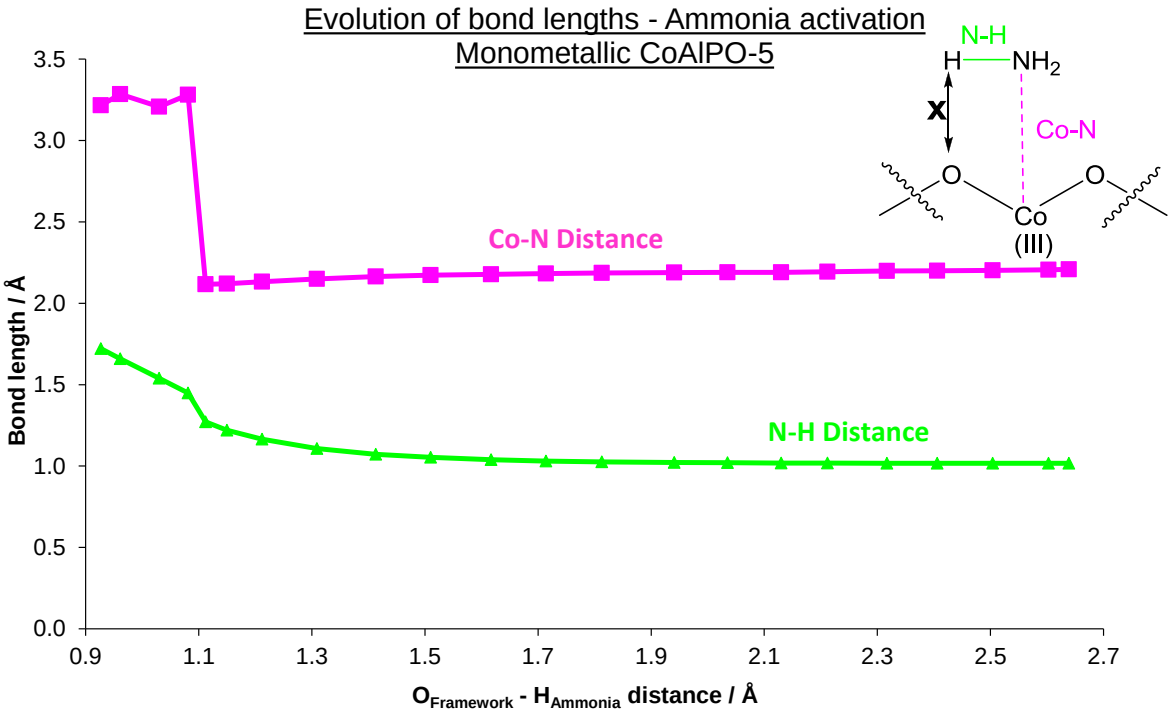

Figure 5.17: The evolution of bond lengths in the monometallic CoAlPO-5 system for the initial ammonia activation step.

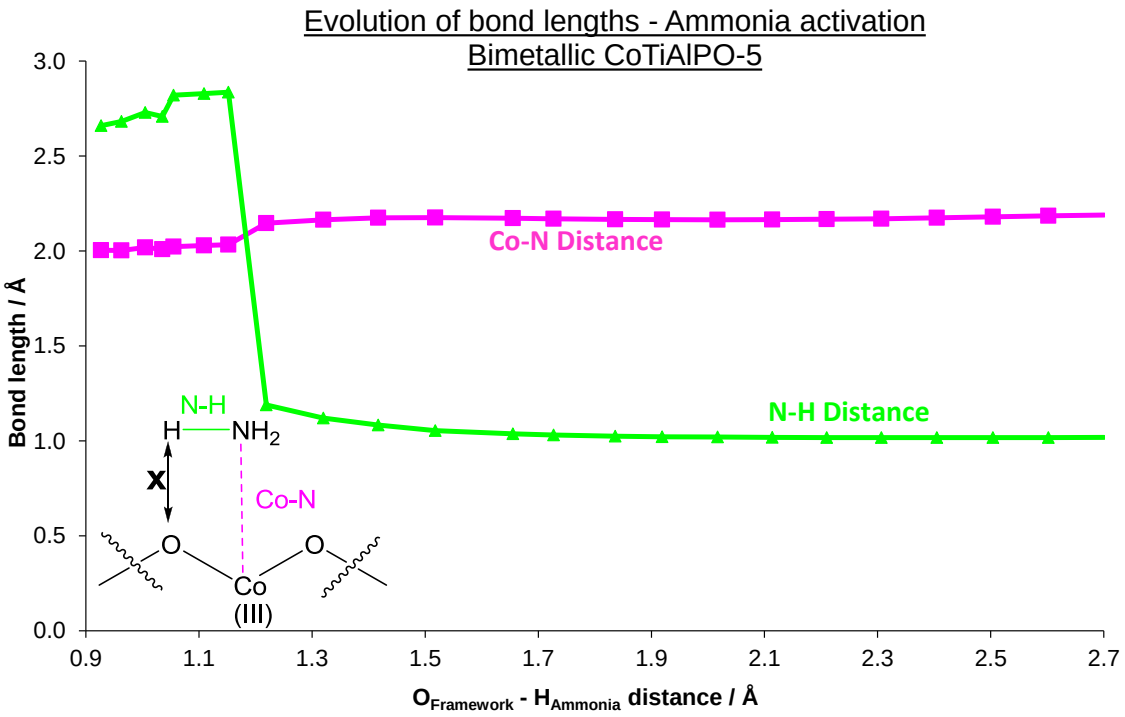

Figure 5.18: The evolution of bond lengths in the bimetallic CoTiAlPO-5 system for the initial ammonia activation step.

Once generated radical species are readily stabilised by the presence of triplet oxygen, as the two oppositely paired spin species combine to form a covalent bond, thus cancelling out the equal and opposite spins.[41,42] The $N_{Ammonia}$-O_{oxygen} distance is selected as the reaction parameter and in both cases shows a significantly lower activation energy and reaction enthalpy than the initial N-H activation step, as expected (Figure 5.19). In contrast to the initial step the activation energy and reaction energy are both lower for the monometallic system than the bimetallic system. This behaviour is attributed to the changes in geometry, particularly the Co-N distance. Recall in the first step the monometallic system had already broken the Co-N bond, which was retained in the bimetallic system. The formation of the NH_2OO radical only slightly extends to Co-N bond in the monometallic system from 3.21 to 3.28 Å (Figure 5.20), given that the Co-N bond is already severed. In the bimetallic system the Co-N is finally broken on addition of the O_2 to form NH_2OO, thus the Co-N bond length now varies from 2.00 to 2.83 Å (Figure 5.21), a significantly larger expansion. Thus the extension of the Co-N bond is responsible for the increased activation energy experienced in the bimetallic system.

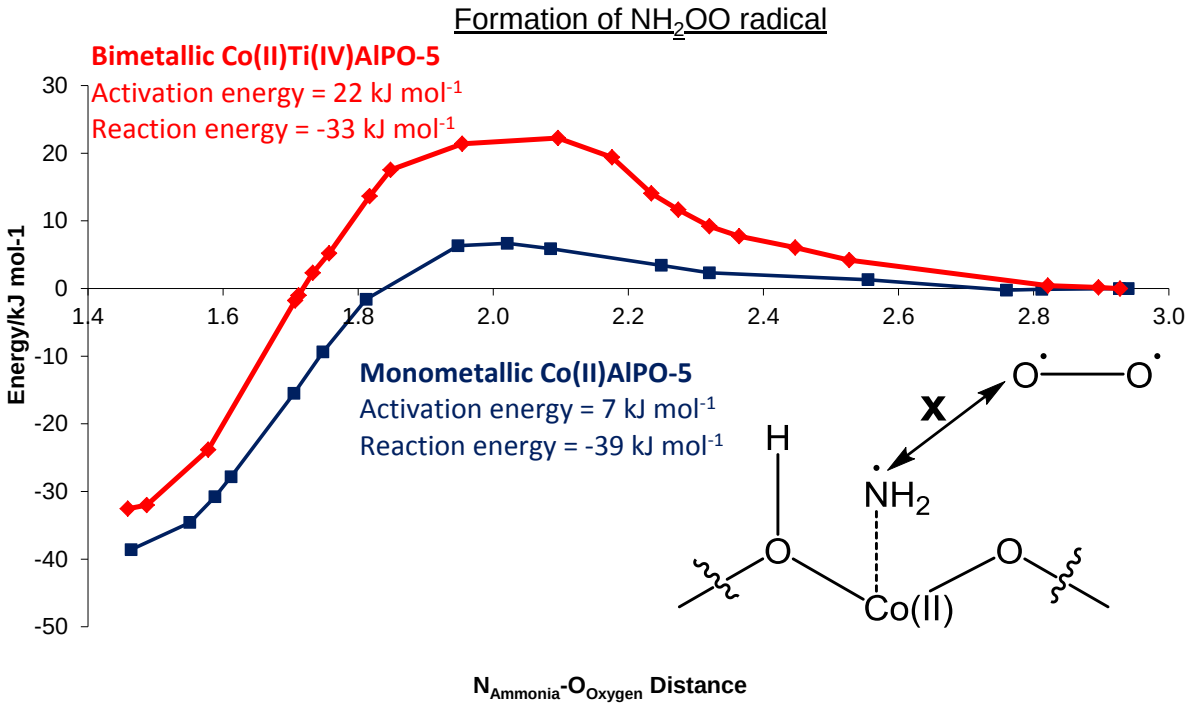

Figure 5.19: Contrasting the energy profile of NH_2OO formation for both monometallic Co^{2+}AlPO-5 and bimetallic $Co^{2+}Ti^{4+}$AlPO-5.

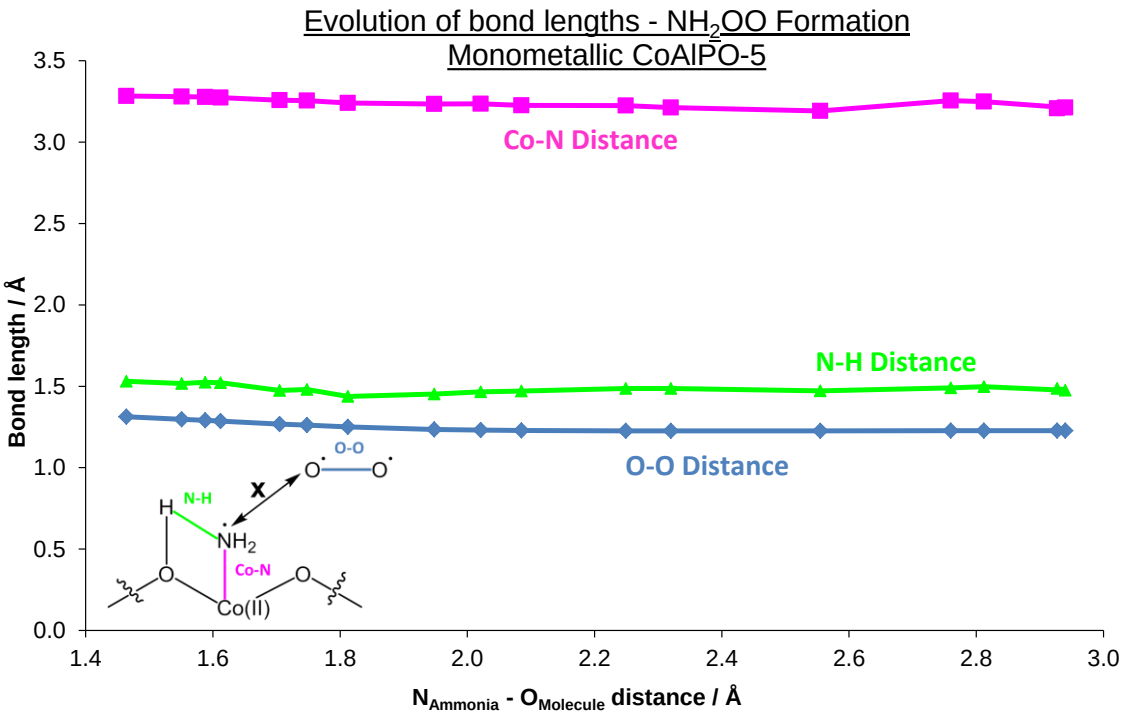

Figure 5.20: The evolution of bond lengths in the monometallic CoAlPO-5 system for the NH_2OO formation step.

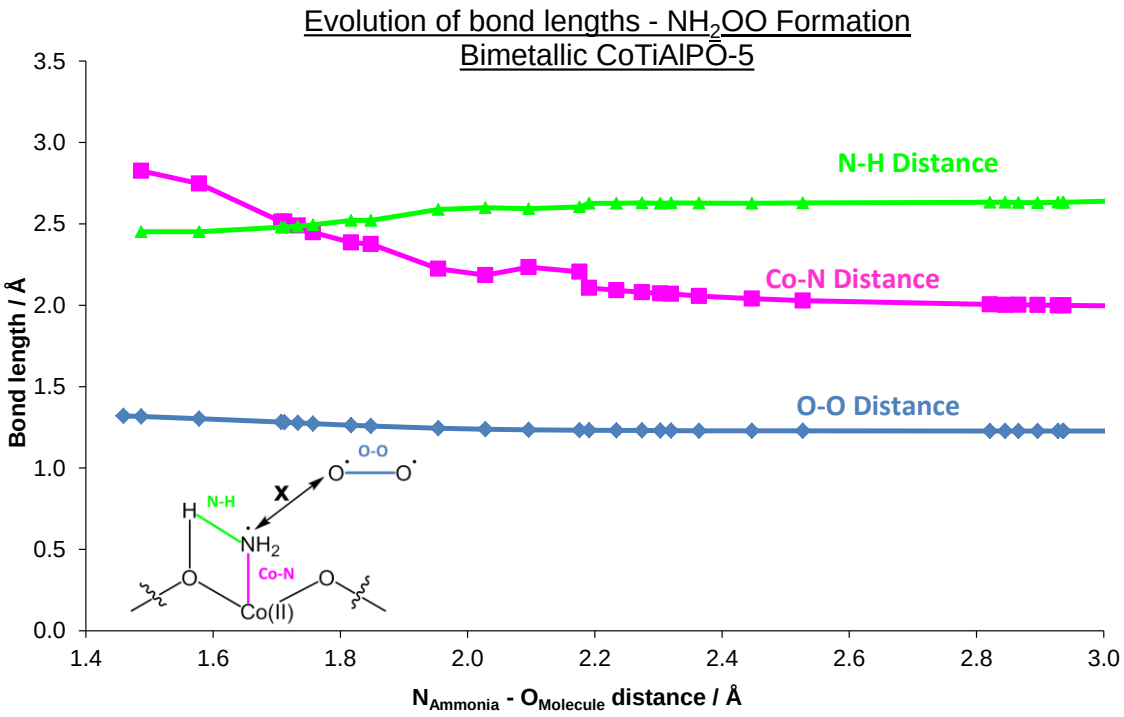

Figure 5.21: The evolution of bond lengths in the bimetallic CoTiAlPO-5 system for the NH_2OO formation step.

Investigation of the electron spins shows little variation between the two systems (Figure 5.22 and 5.23). On approaching the amide radical the spin on the nitrogen is depleted. This is due to the alpha electrons on the nitrogen becoming involved in a covalent bond with one of the two beta electrons on the oxygen molecule, thus three unpaired electrons cancel to one during the formation of the NH_2OO radical species. The remaining spin due to the final unpaired electron is split between the two oxygen atoms with the terminal oxygen possessing twice as much spin as the intermediate oxygen in both cases. Only subtle variations can be seen in the cobalt spin between the two systems. The monometallic system shows no variation in the cobalt spin, maintaining a spin of 2.71 unpaired electrons (Figure 5.22). The bimetallic system shows a slight change from 2.80 to 2.71 unpaired electrons (Figure 5.23). This is again attributed to the breaking of the Co-N bond in the bimetallic system. During the stabilisation of the amide radical some of the spin was transferred from the nitrogen to the cobalt atom, on breaking this bond the spin is transferred back to the NH_2/NH_2OO species, and off the cobalt. Given the subtlety of this change it is believed to be only a symptom of

the Co-N bond breaking. The latter of which is considered to be the primary factor in the discrepancy in energy between the two systems in this secondary reaction step. Though inspite of the energetics favouring the monometallic system in the second reaction step, it is clear that the bimetallic system will still act as a superior catalyst given the lower energy required in the rate determining step, and overall for the whole process.

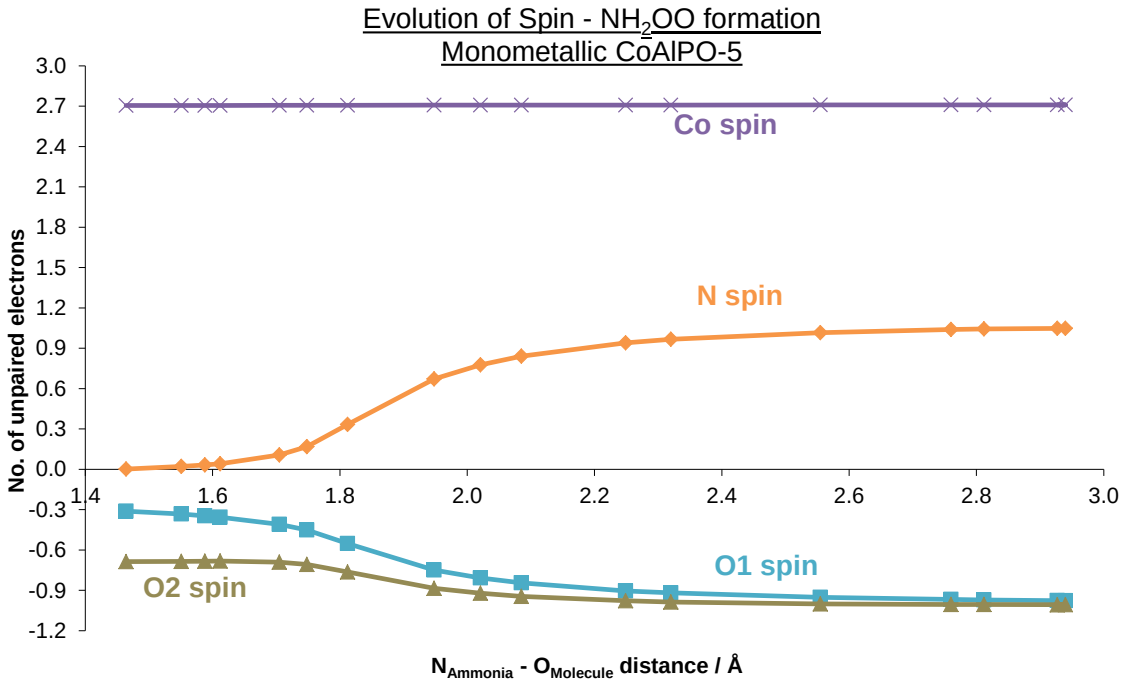

Figure 5.22: The evolution of spin in the monometallic CoAlPO-5 system for the formation of the NH_2OO radical species.

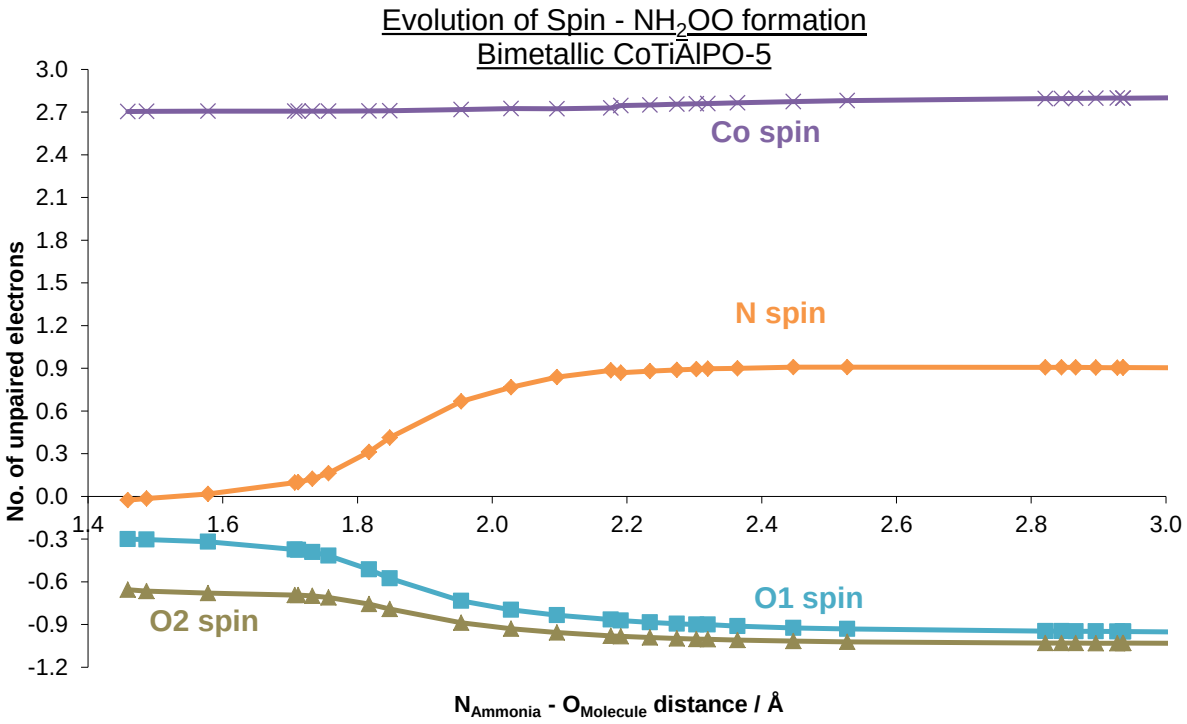

Figure 5.23: The evolution of spin in the bimetallic CoTiAlPO-5 system for the formation of the NH_2OO radical species.

5.4 Conclusions

In summary the synergistic enhancement shown by the bimetallic CoTiAlPO-5 system has been explored, with particular emphasis on the isomorphously substituted tetrahedral $Co^{2+/3+}$ active site. We conclude that the synergistic phenomenon of the bimetallic system can be explained by adjacent substitution of the cobalt and titanium dopants as witnessed through theoretical calculations and experimental findings. This adjacent substitution forces subtle changes in the local environment of the cobalt site in both the bimetallic and monometallic systems. Such variations, provoke variations with the coordination geometry, which then translate into significant modifications in redox behaviour. By modifying the local environment of the bimetallic cobalt site it was shown that the preference for the divalent state is increased, prompting a more energetically favourable rate-determining step in oxidation reactions, explaining the observed catalytic synergy.

By employing periodic DFT calculations we have shown the benefits of careful catalytic design and the benefits of bimetallic substitution. Through careful investigation of the initial reaction steps of the aerobic activation of ammonia we have revealed that the catalytic activity during the rate determining step can be enhanced through the application of a bimetallic CoTiAlPO-5 catalyst. As such we have shown how our previous synthetic and experimental work can be combined to rationally design purpose-made catalysts for targeted green applications such as the ammoxmation of cyclohexanone (Figure 5.24).

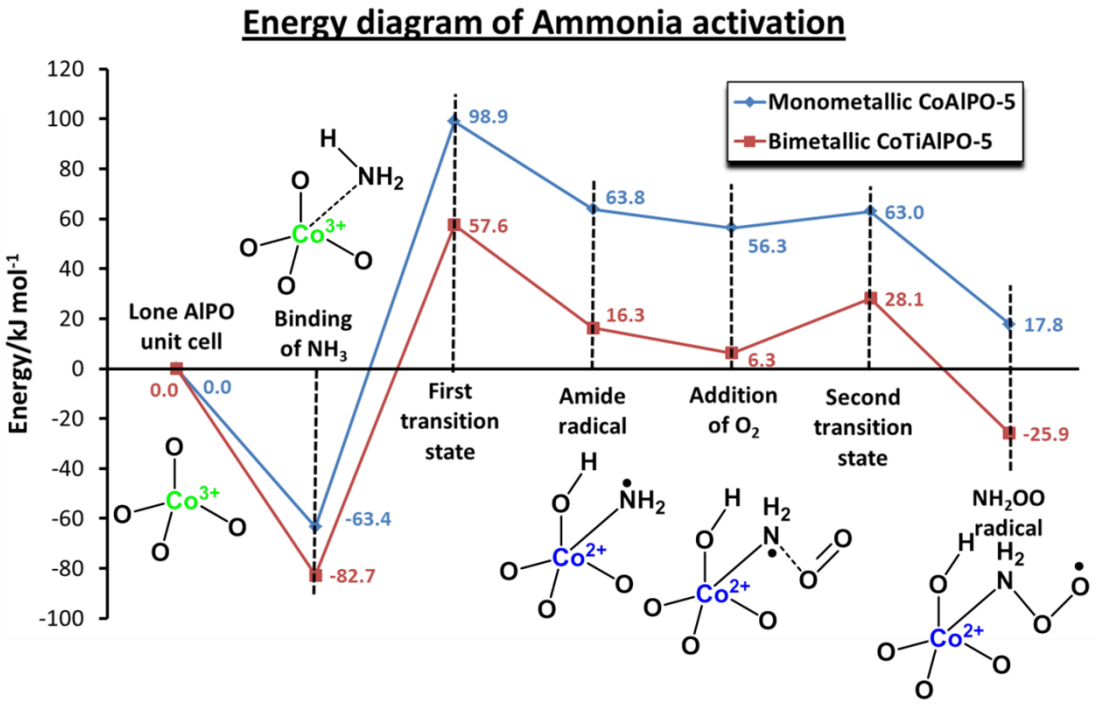

Figure 5.24: Full comparison of the complete energetics required in the first two reaction steps.

5.5 Structural data – Bond lengths and electron spins

Further computational data on undoped AlPO-5

Table 5.7: Bond lengths in undoped AlPO-5.

Atom 1	Atom 2	Bond length/Å
Al1	O1	1.736
Al1	O2	1.743
Al1	O3	1.738
Al1	O4	1.756
O1	P1	1.546
O2	P2	1.537
O3	P3	1.540
O4	P4	1.538
Al1	P1	3.077
Al1	P2	3.089
Al1	P3	3.082
Al1	P4	3.055

Table 5.8: Calculated Mulliken populations for undoped AlPO-5

Atom	Placement	Electron count (α + β)	Electron spin (α – β)
Al1	Central atom	11.057	0.000
O1	First coordination shell (Al1)	9.041	0.000
O2	First coordination shell (Al1)	9.047	0.000
O3	First coordination shell (Al1)	9.048	0.000
O4	First coordination shell (Al1)	9.044	0.000
P1	Second coordination shell (O1)	12.769	0.000
P2	Second coordination shell (O2)	12.761	0.000
P3	Second coordination shell (O3)	12.770	0.000
P4	Second coordination shell (O4)	12.770	0.000

Further computational data on monometallic Co^{2+}AlPO-5

Table 5.9: Bond lengths in monometallic Co^{2+}AlPO-5.

Atom 1	Atom 2	Bond length/Å
Co1	O1 (H1)	2.120
Co1	O2	1.871
Co1	O3	1.897
Co1	O4	1.876
O1 (H1)	P1 (H1)	1.608
O2	P2	1.518
O3	P3	1.520
O4	P4	1.524
Co1	P1 (H1)	3.424
Co1	P2	3.119
Co1	P3	3.100
Co1	P4	3.196
O1	H1	0.992
Co1	H1	2.652

Table 5.10: Calculated Mulliken populations for monometallic Co^{2+}AlPO-5

Atom	Placement	Electron count (α + β)	Electron spin (α – β)
Co1	Central atom	25.402	0.000
O1 (H)	First coordination shell (Co1)	8.890	0.023
O2	First coordination shell (Co1)	9.076	0.082
O3	First coordination shell (Co1)	9.085	0.070
O4	First coordination shell (Co1)	9.082	0.080
P1 (H)	Second coordination shell (O1)	12.742	0.002
P2	Second coordination shell (O2)	12.795	0.005
P3	Second coordination shell (O3)	12.781	0.007
P4	Second coordination shell (O4)	12.795	0.006
H1	Proton (O1)	0.634	0.000

Further computational data on monometallic Co^{3+}AlPO-5

Table 5.11: Bond lengths in monometallic Co^{3+}AlPO-5.

Atom 1	Atom 2	Bond length/Å
Co1	O1	1.816
Co1	O2	1.820
Co1	O3	1.837
Co1	O4	1.822
O1	P1	1.548
O2	P2	1.545
O3	P3	1.541
O4	P4	1.546
Co1	P1	3.139
Co1	P2	3.096
Co1	P3	3.143
Co1	P4	3.130

Table 5.12: Calculated Mulliken populations for monometallic Co^{3+}AlPO-5

Atom	Placement	Electron count (α + β)	Electron spin (α – β)
Co1	Central atom	25.106	3.071
O1	First coordination shell (Co1)	9.041	0.218
O2	First coordination shell (Co1)	9.042	0.218
O3	First coordination shell (Co1)	9.045	0.199
O4	First coordination shell (Co1)	9.053	0.203
P1	Second coordination shell (O1)	12.765	0.004
P2	Second coordination shell (O2)	12.771	0.003
P3	Second coordination shell (O3)	12.760	0.003
P4	Second coordination shell (O4)	12.761	0.003

Further computational data on monometallic Ti^{4+}AlPO-5

Table 5.13: Bond lengths in monometallic Ti^{4+}AlPO-5.

Atom 1	Atom 2	Bond length/Å
Ti1	O1 (H1)	1.987
Ti1	O2	1.775
Ti1	O3	1.765
Ti1	O4	1.751
O1 (H1)	Al1 (H1)	1.792
O2	Al2	1.700
O3	Al3	1.711
O4	Al4	1.751
Ti1	Al1 (H1)	3.425
Ti1	Al2	3.197
Ti1	Al3	3.284
Ti1	Al4	3.362
O1	H1	0.970
Ti1	H1	2.528

Table 5.14: Calculated Mulliken populations for monometallic Ti^{4+}AlPO-5

Atom	Placement	Electron count (α + β)	Electron spin (α – β)
Ti1	Central atom	19.985	0.000
O1 (H)	First coordination shell (Ti1)	8.934	0.000
O2	First coordination shell (Ti1)	9.062	0.000
O3	First coordination shell (Ti1)	9.077	0.000
O4	First coordination shell (Ti1)	9.050	0.000
Al1 (H)	Second coordination shell (O1)	11.058	0.000
Al2	Second coordination shell (O2)	11.081	0.000
Al3	Second coordination shell (O3)	11.062	0.000
Al4	Second coordination shell (O4)	11.070	0.000
H1	Proton (O1)	0.671	0.000

Further computation data on bimetallic $Co^{2+}Ti^{4+}$AlPO-5, containing a Co-O-Ti bridge

Table 5.15: Bond lengths in bimetallic $Co^{2+}Ti^{4+}$AlPO-5, containing a Co-O-Ti bridge.

Atom 1	Atom 2	Bond length/Å
Co1	O1 (H1)	1.973
Co1	O2	1.909
Co1	O3	1.782
Co1	O4	2.005
Ti1	O1 (H1)	1.961
Ti1	O5 (H2)	1.983
Ti1	O6	1.731
Ti1	O7	1.719
O2	P1	1.514
O3	P2	1.519
O4	P3	1.540
O5 (H2)	Al1 (H2)	1.801
O6	Al2	1.703
O7	Al3	1.731
Co1	Ti1	3.266
Co1	P1	3.162
Co1	P2	2.935
Co1	P3	2.927
Ti1	Al1 (H2)	3.535
Ti1	Al2	3.210
Ti1	Al3	3.256
O1	H1	0.973
O5	H2	0.982
Co1	H1	2.488
Ti1	H1	2.624
Ti1	H2	2.494

Table 5.16: Calculated Mulliken populations for bimetallic $Co^{2+}Ti^{4+}$AlPO-5, containing a Co-O-Ti bridge.

Atom	Placement	Electron count (α + β)	Electron spin (α – β)
Co1	Central atom	25.426	2.686
Ti1	Central atom	19.952	0.005
O1 (H)	First coordination shell (Co1 & Ti1)	8.942	0.051
O2	First coordination shell (Co1)	9.078	0.061
O3	First coordination shell (Co1)	9.083	0.085
O4	First coordination shell (Co1)	9.095	0.075
O5 (H)	First coordination shell (Ti1)	8.960	0.000
O6	First coordination shell (Ti1)	9.030	0.001
O7	First coordination shell (Ti1)	9.016	0.000
P1	Second coordination shell (O2)	12.788	0.005
P2	Second coordination shell (O3)	12.809	0.006
P3	Second coordination shell (O4)	12.797	0.004
Al1	Second coordination shell (O5)	11.052	0.000
Al2	Second coordination shell (O6)	11.063	0.000
Al3	Second coordination shell (O7)	11.066	0.000
H1	Proton (O1)	0.671	0.000
H2	Proton (O5)	0.647	0.000

Further computation data on bimetallic $Co^{3+}Ti^{4+}$AlPO-5, containing a Co-O-Ti bridge

Table 5.17: Bond lengths in bimetallic $Co^{3+}Ti^{4+}$AlPO-5, containing a Co-O-Ti bridge.

Atom 1	Atom 2	Bond length/Å
Co1	O1	1.757
Co1	O2	1.860
Co1	O3	1.743
Co1	O4	1.931
Ti1	O1	1.928
Ti1	O5 (H1)	1.988
Ti1	O6	1.744
Ti1	O7	1.768
O2	P1	1.534
O3	P2	1.534

O4	P3	1.557
O5 (H1)	Al1 (H1)	1.805
O6	Al2	1.665
O7	Al3	1.726
Co1	Ti1	3.158
Co1	P1	3.166
Co1	P2	2.999
Co1	P3	3.085
Ti1	Al1 (H1)	3.522
Ti1	Al2	3.126
Ti1	Al3	3.234
O5	H1	0.975
Ti1	H1	2.499

Table 5.18: Calculated Mulliken populations for bimetallic $Co^{3+}Ti^{4+}$AlPO-5, containing a Co-O-Ti bridge.

Atom	Placement	Electron count (α + β)	Electron spin (α – β)
Co1	Central atom	25.165	3.008
Ti1	Central atom	19.995	0.020
O1	First coordination shell (Co1 & Ti1)	8.977	0.419
O2	First coordination shell (Co1)	9.072	0.141
O3	First coordination shell (Co1)	9.040	0.170
O4	First coordination shell (Co1)	9.079	0.168
O5 (H)	First coordination shell (Ti1)	8.952	0.002
O6	First coordination shell (Ti1)	9.040	0.006
O7	First coordination shell (Ti1)	9.046	0.011
P1	Second coordination shell (O2)	12.767	0.005
P2	Second coordination shell (O3)	12.777	0.005
P3	Second coordination shell (O4)	12.762	0.004
Al1	Second coordination shell (O5)	11.050	0.000
Al2	Second coordination shell (O6)	11.067	0.000
Al3	Second coordination shell (O7)	11.068	0.000
H1	Proton (O5)	0.661	-0.001

Further computation data on bimetallic $Co^{2+}Ti^{4+}$AlPO-5, without a Co-O-Ti bridge

Table 5.19: Bond lengths in bimetallic $Co^{2+}Ti^{4+}$AlPO-5, without a Co-O-Ti bridge.

Atom 1	Atom 2	Bond length/Å
Co1	O1 (H1)	2.074
Co1	O2	1.884
Co1	O3	1.903
Co1	O4	1.897
Ti1	O5 (H2)	1.969
Ti1	O6	1.750
Ti1	O7	1.767
Ti1	O8	1.767
O1 (H1)	P1 (H1)	1.619
O2	P2	1.515
O3	P3	1.515
O4	P4	1.532
O5 (H2)	Al1 (H2)	1.784
O6	Al2	1.708
O7	Al3	1.701
O8	Al4	1.671
Co1	P1 (H1)	3.295
Co1	P2	3.267
Co1	P3	3.137
Co1	P4	3.207
Ti1	Al1 (H2)	3.465
Ti1	Al2	3.315
Ti1	Al3	3.253
Ti1	Al4	3.216
O1	H1	0.994
O5	H2	0.986
Co1	H1	2.675
Ti1	H2	2.549

Table 5.20: Calculated Mulliken populations for bimetallic $Co^{2+}Ti^{4+}$AlPO-5, without a Co-O-Ti bridge.

Atom	Placement	Electron count (α + β)	Electron spin (α – β)
Co1	Central atom	25.388	2.722
Ti1	Central atom	19.975	0.006
O1 (H)	First coordination shell (Co1)	8.903	0.026
O2	First coordination shell (Co1)	9.082	0.078
O3	First coordination shell (Co1)	9.071	0.069
O4	First coordination shell (Co1)	9.078	0.066
O5 (H)	First coordination shell (Ti1)	8.975	0.000
O6	First coordination shell (Ti1)	9.059	0.000
O7	First coordination shell (Ti1)	9.067	0.000
O8	First coordination shell (Ti1)	9.071	0.000
P1	Second coordination shell (O1)	12.755	0.002
P2	Second coordination shell (O2)	12.786	0.006
P3	Second coordination shell (O3)	12.793	0.006
P4	Second coordination shell (O4)	12.798	0.007
Al1	Second coordination shell (O5)	11.062	0.000
Al2	Second coordination shell (O6)	11.070	0.000
Al3	Second coordination shell (O7)	11.062	0.000
Al4	Second coordination shell (O8)	11.067	0.000
H1	Proton (O1)	0.634	0.000
H2	Proton (O5)	0.654	0.000

Further computation data on bimetallic $Co^{3+}Ti^{4+}$AlPO-5, without a Co-O-Ti bridge

Table 5.21: Bond lengths in bimetallic $Co^{3+}Ti^{4+}$AlPO-5, without a Co-O-Ti bridge.

Atom 1	Atom 2	Bond length/Å
Co1	O1	1.847
Co1	O2	1.838
Co1	O3	1.752
Co1	O4	1.859
Ti1	O5 (H1)	1.966
Ti1	O6	1.754
Ti1	O7	1.767
Ti1	O8	1.759
O1	P1	1.544
O2	P2	1.541
O3	P3	1.555
O4	P4	1.545
O5 (H1)	Al1 (H1)	1.778
O6	Al2	1.703
O7	Al3	1.702
O8	Al4	1.700
Co1	P1	3.223
Co1	P2	3.184
Co1	P3	3.109
Co1	P4	3.131
Ti1	Al1 (H1)	3.427
Ti1	Al2	3.293
Ti1	Al3	3.213
Ti1	Al4	3.213
O5	H1	0.983
Ti1	H1	2.561

Table 5.22: Calculated Mulliken populations for bimetallic $Co^{3+}Ti^{4+}$AlPO-5, without a Co-O-Ti bridge.

Atom	Placement	Electron count (α + β)	Electron spin (α – β)
Co1	Central atom	25.106	3.071
Ti1	Central atom	19.984	0.000
O1	First coordination shell (Co1)	9.040	0.240
O2	First coordination shell (Co1)	9.045	0.213
O3	First coordination shell (Co1)	9.038	0.203
O4	First coordination shell (Co1)	9.051	0.177
O5 (H)	First coordination shell (Ti1)	8.971	0.000
O6	First coordination shell (Ti1)	9.066	0.000
O7	First coordination shell (Ti1)	9.070	0.000
O8	First coordination shell (Ti1)	9.068	0.000
P1	Second coordination shell (O1)	12.756	0.002
P2	Second coordination shell (O2)	12.764	0.004
P3	Second coordination shell (O3)	12.774	0.002
P4	Second coordination shell (O4)	12.763	0.004
Al1	Second coordination shell (O5)	11.059	0.000
Al2	Second coordination shell (O6)	11.068	0.000
Al3	Second coordination shell (O7)	11.071	0.000
Al4	Second coordination shell (O8)	11.068	0.000
H1	Proton (O5)	0.655	0.000

5.6 Experimental section

Synthesis

The materials were synthesised using previously published procedures.[33] In summary the synthesis method of CoTiAlPO-5 involved mixing aluminium hydroxide hydrate (Aldrich) to a homogeneous solution of phosphoric acid (85% in H2O, Aldrich) in water. An aqueous solutions of cobalt(II) acetate tetrahydrate (Aldrich) and titanium isopropoxide (Aldrich) were added simultaneously. An aqueous solution of N,N-methyldicyclohexylamine (SDA) (Aldrich) was then added slowly with vigorous stirring to obtain a black gel with the composition 0.96Al: 1.50P: 0.80MDCHA: 50H_2O: 0.03Co: 0.03Ti. The gel was sealed in a Teflon-lined stainless steel autoclave and heated at 180 °C under autogeneous pressure for 2 hr. The blue solid product was obtained by filtration, washed with deionised water, and dried in air. The as-prepared sample was calcined under a flow of air at 550 °C for 12 hr yielding a green sample. Similarly CoAlPO-5 was synthesised with the gel ratio of 0.96Al: 1.50P: 0.8MDCHA: 40H_2O: 0.04Co and crystallised for 2 hours at 200 °C. This was calcined at 550°C for 12 hours again yielding a green sample.

EXAFS modelling

The catalyst was calcined prior to the *in situ* XAFS experiments to remove the template and then cycled through an oxidation1-reduction-oxidation2 cycle *in situ* using a custom designed XAFS cell.[43] Approximately 35 mg of ground catalyst powder, for each sample, was pressed into a 4-hole sample holder. The two samples in the holder were loaded into the reactor together so that they were treated at the same time. The samples were translated into the x-ray beam sequentially so that data could be collected from both samples. The oxidation1-reduction-oxidation2 cycle details are given as follows. Oxidation 1: ramp to 150˚C at 5˚C/min in 20% O_2/He and hold for 30 min, followed by cool to RT. Reduction: ramp to 500˚C at 5˚C/min in 100% H_2 and hold for 30 min, followed by cool to RT. Oxidation 2: ramp to 500˚C at 5˚C/min in 20% O_2/He and hold for 30 min, followed by cool to 150˚C. The EXAFS spectra were collected after this oxidation1-reduction-oxidation2 cycle at 150˚C in 20% O_2/He.

EXAFS spectra were collected in transmission mode at the MR-CAT beamline 10ID at the Advanced Photon Source at Argonne National Laboratory. The insertion device x-ray beam was defined to be approximately 1mm in both the vertical and horizontal. A double crystal monochromator with Si(111) crystals was used to select the incident X-ray energy. X-rays of higher harmonic energies were minimized using a Rh-coated mirror. The x-ray energy was calibrated using a Co foil, which was also collected with the measured data by using a reference ionization chamber. The ionization chamber gasses were optimized using 20/80 mixture of N_2/He for the incident x-ray intensity and 100% N_2 for the transmitted and reference x-ray intensity measurements.

The EXAFS spectra were modelled using ARTEMIS[44] and FEFF6.0[45] for the theoretical calculations based on crystal structures obtained by DFT calculations in this study and Co_3O_4. For monometallic CoAlPO, the EXAFS models include two single scattering O paths with Co-O distances of 1.87 and 1.98 Å respectively and one single scattering P path with Co-P distance of 3.1. For bimetallic CoTiAlPO, the EXAFS model included a Co-O-Ti path around 3.26 Å in addition to all the paths used for monometallic CoAlPO model. There are 12 and 16 parameters used to describe the monometallic and bimetallic models listed in Table 5.23: 6 and 8 coordination numbers (CN), 3 and 4 change in path length (ΔR), 2 and 3 mean square displacement of the half path length values (σ^2), and an energy shift parameter (ΔE), for monometallic and bimetallic respectively. The value for S_0^2 (0.82 ± 0.05) was determined from Co foil. The data range from 3.0 to 9.5 $Å^{-1}$ was used in the Fourier transform (FT) with k-weights of 1, 2 and 3. The model was applied to the FT range of 1.2 to 3.4 Å. The EXAFS data and model is shown in Figure 5.1. The EXAFS $\chi(k)\cdot k^2$ model follows the data best in the fitted data range from 3.0 to 9.5 $Å^{-1}$. The model was applied to each data set independently, but both reduction and oxidation2 data sets from the oxidation1-reduction-oxidation2 cycle were modelled simultaneously with only the CN determined independently for each condition. This dramatically increases the information content in the data to 39 independent points and 12 or 16 parameters.

Table 5.23: EXAFS model parameterisation

Neighbor	R (Å)	CN	ΔR (Å)	σ^2 (Å^2)
Co-O1	1.87	4 * F1	ΔRO1	σ^2O
Co-O2	1.98	4 * (1-F1)	ΔRO2	σ^2O
Co-P1	3.10	NP1	ΔRP1	σ^2P
Co-Ti1	3.26	NTi1	ΔRTi1	σ^2Ti

*One energy shift value was also determined for all paths.

Computational calculations

Computational *ab initio* calculations were performed on the University of Southampton Iridis3 supercluster with the CRYSTAL09 periodic DFT code[46] using the B3LYP hybrid-exchange functional.[46-50] The AFI framework was calculated using periodic boundary conditions and was assigned the P1 space group to allow full-optimisation of the unit cell-parameters. The electronic distribution of atoms was described as a linear combination of atomic orbitals and the basis functions are expressed as Gaussian-type orbitals. All aluminium, phosphorus, oxygen and hydrogen atoms were described using a double valence plus polarization basis set whereas titanium and cobalt were described using a triple-valence plus polarization basis set. All basis sets employed were taken from the online library for the CRYSTAL code.[51] The AFI structure was described by modelling one unit cell containing 72 atoms (12 aluminium, 12 phosphorus and 48 oxygen atoms). Cobalt was substituted for aluminium and titanium was substituted for phosphorus. In the case of a charge imbalance (Co^{2+} substituting Al^{3+} or Ti^{4+} substituting for P^{5+}) a proton was attached to an oxygen molecule adjacent to the divalent or tetravalent substituent. Only one substitution was made per metal per unit cell, corresponding to an 8.3 mol% loading, ensuring the metals were sufficiently separate and unable to interact with metals in neighbouring unit cells. In all cases no geometric constraints were applied and all coordinates and unit-cell parameters were free to vary. Each calculation was iteratively repeated until there was no change in geometry, to ensure full optimisation.

5.7 References

1. T. Maschmeyer, F. Rey, G. Sankar and J. M. Thomas, *Nature*, **1995**, *378*, 159-162.
2. A. T. Bell, *Science*, **2003**, *299*, 1688-1691.
3. J. Lee, O. K. Farha, J. Roberts, K. A. Scheidt, S. T. Nguyen, and J. T. Hupp, *Chem. Soc. Rev.*, **2009**, *38*, 1450-1459.
4. R. D. Oldroyd, J. M. Thomas and G. Sankar, *Chem. Commun.*, **1997**, *21*, 2025-2056.
5. A. Corma, L. T. Nemeth, M. Renz, and S. Valenica, *Nature*, **2001**, *412*, 423-425.
6. L. Kesavan, R. Tiruvalam, M. H. Ab Rahim, M. I. bin Saiman, D. I. Enache, R. L. Jenkins, N. Dimitratos, J. A. Lopez-Sanchez, S. H. Taylor, D. W. Knight, C. J. Kiely, and G. J. Hutchings, *Science*, **2011**, *331*, 195-199.
7. A. B. Hungaria, R. Raja, R. D. Adams, B. Captain, J. M. Thomas, P. A. Midgley, V. Golovoko and B. F. G. Johnson, *Angew. Chem. Int. Ed.,* **2006**, *45*, 4782-4785.
8. E. Gianotti, M. Manzoli, M. E. Potter, V. N. Shetti, D. Sun, A. J. Paterson, T. M. Mezza, A. B. Levy and R. Raja, *Chem. Sci.*, **2014**, *5*, 1810-1819.
9. R. M. Leithall, V. N. Shetti, S. Maurelli, M. Chiesa, E. Gianotti and R. Raja, *J. Am. Chem. Soc.*, **2013**, *135*, 2915-2918.
10. J. M. Thomas and G. Sankar, *Acc. Chem. Res.*, **2001**, *34*, 571-581.
11. M. G. O'Brien, A. M. Beale, S. D. M. Jacques, M. Di Michiel and B. M. Weckhuysen, *Appl. Catal. A-Gen.*, **2011**, *391*, 468-476.
12. C. O. Arean, B. M. Weckhuysen and A. Zecchina, A. *Phys. Chem. Chem. Phys.*, **2012**, *14*, 2125-2127.
13. C. Lamberti, S. Bordiga, F. Bonino, C. Prestipino, G. Berlier, L. Capello, F. D'Acapito, F. X. L. I. Xamena and A. Zecchina, *Phys. Chem. Chem. Phys.*, **2003**, *5*, 4502-4509.
14. S. A. Bartlett, P. P. Wells, M. Nachtegaal, A. J. Dent, G. Cibin, G. Reid, J. Evans and M. Tromp, *J. Catal.*, **2011**, *284*, 247-258.
15. J. P. Gilson, C. Fernandez and F. Thibault-Starzyk, *J. Mol. Catal. A-Chem.*, **2009**, *305*, 54-59.
16. R. Raja, G. Sankar and J. M. Thomas, *J. Am. Chem. Soc.*, **1999**, *121*, 11926-11927.
17. J. M. Thomas, R. Raja, G. Sankar and R. G. Bell, *Nature*, **1999**, *398*, 227-230.
18. X. Zhao, Z. Sun, Z. Zhu, A. Li, G. Li and X. Wang, *Catal. Lett.*, **2013**, *143*, 657-665.
19. D. G. Cheng, F. Chen and X. Zhan, *Appl. Catal. A: Gen.*, **2012**, *435-436*, 27-31.
20. H. K. D. Nguyen, T. N. Don, G. Sankar and C. R. A. Catlow, *Catal. Commun.*, **2012**, *25*, 125-129.

21. F. Cora, G. Sankar, C. R. A. Catlow and J. M. Thomas, *Chem. Commun.*, **2002**, *7*, 734-735.
22. J. Y. Wu, S. H. Chien and B. Z. Wan, *Ind. Eng. Chem. Res.*, **2001**, *40*, 94-100.
23. A. M. Beale, G. Sankar, C. R. A. Catlow, P. A. Anderson and T. L. Green, *Phys. Chem. Chem. Phys.*, **2005**, *7*, 1856-1860.
24. G. Sankar, R. Raja and J. M. Thomas, *Catal. Lett.*, **1998**, *55*, 15-23.
25. P. A. Barrett, G. Sankar, C. R. A. Catlow and J. M. Thomas, *J. Phys. Chem.*, **1996**, *100*, 8977-8985.
26. M. Vishnuvarthan, A. J. Paterson, R. Raja, A. Piovano, F. Bonino, E. Gianotti and G. Berlier, *Micropor. Mesopor. Mater.*, **2011**, *138*, 167-175.
27. S. Maurelli, G. Berlier, M. Chiesa, F. Musso and F. Cora, *J. Phys. Chem. C*, **2014**, *118*, 19879-19888.
28. E. Gallo, A. Piovano, C. Marini, O. Mathon, S. Pascarelli, P. Glatzel, C. Lamberti and G. Berlier, *J. Phys. Chem. C*, **2014**, *118*, 11745-11751.
29. A. Alfayate, M. Sanchez-Sanchez, J. Perez-Pariente, *Micropor. Mesopor. Mater.*, **2014**, *190*, 334-345.
30. S. Maurelli, M. Vishnuvarthan, M. Chiesa, G. Berlier and S. Van Doorslaer, *J. Am. Chem. Soc.*, **2011**, *133*, 7340-7343.
31. S. Maurelli, M. Vishnuvarthan, G. Berlier and M. Chiesa, *Phys. Chem. Chem. Phys.*, **2012**, *14*, 987-995.
32. C. Novara, A. Alfayate, G. Berlier, S. Maurelli and M. Chiesa, *Phys. Chem. Chem. Phys.*, **2013**, *15*, 11099-11105.
33. A. J. Paterson, M. E. Potter, E. Gianotti and R. Raja, *Chem. Commun.*, **2011**, *47*, 517-519.
34. J. M. Thomas, R. Raja and D. W. Lewis, *Angew. Chem. Int. Ed.*, **2005**, *44*, 6456-6482.
35. J. M. Thomas and R. Raja, Annu. Rev. Mater. Res., **2005**, *35*, 315-350.
36. M. E. Potter, D. Sun, E. Gianotti, M. Manzoli and R. Raja, *Phys. Chem. Chem. Phys.*, **2013**, *15*, 13288-13295.
37. M. Lefenfeld, R. Raja, A. J. Paterson and M. E. Potter, *US Patent* 021882, **2010**.
38. J. M. Thomas and R. Raja, *Proc. Natl. Acad. Sci.*, **2005**, *39*, 13732-13736.
39. S. O. Lee, R. Raja, K. D. M. Harris, J. M. Thomas, B. F. G. Johnson and G. Sankar, *Angew. Chem. Int. Ed.*, **2003**, *115*, 1558-1561.
40. F. Cora, M. Alfredsson, C. M. Barker, R. G. Bell, M. D. Foster, I. Saadoune, A. Simplerer, and C. R. A. Catlow, *J. Solid State Chem.*, **2003**, *176*, 496-529.

41. L. Gomez-Hortiguela, F. Cora, G. Sankar, C. M. Zicovich-Wilson and C. R. A. Catlow, *Chem. Eur J.*, **2010**, *16*, 13638-13645.

42. L. Gomez-Hortiguela, F. Cora and C. R. A. Catlow, *ACS Catal.*, **2011**, *1*, 18-28.

43. S. R. Bare, G. E. Mickelson, A. Z. Modica Ringwelski, and N. Yang, *Rev. Sci. Instrum.*, **2006**, *77*, 023105/1-023105/6.

44. J. J. Rehr, J. J. Kas, M. P. Prange, A. P. Sorini, Y. Takimoto and F. Villa, *C. R. Physique*, **2009**, *10*, 548-559.

45. M. Newville, B. Ravel, D. Haskel, J. J. Rehr, E. A. Stern and Y. Yacoby, *Physica B.*, **1995**, *208*, 154-156.

46. R. Dovesi, R. Orlando, B. Civalleri, C. Roetti, V. R. Saunders and C. M. Zicovich-Wilson, *Z. Kristallogr.*, **2005**, *220*, 571-573.

47. A. D. Becke, *J. Phys. Chem.*, **1993**, *98*, 5648-5652.

48. C. Lee, W. Yang, R. G. Parr, *Phys. Rev. B*, **1988**, *37*, 785-789.

49. S. H. Vosko, L. Willk and M. Nusair, *Can. J. Phys.*, **1980**, *58*, 1200-1211.

50. P. J. Stephens, F. J. Devlin, C. F. Chabalowski and M. J. Frisch, *J. Phys. Chem.*, **1994**, *98*, 11623-11627.

51. CRYSTAL Basis Sets Library. (http://www.crystal.unito.it/Basis_Sets/Ptable.html) accessed November 2011.

Chapter 6: Conclusions and future work

6.1 Conclusions

The merits of designing specific active sites, their incorporation into microporous frameworks and their use as catalysts have been evaluated. The catalytic potential of these materials has been tested for a variety of sustainable, industrially relevant processes. To gain a greater understanding into the structure-property relationships, which dictate the efficacy of these catalysts, multi-technique characterisation studies were performed. This has resulted in a holistic view of the influence of both the engineered active site and the precise framework architecture into which they have been incorporated. The effect of bimetallic substitution has been investigated using similar methods. Further the use of theoretical DFT methods has permitted further insight into the benefits of bimetallic substitution.

A sub-set of SAPO frameworks with contrasting framework topologies (SAPO-5, SAPO-34, SAPO-37 and SAPO-41), were employed to undertake a fundamental catalysis study on the Beckmann rearrangement of cyclohexanone oxime. The frameworks were specifically chosen so that they possess different pore diameters (ranging from 3.8 – 7.4 Å) and different architectures (1D channel v 3D cage). The samples were synthesised in a phase-pure manner and the acid-sites generated, from the isomorphous substitution of silicon into the framework, were examined using a range of characterisation techniques. ^{29}Si MAS NMR showed that SAPO-34 and SAPO-37 formed isolated silicon sites, generating Brønsted acidity, in contrast SAPO-5 and SAPO-41 showed significant amounts of silicon islanding. The nature of the silicon dopant was intrinsically linked to the type of acid sites generated. The SAPO-34 and SAPO-37 species (with isolated Brønsted acid sites) possessed significantly more acid sites than the SAPO-5 or SAPO-41. Through a combination of CO probed FT-IR and NH_3-TPD it was shown that the acid sites in SAPO-34 were significantly stronger than those in the SAPO-37 species, whereas the SAPO-5 and SAPO-41 systems possessed similar strength acid sites. These findings were in agreement with the similar substitution mechanism in operation, as seen by the ^{29}Si MAS NMR. The systems were also probed using collidine-probed FT-IR, which revealed that the collidine only had complete access to the SAPO-37

system, with limited access to the interior of SAPO-5. It was concluded that the collidine could only access surface sites in the SAPO-34 system. The collidine findings were commensurate with the catalytic results for the liquid phase Beckmann rearrangement of cyclohexanone oxime. This suggests that the internal diffusion of cyclohexanone oxime, and therefore access to the acid sites located within the microporous framework, is vital for enhancing the activity of this reaction. In contrast the findings from the vapour-phase Beckmann rearrangement at 400 °C suggested that at higher temperatures the surface sites played a fundamental role, as witnessed by the enhanced caprolactam yield achieved by SAPO-34. The high conversions achieved in the liquid-phase Beckmann rearrangement by SAPO-37 merited further testing and synthesis optimisation. As such, an investigation into the effect of modifying the silicon loading was performed. It was concluded that increased silicon loading facilitated type III substitution of the silicon, and formed fewer, and stronger, Brønsted acid sites. This subsequently led to reduced activity and selectivity. By limiting the silicon loading it was possible to form the isolated acid sites in a targeted manner, thus increasing the yield of caprolactam. By performing this reaction under anhydrous conditions it was found that near-quantitative yields of caprolactam could be achieved at temperatures as low as 130 °C in less than 5 hours, making it of considerable industrial interest.[1]

Once the effect of specific frameworks was investigated, the effect of bimetallic substitution on both the vapour-phase Beckmann rearrangement and the isopropylation of benzene was examined. The AlPO-5 topology was selected given its robustness and relative ease to synthesise. It was shown that the incorporation of three different dopants (Mg^{2+}, Zn^{2+} and Si^{4+}), provoked different catalytic responses from both the reactions tested. It was shown that while the MgAlPO-5 performed well for the isopropylation reaction (which is known to require strong acid sites), and the SiAlPO-5 performed well for the Beckmann rearrangement (known to require weak acid sites), the ZnAlPO-5 performed poorly for both reactions. By considering the signal intensities in the CO-probed FT-IR spectra of these three systems (and comparing them to the undoped AlPO-5), it was found that Mg^{2+} and Si^{4+} had both undergone framework substitution, as seen by the presence of increased Brønsted acidity. In contrast the incorporation of zinc was found to have little effect on the Brønsted acidity, thus is believed to have formed extra framework ZnO species.

By using lutidine as a probe it was possible to quantify the strength of the brønsted acid sites by observing the peak position of the v_{8a}(CC) stretch. The combination of the two FT-IR techniques confirmed the presence of strong Brønsted acid sites in MgAlPO-5, weak sites in SiAlPO-5 and an absence of Brønsted acidity in ZnAlPO-5. New synthetic protocols were designed to create MgZnAlPO-5 and ZnSiAlPO-5. Contrasting the activity of these two samples with the appropriate monometallics showed that the MgZnAlPO-5 produced more caprolactam and less cumene. In contrast the ZnSiAlPO-5 produced less caprolactam and more cumene. The contrasting behaviour of zinc with different metals and difference reactions suggests that it is acting as neither poison nor promoter; instead it must be modifying the Brønsted acid sites to alter the catalytic behaviour. The combination of CO and lutidine-probed FT-IR showed that the presence of zinc was lowering the total acidity of the samples and altering the acid strength. It was found the addition of zinc was weakening the strong acid sites present in MgAlPO-5, and strengthening the weak acid sites in SiAlPO-5. This shows that by forming bimetallic zinc-containing AlPO samples one can selectively alter the properties of the acid sites by forming specific metal-metal interactions.[2] In contrast the combination of Mg^{2+} and Si^{4+} species to yield MgSiAlPO-5 resulted in improved yields of both caprolactam and cumene. This is attributed to the combination of the two acid sites improving the activity of different steps in the multi-step mechanism of the isopropylation and the Beckmann reactions. Thus different acid sites were able to enhance different steps of the pathway.[3]

Finally the effects of bimetallic substitution were investigated using a combined EXAFS and DFT study on CoTiAlPO-5. Previous work on CoTiAlPO-5 had shown that a catalytic synergy exists between the $Co^{2+/3+}$ and Ti^{4+} ions for oxidation reactions, which only occurs when both ions are simultaneously substituted into the same framework.[4] This phenomenon was first investigated using XAS techniques, which revealed that a Co-O-Ti bond is present in the bimetallic system in both its oxidised and reduced forms, however this species is not present at all in the monometallic species. This confirmed the proximity of the two metals in the system. Periodic DFT calculations confirmed the preference of the two elements to undergo adjacent isomorphous substitution. Further, these structural investigations revealed that the behaviour of the cobalt ion is subtly different between the two systems. It was shown that when

the titanium is adjacent to the cobalt, the redox potential of the cobalt is modified, thus stabilising the divalent Co^{2+} state to a greater extent than in the monometallic system. Previous work has shown that the rate-determining step in oxidation reactions involves the reduction of Co^{3+} to Co^{2+}, thus stabilising the Co^{2+} state can lower than transition state energy of the rate-determining-step.[5] This notion was furthered by considering the initial steps in the activation of ammonia to form hydroxylamine. It was found that given the enhanced redox potential in CoTiAlPO-5 over CoAlPO-5, the activation energy of the initial step (breaking of the N-H bond) was lower in the bimetallic system. This should then lead to it being a more suitable and effective catalyst for this reaction. By investigating the spins and bond lengths of the step it was shown that the bimetallic system retains the Co-N bond, which stabilises the NH_2radical formed, whereas the monometallic system does not. The stabilisation of the NH_2 radical by O_2 to form the NH_2OO radical was also investigated. The activation energy of this step was found to be significantly lower than that of the initial ammonia activation step. Thus the enhanced activity of the bimetallic system was linked to its greater redox potential and therefore the retention of the Co-N bond.

In conclusion a range of novel bimetallic sites were synthesised, tested and investigated using a range of techniques. It is hoped that the synthetic methods and active-site design strategies used in this work will be further developed to create more specifically designed active sites that may enhance the catalytic activity of a range of industrial processes.

6.2 Future work

There are three main areas in which this work may be extended, these are:

- Development of new catalyst design strategies
- The use of new substrates
- Further characterisation studies

Development of new catalyst design strategies - Hierarchical materials

While microporous materials have many advantages, offering a range of different selectivities designed to control the final product of the reaction, they are by their very nature limited by the micropores themselves. The use of narrow pore channels (< 10 Å) means that even the most active reactions will eventually be limited by diffusion of reactants to the active site, and of products away from the active site. This limited diffusion has been shown previously to be one of the primary reasons for catalyst deactivation through 'coking' mechanistic pathways.[6] In zeolite science there has recently been significant interest in developing hierarchically porous materials, a microporous material, intertwined with bisecting amorphous mesopores. It is believed that the larger mesopores aid diffusion of reactants, and therefore extend the lifetime of the catalysts for a range of processes.[7] By applying similar synthetic techniques (soft-templating) one can envisage forming similar AlPO materials, with mesopores existing within the microporous framework. This could be achieved by incorporating surfactant molecules, such as DMOD ([3-(trimethoxysilyl)propyl]-octa- decyldimethyl-ammonium chloride) or CTAB (hexadecyltrimethylammonium bromide), into the microporous gel synthesis. This type of material presents new challenges in characterisation, namely showing that there is only one phase present which possesses both micropores and mesopores, as opposed to two separate phases. Through a combined use of TEM and BET techniques it is possible to allude to the presence of one phase.

In these systems there exists the potential to create modified active sites. The use of surfactants may alter the crystallisation kinetics of the metal-doped systems, leading to the formation of different active sites within the mesopores. Further to this it is possible to incorporate new active sites into the hierarchical system that could not be introduced into microporous materials owing to size constraints. An example of this would be metal nanoclusters. These species are too large to fit inside a micropore, however they could be tethered to the mesopores. This would then ensure that different species were present inside the micropores and mesoporoes, which could aid bifunctional catalysis.

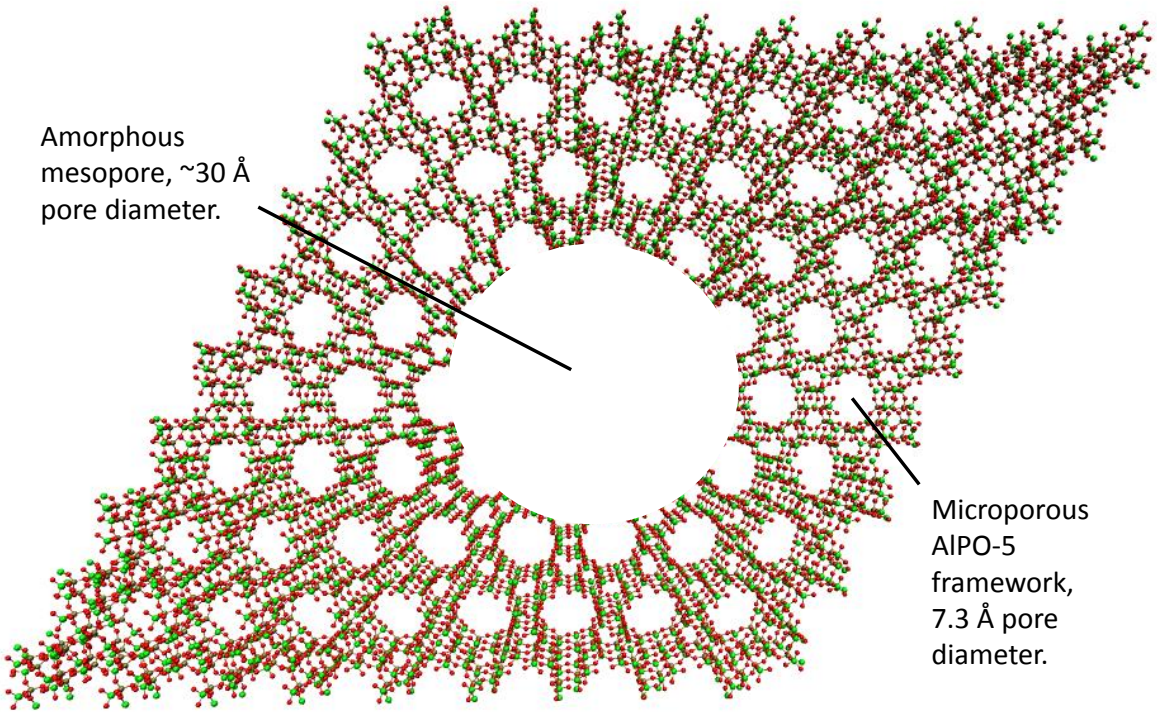

Figure 6.1: Demonstrating hierarchical molecular sieves.

Finally if the same active sites that are present in the micropores can be engineered into the mesopores, then this allows a host of bulkier reactants to be employed with an AlPO catalyst. This is something that could be of significant benefit in the pharmaceutical industry, expanding the scope of useful reactions performed by AlPOs.

Development of new catalyst design strategies - Introduction of organic groups

The development of novel zeotype materials represents a promising strategy in tackling the environmental issues of the developed world, such as sustainable energy production and carbon capture. To date zeolites are considered the industrial standard for many environmental applications, yet their rigid inorganic framework hinders the precise modifications that are routinely employed in organic synthesis. These limitations prompted the evolution of metal-organic-frameworks, which whilst offering a plethora of post-synthesis possibilities are impeded by their limited stability. As such, the ability to form a material combining a stable inorganic support with a tuneable organic entity is highly desirable from an academic and industrial standpoint. While this

methodology has been investigated for zeolites, few groups have attempted analogous approaches with aluminophosphates (AlPOs).

The AlPO literature contains a myriad of examples of framework substitution, the vast majority of which is limited to transition-metal dopants. Through the isomorphous substitution of organosilyl groups it is possible to generate an organic moiety inside the microporous framework.[8] Whilst a whole spectrum of organosilyl species exists, effective design strategies need to be engineered for facilitating a wider range of post-synthetic applications. The prospect of producing a versatile material, capable of anchoring a range of functional groups for gas-adsorption and organocatalysis in one-step is appealing. Further it makes the thiol-silyl AlPO species highly versatile and a promising prospect for generating the first dextrous organically tethered AlPO system.

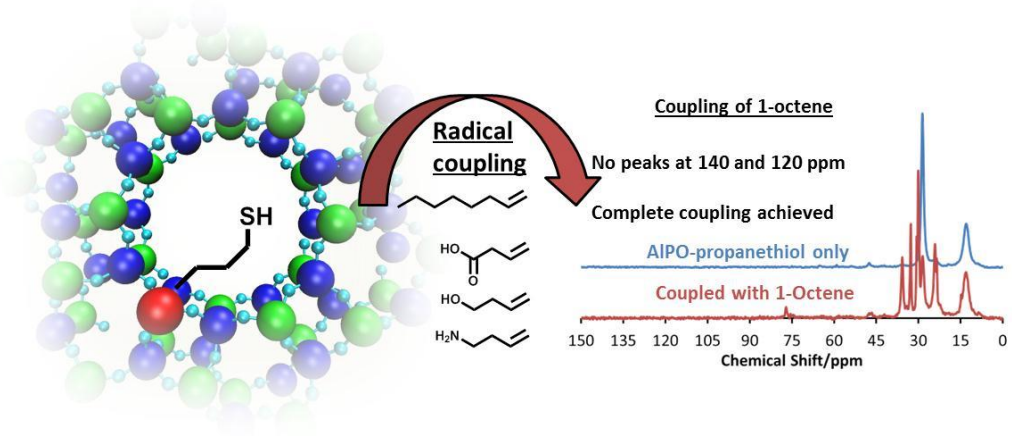

Figure 6.2: Schematic of radical coupling reactions and tethering possibilities.

Further to this one may utilise powerful Au-S bonds to generate a range of metal nanoparticles within the AlPO framework using similar technologies, which could be utilised for oxidation reactions:

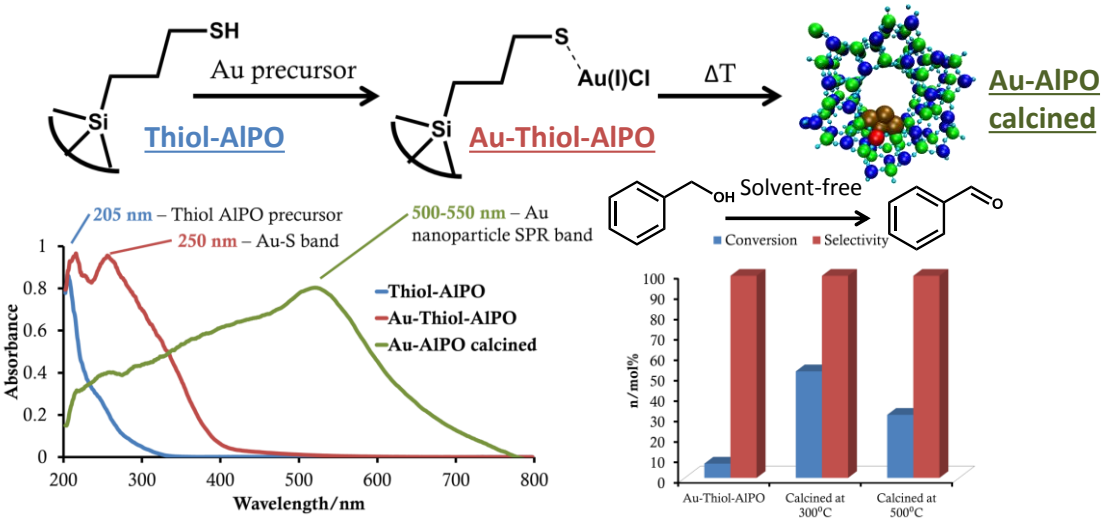

Figure 6.3: Generation and activity of Au-nanoparticles for the oxidation of benzyl alcohol. Reaction conditions: 94°C, 3hrs, 5.2 mmol of benzyl alcohol, 7.8 mmol of TBHP, 50 mg of catalyst.

Thus there is significant scope for combining AlPO frameworks (even metal-doped AlPO frameworks) with organothiol precursors to manufacture a range of novel active sites or organic species within an AlPO pore.

The use of new substrates - Biomass transformations

The use of biomass feedstocks is of significant interest in increasing sustainability in a wide range of reactions. This has led to alternative pathways and even alternative precursors being used in a range of processes. As an example terephthalic acid is an important precursor in the plastics and polymer industry, however it is primarily produced from non-renewable fossil fuels, however more recently FDCA (2,5-Furandicarboxylic acid) is being explored as an alternative. This notion is appealing given the sustainable way in which it can be produced from cellulose.

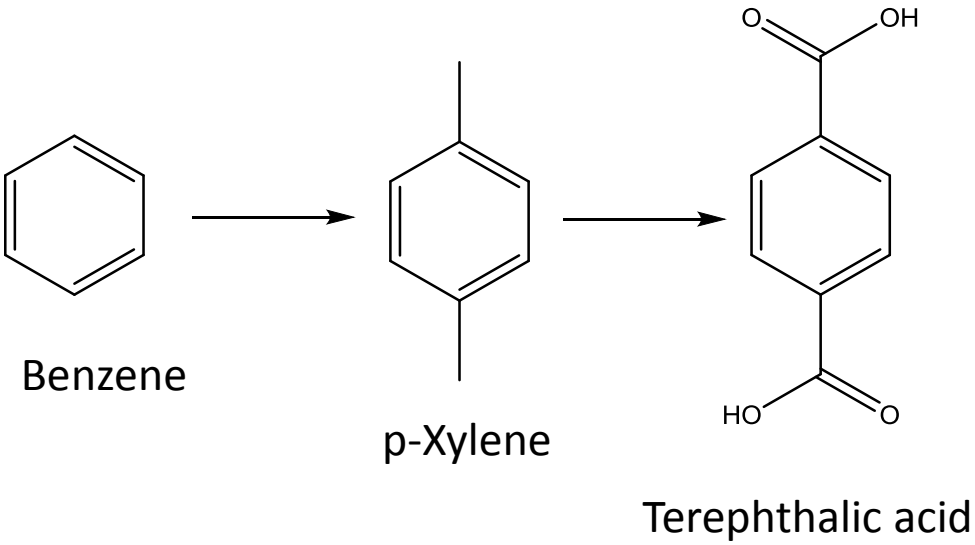

Figure 6.4: Synthetic pathway to terephthalic acid.

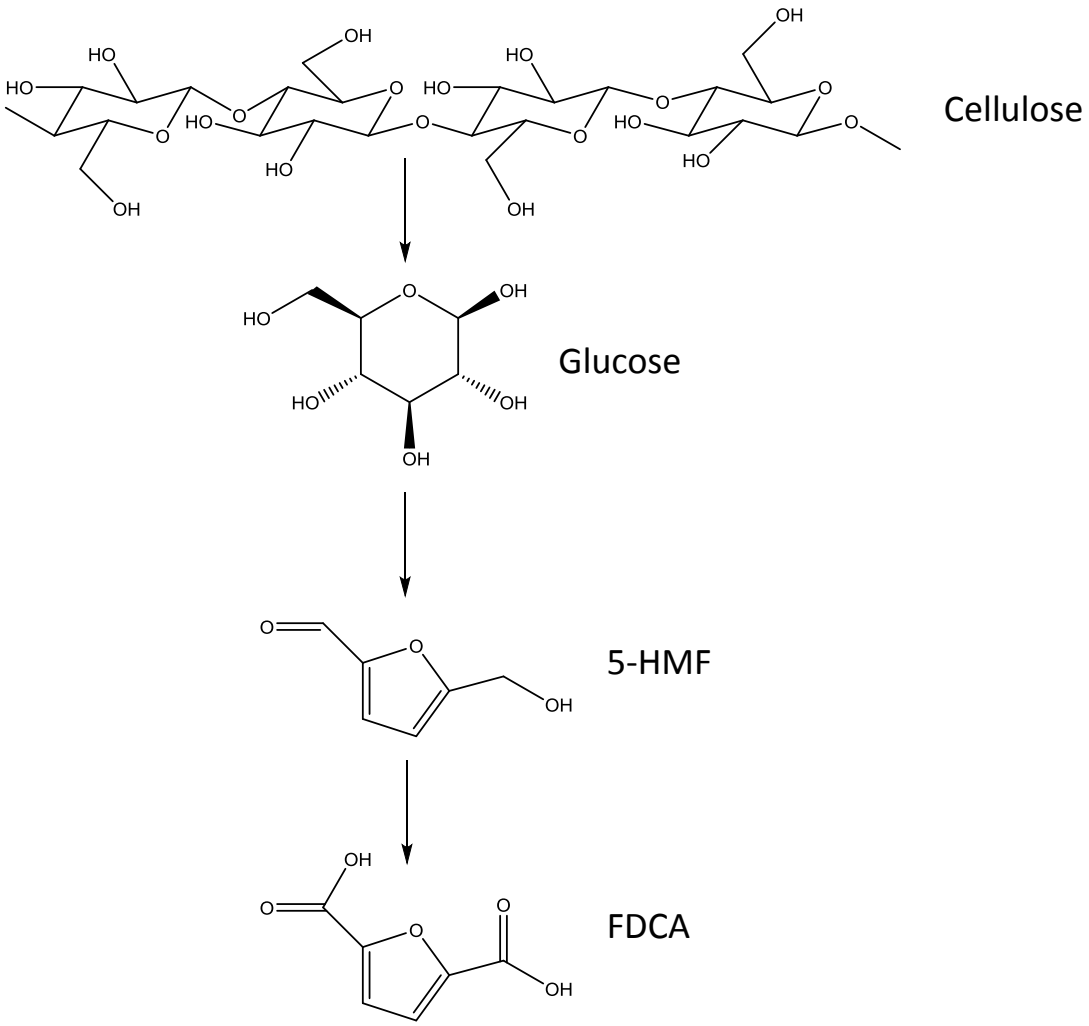

Figure 6.5: Sustainable synthetic pathway to FDCA.

AlPOs in particular would be of great interest for this procedure, given their ability to generate bifunctional (brønsted acid and redox) catalysts. By employing similar catalysts to the production of ε-caprolactam (MnMgAlPO-5)[9,10] it would be possible for the acidic magnesium sites to perform the dehydration reaction of glucose to 5-HMF, whilst the redox active manganese sites form then perform the oxidation of 5-HMF to FDCA, utilising tandem catalysis methods. Given the vast range of sites it is possible to engineer into such molecules and the control over the framework, they would be excellent candidates for performing this type of reactions.

The use of new substrates - Dehydration of bioethanol

There has been significant interest in the use of bio-ethanol as a feedstock for ethylene production. Previously it has been demonstrated that metal-doped SAPOs and AlPOs are capable of efficiently performing this reaction at low temperature (< 300 °C).[11] Similar protocols to form novel bimetallic acid sites as described previously in this work, may be used to modify the active sites to enhance the activity and specificity of this reaction. Currently the mechanism by which this reaction occurs is under debate, specifically the role of diethyl ether.

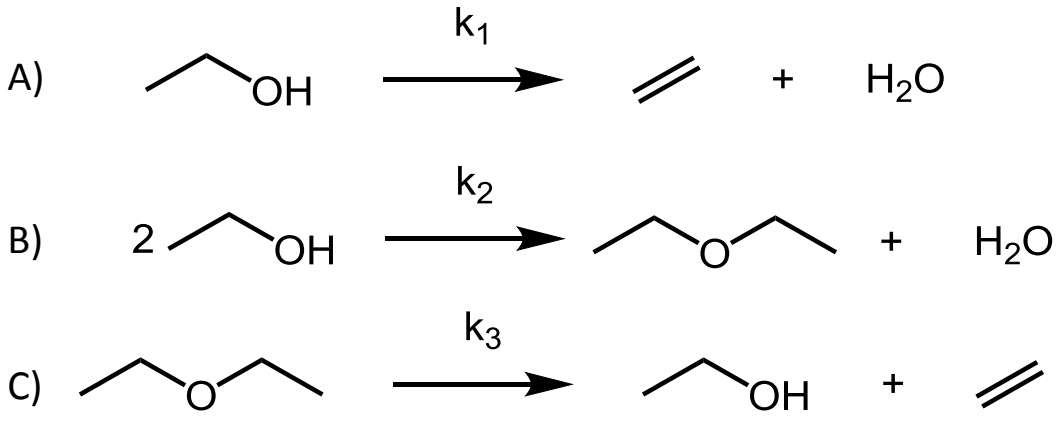

Figure 6.6: Scheme of the ethanol dehydration mechanism.

The mechanism could be uncovered by performing a kinetic study and monitoring the concentrations of the ethanol, diethyl ether and ethylene. This could be in the form of a catalytic study, alternatively an *in situ* MAS NMR study

observing the ^{13}C nuclei, or a DRIFTS study to observe the signals from a doped solid pellet of catalyst.

By uncovering the mechanism it would then be possible to design the specific active site and optimise the reactivity of the rate-determining step, this would allow near quantitative yields of ethylene to be formed, potentially at temperatures less than 200 °C.

Further characterisation studies

The use of zeolites and analogous zeotype catalysts is prolific in a wide-range of industrial processes. Their dominance is particularly note-worthy in the petrochemical industry; however such materials are also becoming pivotal in other areas such as the polymers and plastics industry. A particularly noteworthy example is the gas-phase Beckmann rearrangement of cyclohexanone oxime to produce ε-caprolactam (the monomer for nylon-6). This process aims to reduce the use of mineral acids and promotes the use of a solid-acid catalyst (silicate-1, MFI) to effect the Beckmann rearrangement, in the vapour-phase, at temperatures of around 300 °C. Given the attractive merits of minimising waste and improving atom efficiencies, there has been significant interest in the use of HZSM-5 for this reaction, both from an academic and industrial perspective. A wide-range of structural and physico-chemical studies have been carried out on HZSM-5, with a view to investigating aspects of the process, ranging from catalyst composition, the exact nature of the acid site, interaction with solvents, reactants, by-products, catalyst deactivation and diffusion to name but a few.[12]

To date, there is still significant debate in the academic literature as to the role of the internal and external acid sites for the Beckmann rearrangement, an important catalytic transformation. The root of the uncertainty lies in the similarity in the pore dimensions of the 10-ring pore aperture in the MFI topology (5.1 x 5.5 Å and 5.3 x 5.6 Å pores) and the size of the cyclohexanone oxime molecule (~5.0 Å). In the vapour-phase, reaction temperatures of 300 °C can allow diffusion to play a crucial role in the catalytic processes and, *in situ* operando and spectroscopic techniques, which can allow the diffusion of such

molecules to be monitored at the molecular level, are of great interest for understanding the kinetics and thermodynamics associated with this process.

There have been very few reports in the open literature that demonstrate the effectiveness of catalysing the Beckmann rearrangement in the liquid phase.[11] Whilst it has been shown that the MFI framework of HZSM-5 was highly active in the vapour-phase,[12] it exhibited significantly less activity than the larger-pore faujasitic framework of zeolite-Y (12 membered rings, 7.4 Å) with identical Si/Al ratio (both 15). In light of this, we have targeted a design strategy that specifically tailors and modulates active acid-sites within the larger pore-aperture of faujasite, leading to the design and creation of a silicon-doped aluminophosphate analogue; SAPO-37.[11] It is believed that at the lower temperatures of 130 °C, utilised in the liquid-phase process, diffusion into the micropores and availability of weak Brønsted acid sites in the vicinity, plays a cardinal role in influencing the activity and selectivity of the reaction. In contrast, with the higher temperature gas-phase reaction, diffusion of the oxime molecule directly into the pores is much more readily facilitated due to thermodynamic factors. Currently it is unknown whether this behaviour is a direct result of the temperature limiting diffusion to the internal active (acid) sites, or whether this is a consequence of different reaction pathways occurring at different locations (surfaces or internal) of active site. In order to find this out a QENS (Quasi-Elastic Neutron Scattering experiment) using cyclohexanone oxime as an organic dopant molecule would be highly beneficial. By directly observing the diffusion behaviour of this molecule among these specific frameworks it would be possible to gain significant insight into the nature of this framework.

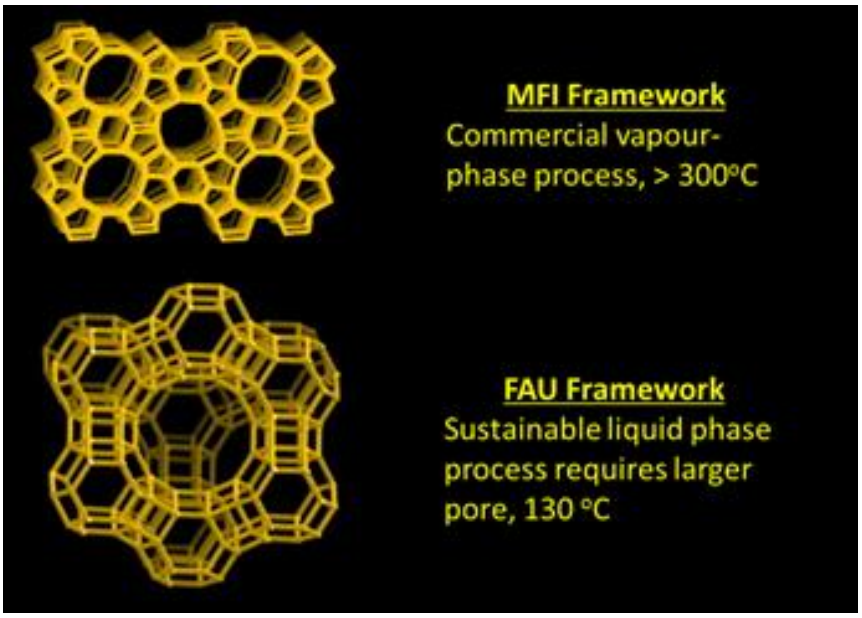

Figure 6.7: Summary of catalytic findings based on framework topology for the Beckmann rearrangement of cyclohexanone oxime.

6.3 References

1. A. B. Levy, R. Raja and M. E. Potter, *US Pat.*, US20130109851, **2013**.
2. M. E. Potter, D. Sun, E. Gianotti, M. Manzoli and R. Raja, *Phys. Chem. Chem. Phys.*, **2013**, *15*, 13288-13295.
3. E. Gianotti, M. Manzoli, M. E. Potter, V. N. Shetti, D. Sun, A. J. Paterson, T. M. Mezza, A. Levy and R. Raja, *Chem. Sci.*, **2014**, *5*, 1810-1819.
4. J. Paterson, M. E. Potter, E. Gianotti and R. Raja, *Chem. Commun.*, **2011**, *47*, 517-519.
5. L. Gomez-Hortiguela, F. Cora, G. Sankar, C. M. Zicovich-Wilson and C. R. A. Catlow, *Chem. – Eur. J.*, **2010**, *16*, 13638-13645.
6. T. Takahashi, T. Kai and E. Nakao, *Appl. Catal. A: Gen.*, **2004**, *262*, 137-142.
7. R. Srivastava, M. Choi and R. Ryoo, *Chem. Commun.*, **2006**, *43*, 4489-4491.
8. K. Maeda, Y. Mito, T. Yanagase, S. Haraguchi, T. Yamazaki and T. Suzuki, *Chem. Commun.*, **2007**, *3*, 283-285.
9. R. Raja, G. Sankar and J. M. Thomas, *J. Am. Chem. Soc.*, **2001**, *123*, 8153-8154.
10. J. M. Thomas and R. Raja, *Proc. Natl. Acad. Sci. U. S. A.*, **2005**, *102*, 13732-13736.
11. M. Lefenfeld, R. Raja, A. J. Paterson and M. E. Potter, *US Pat.*, US2010085708, **2010**.
12. Y. Izumi, H. Ichihashi, Y. Shimazu, M. Kitamura and H. Sato, *Bull. Chem. Soc. Jpn.*, **2007**, *80*, 1280-1287.

Acknowledgements

Four years always sounds like an awful lot of time until you actually try to look back at it, and then for some reason it seems so very short! They do say that time flies when you're having fun, and these last four years have been very good times. Looking back there's very little I would do differently, which has to be one of the biggest testaments to how much you've enjoyed your time. My PhD would obviously not have been anywhere near as enjoyable if it weren't for the people I spent it with. At the end of the day it's the people that make an experience what it is, and I consider myself very proud and fortunate to have spent my time with such an excellent group of people. I could go through everyone and give them their own acknowledgement, though there are a few who stand-out and deserve personal mentions.

Firstly, and most importantly I would like to thank my supervisor, Dr. Robert Raja. I still remember asking to work in his group at the end of my second year of my undergrad and thankfully he said yes! I've not looked back since and couldn't really imagine enjoying a PhD as much as I have done in his group. Robert has been a true friend over these last years. The amount he genuinely cares for his students clearly shines through, one of the many things that make him a fantastic boss. Don't get me wrong I've been tearing my hair out because of him on multiple occasions! But in hindsight they were all for my own good. He has been a faultless supervisor, mentor and friend over the years and someone I am truly, truly grateful to, for helping me with all the ups-and-downs over the years. Thank you Robert!

I would also like to thank my industrial supervisor Dr Alan Levy for his contributions to this PhD, for his funding and his understanding over the last four years and also for his insights, help and guidance.

I've also got to extend my thanks to Dr. David Xuereb. David was a fantastic friend and always understanding and always helped me look at things in a different light, not just in chemistry. He was genuinely a pleasure to work with and someone who lead by example both in chemistry and in life. I learned a lot from him and am grateful for all the life lessons and laughs. I wish you and Holly all the best in life!

My next partner in crime I'd like to thank goes to the soon-to-be Dr. Adam Keates. A late addition to the Raja group, but a most welcome one. Since our undergrad your relaxed and laid-back attitude to life has been an excellent source of calm for me. The number of times I must have vented at you and I came away feeling better must be nearing triple figures! I hope legends of our lab-based pranks out-last both of us in the Raja group!

I would also like to extend my thanks to Stephanie Newland, whose constant cheerful disposition and liberal and realistic view to life and work has been an excellent complement to my own personal style of cynical semi-organised chaos. Despite my initial reservations, she has been a delight to work with, spend beam-times with and go on conference with! Steph, I hope you never have to talk about aluminium sources again after I'm gone!

PhD's are difficult at times. Some may consider this an understatement. But, everyone will agree there are many times when you need the love and support of friends around you. I can't name all my friends here, but a special thank you goes to another soon-to-be Dr. Isabelle Kirby. Over the four years she has helped me, and helped to organise me a lot! Our sessions complaining about the occasionally moronic undergrads we had to teach, and shared pains over PhD life, and for everything else were very much appreciated. Cheers Issy!

Speaking of undergrads, sometimes you meet your best friends in places you'd never expect. For myself, I never expected to encounter two exceptional people in teaching labs, of all places! Despite this I consider myself incredibly lucky that I met two fantastic young-women whilst teaching, Sivan Van Aswegen and Stephanie Chapman. You two have both been an absolute rock for me, my confidants, and two of the best friends I will ever have. You've both been there for me through thick and thin and for some bizarre reason have always shown me unquestionable loyalty and support. I'll always remember the times we spent together because they meant so very much to me. I cannot thank you both enough for everything you've done for me, you'll never know how much it meant to me. Between the two of you, you know how to save a life.

Finally, I would like to thank my wife, Emma. For all the times she's heard me complain, all the annoyed phone calls, all the times I've talked nonsensical science at her, all the times she's driven me to the lab late at night, all the times she's told me it'll be ok, all the times she's been there for me after a

hard day. The list goes on. I am incredibly grateful to her for all her contributions, support and love.

To all my collaborators and co-authors, thank you so much for all your time, your expertise, your knowledge and wisdom and your help! It has been very much appreciated!

To the rest of the Raja group, post-graduates, post-docs and under-graduates, past and present, thanks for the memories, the good times, the bad times, the trips to the Drummond, the wine, the cheese, the help, the room of consequence and most importantly the laughs! Cheers guys! Take care, look after each other and good luck with everything!